UNIVERSITÀ DI PARMA

# UNIVERSITÀ DEGLI STUDI DI PARMA

DOTTORATO DI RICERCA IN
Scienza e Tecnologia dei Materiali

CICLO XXXVI

# Eco-design of advanced materials for the protection of the environment and human health

Coordinatore:
Chiar.mo Prof. Dalcanale Enrico

Tutore:
Chiar.ma Dott.ssa Blosi Magda

Dottorando: Brigliadori Andrea

Anni Accademici 2020/2021 – 2022/2023

# Eco-design of advanced materials for the protection of the environment and human health

All or part of this work has been or will be published in scientific papers in peer-reviewed scientific journals.

# Abstract

The widespread manufacturing of nanomaterials and nano-enabled products (NEPs) has led to concerning human and environmental exposure levels. The lack of knowledge regarding the occupational, consumer, and environmental potential adverse effects of this burgeoning technology has ignited serious safety issues and highlighted the importance of a comprehensive risk evaluation. Safety and Sustainability by Design (SSbD) is a concept that thanks to a prevention approach aims to reduce the hazards at the early stages of product development. The combined implementation of safety measures and risk assessment will have to meet regulatory infrastructures to deliver SSbD guidelines and tools. To reach this goal it will be crucial to monitor the effects of these products and their manufacturing processes on human and environmental health. Structure-properties correlations must be studied to determine general guidelines and deliver safer and more sustainable design alternatives to the actual nanomaterials. A proper design of the synthesis step directly affects the structure of the nanomaterials allowing to building of the desired physicochemical, functional, and safety profiles. In this context, the design or re-design of a nanomaterial is an early-stage measure that can effectively improve the safety and sustainability of the product creating a bridge between design space and functional properties. A full life cycle assessment is required to link the nanomaterials design step to the nano-enabled products manufacturing, use phase, and end of life.

To contribute to this research field, during this work, three main topics were assessed: the synthesis of antimicrobial silver nanoparticles and their implementation into several case studies, the synthesis of gold-platinum nanoparticles for application as a catalyst in biomass valorization, and the production of biopolymeric scaffolds embedding natural-derived active phases for the wastewater remediation.

Three AgNPs synthesis methods using different capping agents were studied:

- *Quaternized hydroxyethyl cellulose* is a natural-derived biopolymer with positive charged quaternary ammonium groups that confers antibacterial activity to this compound.
- *Curcumin* is a natural-derived organic molecule with intrinsic antimicrobial and antioxidant properties.
- *Cyclic lipopeptide biosurfactant* derived from bacterial metabolism which possesses antimicrobial properties thanks to its cell wall lysis capability.

A wide-ranging physicochemical characterization (TEM, XRD, ICP-OES, UV-Vis, DLS, ELS) was performed to correlate synthesis parameters to physicochemical and functional properties.

The so-obtained AgNPs were tested against Gram-negative (*Escherichia coli*) and Gram-positive (*Staphylococcus aureus* and *Listeria innocua*) bacteria, demonstrating excellent antibacterial activity against all the tested bacterial strains. Antiviral tests were performed against the SARS-CoV-2 enveloped virus and BK polyomavirus non-enveloped virus, proposing an antiviral mechanism of action of AgNPs involving the interaction of AgNPs with the viral envelope inhibiting the attachment to cell's receptors.

The most active AgNPs variants were selected for the implementation into nano-enabled products within different case studies: antimicrobial textiles, paper, and biopolymeric film and scaffolds. The antimicrobial properties were successfully transferred from the nanomaterial to the nano-enabled product. Thanks to these case studies workers, users, and environmental exposures were assessed. NEPs antibacterial efficacy and product durability were evaluated.

The Safe and Sustainable by Design approach was applied for the synthesis of gold-platinum nanoparticles catalysts. The green chemistry principles were implemented on multiple levels, first for the safe and sustainable synthesis of the nanoparticles and then in their application for biomass valorization by converting biomass wastes into chemical building blocks. Two different gold-platinum nanoparticles structures were studied core-shell (gold core and a platinum external shell) and alloy. The correlation between the structure and the catalytic activity of these materials was studied thanks to an in-depth physicochemical characterization (TEM, XRD, ICP-OES, UV-Vis, DLS, ELS). The catalytic activity was evaluated in the model reaction of hydrogenation of nitrophenol to aminophenol. Synergistic effects were observed for the bi-metallic nanoparticles, thanks to which a reduced load of platinum allows excellent catalytic activity.

The increasing contamination of hydric resources caused by human activities has highlighted the necessity to develop new technologies for wastewater remediation. From a circular economy perspective, natural adsorbent materials were selected for this purpose. Clays and hydrotalcites share a layered structure able to host counterions, the deriving ion exchange capability has been efficiently exploited for the adsorption of heavy metals and organic pollutants. The selected adsorbents were characterized by XRD, BET, and ELS, subsequently, they were tested in the adsorption of simulated pollutants, namely the cationic dye rhodamine B, anionic dye methyl orange, and copper (II) cation. Clays and hydrotalcites were embedded into renewable seaweed-derived biopolymeric scaffolds made of k-carrageenan, chitosan, or agarose to improve their handleability. The pollutants adsorption tests were replicated on the scaffolds and the resulting adsorption process kinetic followed the pseudo-second-order model.

# Table of contents

# List of abbreviations

| | |
|---|---|
| AgCMC | Carboxymethyl cellulose-capped silver nanoparticles |
| AgCur | Curcumin-capped silver nanoparticles |
| AgEC | Ethyl cellulose-capped silver nanoparticles |
| AgHEC | Quaternized hydroxyethyl cellulose-capped silver nanoparticles |
| AgHEC_n | Hydroxyethyl cellulose-capped silver nanoparticles |
| AgHPC | Hydroxypropyl cellulose-capped silver nanoparticles |
| AgNPs | Silver nanoparticles |
| AgSur | Sodium surfactin-capped silver nanoparticles |
| AuNPs | Gold nanoparticles |
| AuPtNPs | Gold-platinum nanoparticles |
| AuPtNPs-a | Gold-platinum nanoparticles alloy |
| AuPtNPs-cs | Gold-platinum nanoparticles core-shell |
| CAS | Chemical Abstracts Service |
| $CC_{50}$ | Cytotoxic concentration causing 50 % cells viability reduction |
| CMC | Carboxymethyl cellulose |
| Cur | Curcumin |
| DLS | Dynamic light scattering |
| DoE | Design of Experiment |
| EC | Ethyl cellulose |
| EDX | Energy dispersive x-ray spectroscopy |
| ELS | Electrophoretic light scattering |
| FtsZ | Filament temperature-sensitive protein Z |
| HAADF | High-angle annular dark field |
| HEC | Quaternized hydroxyethyl cellulose |
| HEC_n | Hydroxyethyl cellulose |
| HPC | Hydroxypropyl cellulose |
| HRTEM | High-resolution transmission electron microscopy |
| $IC_{50}$ | Inhibitory concentration causing 50 % viral replication reduction |
| ICP-MS | Inductively coupled plasma – mass spectroscopy |
| ICP-OES | Inductively coupled plasma – optical emission spectroscopy |
| ICV | Internal calibration verification |
| IEP | Isoelectric point |

| | |
|---|---|
| MeNPs | Metallic nanoparticles |
| MIC | Minimum inhibitory concentration |
| MWCO | Molecular weight cut-off |
| n.d. | Not detected/not determined |
| NMWL | Nominal molecular weight limit |
| NPs | Nanoparticles |
| PDI | Polydispersity index |
| PtNPs | Platinum nanoparticles |
| PVP | Polyvinylpyrrolidone |
| ROS | Reactive oxygen species |
| RT-qPCR | Real-time quantitative polymerase chain reaction |
| SAED | Selected area electron diffraction |
| SEM | Scanning electron microscopy |
| SI | Selectivity index |
| SPR | Surface plasmon resonance |
| STEM | Scanning transmission electron microscopy |
| Sur | Sodium surfactin |
| TEM | Transmission electron microscopy |
| TRL | Technology readiness level |
| UV-Vis | Ultraviolet-visible |
| XRD | X-ray diffraction |

# Chapter 1

*Introduction*

## 1.1. Nanotechnology and nanosafety

***Nanotechnology*** – The concepts underlying "nano-technology" were first introduced, even before the term was officially recognized, in a lecture delivered by Physics Professor Richard Feynman at a meeting of the American Physical Society at Caltech on December 29, 1959. This lecture marked the inception of the concept and study of nanotechnology.[1] The term "nanotechnology" was first introduced in 1974 by Norio Taniguchi, a professor at Tokyo Science University, with the following definition: "Nano-technology mainly consists of the processing of separation, consolidation, and deformation of materials by one atom or one molecule".[2] Subsequently, the United States National Nanotechnology Initiative defined nanotechnology as the manipulation of matter that has at least one dimension ranging from 1 to 100 nanometers.[3,4] This scale, often referred to as the nanoscale, is where surface area and quantum mechanical effects become significant in defining the properties of matter.[5] The term "nanotechnology" encompasses all research and technologies that interact with these unique properties. Hence, it's common to see the terms "nanotechnologies" and "nanoscale technologies" used to denote a wide spectrum of research and applications linked by their size. In its early stages, nanotechnology was described as the specific technological aim of accurately manipulating atoms and molecules to construct products on a larger scale, a concept now known as molecular nanotechnology.[6]

Nanotechnology inherently including scientific disciplines as varied as surface science, organic chemistry, molecular biology, semiconductor physics, energy storage, engineering, microfabrication, and molecular engineering.[7,8,9,10] The related research and applications are just as diverse, extending from enhancements of traditional device physics to entirely novel methods based on molecular self-assembly. This includes the development of new materials with nanoscale dimensions as well as the direct manipulation of matter at the atomic level.[11]

The future implications of nanotechnology are currently a topic of discussion among scientists. Nanotechnology holds the potential to generate a plethora of new materials and devices with a wide array of applications, such as in the fields of nanomedicine, nanoelectronics, biomaterials, energy production, and consumer products. However, like any emerging technology, nanotechnology also brings with it a host of issues, including worries about the toxicity and environmental impact of nanomaterials, their potential influence on the global economy, and even fears about possible catastrophic scenarios. These concerns have sparked a debate among the scientific community and governments about the need for specific regulations for nanotechnology.[12]

***Nanosafety*** – During the early stages of nanomaterials (NMs) investigation, they were believed to possess similar toxicity levels to their micro and macroscopic counterparts.[13] However, research has indicated that materials at the nanoscale display different physicochemical properties compared to the original macroscopic-sized material, thereby altering their behavior and reactivity in biological systems. The new available information raised questions regarding the validity of traditional methods used to assess the harmful effects of nanomaterials.[14,15] According to "REACH" (Registration, Evaluation, Authorization, and Restriction of Chemical Substances), the safety evaluation of NMs should adhere to the risk assessment methodology used for conventional chemicals. This methodology is based on three requirements: evaluation of effects, exposure assessment, and risk characterization.[15,16] *In-vitro* and/or *in-vivo* experiments should assist the adverse effects assessment related to a real scenario estimated exposure routes to implement suitable testing and risk prevention measures for manufacturers and users.[17] An in-depth physicochemical characterization of the tested nanomaterials could be helpful for the correlation of physicochemical properties to the toxicity, most relevant physicochemical parameters that may influence toxicity are usually considered the size distribution, aggregation/agglomeration status, shape, surface area, reactivity, water solubility, surface properties, and long-term stability.[18,19] Therefore, it is crucial to understand the complete manufacturing process and the most probable exposure routes. Finally, it is fundamental to select a suitable testing strategy and to make recommendations on risk prevention measures.[15]

Nanosafety is concerned with evaluating the potential risks that nanomaterials pose to human and environmental health, including their ecological impact and toxicity levels.[20] Over the past two decades, there has been a significant increase in studies related to nanosafety, revealing conflicting results and failing to definitively establish the safety of nanomaterials.[15,21]

Nanomaterials are not all identical in their creation, implying that even minor differences in material properties can lead to variations in biological responses.[20,22] The proliferation of nanomaterials in a large variety of applications such as medical devices, pharmaceuticals, cosmetic products, and other applications interacting with biological systems has highlighted significant concerns about potential toxic effects on human health and the environment.[15,23]

Despite a decade's worth of knowledge on nanotoxicity, predicting the biological interactions nanomaterials remains challenging.[24] Nevertheless, safety protocols have been established in the manufacturing, commercial, and medical sectors.[15]

## 1.2. Safe and sustainable by design

The European Union is striving to achieve a climate-neutral economy with zero net greenhouse gas emissions by 2050, and a pollution-free environment as outlined in the sustainability chemical strategy as part of the EU Green Deal, which is dedicated to addressing climate and environmental issues.[25,26] To achieve these objectives, innovative strategies like the Safe-and-Sustainable-by-Design (SSbD) are needed. This approach focuses on the safety and sustainability of materials, products, and processes throughout their full life cycles.[27] The EU Research and Innovation program Horizon 2020, funded projects under the call "Foundations for tomorrow's industry - Safe by design, from science to regulation: metrics and main sectors / multi-component nanomaterials", that are developing methods, infrastructures, and regulations for implementing SSbD principles in the nanotechnology field assisting the European Commission in achieving the SSbD policy goals. Thanks to real industrial case studies, these projects will provide a range of digital products to promote and streamline the selection of design options and the decision-making process which address the life cycle of manufactured nanomaterials and/or advanced materials.[27]

The European Commission (EC) Joint Research Center (JRC) introduced a framework that defines the criteria and evaluation procedures for chemicals and materials under the Safe-and-Sustainable-by-Design (SSbD) concept.[28] This framework anticipates the assessment of a chemical's entire life cycle, evaluating human and environmental safety, as well as other relevant dimensions such as environmental, economic, and social sustainability. All of these aspects must be considered since the design or re-design stage of the desired product or process focusing on the functional properties desired.[27]

Even if the most impactful part for a SSbD approach may be the early phases of development of a new material, technology, or process, it is fundamental to apply these criteria and principles all along the life cycle.[29] An optimal design may improve not only the functional properties of the material, but also other important safety parameters along the productive process, such as the workers' exposure during its processing and manufacturing, environmental release and human hazards during the use phase, and finally disposal side effects. Multiple variables and dimensions must be considered all along the life cycle, increasing the difficulty level of these assessments, these kind of interventions are easier if performed at early stages of the product development, especially if already considered in the first design, because modify an already running process may be more complicated, costly, and less effective.[27,30]

The actual challenge involves the identification of impactful and effective criteria to apply the SSbD approach as best as possible to improve all the concerned aspects: human and environmental health, and economic and social sustainability. For a quantitative evaluation it will be necessary to establish thresholds that define whether a product or process meets SSbD criteria, to do it the best solution may be to identify some key performance indicator that represent the goal for each design spaces.[27,31]

## 1.3. Green chemistry

The term green chemistry was first coined in 1991 by Paul Anastas, Professor at the University of Berkley. It was refereed to new priorities for scientific and technological research and innovation, and it was based on solid principles aimed at eliminating or avoiding the use and generation of hazardous substances or procedure. Later, in 1998 Paul Anastas and John Warner provided 12 main principles defining green chemistry as a path for the development of greener chemicals, processes, and products.[32,33,34] The 12 principles may be summarized as follow:

- Prevention of wastes production.
- Atom economy to maximize the incorporation of reagents in final products.
- Less hazardous chemical syntheses designed to adopt and produce little or non-toxic and non-ecotoxic substances.
- Design safer chemicals preserving their efficacy.
- Safer solvents and auxiliaries substituting unnecessary hazardous ones.
- Design for energy efficiency performing synthesis at ambient temperature and pressure, when possible, to reduce environmental and economic impact.
- Use of renewable feedstocks when it is feasible to substitute depleting ones.
- Reduce derivatives when unnecessary to reduce reagents consumption and wastes production.
- Catalysis is preferred to stoichiometric reactions.
- Design for degradation to break down into innocuous and non-persistent products.
- Real-time analysis for pollution prevention to avoid the formation of hazardous substances.
- Inherently safer chemistry for accident prevention to minimize chemical accidents.

These concepts should be applied also in the synthesis of nanomaterials, where the maximization of reagents incorporation into products, the use of renewable material and energy sources, the implementation of safe and benign substances, the energy efficiency, and the waste production are as impactful as for classic chemistry.

## 1.4. Nanomaterials

Nanoscience and nanomaterials have aroused considerable interest in the scientific community. Nanomaterials are materials with size ranging from 1 to 100 nanometers representing a junction point between atomic-molecular scale and macroscopic scale also known as bulk phase.[35] The increased interest in the investigation and use of nanoparticles is attributed to the American theoretical physicist Richard Phillips Feynman, who in 1959 during a speech to the American Physical Society spoke about the possibility of combining atoms on a small scale thus leading to the formation of nanomaterials.[36] Because of the nanometric size of this class of materials, and subsequently the greater surface/volume aspect ratio, nanomaterials usually have different characteristics and properties than the same bulk material. Therefore, nanomaterials owe their uniqueness to the synergy between common properties of matter, such as conductivity, hardness, melting point, and the most peculiar properties of the atomic-molecular world, such as wave-particle duality or quantum effects.

***Size effect*** – The effect of dimension is a determining factor describing the behavior of nanomaterials, as it affects their structural, chemical, thermodynamic, electronic and spectroscopic characteristics.[37,38] In particular, due to the high surface/volume ratio, they have a high reactivity, decreasing the size the percentage of atoms present on the surface increases, which makes them particularly suitable for specific applications such as catalysts, adsorbents, or for biological interactions. When the aspect ratio reaches values of $10^6$-$10^7$ $cm^{-1}$, the surface energy acquires significant importance, in this way different physicochemical behaviors of nanomaterials respect to the equivalent massive materials are justified. In fact, in nanometric particles, surface atoms are only partially coordinated, so they are in a different energy state respect internal atoms. Surfaces, as well as dimensions, play a decisive role in any class of nanomaterial, affecting most of its properties.[39] Therefore, it is possible to find a close correlation between nanomaterial size and its physicochemical properties, for example in terms of optical, electronic, and magnetic properties, making this class of compounds particularly versatile and interesting. For this reason, nanomaterials and nanoparticles are studied and applied in a wide range of disciplines, from energy, medicine, nanoengineering, optic, cosmetic, food, catalytic fields.

***Nanomaterials preparation methods*** – Nanomaterials are strongly influenced, in terms of structure and physicochemical properties, by the preparation method used. The synthesis of nanostructured materials is mainly based on the two following approaches:

- Bottom-up: the nanomaterial is obtained starting from the individual atoms, suitably assembled, through chemical reactions (typically by chemical or biological synthesis), allowing the conversion of the precursor to the nanophase, controlling its characteristics and possibly reaching the desired size. Therefore, these are chemical reactions, conducted in liquid or gaseous phase, in which, through accurate reaction parameter control, such as temperature, precursor concertation, type and amount of reducing and capping agent, the particles nucleation/growth equilibrium may be manipulated. The purpose is to develop a synthesis procedure able to control the final properties of the material. The desired product can be either a stable colloidal suspension of nanoparticles, avoiding the formation of agglomerations eventually by adding electrostatic or steric stabilizers, or a nanophase to be precipitated and isolated from the reaction environment.
- Top-down: this approach usually consists of a mechanical grinding process (physical synthesis) in which macroscopic materials are crushed to form nanosized particles. It should be noted that this process can cause the presence of impurities in the product due to the simultaneous crushing of the grinding bodies.

Both approaches can be conducted in gas, liquid, or solid state, as well as in supercritical fluids or vacuum. The main objectives of most synthetic processes are to control: particle size, particle shape, size distribution, composition, and the degree of agglomeration for colloidal systems. The control of these parameters is becoming increasingly necessary, in fact, in nanotechnology the study structure-properties correlations is fundamental to better understand the enormous potential of these materials.[40,41,42]

***Colloidal systems*** – Colloidal nanosuspensions are a particularly interesting form to produce and exploit nanomaterials. These systems are constituted by a discontinuous nanometric phase with diameter comprised between 1 nm and 1 μm, and a continuous dispersing phase, identified as solvent. Typically, such colloidal particles are characterized by a high surface/volume ratio, strongly influencing the properties of the colloid itself. As colloidal stability is intended the ability of nanoparticles to remain suspended over time, avoiding aggregation, agglomeration, coagulation, and sedimentation phenomena. Therefore, the stabilization mechanisms of the colloids are fundamental to avoid these phenomena, all the destabilizing processes are thermodynamically guided by the need of the colloids to minimize the free surface energy and

therefore the liquid-solid interface, thus leading to suspension instability. In fact, colloidal nanoparticles are only kinetically stable and therefore they must be stabilized to avoid thermodynamically favored sedimentation leading phenomena.

***Colloids stability*** – The Derjaguin-Landau-Verwey-Overbeek (DLVO) model allows the mathematical study of properties and stability of colloidal systems by analyzing the interaction between two particles immersed in a liquid. Specifically, the degree of stability of a suspension is quantified by calculating the interaction potential between two electrostatically charged surfaces immersed in a fluid. Conventionally, when the potential is positive there is a repulsion between the two surfaces, when the potential assumes negative value, attractive forces prevail.[43] For the calculation, colloidal particles are approximated to spheres of uniform diameter, therefore, the colloid-colloid interactions are approximated by sphere-sphere geometries. Classical DLVO theory defines the interaction potential between two electrostatically charged colloidal particles as the result of two different contributions:

- Attractive forces of Van der Waals. Such interactions are unidirectional, short-ranged, and relatively weak forces compared to other intermolecular interactions. Essentially, they are forces of a physical nature due to the reciprocal interactions between charges (temporary or permanent).
- Electrostatic repulsive forces connected to the electric double layer of counterions. This interaction is appreciable for nanoparticles dispersed in a liquid phase containing ions. In these cases, shells of positively or negatively charged ions surround the surface of the nanoparticles to form an electrical double layer, thus providing an electrostatic force capable of keeping nanoparticles separate from each other.

The total interaction potential will be the sum of the individual potentials related to attractive and repulsive forces, and it represents the potential energy expressed in joule. It is possible to represent in a graph the trend of the resulting potential as a function of the distance between the two charged surfaces to obtain different profiles. As it can be observed in Figure 1, the stability of the colloidal suspensions is strongly linked to the distance between the nanoparticles. When the contributions of the attractive and repulsive forces are comparable, the resulting potential profile is constituted by a primary minimum and a secondary minimum. At small separation distances attractive forces prevail reduction in the interaction potential resulting in the so-called primary minimum. If Van der Waals attractive forces are significantly stronger than repulsive ones, they can prevent the formation of stable systems leading to the agglomeration irreversible attachment. At small distances the electrostatic repulsion increases as interference generated by

the interpenetration or overlapping of the electrical double layers. It follows that the potential energy associated with these forces is positive and so a net repulsive energy is generated as well as the work required to distort the diffuse double layer and to expel solvent molecules and counterions increases as particles approach. At greater distances, there is a secondary minimum, weaker than the first, in which the particles can deposit under the action of weak attractive forces. Deposited colloids can be released due to changes in the physicochemical conditions of the suspension such as pH and salinity. This kind of attachment is referred to as reversible or more commonly as flocculation.[44,45]

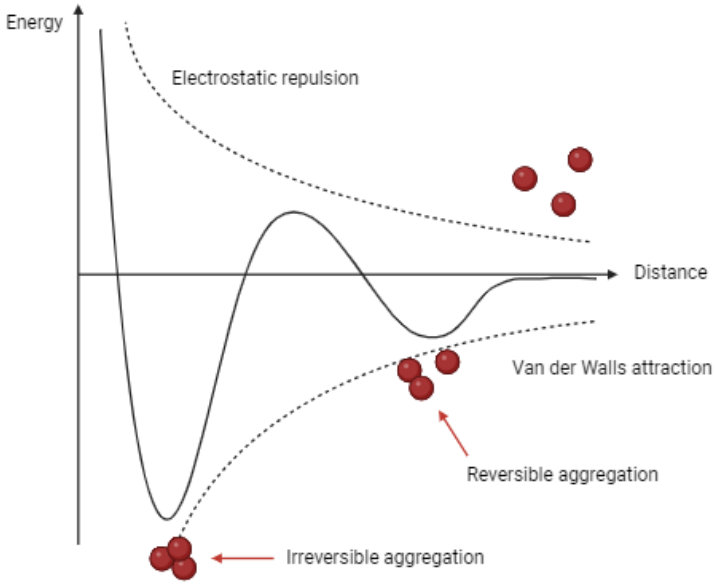


*Figure 1 – Illustration of the repulsive and attractive forces contributions to the total energy according to DLVO theory. Reversible and irreversible aggregation phenomena occur respectively corresponding to relative and absolute minimum in energy as function of the distance between the particles.*

Summarizing, the stability of colloidal systems is determined by the sum of repulsive forces and attractive forces that are established between the colloids and the distance between them, to obtain a stable suspension the resultant force must be repulsive. Otherwise, particles would aggregate and tend to precipitate. For this purpose, the stabilization of a colloidal system aims to increase nanoparticles distance by adding deflocculant agents in solution, in order to increase the diameter of the electronic double layer and thus decrease the possibility of facing agglomeration and sedimentation phenomena. The main stabilization mechanisms of a colloidal system are essentially of two different types, Figure 2, that can be combined together to enhance the stability of suspended nanoparticles:

- Electrostatic stabilization. The repulsive forces of electrostatic nature acting between the colloidal particles fight against attractive Van der Waals forces thanks to the electrostatic repulsion generated by the superimposition of electric double-layer regions consisting of charges of the same sign. This type of stabilization is strongly dependent on the ionic force of the solution, stronger ionic force determines weaker electrostatic stabilization until aggregation phenomenon and consequent variation of the optical properties. In fact, dispersions can be destabilized by increasing the concentration of electrolytes that will screen the electrostatic repulsion between the surfaces of the nanoparticles, leaving unaltered the interactions of Van der Waals.
- Steric stabilization. The repulsive forces of steric nature are due to the presence of polymers or other macromolecules or molecules covalently bonded on the surface of the dispersed particles providing a spatial impediment. These macromolecules, prevent the approach of colloidal particles with each other hindering their coagulation. The addition of these compounds leads to a repulsive steric stabilization that is independent of the ionic force.

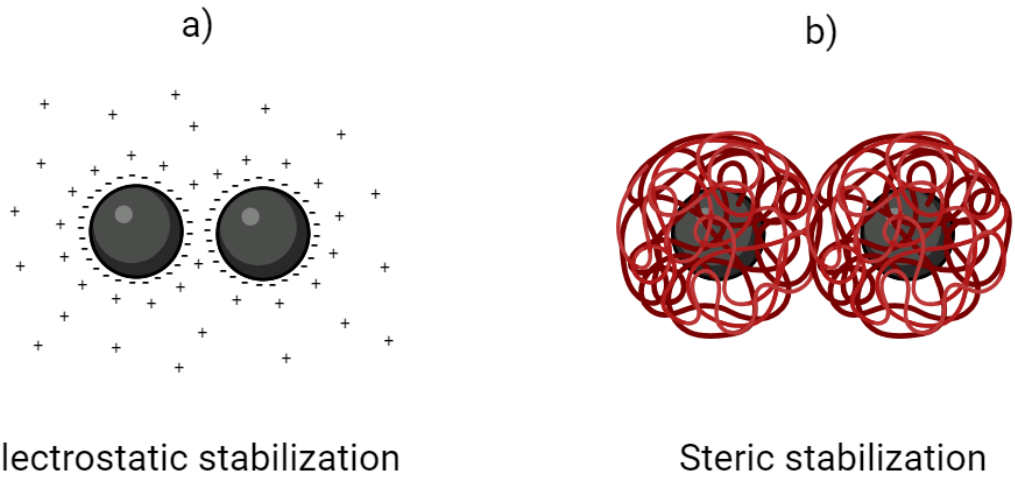


*Figure 2 – Stabilization mechanisms for colloidal nanoparticles: a) electrostatic stabilization promoted by the repulsion of the same surface charge and the electrical double-layer surrounding the nanoparticles; b) steric stabilization due to the physical hindrance of a steric agent coating the nanoparticles.*

## 1.5. References


1. Adya, A. K. & Canetta, E. *Nanotechnology and Its Applications to Animal Biotechnology*. *Animal Biotechnology: Models in Discovery and Translation* (Elsevier, 2013). doi:10.1016/B978-0-12-416002-6.00014-6.
2. Nimesh, S. Nanotechnology: an introduction. *Gene Ther.* 1–12 (2013) doi:10.1533/9781908818645.1.
3. Severino, P. *et al.* Advances in nanobiomaterials for topical administrations: new galenic and cosmetic formulations. *Nanobiomaterials Galen. Formul. Cosmet. Appl. Nanobiomaterials* 1–23 (2016) doi:10.1016/B978-0-323-42868-2.00001-2.
4. Hardy, A. *et al.* Guidance on risk assessment of the application of nanoscience and nanotechnologies in the food and feed chain: Part 1, human and animal health. *EFSA J.* 16, (2018).
5. Li, X. *et al.* Effects of physicochemical properties of nanomaterials on their toxicity. *J. Biomed. Mater. Res. - Part A* 103, 2499–2507 (2015).
6. Ramsden, J. J. What is nanotechnology? *Nanotechnol. Perceptions* 1, 3–17 (2005).
7. Saini, R., Saini, S. & Sharma, S. Nanotechnology: The future medicine. *J. Cutan. Aesthet. Surg.* 3, 32 (2010).
8. Lyon, D. & Hubler, A. Gap size dependence of the dielectric strength in nano vacuum gaps. *IEEE Trans. Dielectr. Electr. Insul.* 20, 1467–1471 (2013).
9. Hübler, A.W. and Osuagwu, O. (2010), Digital quantum batteries: Energy and information storage in nanovacuum tube arrays. Complexity, 15: 48-55. https://doi.org/10.1002/cplx.20306.
10. Shinn, E., Hübler, A., Lyon, D., Perdekamp, M.G., Bezryadin, A. and Belkin, A. (2013), Nuclear energy conversion with stacks of graphene nanocapacitors. Complexity, 18: 24-27. https://doi.org/10.1002/cplx.21427.
11. Belkin, A., Hubler, A. & Bezryadin, A. Self-Assembled Wiggling Nano-Structures and the Principle of Maximum Entropy Production. Sci Rep 5, 8323 (2015). https://doi.org/10.1038/srep08323.
12. Cristina Buzea, Ivan I. Pacheco, Kevin Robbie; Nanomaterials and nanoparticles: Sources and toxicity. Biointerphases 1 December 2007; 2 (4): MR17–MR71. https://doi.org/10.1116/1.2815690.
13. Shuguang Wang, Wentong Lu, Oleg Tovmachenko, Uma Shanker Rai, Hongtao Yu, Paresh Chandra Ray; Challenge in understanding size and shape dependent toxicity of

gold nanomaterials in human skin keratinocytes. Chemical Physics Letters Volume 463, Issues 1–3, 22 September 2008, Pages 145-149.

14. Nel A, Xia T, Mädler L, Li N. Toxic potential of materials at the nanolevel. Science. 2006 Feb 3;311(5761):622-7. doi: 10.1126/science.1114397. PMID: 16456071.
15. Zielińska, A.; Costa, B.; Ferreira, M.V.; Miguéis, D.; Louros, J.M.S.; Durazzo, A.; Lucarini, M.; Eder, P.; V. Chaud, M.; Morsink, M.; et al. Nanotoxicology and Nanosafety: Safety-by-Design and Testing at a Glance. Int. J. Environ. Res. Public Health 2020, 17, 4657. https://doi.org/10.3390/ijerph17134657
16. Kathrin Schwirn, Doris Voelker, Wiebke Galert, Joris Quik, and Lars Tietjen; Environmental Risk Assessment of Nanomaterials in the Lightof New Obligations Under the REACH Regulation: WhichChallenges Remain and How to Approach Them? Integrated Environmental Assessment and Management, 2020, Volume 16, Number 5, pp. 706–717.
17. Margarethe Hofmann-Amtenbrink, David W. Grainger, Heinrich Hofmann, Nanoparticles in medicine: Current challenges facing inorganic nanoparticle toxicity assessments and standardizations, Nanomedicine: Nanotechnology, Biology and Medicine, Volume 11, Issue 7, 2015, Pages 1689-1694, ISSN 1549-9634, https://doi.org/10.1016/j.nano.2015.05.005.
18. Boros, B.-V.; Ostafe, V. Evaluation of Ecotoxicology Assessment Methods of Nanomaterials and Their Effects. Nanomaterials 2020, 10, 610. https://doi.org/10.3390/nano10040610.
19. Liu X, Tang K, Harper S, Harper B, Steevens JA, Xu R. Predictive modeling of nanomaterial exposure effects in biological systems. Int J Nanomedicine. 2013;8(Supplement 1 Nanoinformatics):31-43. https://doi.org/10.2147/IJN.S40742.
20. Pedro M. Costa, Bengt Fadeel, Emerging systems biology approaches in nanotoxicology: Towards a mechanism-based understanding of nanomaterial hazard and risk, Toxicology and Applied Pharmacology, Volume 299, 2016, Pages 101-111, ISSN 0041-008X, https://doi.org/10.1016/j.taap.2015.12.014.

21 Harald F. Krug, Nanosafety Research—Are We on the Right Track? Angew. Chem. Int. Ed. 2014, 53, 12304-12319. DOI: 10.1002/anie.201403367.

22. Motta, G.; Gualtieri, M.; Saibene, M.; Bengalli, R.; Brigliadori, A.; Carrière, M.; Mantecca, P. Preliminary Toxicological Analysis in a Safe-by-Design and Adverse Outcome Pathway-Driven Approach on Different Silver Nanoparticles: Assessment of Acute Responses in A549 Cells. Toxics 2023, 11, 195.

https://doi.org/10.3390/toxics11020195.

23. Paresh Chandra Ray, Hongtao Yu, Peter P. Fu. Toxicity and Environmental Risks of Nanomaterials: Challenges and Future Needs. Journal of Environmental Science and Health, Part C, Environmental Carcinogenesis and Ecotoxicology Reviews, Volume 27, 2009 - Issue 1, Pages 1-35. https://doi.org/10.1080/10590500802708267.
24. Mingzhu Zhou, Xiaoqian Ge, Da-Ming Ke, Huan Tang, Jun-Zheng Zhang, Matteo Calvaresi, Bin Gao, Lining Sun, Qianqian Su, Haifang Wang. The Bioavailability, Biodistribution, and Toxic Effects of Silica-Coated Upconversion Nanoparticles in vivo. Frontiers in Chemistry, 2019, Sec. Nanoscience, Volume 7 - 2019| https://doi.org/10.3389/fchem.2019.00218.
25. Jesús M. López De Ipiña et al. Digital Twins applied to the implementation of Safe-by-Design strategies in nano-processes for the reduction of airborne emission and occupational exposure to nano-forms. 2021, J. Phys.: Conf. Ser. 1953, 012010, DOI 10.1088/1742-6596/1953/1/012010.
26. Koivisto AJ, Spinazzè A, Verdonck F et al. Assessment of exposure determinants and exposure levels by using stationary concentration measurements and a probabilistic near-field/far-field exposure model. Open Res Europe 2021, 1:72 (https://doi.org/10.12688/openreseurope.13752.1).
27. Irini Furxhi et al. Status, implications and challenges of European safe and sustainable by design paradigms applicable to nanomaterials and advanced materials. RSC Sustain., 2023,1, 234-250. DOI https://doi.org/10.1039/D2SU00101B.
28. Caldeira, C., Garmendia Aguirre, I., Tosches, D., Mancini, L., Abbate, E., Farcal, R., Lipsa, D., Rasmussen, K., Rauscher, H., Riego Sintes, J., Sala, S. Safe and Sustainable by Design chemicals and materials. Application of the SSbD framework to case studies, Publications Office of the European Union, Luxembourg, 2023, doi:10.2760/329423, JRC131878.
29. Susan Dekkers, Susan W.P. Wijnhoven, Hedwig M. Braakhuis, Lya G. Soeteman-Hernandez, Adrienne J.A.M. Sips, Isabella Tavernaro, Annette Kraegeloh, Cornelle W. Noorlander, Safe-by-Design part I: Proposal for nanospecific human health safety aspects needed along the innovation process, NanoImpact, Volume 18, 2020, 100227, ISSN 2452-0748, https://doi.org/10.1016/j.impact.2020.100227.
30. Tavernaro I, Dekkers S, Soeteman-Hernández LG, Herbeck-Engel P, Noorlander C, Kraegeloh A. Safe-by-Design part II: A strategy for balancing safety and functionality in the different stages of the innovation process. NanoImpact. 2021 Oct;24:100354. doi:

10.1016/j.impact.2021.100354. Epub 2021 Sep 3. PMID: 35559813.

31. Mech A, Gottardo S, Amenta V, Amodio A, Belz S, Bøwadt S, Drbohlavová J, Farcal L, Jantunen P, Małyska A, Rasmussen K, Riego Sintes J, Rauscher H. Safe- and sustainable-by-design: The case of Smart Nanomaterials. A perspective based on a European workshop. Regul Toxicol Pharmacol. 2022 Feb;128:105093. doi: 10.1016/j.yrtph.2021.105093. Epub 2021 Dec 2. PMID: 34864125; PMCID: PMC8795056.
32. Paul Anastas and Nicolas Eghbali. Green Chemistry: Principles and Practice. Chem. Soc. Rev., 2010,39, 301-312. https://doi.org/10.1039/B918763B.
33. Anastas, Paul T, and John C Warner, Green Chemistry: Theory and Practice (Oxford, 2000; online edn, Oxford Academic, 31 Oct. 2023), https://doi.org/10.1093/oso/9780198506980.001.0001.
34. Anastas, P. T.; Warner, J. C. Green Chemistry: Theory and Practice, Oxford University Press: New York, 1998, p.30.
35. C. N. R. Rao and A. K. Cheetham, J. Mater. Chem., 2001,11, 2887-2894.
36. Richard P. Feynman, There's Plenty of Room at the Bottom, Feynman's Talk. doi:10.1201/9780429500459.
37. Park, J.-I., Kang, N.-J., Jun, Y.-W., Oh, S.J., Ri, H.-C. and Cheon, J. (2002), Superlattice and Magnetism Directed by the Size and Shape of Nanocrystals. ChemPhysChem, 3: 543-547. https://doi.org/10.1002/1439-7641(20020617)3:6<543::AID-CPHC543>3.0.CO;2-E.
38. K Madhusudan Reddy, Sunkara V Manorama, A Ramachandra Reddy, Bandgap studies on anatase titanium dioxide nanoparticles, Materials Chemistry and Physics, Volume 78, Issue 1, 2003, Pages 239-245, ISSN 0254-0584, https://doi.org/10.1016/S0254-0584(02)00343-7.
39. Roduner E. Size matters: why nanomaterials are different. Chem Soc Rev. 2006 Jul;35(7):583-92. doi: 10.1039/b502142c. Epub 2006 May 4. PMID: 16791330.
40. Abid N, Khan AM, Shujait S, Chaudhary K, Ikram M, Imran M, Haider J, Khan M, Khan Q, Maqbool M. Synthesis of nanomaterials using various top-down and bottom-up approaches, influencing factors, advantages, and disadvantages: A review. Adv Colloid Interface Sci. 2022 Feb;300:102597. doi: 10.1016/j.cis.2021.102597. Epub 2021 Dec 29. PMID: 34979471.
41. Arole, Dr. Vasanti and Prof. S. V. Munde. “FABRICATION OF NANOMATERIALS BY TOP-DOWN AND BOTTOM-UP APPROACHES – AN OVERVIEW.” (2014).

42. Zhang XF, Liu ZG, Shen W, Gurunathan S. Silver Nanoparticles: Synthesis, Characterization, Properties, Applications, and Therapeutic Approaches. Int J Mol Sci. 2016 Sep 13;17(9):1534. doi: 10.3390/ijms17091534. PMID: 27649147; PMCID: PMC5037809.
43. Alain Roucoux, Jürgen Schulz, and Henri Patin. Reduced Transition Metal Colloids: A Novel Family of Reusable Catalysts? Chem. Rev. 2002, 102, 10, 3757–3778. https://doi.org/10.1021/cr010350j.
44. Mats Larsson et al. Suspension stability; why particle size, zeta potential and rheology are important. Annual transaction of the nordic rheology society, vol. 20, 2012.
45. Walter, Aurelie, Garofalo, Antonio, Parat, Audrey, Martinez, Herve, Felder-Flesch, Delphine and Begin-Colin, Sylvie. "Functionalization strategies and dendronization of iron oxide nanoparticles" Nanotechnology Reviews, vol. 4, no. 6, 2015, pp. 581-593. https://doi.org/10.1515/ntrev-2015-0014.

# Chapter 2

*Objectives*

## 2.1. Aim of the work

Today's sustainability challenges involve transitioning to a green and circular economy through resource efficiency, with the aim of improving both human and planet health. Several strategies have been applied and others have been proposed for the implementation in the near future to move in this direction. The 2030 Agenda for Sustainable Development is a plan of action endorsed in 2015 by all the Members States of the United Nations. It consists of 17 Sustainable Development Goals (SDGs) aiming to protect the planet and environment ensuring the peace and prosperity for all people.[46] The European Green Deal is a strategic initiative proposed by the European Commission to transform the European Union (EU) into a modern, resource-efficient, and competitive economy by 2050.[47]

In order to achieve these objectives, it is crucial to minimize the impact of materials right from the design phase. This principle forms the foundation of the eco-design approach, which involves designing a product in a way that respects the environment and prevents any negative impact from the earliest stages of material design. In this regard, the development of new advanced materials with enhanced functionality in the field of clean technology is of paramount importance. The European Project ASINA is studying the implementation of the Safe and Sustainable by Design (SSbD) approach to nanomaterials, which is a subset of the broader concept of eco-design. Some of the results presented in this work have been collected within ASINA.[48]

The eco-design approach has been utilized for the development of numerous nanomaterials, which boast enhanced safety and sustainability profiles. These nanophases find applications in various fields, including antimicrobial products, catalysis, and wastewater remediation. The primary objectives of this thesis work are:

- Development of silver nanophases through green synthesis, with the aim of triggering new synergistic effects to maximize the antimicrobial functionality, both antibacterial and antiviral, while minimizing the toxicological and ecotoxicological impacts.
- Determination of the optimal synthesis conditions to maximize antimicrobial effects, while formulating hypothesis regarding the possible mechanism of actions.
- Assessment of various applications and key performance indicators (KPIs), adhering to the SSbD approach throughout the different stages of the product life cycle.
- Enhancement of the knowledge pertaining to nanomaterials, their impact on human and environmental health, and with their potential applications in industrial products.

- Optimization of new green synthesis methodologies, proposed as alternatives to conventional development methods for catalyst that can be used in the field of biomass valorization.
- Development of innovative advanced materials for the wastewater remediation, capable of utilizing natural and renewable materials, thereby highlighting enhanced sustainability in line with the principles of the European Green Deal and circular economy.

## 2.2. Structure of the research activity

The research activity and the structure of this thesis were branched on 3 parallel topics, all of them developed under an eco-design perspective of new and advanced materials. Part of the results stems from the European Collaborative project ASINA based on the implementation of the Safe and Sustainable by Design (SSbD) framework in the development of functional nano-enabled products.[48] Here it is summarized the content of the following chapters, depicted by the concept map in Figure 3.

The main topic addresses the preparation antimicrobial nanophases (Chapter 3), their characterization and exploitation for different application field (Chapter 4).

In the second topic, the green chemistry principles, aligned with the SSbD approach, were implemented to obtain metal nanoparticles applied as catalysts in the biomass valorization field (Chapter 5).

Finally, the wastewater remediation sector was explored exploiting natural derived active materials for the removal of harmful pollutants, (Chapter 6).

A detailed view of the next chapters content is here presented:

- Chapter 3: *Design of safe and sustainable synthesis of antimicrobial silver nanoparticles*. In this chapter, three different natural derived capping agents were exploited for the production of antimicrobial silver nanoparticles (AgNPs). Quaternized hydroxyethyl cellulose biopolymer, curcumin extracted from the rhizome of the *Curcuma longa*, and sodium surfactin a biosurfactant derived from bacterial metabolism were exploited as renewable and green reagents. The synthesis parameters were explored to design a set of variants for each capping agent to correlate synthesis parameters to physicochemical properties and antimicrobial activity against bacteria and viruses.
- Chapter 4: *Production of nano-enabled products implementing antimicrobial silver nanoparticles on different substrates*. Different case studies were addressed to implement the nanophases (AgNPs) described in Chapter 3 into nano-enabled products (NEPs) and devices: fabrics, paper, and biopolymeric films and scaffolds. In this way, it was possible focus on the manufacturing and use phase steps of the product life cycle. The efficiency of the manufacturing processes was compared and a set of key performance indicator (KPIs) as functionality, durability, potential human exposure, and environmental pollution associated to the manufactured NEPs were investigated.
- Chapter 5: *Green synthesis of noble metals-based nanoparticles for catalytic applications*. The green chemistry principles, aligned with the SSbD approach, were

implemented in the design of gold-platinum based catalyst applied in the biomass valorization field. Gold-platinum alloy and core-shell nanoparticles were synthesized and their structure-catalytic activity correlation was assessed. The intended application of these catalysts is the conversion of biomass-derived molecules into key building blocks for the chemical industry.

- *Chapter 6*: *Functional materials for wastewater remediation*. In this chapter, natural solutions were explored for the remediation of wastewaters. Adsorbent materials, like clays, hydrotalcites, and microalgae were exploited for the removal of heavy metals and organic pollutants, while photocatalytic phases were implemented for the degradation of organic matter. These active phases handleability was improved by encapsulation in granulated powders or by embedding into biopolymeric matrixes. Finally, the products were tested into a semi-mobile device for water treatment.

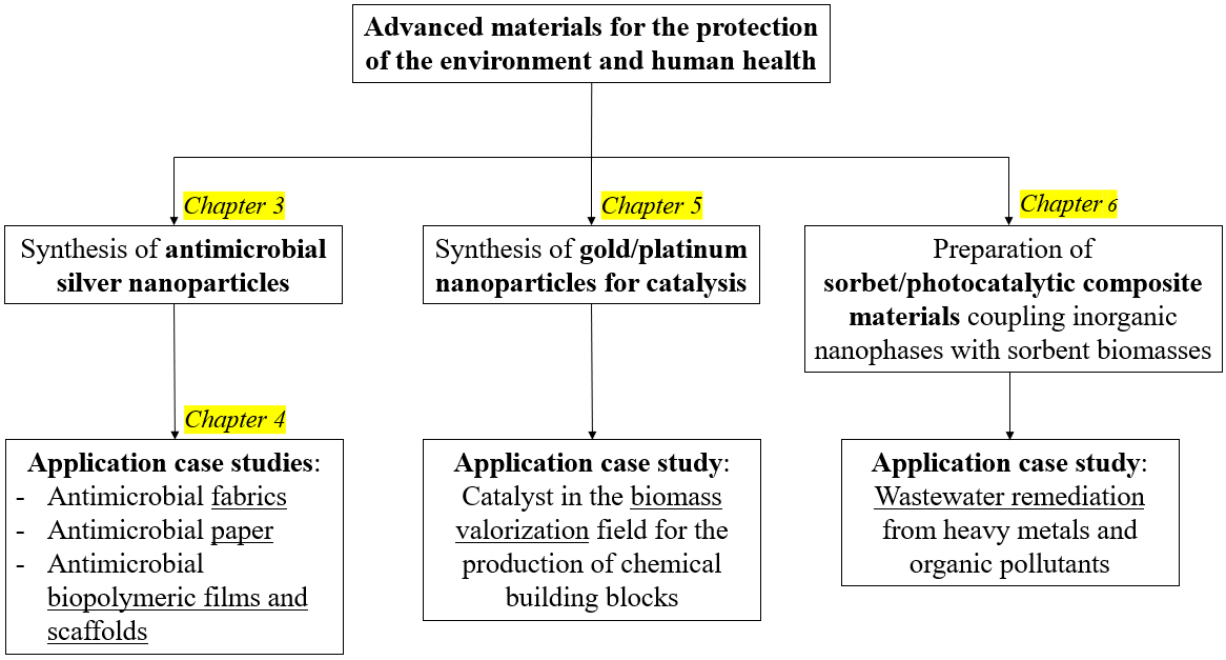


*Figure 3 – Concept map of the research work presented in the following chapters of this thesis.*

## 2.3. References

46. Transforming our world: the 2030 Agenda for Sustainable Development. https://sustainabledevelopment.un.org/content/documents/21252030%20Agenda%20for%20Sustainable%20Development%20web.pdf?source=patrick.net.
47. The European Green Deal Striving to be the first climate-neutral continent. https://commission.europa.eu/strategy-and-policy/priorities-2019-2024/european-green-deal_en.
48. ASINA project | Safe-by-design of Nano Product Development (asina-project.eu).

# Chapter 3

## *Design of safe and sustainable synthesis of antimicrobial silver nanoparticles*

Part of the content of this chapter has been published as A. L. Costa et. al. "Eco design for Ag-based solutions against SARS-CoV-2 and *E. coli*" Environ. Sci.: Nano, 2022, 9, 4295-4304.

## 3.1. Introduction

The recent global emergency due to the COVID-19 pandemic, caused by severe acute respiratory syndrome coronavirus 2 (SARS-CoV-2), pointed out the need to develop new strategies for the containment of the disease, in particular during the initial phase of propagation of the virus.[49] Another very topical issue is the growing development of antibiotic resistant bacterial strains.[50] This is another important medical problem that will have to be faced soon. In the absence of known long-term effective therapies and definitive vaccines, it is logical to move towards disease control strategies that exploit low-cost materials and products, available and with antimicrobial properties already tested against the targeted pathogens. In this field, silver nanoparticles have been proposed and studied at different level as general-purpose antimicrobial agent, able to help in the fight against both viruses and bacteria. Silver nanoparticles exploit their nanosized and the correlated favorable surface/volume aspect ratio to interact with viruses, bacteria, and biological components, to penetrate cell wall, and to produce reactive oxygen species (ROS).[51]

***Silver nanoparticles*** – At present, silver nanoparticles (AgNPs) are among the most researched and frequently utilized nanomaterials because of their adaptability and usefulness in diverse fields such as health, environment, and various industrial sectors, positively contributing to the economy.[52,53,54,55] AgNPs are highly utilized in industrial and commercial sectors due to their unique properties such as antimicrobial action against a broad variety of pathogens and microorganisms such as bacteria, viruses, fungi, and protozoa, but also thanks to their chemical stability, catalytic activity, electrical and thermal conductivity, and relatively low production cost. As a result, they find extensive use as antibacterial, antiviral, antifungal, anti-inflammatory, anti-tumor, and regenerative, agents, but also as biosensor, and catalyst.[56] They are also found in products across various industries like textile, pharmaceutical, hygiene, cleaning products, food, agricultural, and many others, leading to potential human and environmental exposure.[57] AgNPs have a broad range of applications in medicine, such as coating medical devices, preparing nanogels, or producing formulations for skin lesions.[58,59,60,61,62]

The synthesis of AgNPs requires careful control of parameters to ensure reproducible production.[63] The toxicity of AgNPs is dependent on several factors, including how the colloidal suspension is prepared, the physicochemical nature of particles, the aggregation state, the dose, the nature of the living organism, the cell type, and its morphology.[64] Generally, it has been observed that low concentrations of AgNPs exhibit negligible toxicity in *in-vitro* and *in-vivo* assays. As AgNPs concentration increases, the toxicity of the nanoparticles and their

accumulation in various tissues and organs also tend to increase. At high concentrations, the inhalation or ingestion of AgNPs can cause adverse effects and may even result in tissue death.[65,66]

***Antibacterial activity*** – Most of the recent developed antibacterial agents are chemically modified natural compounds. The long-term widespread use and abuse of these antibacterial agents has favored the evolution of antibiotic resistant bacterial strands. The decreasing effectiveness of the commonly used drugs it is a relevant emergency that still places infectious diseases as one of the biggest health challenges worldwide. The antibiotic resistance, leads looking for alternative solution or increasing the dosage till the toxicity limit. For these reasons, the development of alternative strategies for the treatment of bacterial pathogens is of an absolute importance. Among various solutions, antimicrobial nanoparticles are likely to satisfy most of the request in terms of efficacy and microbial resistance. Silver nanoparticles have gained interest thanks to their wide-ranging antiviral, antibacterial and antifungal properties, in the case of bacterial pathogen AgNPs are able to kill the bacteria or slow down its growth rate, with limited toxicity for the infected organism. It is possible to summarize the main mechanisms of action of silver nanoparticles against bacteria in four main categories:

1. Adhesion of the AgNPs on the bacterial cell wall thanks to electrostatic interactions, causing irreversible morphological modification and in increase in the permeability, resulting in cell wall rupture;[67]
2. AgNPs penetration into bacterial cells causing intracellular damages;
3. Induction of oxidative stress by producing reactive oxygen species that leads to bacterial toxicity;
4. $Ag^+$ ion released by the dissolution of AgNPs in the intra- and extracellular environment causing biological damages.[68,69]

Differentiated mechanisms of action help in the fight against resistant bacterial strands. From this point of view silver nanoparticles may be an interesting alternative to the conventional antibiotics for the treatment of bacterial pathogens.

***Antiviral activity*** – The viral infective process is generally based on the virus adsorption on the cell wall, penetration within the cell, uncoating, virus replication, cell death, and virus release. Therefore, antiviral nanoparticles have the primary role of inhibiting at least one of these steps, in this way it is possible to classify antiviral agent depending on their mechanism. Most of the viral infection start with a selective attack to a protein target on the cell surface, if nanoparticles

can effectively inhibit the interaction, they can be used as broad-spectrum antiviral agents capable of suppressing or inhibiting this first step of viral infection. The most direct action is the virus inactivation exploiting physical or chemical mechanisms that modify the viral envelope, capsid, drastically reducing the virulence. A second mechanism is to avoid the cell wall penetration, modifying the receptor sites of the host cell or the virus. If these solutions are not available, it is possible to prevent the virus replication usually obtained by suppressing the expression of the enzymes involved in the DNA or RNA replication.[70]

Employing antiviral nanophases may reduce the risk of infection preventing pandemic like COVID-19. The implementation of silver nanoparticles as antiviral therapy treating COVID-19 affected patients is based on the hypothesis that silver nanoparticle will interact with the spike protein of the virus, inhibiting its capability of attacking human cells. Moreover, the release of silver cations combines a direct action of $Ag^+$ on the virus viability with a decrease of the local pH creating a hostile environment for the virus.[71]

***Antimicrobial medical products implementing nanoparticles*** – Nowadays, infective diseases caused by pathogens like virus, bacteria, and fungi represent serious threat for human health that can turn out into extended socio-economic problems. Although important progresses have been achieved in healthcare standard, the rapid growth of antibiotic-resistant bacteria and the evolution of stronger and more infective viral variants, highlight the urge of new safer and more effective antimicrobial agents. In the last decades, the coupling of nanophases with biomolecule have been widely studied and exploited for auto-sanitizing products, medical devices, and drug delivery.[72] Nanoparticles mediated drug delivery has demonstrated huge advantages in terms of targeting the desired area and active principle modulated release. These therapies have been adapted in clinic trials confirming targeted delivery, better solubility, and limited toxicity. Specific nanophases and drugs formulation may further increase the selectivity of the drug, granting safer and more effective therapies. Biopolymer based hydrogel have been widely investigated in this field thanks to their properties, like swelling behavior, pore size, biodegradation, and capability of incorporate drugs and nanophases. Drugs incorporation into a hydrogel have a significant impact on its targeting, release and regulation. For example, antimicrobial drug delivery system based on pH sensible hydrogels nanocomposite have been synthesized by combining polyvinyl alcohol and silver nanoparticles with citric acid for the delivery of ciprofloxacin. The as synthesized hydrogel acted as pH sensible drug delivery system for ciprofloxacin improving antimicrobial activity against *S. aureus* and *E. coli*.[73]

***Eco-design and synergistic effects*** – Over the years lot of techniques have been developed to evaluate the environmental impact of products and processes. The most common problems resulting from using a standard approach are the analysis of the environmental aspect as independent from product functionality or process requirements, moreover these evaluations are usually performed on already running processes and commercial products. It is of fundamental importance the integration of environmental aspects in the early stages of product and process design, together with a multicriteria approach that allows to balance environmental requirements with product functionality, and other requirements. As eco-design is intended the integration of environmental aspects in the design and development of a product, pursuing a reduction of negative environmental impacts throughout all the life cycle of the product (ISO 14006:2011).[74] The concept of sustainable development forced society and industry to move toward a new way of development, since the environmental degradation is a real global problem. In this perspective, new technologies bloomed to overcome the challenges related to environmental and human health. New green technologies implementing the Green Chemistry principles focusing on sustainability and life cycle assessment have been developed.[75] The Green Chemistry is a discipline voted to the improvement efficiency, safety, and wastes production of chemical processes. Considering impossible to completely erase the use of hazardous substances, it is important to minimize their application and avoid their release in the environment coupling a correct wasted disposal. Green Chemistry may be defined in a larger way of thinking as the application in the chemical industry of the sustainable development principles. The ideas laying behind the Green Chemistry are to reduce the consumption of raw material, avoid the use of unnecessary hazardous materials, and correct wastes disposal, in line with industrial ecology which is pushing in direction of sustainable resources and recycled materials.[76] These guidelines should be applied all along the life cycle of product and processes, increasing efficiency and reducing human hazards, environmental impacts, and wastes production, reaching sustainability goals.[77] Thanks to a proper design of the product it is possible to overcome tradeoffs resulting in synergistic effects improving the effectiveness of the material. As synergistic effects are intended the combined actions one or more agents with specific properties interacting to reach results other way impossible for the single components. In this way, the final product properties are maximized respect to the raw materials. In this perspective, coupling AgNPs with eco-friendly compounds could allow to maximize the biocompatibility and the antimicrobial properties of the product, promoting an improvement of safety and sustainability.[78]

***Safe and sustainable by design synthesis of silver nanoparticles*** – In line with the sustainable development goals indicated by the United Nations in the 2030 Agenda for Sustainable Development and with the strategies promoted by the European Green Deal, the world attention is increasingly oriented to the development of green processes with a low environmental impact, that exploit renewable and non-toxic raw materials.[79,80] This behavior is strongly considered in the production of advanced and nanomaterials, where the scientific community is promoting important results in these research topics. The development of eco-friendly synthesis for nanomaterials is being largely studied, implementing protocols involving the use of non-toxic or low toxicity reagents, exploiting natural based and renewable raw materials. Silver nanoparticles can be obtained by top-down approaches, by the miniaturization of macroscopic phases, or by bottom-up approaches, where the nanomaterials are assembled starting from atom, molecules, or clusters. The eco-design is more relevant in a bottom-up approach, under which the synthesis of silver nanoparticles may be performed via chemical reduction of a silver salt precursor thanks to the classic inorganic chemistry compounds supported by appropriated stabilizing agents, or alternatives green synthesis have been developed, exploiting natural derived reducing and capping agents, like plant or fungi extracts, or specific biomolecule. Another alternative is constituted by biosynthesis where living plants, bacteria, or fungi are exploited for the synthesis of the nanoparticles. In general, bottom-up approaches, whether they are chemical, green, or biological synthesis, require the reduction of a precursor based on a silver salt. The reduction reaction of the $Ag^+$ cation to metallic silver and its standard reduction potential are reported in Equation 1.[81]

$$Ag^+ + e^- \leftrightarrow Ag_{(s)} \quad 0.7996\,V \qquad \text{Equation 1}$$

Willing to focus on a bottom-up green synthesis of silver nanoparticles, natural derived reducing and capping agents were exploited, ranging from biopolymers, organic molecules, and biosurfactants. In this way the biomass and biological derived raw materials were valorized in the synthesis of an antimicrobial agent. The selected candidates for this scope possess intrinsic antimicrobial properties to explore potential synergistic effect with the silver nanoparticles. Several studies have demonstrated how the antimicrobial properties of silver nanoparticles are significantly influenced by their physicochemical properties, like size, shape, and surface chemistry.[82,83] The eco-designed alternatives were widely and deeply characterized to correlated design and compositional parameters to functional properties.

## 3.2. Results and discussion

Three different natural derived products were selected as capping agent for the eco-friendly synthesis of silver nanoparticles. The syntheses were adapted to the specific requirements of the selected compound, but the general principles are preserved: avoid the use of hazardous or harmful reagents, room-temperature or microwave assisted synthesis, and avoid the use of organic solvents working in water environment. The first solution involves the use of a biopolymer as capping agent, which is quaternized hydroxyethyl cellulose, a positively charged macromolecule obtained by the functionalization of the hydroxyethyl cellulose, with intrinsic antibacterial properties.[84] The second one works with curcumin, an organic molecule extracted from *Curcuma longa*, long known as a natural remedy against inflammatory process and pathogens infection, more recently several literature studies have demonstrated it beneficial properties.[85] Lastly, sodium surfactin was tested as capping agent for the synthesis of silver nanoparticle. It is a biosurfactant obtained from bacterial metabolism that has demonstrated promising antimicrobial and soil remediation properties.[86,87] The alternatives proposed were selected based on the intrinsic properties of the capping agent, and the synthetic process of the nanophase was aimed at synergic interaction between the AgNPs and the capping agent in order to improve the beneficial antimicrobial properties of both. The molecular structure of the three compounds used as capping agent is represented in Figure 4.

In this chapter it will be deeply studied the optimization process of the synthesis of these three variants of silver nanoparticles. They were widely characterized from the physicochemical point of view and the most promising alternatives were tested against Gram-negative and Gram-positive bacteria, and against enveloped and non-enveloped viruses.

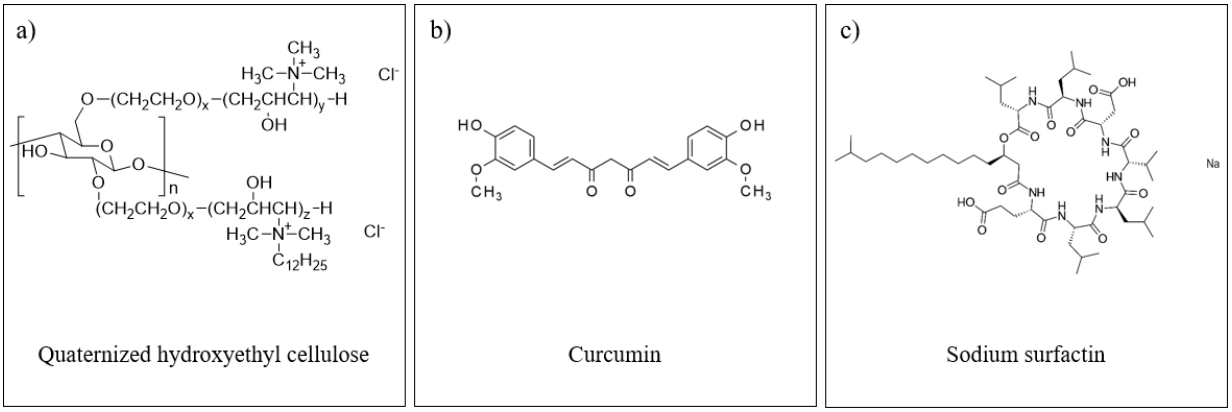


*Figure 4 – Molecular structures of the selected natural and bio-derived capping agents: a) quaternized hydroxyethyl cellulose biopolymer, b) curcumin molecule, and c) sodium surfactin biosurfactant.*

### 3.2.1. Hydroxyethyl cellulose capped silver nanoparticles

Hydroxyethyl cellulose capped silver nanoparticles synthesis patented in CNR-ISSMC uses quaternized hydroxyethyl cellulose as reducing and capping agent and sodium hydroxide as reaction initiator.[88] It is an eco-friendly and easily scalable synthesis of AgNPs developed in a safe and sustainable by design (SSbD) perspective. The reaction is fully carried out at room temperature in water environment, AgNPs are nucleated within the biopolymeric cellulose matrix. Quaternized hydroxyethyl cellulose is known in cosmetic field as Polyquaternium-67 and it finds use as conditioner into personal-care products to help deliver and deposit beneficial ingredients such as emollients, sunscreens, and fragrances to the skin and hair.[89,90] This family of products based on quaternary ammonium salts of hydroxyethyl cellulose are typically white to off-white powders or granules with amine odor.[91] Polyquaternium-67 structure is reported in Figure 5, these polymers are prepared by substituting trimethyl ammonium and dimethyldodecyl ammonium compounds onto hydroxyethyl cellulose.[92] The molecules are cationic because they possess positive charges at the nitrogen atoms and have chloride counter ions. Typically, SoftCAT products contain about 91% polymer, with the balance water, sodium chloride, sodium acetate, and isopropyl alcohol.[89,91,92] Quaternized hydroxyethyl cellulose it is highly active in preventing Gram-negative infections and resistance, in fact it was coupled with AgNPs to promote antimicrobial synergistic effects.[93]

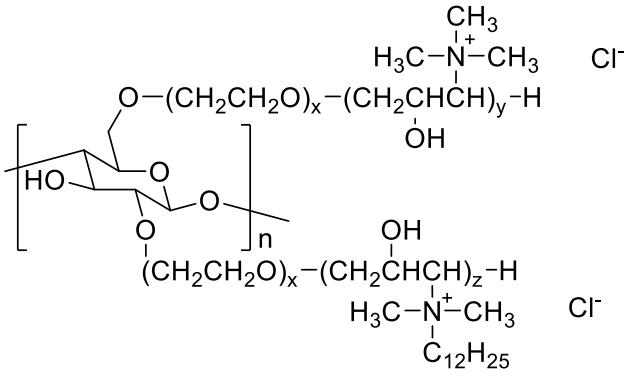


*Figure 5 – Quaternized hydroxyethyl cellulose molecular structure.*

***Design of experiment*** – To optimize the antimicrobial properties of AgHEC, both against viruses and bacteria, a design of experiment (DoE) was built exploring the reagents molar ratios as independent variables: HEC/Ag and NaOH/Ag. Working at room temperature, HEC and NaOH contents are considered as the main driving force responsible for the AgNPs nucleation and growth mechanisms. In the graph in Figure 6 are reported the explored points of this

bidimensional space created by reagents molar ratios. In red is represented the standard synthesis used as starting point, in black all the other synthesis performed, characterized, and tested.

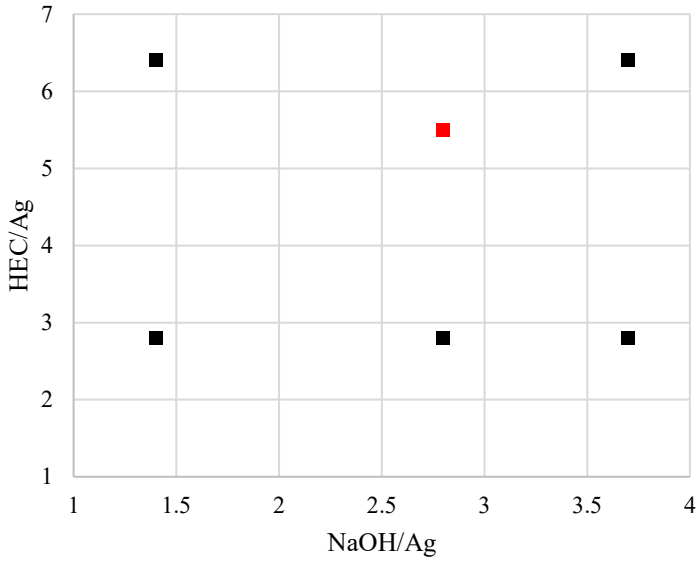


*Figure 6 – Design of experiment assessed to optimize the reagent molar ratios (HEC/Ag and NaOH/Ag) of the AgNPs synthesis performed using quaternized hydroxyethyl cellulose as capping agent. In red is reported the starting composition used as reference (AgHEC_5.5_2.8), in black the composition of the other samples.*

In the following Table 1 are summarized the reagents molar ratios of the abovementioned synthesis. The samples were labeled reporting first HEC/Ag and second NaOH/Ag molar ratios.

*Table 1 – AgHEC based nanoparticles compositions and reagent molar ratios.*

| Sample | HEC/Ag molar ratio | NaOH/Ag molar ratio |
|---|---|---|
| AgHEC_5.5_2.8 | 5.5 | 2.8 |
| AgHEC_2.8_1.4 | 2.8 | 1.4 |
| AgHEC_2.8_2.8 | 2.8 | 2.8 |
| AgHEC_2.8_3.7 | 2.8 | 3.7 |
| AgHEC_6.4_1.4 | 6.4 | 1.4 |
| AgHEC_6.4_3.7 | 6.4 | 3.7 |

To better understand the correlation between the chemical composition of these NPs and the final antimicrobial properties of the products, a wide-ranging physicochemical characterization has been carried out on the samples produced.

***UV-Vis spectroscopy*** – The first qualitative indicator for a successful synthesis of AgNPs is the typical yellow color generated by the surface plasmon resonance phenomenon occurring in presence of colloidal AgNPs. The wavelength of the registered peaks is consistent with the formation of AgNPs. Thanks to UV-Vis spectroscopy the absorbance peak position and shape were observed, which may be used as a qualitative indicator of size and morphology of the analyzed NPs. In fact, as reported in literature, the UV-Vis spectrum of AgNPs depends on the size and morphology of the nanoparticles, and it also depends on the surrounding media created by the capping agent and the solvent. Previous results report silver nanoparticles with size range of 25-50 nm absorption peak around 390-420 nm, furthermore spherical nanoparticles are reported to absorb at 410-450 nm.[94,95,96,97,98]

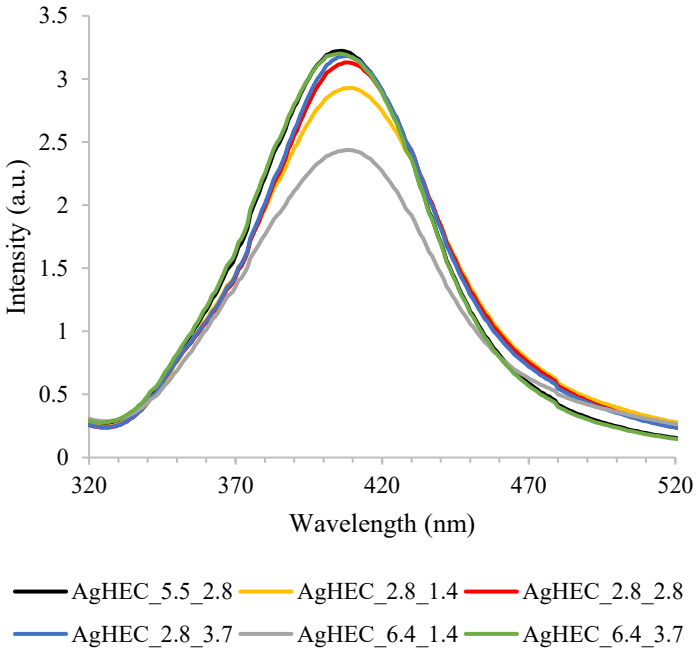


*Figure 7 – UV-Vis absorption spectra comparison of the synthesized AgHEC samples: AgHEC_5.5_2.8, AgHEC_2.8_1.4, AgHEC_2.8_2.8, AgHEC_2.8_3.7, AgHEC_6.4_1.4, and AgHEC_6.4_3.7. All the reported compositions present the typical SPR absorption peak of AgNPs with maximum absorption in the wavelength range of 405-409 nm.*

In Figure 7 are reported the absorption spectra of the set of AgHEC synthesis considered, it is possible to see a similar behavior for the different compositions in terms of peak maximum (also reported in Table 2), shape, and intensity.

*Table 2 – UV-Vis absorption peaks of AgHEC based nanoaprticles.*

| Sample | UV-Vis absorption $\lambda_{max}$ (nm) |
|---|---|
| AgHEC_5.5_2.8 | 406 |
| AgHEC_2.8_1.4 | 409 |
| AgHEC_2.8_2.8 | 408 |
| AgHEC_2.8_3.7 | 408 |
| AgHEC_6.4_1.4 | 408 |
| AgHEC_6.4_3.7 | 405 |

In comparison with the standard composition (AgHEC_5.5_2.8) it is possible to observe a lesser blue-shift for AgHEC_6.4_3.7 usually representative of smaller sized NPs, this is one of the AgNPs variant with the higher amount of capping agent. The other compositions are characterized by a little red-shift.

*Table 3 – Total silver concentration and $Ag^+$ conversion of AgHEC based nanoparticles determined by ICP-OES.*

| Sample | Total Ag concentration ($mg \cdot L^{-1}$) | $Ag^+$ conversion (%) |
|---|---|---|
| AgHEC_5.5_2.8 | 4501 ± 71 | 99.94 ± 0.02 |
| AgHEC_2.8_1.4 | 4927 ± 65 | 99.71 ± 0.05 |
| AgHEC_2.8_2.8 | 4083 ± 63 | 99.97 ± 0.03 |
| AgHEC_2.8_3.7 | 3927 ± 49 | 99.94 ± 0.08 |
| AgHEC_6.4_1.4 | 5174 ± 81 | 99.91 ± 0.04 |
| AgHEC_6.4_3.7 | 3113 ± 43 | 99.96 ± 0.02 |

***Silver quantification by ICP-OES*** – Quantitative information regarding the silver nitrate precursor used in the synthesis and the final silver concentration in the products was assessed by ICP-OES. The samples were acidic digested and then analyzed to determine the total Ag concentration, while the diluted suspensions were previously filtered to analyze only the unreacted silver cations. Results reported in Table 3 demonstrated quantitative conversion for all the conditions reported. It was observed that reducing the amount of capping agent to molar ratios HEC/Ag lower than 2.8 led to unstable suspensions that showed coarse precipitate. As an example, the composition AgHEC_1.4_2.8 demonstrated good $Ag^+$ conversion, ≈ 99.9%, but the reduced amount of HEC determined the formation of large particles with hydrodynamic diameter 3280 ± 370 nm, leading toward a fast precipitation of the unstable product. A relevant red-shift

was observed for the UV-Vis absorption peak at 424 nm, and the low absolute value of the zeta potential contributed to its instability, 3.9 ± 0.2 mV at pH 11.37.

***Transmission electron microscopy*** – All the synthesized AgHEC nanoparticles were observed by transmission electron microscopy. AgHEC_5.5_2.8 and AgHEC_6.4_1.4 were identified as the most relevant samples, and their TEM images are here reported.

AgHEC_5.5_2.8 phase contrast TEM images, reported in Figure 8, show the presence of particles well dispersed on the carbon film which size ranges from 5 - 50 nm. HRTEM images in Figure 9 highlight that the particles are crystalline and are formed by twinned domains. HAADF-STEM images in Figure 10 were used for statistical size analysis measuring the major and minor axis of each particle. SAED diffraction pattern and the relative rotational average reveal that all rings can be indexed as silver lattice planes. The morphological analysis demonstrated spheroidal nanoparticles with long axis estimated mean value of 14.6 ± 0.7 nm and short axis 12.4 ± 0.6 nm, with a confidence interval of 99%. The statistical distribution is reported in graphs in Figure 11.

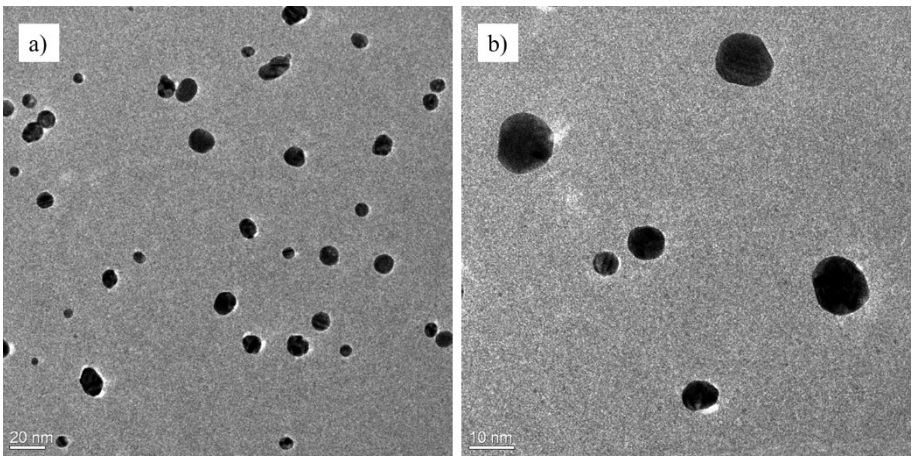


*Figure 8 – a) and b) phase contrast TEM images of AgHEC_5.5_2.8 showing particles size ranging from 3-20 nm.*

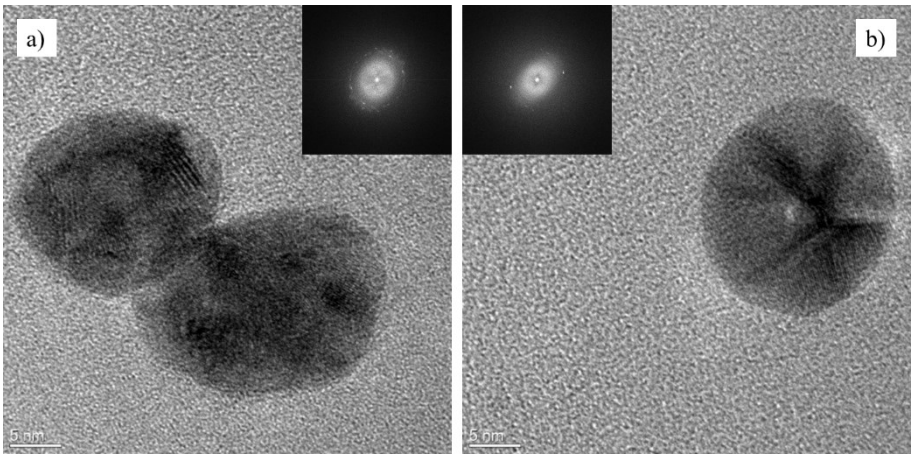


*Figure 9 – a) and b) HRTEM images of AgHEC_5.5_2.8 showing crystalline NPs formed by twinned domains.*

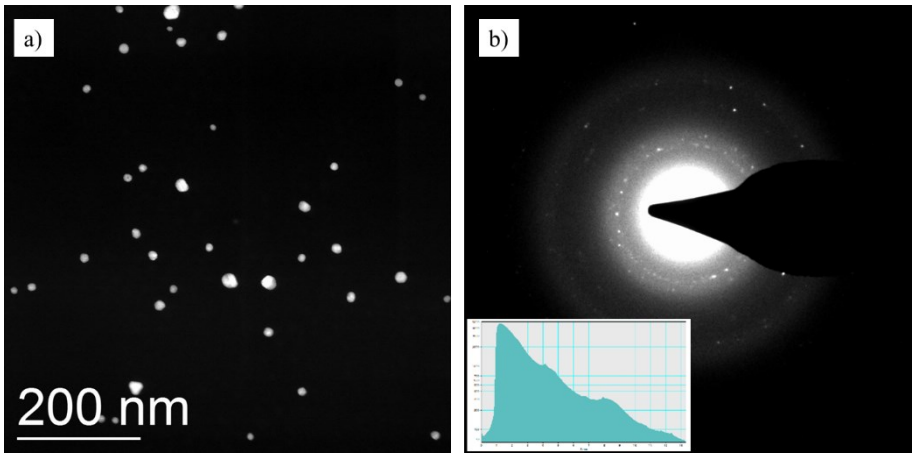


*Figure 10 – a) HAADF-STEM image of AgHEC_5.5_2.8 used for the particles size statistical analysis. b) SAED image of AgHEC_5.5_2.8 showing the diffraction pattern of metallic silver lattice planes.*

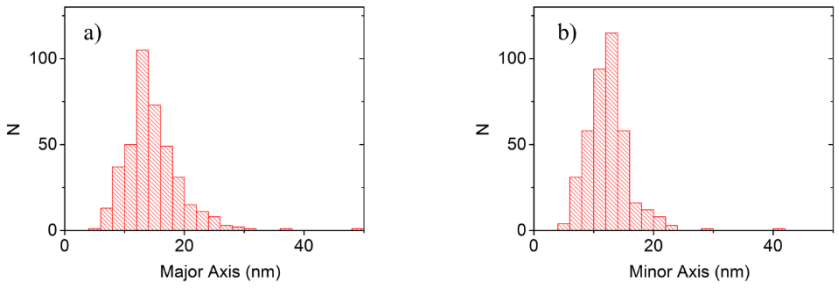


*Figure 11 – Size distribution statistical analysis of the dimensions of the sample AgHEC_5.5_2.8: a) major axis population distribution 14.6 ± 0.7 nm; b) minor axis population distribution 12.4 ± 0.6 nm. The diameter measurements are reported with a confidence interval of 99%.*

AgHEC_6.4_1.4 HAADF-STEM images (Figure 12) and SAED analysis revealed crystalline AgNPs with size ranging from 4 to 50 nm. They are well dispersed on the support carbon film. These images were used for statistical size analysis measuring the major and minor axis of each

particle. SAED diffraction pattern and the relative rotational average show in Figure 12 demonstrate that all rings can be indexed as silver lattice planes. The statistical analysis reported in the graphs Figure 13 results in a long axis estimated value of 14.4 ± 0.8 nm and a short axis 12.2 ± 0.6 nm, with a confidence interval of 99 %.

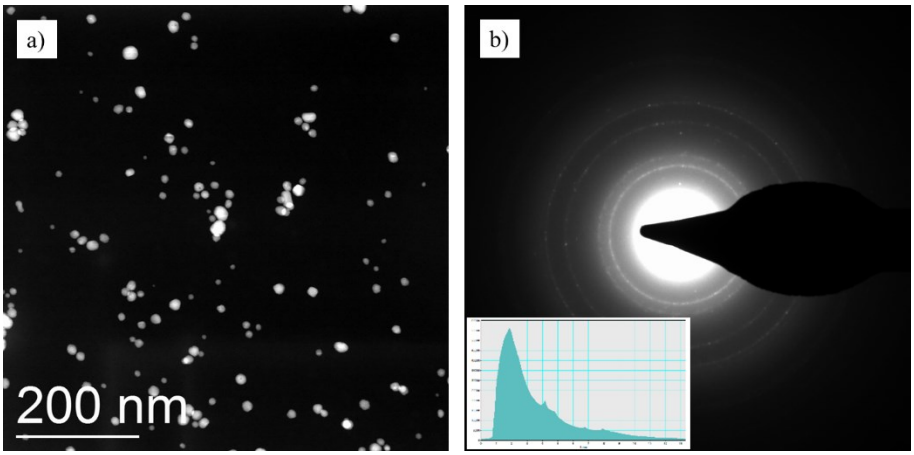


*Figure 12 - a) HAADF-STEM image of AgHEC_6.4_1.4 used for the particles size statistical analysis showing particles size ranging from 4-50 nm. b) SAED image of AgHEC_6.4_1.4 showing the diffraction pattern of crystalline metallic silver lattice planes.*

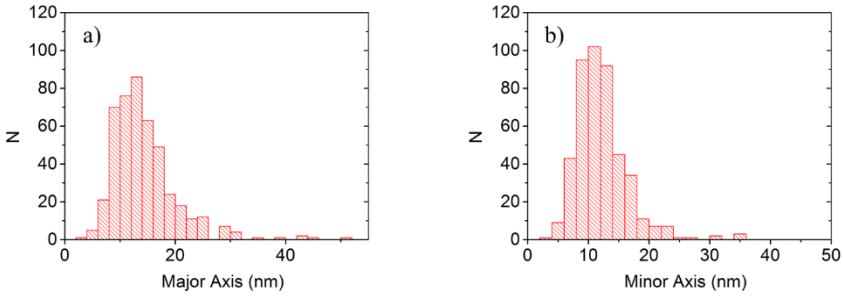


*Figure 13 - Size distribution statistical analysis of the dimensions of the sample AgHEC_6.4_1.4: a) major axis population distribution 14.4 ± 0.8 nm; b) minor axis population distribution 12.2 ± 0.6 nm. The diameter measurements are reported with a confidence interval of 99%.*

*Table 4 – TEM size of AgHEC based nanoparticles. Long and short axes are reported with an interval of confidence of 99%.*

| Sample | Long axis (nm) | Short axis (nm) |
|---|---|---|
| AgHEC_5.5_2.8 | 14.6 ± 0.7 | 12.4 ± 0.6 |
| AgHEC_6.4_1.4 | 14.4 ± 0.8 | 12.2 ± 0.6 |
| AgHEC_2.8_1.4 | 17 ± 1 | 15 ± 1 |
| AgHEC_2.8_2.8 | 18.4 ± 0.8 | 15.4 ± 0.6 |
| AgHEC_2.8_3.7 | 18.4 ± 0.8 | 15.7 ± 0.7 |
| AgHEC_6.4_3.7 | 15.6 ± 0.9 | 13.2 ± 0.7 |

Similar considerations were formulated for the other samples, the statistical analysis results are reported in Table 4.

On average, AgHEC_6.4_1.4 demonstrated the smallest sized population, this is a promising result for the antimicrobial properties, where reduced dimensions favor both the $Ag^{+}$ ion release equilibrium due to an enhanced surface/volume aspect ratio, and also the interaction of the nanoparticles with the pathogens. In the size ranking AgHEC_6.4_1.4 is directly followed by AgHEC_5.5_2.8, then come all the other compositions. These two samples were selected for an in-depth statistical analysis of the particle's dimensions, three different magnification set of images were collected and an average size was calculated for each magnification, 50 kx, 100 kx, and 400 kx. The final comparison was assessed based on the general average diameter of the three magnifications. These measurements were conducted on the JEOL 2100 FE. TEM samples were prepared by drop-casting nanomaterials suspensions onto lacey carbon films on 300 mesh copper grids and allowing them to dry before imaging.

The results collected during this second TEM measuring campaign point out slightly different average diameter for the two samples. In particular, the size of AgHEC_5.5_2.8 reported in Figure 14 and Table 5, was 17.9 ± 6.2 nm and confirmed to be larger than AgHEC_6.4_1.4 reported in Figure 15 and Table 6, which resulted to be 12.9 ± 4.9 nm. In this case, a more marked difference between the two populations was registered. AgHEC_6.4_1.4 confirmed the smallest sized population and represent the most promising candidate as an effective antimicrobial agent.

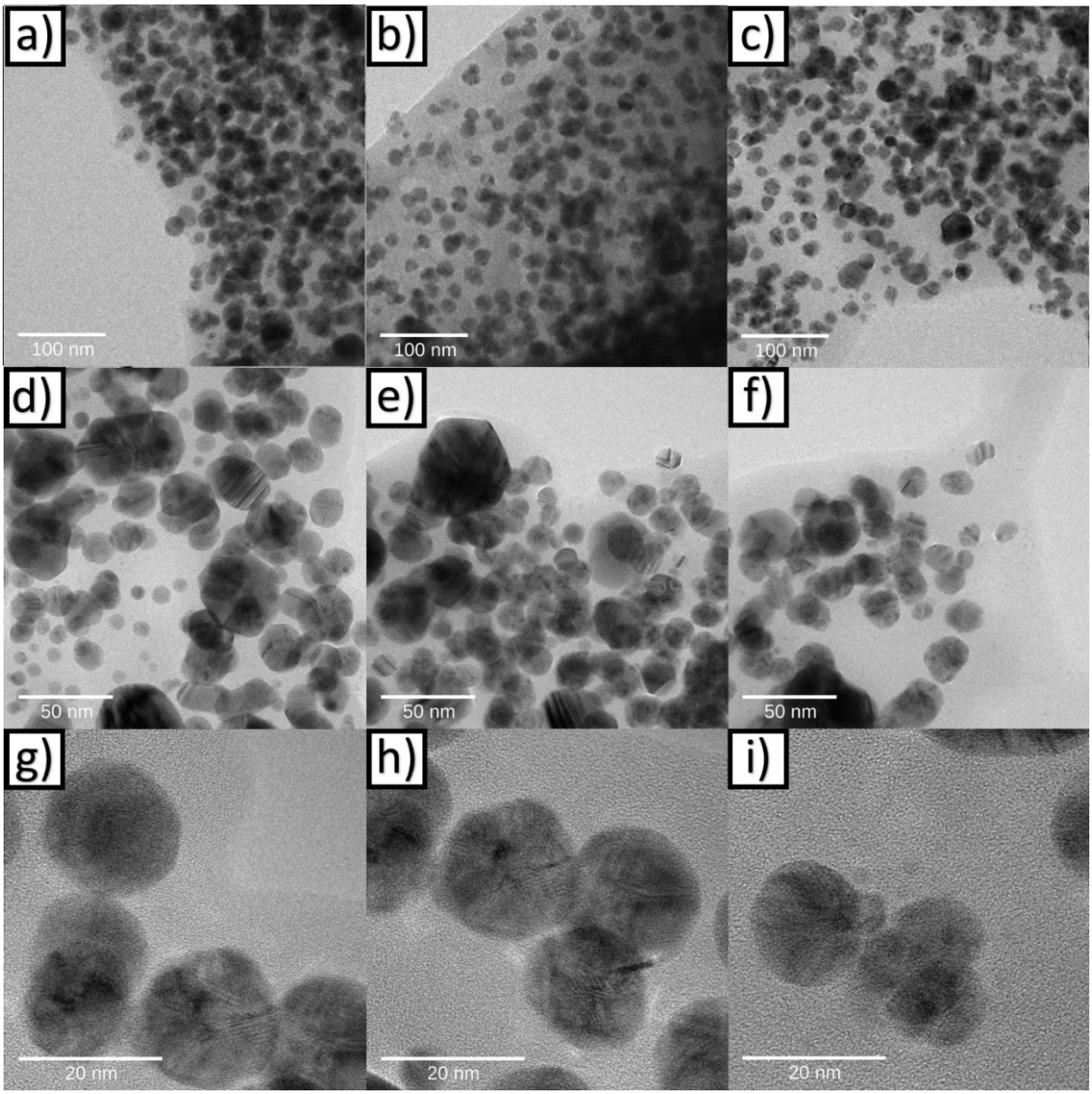


*Figure 14 – TEM micrographs of AgHEC_5.5_2.8: a), b), and c) images recorded at a magnification of 50 kx; d), e), and f) images recorded at a magnification of 100 kx; g), h), and i) images recorded at a magnification of 400 kx.*

*Table 5 – Average TEM size of AgHEC_5.5_2.8, calculated at different magnifications.*

| AgHEC_5.5_2.8 | 50 kx | 100 kx | 400 kx | Total |
|---|---|---|---|---|
| Average | 17.70 | 16.20 | 28.612 | 17.929 |
| Standard deviation | 4.390 | 5.393 | 9.886 | 6.168 |

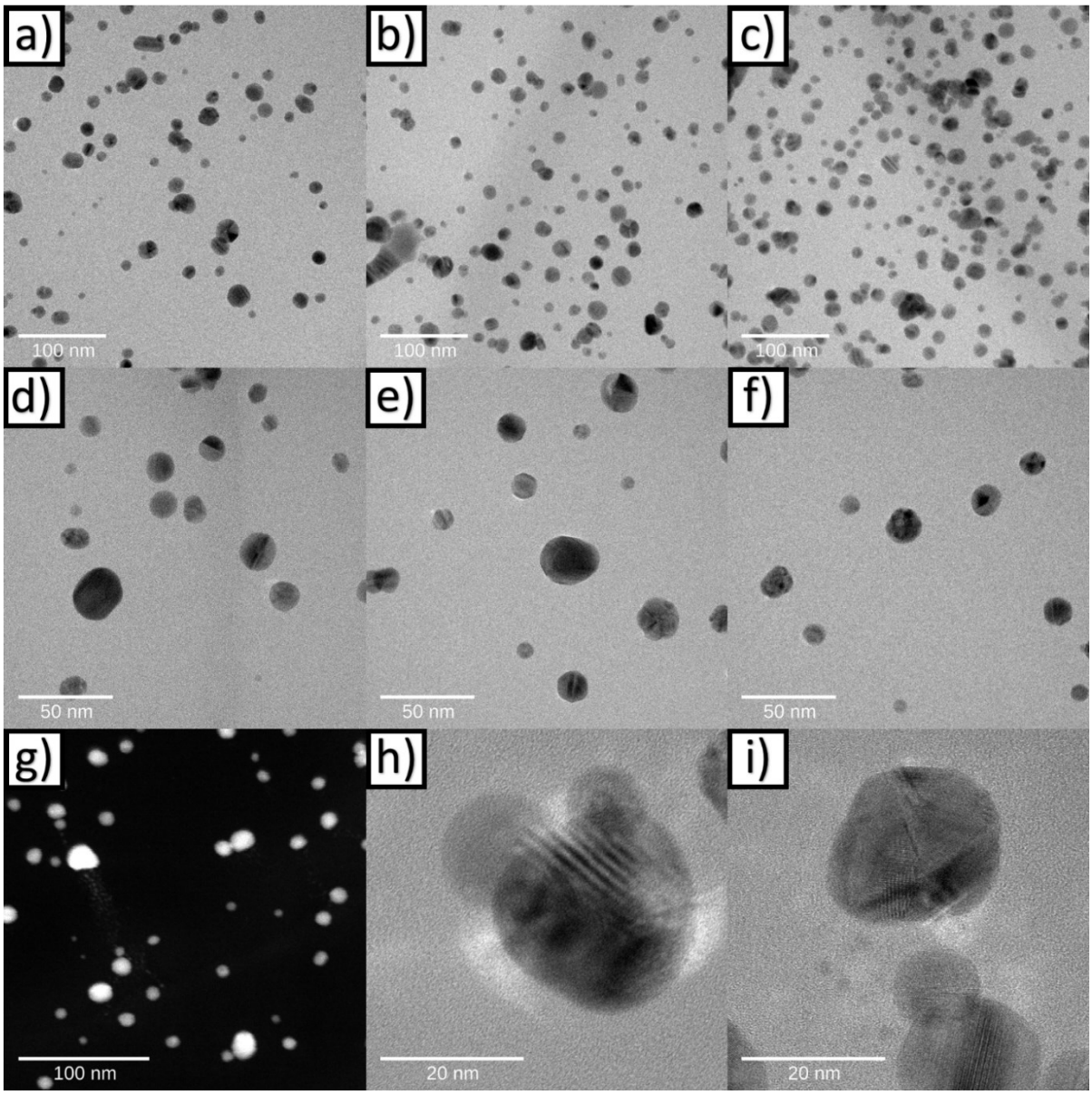


*Figure 15 - TEM micrographs of AgHEC_6.4_1.4: a), b), and c) images recorded at a magnification of 50 kx; d), e), and f) images recorded at a magnification of 100 kx; g) dark field image recorded at a magnification of 50 kx; h) and i) images recorded at a magnification of 400 kx.*

*Table 6 – Average TEM size of AgHEC_6.4_1.4, calculated at different magnifications.*

| AgHEC_6.4_1.4 | 50 kx | 100 kx | 400 kx | Total |
|---|---|---|---|---|
| Average | 12.893 | 12.144 | 17.880 | 12.906 |
| Standard deviation | 4.927 | 4.469 | 6.292 | 4.945 |

***X-ray diffraction spectroscopy*** – XRD analysis confirmed the formation of the face centered cubic structure of a metallic silver phase (JCPDS card No. 87-0717), highlighting its

characteristic diffraction peaks at 2θ 38.1, 44.2, 64.4, and 77.4 ° respectively representing (111), (200), (220), and (311) faces.

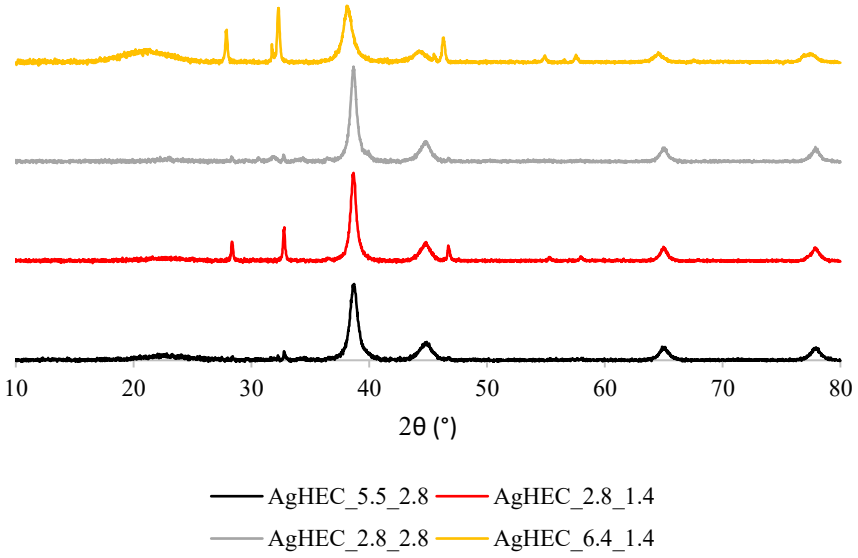


*Figure 16 – XRD spectra comparison of AgHEC_5.5_2.8, AgHEC_2.8_1.4, AgHEC_2.8_2.8, and AgHEC_6.4_1.4. The samples show the typical face-centered cubic pattern of metallic silver.*

All the samples analyzed, spectra reported in Figure 16, revealed the formation of metallic silver nanoparticles, together with secondary phases observed. In particular, for samples with reduced amount of NaOH (NaOH/Ag molar ratio 1.4), it was possible to identify the presence of cubic AgCl (JCPDS card No. 31-1238), with the main peak (200) at 32.6 ° and secondary peaks (111) and (220) respectively at 27.9 and 46.6 °, lower intensity signals are also detected for face (311) and (222) respectively at 2θ 55.2 and 57.8 °.[99] The lower amount of sodium hydroxide in the syntheses may have determined a non-quantitative reduction of the silver nitrate precursor, generating the insoluble silver chloride phase reacting with the chloride counterion of the quaternary ammonium functionalities of the HEC capping agent. Lower intensity signals were detected for NaCl, ICSD 18189 (PDF 01-072-1668), at 31.7 and 45.5 ° representative of (200) and (220) peaks, obtained as reaction coproduct. In the samples with the highest amount of capping agent, AgHEC_5.5_2.8 and even more in AgHEC_6.4_1.4, it is clearly observable a broad band about 20 °, typical of amorphous phases, in this case the quaternized hydroxyethyl cellulose.

The main diffraction peak (111) at 38.1 ° was used for the crystallite size calculation by Scherrer's equation, resulting of about 10 nm, specific results are reported in Table 7.

*Table 7 – Crystallite size of AgHEC-based nanoparticles calculated applying the Scherrer's equation on the main diffraction peak.*

| Sample | Crystallite size (nm) |
|---|---|
| AgHEC_5.5_2.8 | 8.0 |
| AgHEC_6.4_1.4 | 9.3 |
| AgHEC_2.8_1.4 | 12.5 |
| AgHEC_2.8_2.8 | 11.2 |

The crystallite size results are slightly larger for less quaternized hydroxyethyl cellulose-loaded samples (AgHEC_2.8_1.4 and AgHEC_2.8_2.8), which may be representative of an enlargement of the nanoparticles in the presence of a lesser amount of capping agent. For what concerns the results of AgHEC_5.5_2.8 and AgHEC_6.4_1.4 there is an inversion in size respect to the TEM values. In general, the recorded crystallite size is smaller than the TEM size, this is probably due to the fact that the nanoparticles may not be constituted by a single homogenous crystalline domain. The crystallization process may have been influenced by the different reaction conditions, leading to smaller crystals for AgHEC_5.5_2.8 even if the smaller nanoparticles recorded by TEM are AgHEC_6.4_1.4.[100,101,102,103]

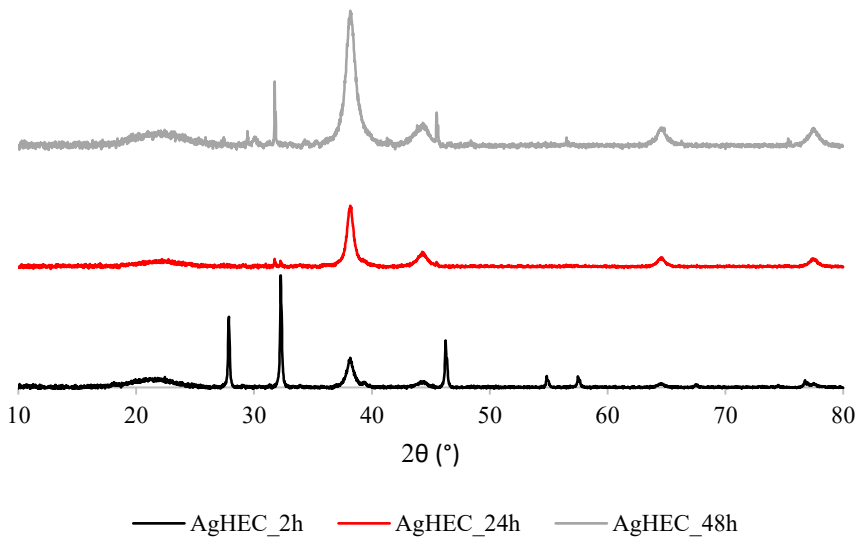


*Figure 17 – XRD spectra evolution over time during the 48 hours aging following AgHEC_5.5_2.8 synthesis. The metallic silver diffraction peaks are more intense increasing the aging time.*

The evolution over time during the 48 hours of aging of the freshly synthesized AgHEC samples has been monitored by XRD analysis. In Figure 17 are reported spectra at 2, 24, and 48 hours of

AgHEC_5.5_2.8, where the signal of the main diffraction peaks of metallic silver increase with time, and the opposite for the silver chloride which is converted to NPs.

***Hydrodynamic diameter*** – The study of the colloidal properties of these samples started from the determination of the hydrodynamic diameter, that take into consideration all the coordination sphere surrounding the nanoparticles. Using as capping agent a biopolymer means that this size is mostly influenced by the biopolymer itself. In fact, it was not possible to observe nanoparticle-specific trends in terms of hydrodynamic size and polydispersity index, but in general it is the HEC load that determines the size, higher HEC loads involve larger hydrodynamic diameter, Table 8. The same trend was observed for blank suspensions analyzed. All the compositions were at least one order of magnitude larger than the TEM size of the corresponding nanoparticles, moreover the PDI highlighted polydisperse population for all the samples, due to the polydisperse nature of the biopolymer used as a capping agent.

*Table 8 – Average hydrodynamic diameter and polydispersity index of AgHEC-based nanoparticles and HEC blanks.*

| Sample | Average hydrodynamic diameter (nm) | PDI |
|---|---|---|
| AgHEC_5.5_2.8 | 286 ± 5 | 0.323 ± 0.004 |
| AgHEC_2.8_1.4 | 219.3 ± 0.5 | 0.267 ± 0.007 |
| AgHEC_2.8_2.8 | 174 ± 1 | 0.272 ± 0.001 |
| AgHEC_2.8_3.7 | 204 ± 2 | 0.239 ± 0.012 |
| AgHEC_6.4_1.4 | 343 ± 9 | 0.321 ± 0.013 |
| AgHEC_6.4_3.7 | 298 ± 10 | 0.431 ± 0.079 |
| HEC_5.5_2.8 | 306 ± 57 | 0.480 ± 0.037 |
| HEC_2.8_2.8 | 65 ± 9 | 0.437 ± 0.103 |
| HEC_6.4_1.4 | 338 ± 83 | 0.835 ± 0.135 |

It is interesting to observe the size population distribution reported in Figure 18. A HEC/Ag molar ratio of 2.8 leads to a monomodal distribution, while 5.5 and 6.4 reveal a bimodal distribution with a larger main population due to higher quaternized hydroxyethyl cellulose load, and smaller sized particles, in the range of 30-90 nm. These samples have demonstrated to be more stable thanks to the higher load of capping agent, and at the same time, they revealed an enhanced antimicrobial activity that may be due to the smaller sized population.

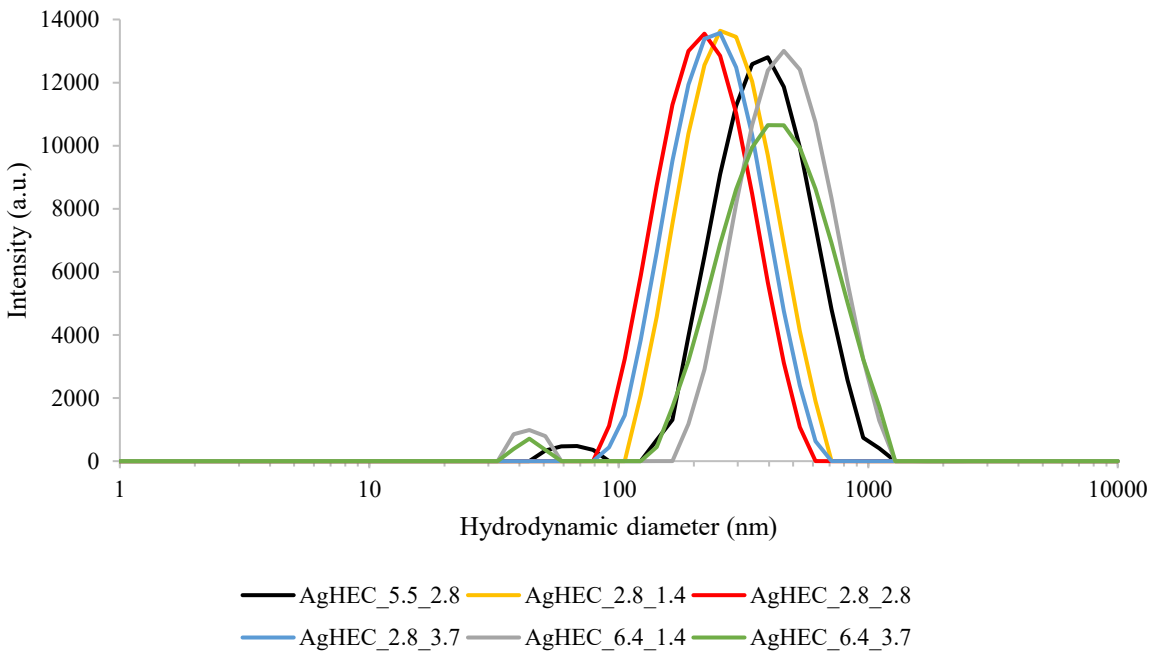


*Figure 18 – Hydrodynamic diameter population distribution determined by DLS analysis of the samples: AgHEC_5.5_2.8, AgHEC_2.8_1.4, AgHEC_2.8_2.8, AgHEC_2.8_3.7, AgHEC_6.4_1.4, and AgHEC_6.4_3.7.*

The size population of blanks reported in Figure 19 revealed more polydisperse and multimodal distributions, with larger aggregates. This demonstrate that the synthesis of AgNPs within the biopolymer structure increased the order of the system developing a more homogenous population since HEC is coordinated to AgNPs as a surrounding shell.

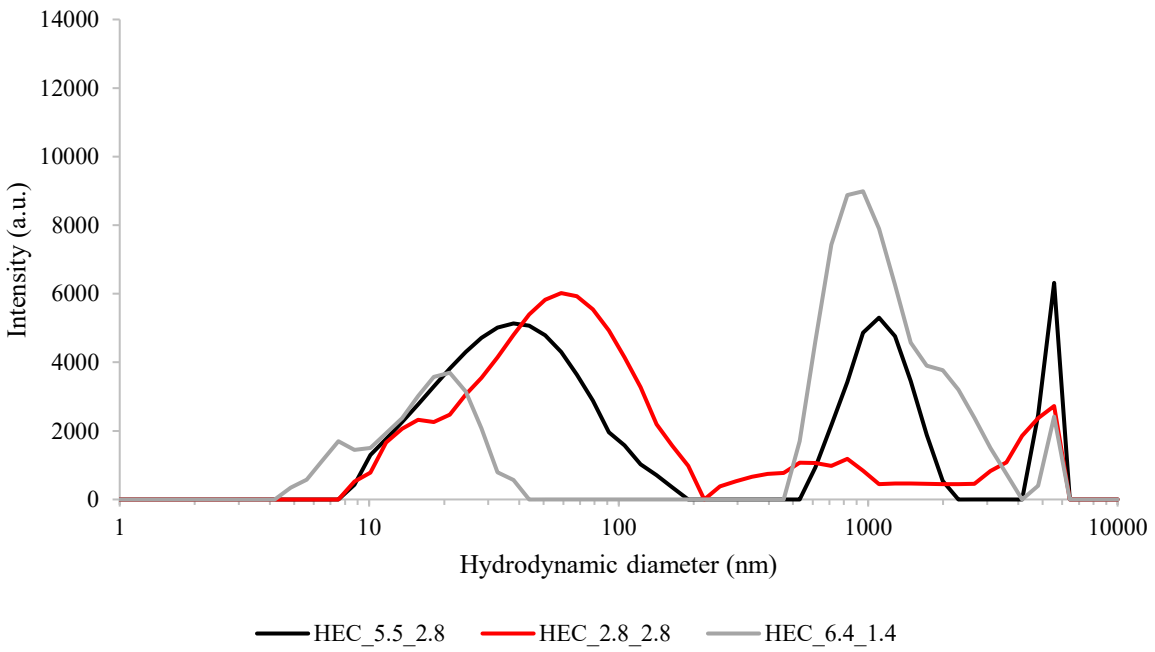


*Figure 19 – Hydrodynamic diameter population distribution determined by DLS analysis of the blanks: HEC_5.5_2.8, HEC_2.8_2.8, and HEC_6.4_1.4.*

*Table 9 – Zeta potential and pH of AgHEC-based nanoparticles and HEC blanks.*

| Sample | Zeta potential (mV) | pH |
|---|---|---|
| AgHEC_5.5_2.8 | 16.5 ± 0.3 | 10.32 |
| AgHEC_2.8_1.4 | 15.2 ± 0.1 | 9.27 |
| AgHEC_2.8_2.8 | 11.5 ± 0.4 | 10.51 |
| AgHEC_2.8_3.7 | 11.3 ± 0.3 | 10.80 |
| AgHEC_6.4_1.4 | 20.1 ± 0.4 | 9.58 |
| AgHEC_6.4_3.7 | 15.6 ± 0.6 | 10.63 |
| HEC_5.5_2.8 | 12 ± 2 | 11.12 |
| HEC_2.8_2.8 | 18.7 ± 0.6 | 11.38 |
| HEC_6.4_1.4 | 11 ± 3 | 10.84 |

***Zeta potential*** – The zeta potential gives information about the electrostatic repulsion between the nanoparticles in suspension, subsequently a suggestion related to the colloid stability. Higher zeta potential absolute values represent higher nanoparticles stability, HEC as capping agent confers positive charge to the silver nanoparticles, about 10-20 mV. In general, this is not a value high enough to grant excellent suspension stability, but HEC combines this positive charge generated by quaternary ammonium functionalities in its structure, with the steric hindrance due

to the polymeric chains that promote the colloidal stability granting these samples several months of shelf-life, when stored at 4 °C in dark conditions. As reported in Table 9, the combination of a high HEC/Ag and a low NaOH/Ag gives the highest zeta potentials.

The zeta potential of the most relevant composition, AgHEC_5.5_2.8 and AgHEC_6.4_1.4, was titrated as function of the pH. Titrations were conducted with HCl to move toward acidic conditions and NaOH for a basic environment. As it is possible to see by the graph in Figure 20, the two samples exhibit similar behavior, with a zeta potential about 15-20 mV in the range 2-10 unit of pH, a strongly acid environment favors Ag dissolution phenomenon, and moving towards more basic pH the $OH^-$ ions neutralized the positive charge of the quaternized hydroxyethyl cellulose, leading to the isoelectric point (IEP), the pH that correspond a zeta potential of 0 mV, which is about 12.5 for AgHEC_6.4_1.4. The full titration gives information abut the pH use range of these materials, that are stable in the pH interval 2-10.

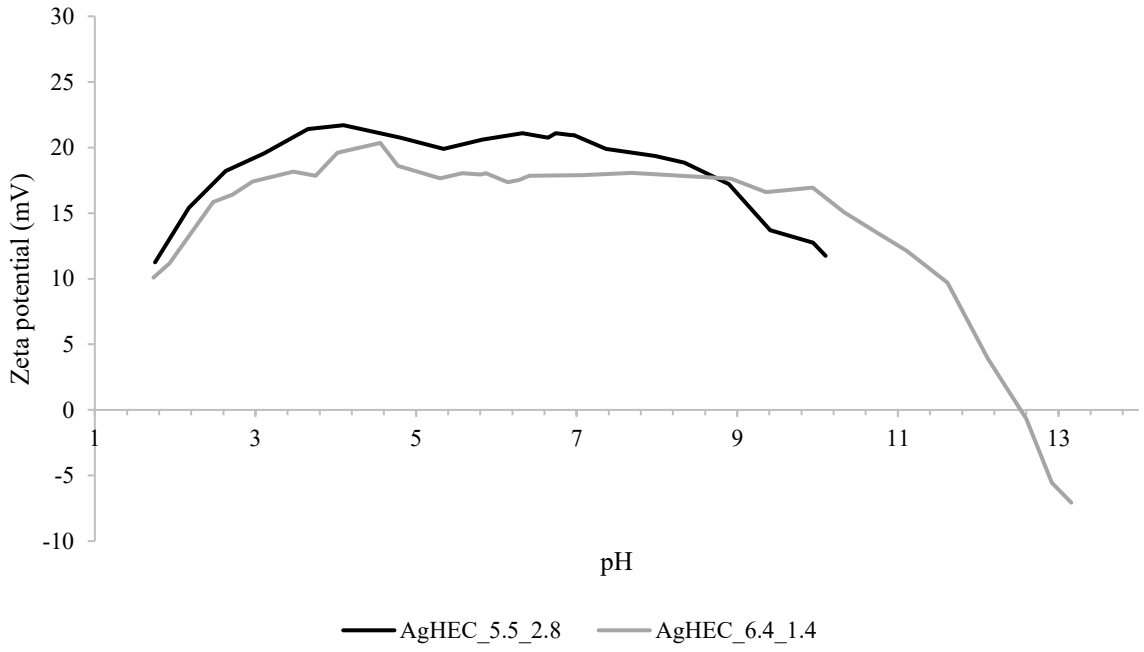


*Figure 20 – Zeta potential titrations as function of the pH of the samples AgHEC_5.5_2.8 and AgHEC_6.4_1.4. The isoelectric point of AgHEC_6.4_1.4 resulted to be at pH ≈ 12.5.*

***Alternative cellulose-based capping agents*** – Quaternized hydroxyethyl cellulose it is a biopolymer functionalized substituting at a certain degree quaternary ammonium functionalities on the hydroxyethyl cellulose skeleton. In this way, a positive charge was attributed to the capping agent. To verify the importance of the structure of the capping agent, similar compounds were used to reproduce the synthesis of AgHEC_5.5_2.8. The selected candidates were:

carboxymethyl cellulose (CMC), ethyl cellulose (EC), hydroxy ethyl cellulose (HEC_n), and hydroxypropyl cellulose (HPC). Hydroxy ethyl cellulose (HEC_n) is the base structure of the capping agent used for the AgHEC samples, but non-quaternized.

The as synthesized products were diluted and characterized. UV-Vis spectroscopy revealed the absorption peak related to AgNPs surface plasmon resonance, about 400 nm, only for AgCMC and AgHEC_n, Figure 21. As expected HEC_n gives a behavior similar to HEC. An absorption in the UV range was observed for AgHPC. No absorption peaks were observed for the blanks.

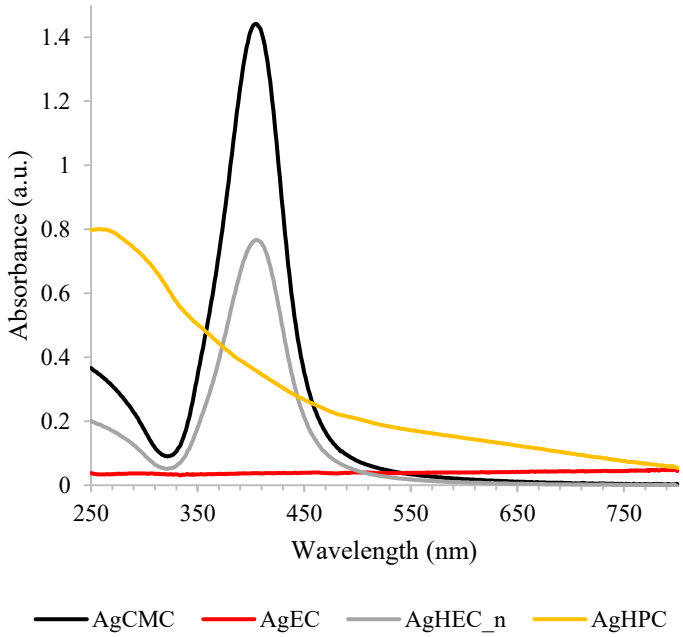


*Figure 21 – UV-Vis absorption spectra comparison of the synthesized alternatives to AgHEC: AgCMC, AgEC, AgHEC_n, and AgHPC. Only AgCMC and AgHEC_n presented the typical SPR absorption peak of AgNPs with maximum absorption at wavelength 405 nm, no absorption was monitored for AgEC, and the absorption peak of AgHPC lies in the UV region at wavelength 256 nm.*

*Table 10 – UV-Vis absorption peaks of carboxymethyl cellulose, ethyl cellulose, hydroxyethyl cellulose and hydroxypropyl cellulose capped AgNPs.*

| Sample | UV-Vis absorption $\lambda_{max}$ (nm) |
|---|---|
| AgCMC | 405 |
| AgEC | n.d. |
| AgHEC_n | 405 |
| AgHPC | 256 |

The maximum absorption for each sample is reported in Table 10, 405 nm peak is observed for both AgCMC and AgHEC_n, these are the only solution that lead to AgNPs formation. An absorption in the UV at 256 nm is revealed by AgHPC, and no peak for AgEC.

Due to the poor synthesis results and the difficulty in the acidic digestion, AgEC silver concentration and conversion were not assessed by ICP-OES, other samples results are reported in Table 11. It is possible to observe nearly quantitative conversion of the silver precursor for all the other syntheses, but at least for AgHPC the main product is not AgNPs since the surface plasmon resonance absorption is not present. Some other phases may have been formed, like silver oxide or carbonate.

*Table 11 – Total silver concentration and $Ag^+$ conversion of alternative cellulose derived capping agents (CMC, EC, HEC_n, and HPC), determined by ICP-OES.*

| Sample | Total Ag concentration ($mg \cdot L^{-1}$) | $Ag^+$ conversion (%) |
|---|---|---|
| AgCMC | 4792 ± 119 | 99.9 ± 0.1 |
| AgEC | n.d. | n.d. |
| AgHEC_n | 6386 ± 199 | 99.97 ± 0.02 |
| AgHPC | 5049 ± 45 | 99.03 ± 0.08 |

*Table 12 – Average hydrodynamic diameter and polydispersity index of alternative cellulose derived capping agents (CMC, EC, HEC_n, and HPC) and their blanks.*

| Sample | Average hydrodynamic diameter (nm) | PDI |
|---|---|---|
| AgCMC | 410 ± 4 | 0.487 ± 0.011 |
| AgEC | 1694 ± 921 | 0.857 ± 0.164 |
| AgHEC_n | 179 ± 4 | 0.324 ± 0.035 |
| AgHPC | 253 ± 7 | 0.268 ± 0.005 |
| CMC | 101 ± 138 | 0.460 ± 0.120 |
| EC | 4156 ± 58 | 1.000 ± 0.000 |
| HEC_n | 81 ± 5 | 0.554 ± 0.177 |
| HPC | 49 ± 26 | 0.260 ± 0.105 |

The DLS analysis confirmed what it was possible to see by naked eye, AgEC resulted in coarse aggregates in the size microns. The other synthesis gave more reliable results, the size and PDI

are comparable with the standard AgHEC_5.5_2.8 composition. Polydisperse and bimodal populations were registered for the samples, while strongly polydisperse and multimodal population were observed for blanks, Table 12.

The zeta potential of all the alternatives tested for the synthesis of these AgNPs resulted negative as it is possible to read in Table 13. Carboxymethyl cellulose and ethyl cellulose determine a strongly negative zeta potential respectively -56 and -41 mV, while hydroxyethyl cellulose and hydroxypropyl cellulose zeta potential are slightly negative and close to 0 mV. The same trends are observed for the blanks.

*Table 13 – Zeta potential and pH of alternative cellulose derived capping agents (CMC, EC, HEC_n, and HPC) and their blanks.*

| Sample | Zeta potential (mV) | pH |
|---|---|---|
| AgCMC | -56 ± 2 | 10.80 |
| AgEC | -41 ± 2 | 10.63 |
| AgHEC_n | -6.80 ± 0.07 | 10.67 |
| AgHPC | -3.2 ± 0.2 | 10.76 |
| CMC | -32 ± 3 | 11.03 |
| EC | -23 ± 2 | 11.14 |
| HEC_n | -2.5 ± 0.5 | 11.04 |
| HPC | -1 ± 1 | 11.08 |

The main problem in the substitution of the capping agent is to reach the same long-term stability granted by HEC. All the tested alternatives tend to precipitate after short storage times of few days or weeks observed also for the most stable composition, even AgCMC which is the only variant promoting the formation of AgNPs and a high electrostatic repulsion that should lead to a good stabilization. Summarizing, the capping agent plays a crucial role in the synthesis and the stabilization of the NPs. In this particular synthesis of AgNPs, quaternized hydroxyethyl cellulose shows outstanding performances respect to other biopolymer with similar molecular structure. This is most likely due to the quaternary ammonium functionalities that shift the zeta potential from negative to positive and the distributions of the polymeric chain surrounding the Ag core. Ethyl cellulose gives coarse aggregates, hydroxypropyl cellulose generate a different phase respect the desired metallic silver, and carboxymethyl cellulose and hydroxyethyl cellulose do not grant long term stability. All these considerations lead to the selection of quaternized hydroxyethyl cellulose as optimal capping agent for this eco-friendly synthesis of AgNPs.

### 3.2.2. Curcumin capped silver nanoparticles

Curcumin is an organic molecule that constitute the main bioactive molecule extracted from the rhizome of the *Curcuma longa*. Curcuminoids are the active compounds of *Curcuma longa* and are constituted mainly by curcumin (77 %), demethoxycurcumin (17 %), and bisdemethoxycurcumin (3 %), their molecular structures are schematized in Figure 22. As alternative from the extraction of the molecule, curcumin can also be synthesized by chemical way and its production from microorganisms is object of study.[104]

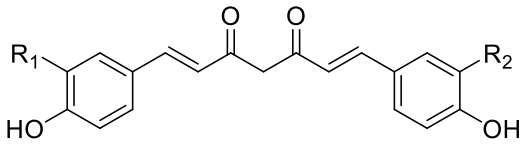


Curcumin: $R_1 = R_2 = OCH_3$

Demethoxycurcumin: $R_1 = OCH_3$; $R_2 = H$

Bisdemethoxycurcumin: $R_1 = R_2 = H$

*Figure 22 – Curcuminoids molecular structure: curcumin, demethoxycurcumin, and bisdemethoxycurcumin.*

It is an interesting molecule since it is historically part of the Asian pharmacology and medicine thanks to its various beneficial biological properties and intrinsic low toxicity. Several studies have demonstrated anti-inflammatory, antioxidant, anti-mutagenic, wound healing, neuroprotective, antimicrobial, and biofilm inhibition properties. Unfortunately, practical applications of curcumin are impaired due to the limited solubility in water and the molecule susceptibility to heat, light, alkaline conditions, metal ions, enzymes, oxygen, and ascorbic acid.[105]

The mechanism of the antibacterial action of curcumin is divided into several levels against both Gram-positive and Gram-negative bacteria.[106,107] The first recognized activity is the cell membrane disruption, thanks to its lipophilicity curcumin attacks the liposome bilayer damaging the permeability and integrity of bacterial cell membrane.[108] The inhibition of bacterial quorum sensing system, which is a cell-cell communication system, helps in preventing both biofilm formation and bacterial adhesion to host receptors.[109,110,111,112,113] Another important mechanism is the inhibition of bacterial cell division thanks to the blocking of the filament temperature-sensitive protein Z (FtsZ), essential for the bacterial cell division.[114,115,116] Curcumin at minimum inhibitory concentration (MIC) induces the production of reactive oxygen species (ROS) in bacterial cells, resulting in apoptotic-like death processes.[117] Absorbing the visible light in the

wavelength range of 455-460, curcumin can act as photosensitizer inducing phototoxicity in bacteria exposed to blue light irradiation. Gram-positive bacteria are more sensitive to these photoinduced processes, probably due to the more robust outer membrane of Gram-negative bacteria.[118] Other recognized activities involve the perturbation of the bacterial cell metabolism and the intracellular bacterial infection and proliferation.[119,120]

Literature studies report that AgNPs can act in a synergistic way with their stabilizing agent and dispersing matrix by enhancing the inhibitory effect of traditional antimicrobial agents.[121] Curcumin is a very promising molecule thanks to all its beneficial properties and it may be an excellent capping agent for the production of metallic nanoparticles, in particular antimicrobial silver nanoparticles.[122] In this way, it is desired to exploit synergistic effect between the metallic core of the nanoparticles and the organic coating to develop stronger antimicrobial properties and also to reduce the susceptibility of the curcumin in unfavorable environments. In this perspective an eco-friendly and easily scalable synthesis of AgNPs was developed exploiting curcumin as reducing and chelating agent.

Curcumin (Cur) capped silver nanoparticles (AgCur) were synthesized using the curcumin as reducing and capping agent. The curcumin molecule, reported in Figure 23, is recognized in literature to be a natural derived antimicrobial and antioxidant agent, also it has been investigated as antitumoral.[123]

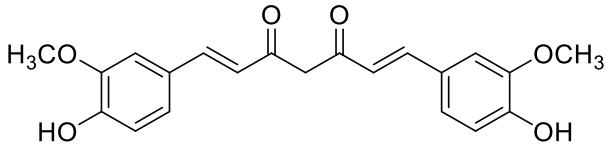


*Figure 23 – Curcumin molecular structure.*

Curcumin molecule undergoes keto-enol tautomerism, enolic form is favored in organic solvents while the keto form is favored in water.[124] The limit structures are reported in Figure 24.[125]

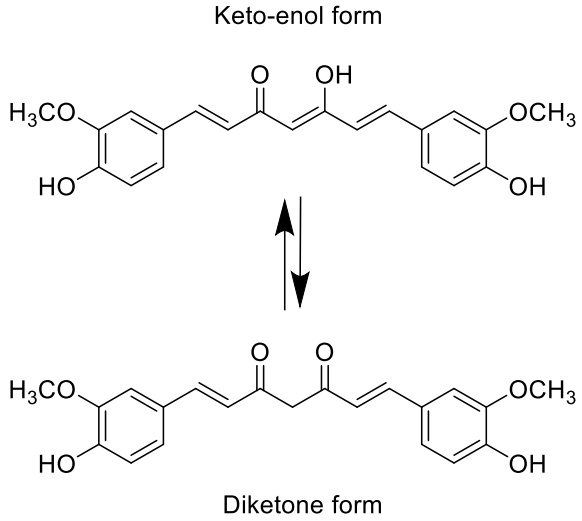


*Figure 24 – Limit structures of the curcumin keto-enol tautomerism.*

***Design of experiment*** – The use of curcumin in the green synthesis of antimicrobial AgNPs is being investigated looking for a synergistic effect between the organic molecule and inorganic silver in terms of antibacterial and antiviral activity.[126] Curcumin is an orange powder hardly soluble in water, it is better soluble in basic water where it confers a red coloration to the solution. Once the silver is added the suspension turns immediately to brown, optical evidence of AgNPs formation. Throughout a DoE, the bidimensional space created by Cur/Ag and NaOH/Ag molar ratios has been explored. The 5 syntheses reported in the graph in Figure 25 were designed to determine the best composition in terms of colloidal stability and antimicrobial properties. The tested compositions are reported in black in the graph, while the optimized one is represented in red.

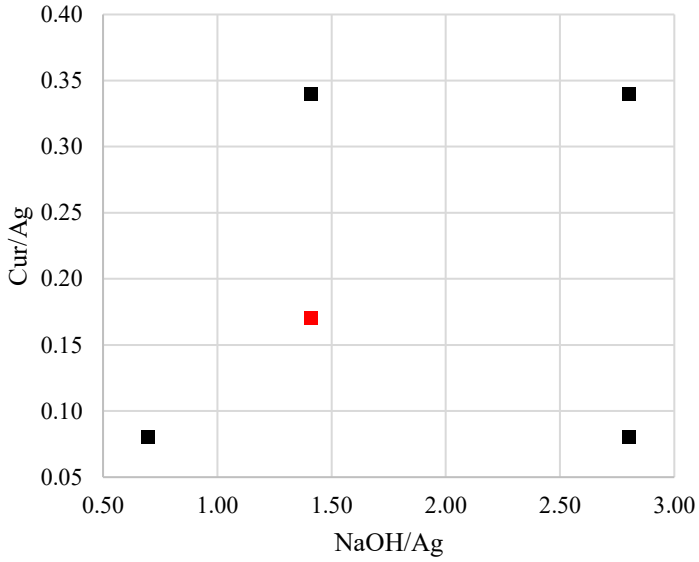


*Figure 25 – Design of experiment assessed to optimize the reagent molar ratios (Cur/Ag and NaOH/Ag) of the AgNPs synthesis performed using curcumin as capping agent. In red is reported the starting composition used as reference (AgCur), in black the composition of the other samples.*

Table 14 reports reagents molar ratios of the tested synthesis compositions.

*Table 14 – Curcumin-capped silver nanoparticles composition and reagent molar ratios.*

| Sample | Cur/Ag molar ratio | NaOH/Ag molar ratio |
|---|---|---|
| AgCur | 0.17 | 1.41 |
| AgCur_A | 0.08 | 0.70 |
| AgCur_B | 0.34 | 1.41 |
| AgCur_C | 0.34 | 2.80 |
| AgCur_D | 0.08 | 2.80 |

Further investigations have been carried out, hydroalcoholic mixture in different water-ethanol ratios was used as reaction environment to favor the difficult solubilization of curcumin in water, and additional capping agents were tested such as polyvinylpyrrolidone or casein hydrolysate, in particular casein micelles can form a fluorescent complex with curcumin which could be useful to track the NPs during the application and characterization.[127]

***UV-Vis spectroscopy*** – UV-Vis analysis was carried out on the curcumin capped silver nanoparticles looking for the surface plasmon resonance (SPR) peak typical of AgNPs in the 400-420 nm range. As reported in Figure 26, there are some compositions selected thanks to the

DoE that show better results in terms of SPR phenomenon, in particular AgCur, AgCur_Cas, AgCur_B, and AgCur_C, while there is a very low intensity peak for AgCur_D, and a flat line for AgCur_A. The reduced amount of curcumin in these last two samples leads toward a more complicated reduction of the silver precursor and an unstable product characterized by coarse aggregates and fast precipitations of micro- and macroscopic matter. In this case, it is also interesting to observe the UV-Vis spectra of the blanks, in fact, curcumin water solutions are typically orange, which turns to red once the sodium hydroxide is added. Depending on the relative content of curcumin and sodium hydroxide, different absorption profiles are obtained as reported in Figure 27. They are all characterized by 1 or 2 peaks in the visible region and an increasing absorption moving toward the UV range. Curcuminoids are characterized by two main absorption peaks, at ≈ 425 nm corresponding to the enol-form and at ≈ 360 nm corresponding to the keto-form. In polar solvents like methanol only enol-form is observed, while in water an equilibrium between the two species is established.[128,129,130,131] The curcumin spectrum is not found in the silver-based samples, indicating a predominance of the SPR signal and a modification of the interaction with light if compared to the free curcumin solution.

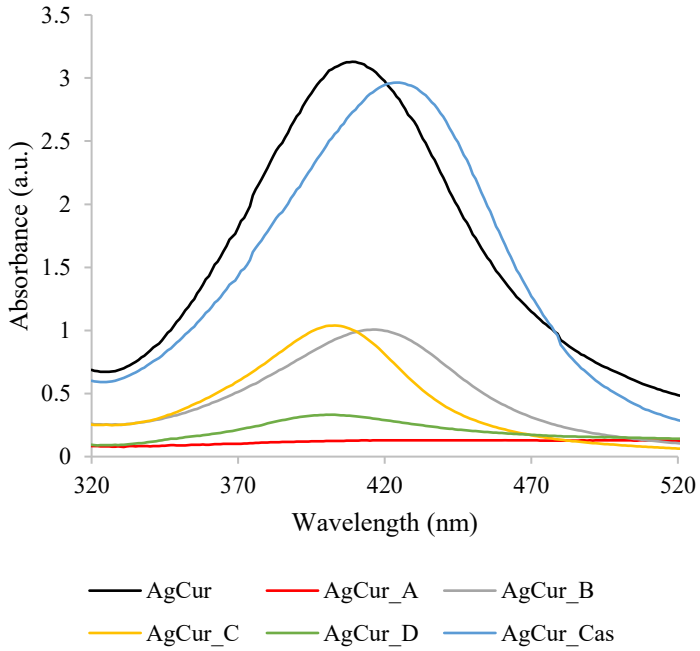


*Figure 26 – UV-Vis absorption spectra comparison of the synthesized AgCur samples: AgCur, AgCur_A, AgCur_B, AgCur_C, AgCur_D, and AgCur_Cas. AgCur, AgCur_C and AgCur_D compositions present the typical SPR absorption peak of AgNPs with maximum absorption in the wavelength range of 401-409 nm. No absorption was recorded for AgCur_A, while a red-shift was observed for AgCur_B (417 nm) and AgCur_Cas (424 nm).*

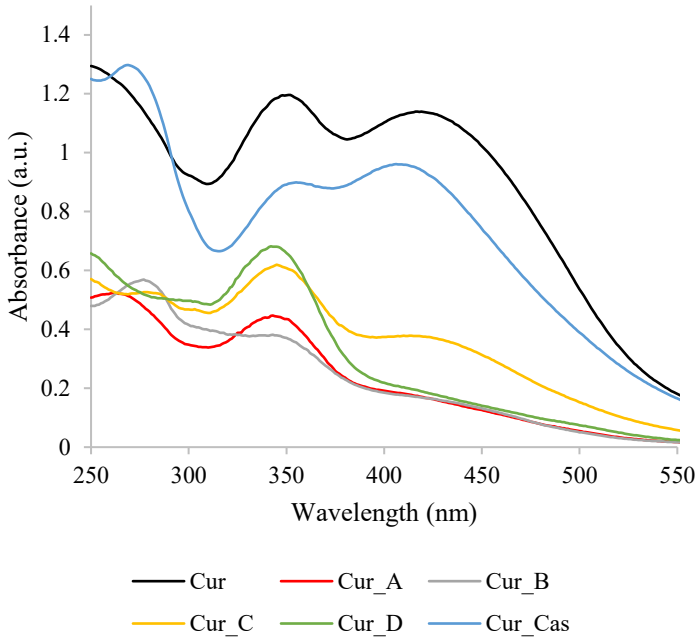


*Figure 27 – UV-Vis absorption spectra comparison of the curcumin-based blanks: Cur, Cur_A, Cur_B, Cur_C, Cur_D, and Cur_Cas. The samples presented curcuminoids two main absorption peaks: enol-form at ≈ 425 nm and keto-form at ≈ 360 nm.*

*Table 15 – UV-Vis absorption peaks of curcumin-capped AgNPs and their blanks.*

| Sample | UV-Vis absorption $\lambda_{max}$ (nm) |
|---|---|
| AgCur | 409 |
| AgCur_A | n.d. |
| AgCur_B | 417 |
| AgCur_C | 403 |
| AgCur_D | 401 |
| AgCur_Cas | 424 |
| Cur | 419, 351, < 250 |
| Cur_A | 343, 261 |
| Cur_B | 343, 277 |
| Cur_C | 413, 345, < 250 |
| Cur_D | 345, < 250 |
| Cur_Cas | 406, 355, 269 |

Considering AgCur as the reference composition, a red-shift was observed for AgCur_B and AgCur_Cas. In the case of the casein containing composition it may be this variation influencing

the maximum absorption, while in the case of AgCur_C it may be due to the increased curcumin content. In Table 15 are reported the maximum absorption peaks of all the samples analyzed.

***Silver quantification by ICP-OES*** – The quantitative information regarding the silver concentration and precursor conversion were obtained by ICP-OES analysis. The samples were acidic digested for the analysis, for the quantification of the unreacted silver cations they were previously filtered by centrifugation. The results reported in Table 16 point out an average slightly higher concentration respect to the theoretical 5000 $mg \cdot L^{-1}$, this may be due to the fact that the reaction is conducted in temperature and even working with reflux some water evaporated during the process. More interesting is the quantitative conversion obtained for most of the synthesis (> 99.6 %), except AgCur_Cas where the casein may interfere with the reaction, and AgCur_A where the combination of reduced Cur/Ag and NaOH/Ag molar ratios lead to a limited conversion and an unstable coarse product. Based on these preliminary results, the formulation containing the lowest amount of curcumin (AgCur_A and AgCur_D) were discarded due to conversion and stability problems, and AgCur_Cas represent an alternative that may be interesting only in the case the fluorescent properties of the curcumin-casein complex can be exploited.

*Table 16 – Total silver concentration and $Ag^+$ conversion of curcumin-capped silver nanoparticles, determined by ICP-OES.*

| Sample | Total Ag concentration ($mg \cdot L^{-1}$) | $Ag^+$ conversion (%) |
|---|---|---|
| AgCur | 6582 ± 384 | 99.6 ± 0.2 |
| AgCur_A | 6017 ± 219 | 72 ± 1 |
| AgCur_B | 5778 ± 424 | 99.89 ± 0.02 |
| AgCur_C | 5832 ± 279 | 99.98 ± 0.01 |
| AgCur_D | 6598 ± 204 | 99.98 ± 0.01 |
| AgCur_Cas | 6611 ± 378 | 96.2 ± 0.2 |

***Transmission electron microscopy*** – TEM was used for the morphological study of the curcumin capped silver nanoparticles. The reference composition AgCur images are reported in Figure 28. HAADF-STEM images show crystalline AgNPs with size ranging from 5 to 37 nm. They are well dispersed on the support carbon film. These images were used for statistical size analysis measuring the major and minor axis of each particle. SAED diffraction pattern and the relative rotational average reveal that all rings can be indexed as silver lattice planes.

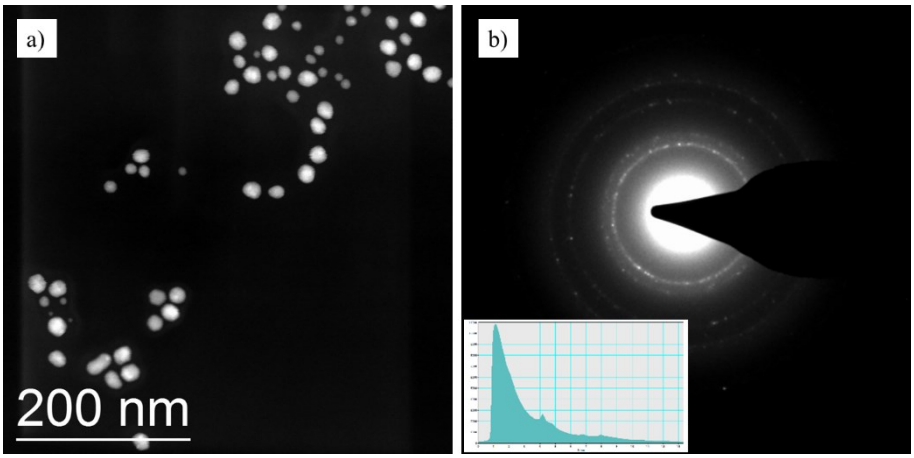


*Figure 28 – a) HAADF-STEM image of AgCur used for the particles size statistical analysis showing particles size ranging from 5-37 nm. b) SAED image of AgCur showing the diffraction pattern of crystalline metallic silver lattice planes.*

The size of 513 NPs in different images were measured resulting in a long axis estimated mean value 16.7 ± 0.7 nm and a short axis 14.0 ± 0.5 nm with a confidence interval of 99 %. From the histograms reported in Figure 29 it is possible to argue that both the distributions are bi-modal. Using graphical interpolation methods, it is possible to estimate that the smallest particles have long axis 11 ± 2 nm and short axis 9 ± 2 nm, while the larger particles have long axis 19 ± 2 nm and short axis 16 ± 2 nm.

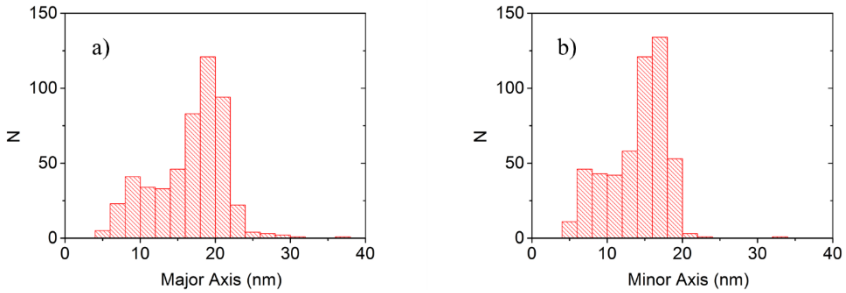


*Figure 29 – Size distribution statistical analysis of the dimensions of the sample AgCur: a) major axis population distribution 16.7 ± 0.7 nm; b) minor axis population distribution 14.0 ± 0.5 nm. The diameter measurements are reported with a confidence interval of 99%.*

AgCur_Cas HAADF-STEM images, reported in Figure 30, show crystalline AgNPs with size ranging from 5 to 30 nm. They are well dispersed on the support carbon film. These images were used for statistical size analysis.

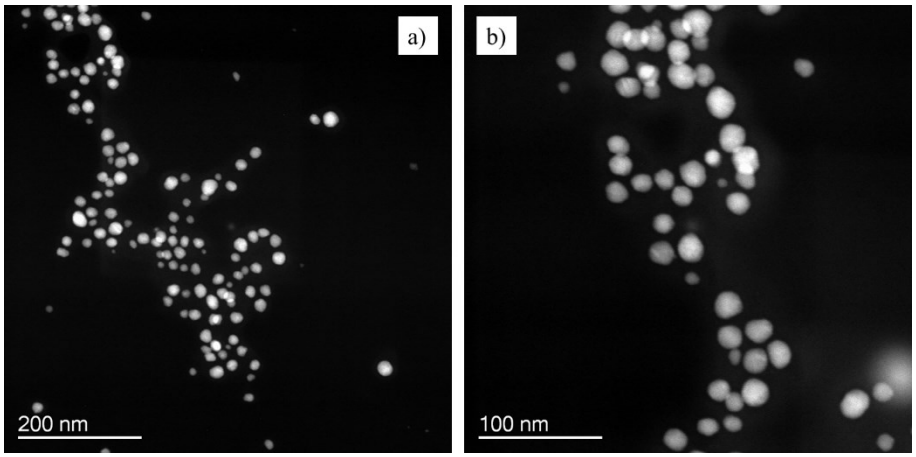


*Figure 30 – a) and b) HAADF-STEM image of AgCur_Cas used for the particles size statistical analysis showing crystalline particles with size ranging from 5-30 nm.*

AgCur_Cas NPs have elliptical shape and consequently the major and the minor axes of 334 NPs were measured resulting in a long axis estimated average value of 16.2 ± 0.6 nm and a short axis of 13.6 ± 0.6 nm with a confidence interval of 99 %. Both the statistical distributions reported in Figure 31 are bimodal and it is possible to identify two groups of particles, the slightly less populated smaller distribution, with the median value of the major and minor axis of 11 and 9 nm, and the larger distribution with median major and minor axis values of 18 and 15 nm.

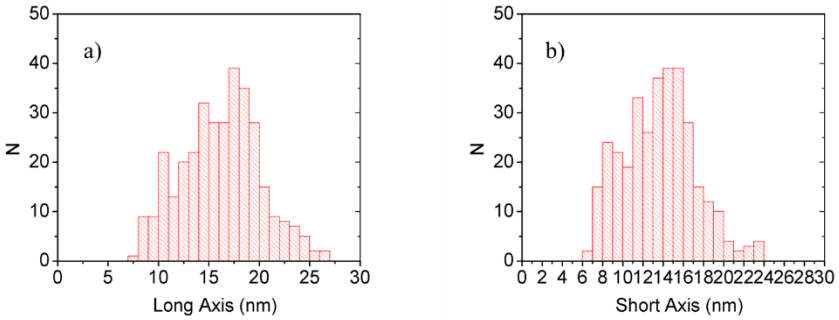


*Figure 31 - Size distribution statistical analysis of the dimensions of the sample AgCur_Cas: a) long axis population distribution 16.2 ± 0.6 nm; b) short axis population distribution 13.6 ± 0.6 nm. The diameter measurements are reported with a confidence interval of 99%.*

AgCur and AgCur_Cas have demonstrated to have similar morphology and comparable dimensions. From an indept analysis of the statistical distribution of the two bimodal populations, AgCur results in having a slighly bigger NPs, about 1 nm, populating the larger group of Nps. This may be due to the use of casein as additional capping agent limiting the growth of larger

nanoparticles, but also the different conversion of the two syntheses (99.6 % AgCur and 96.2 % AgCur_Cas) that could lead to a limited accretion of AgCur_Cas.

***X-ray diffraction spectroscopy*** – AgCur and AgCur_Cas XRD spectra, reported in Figure 32, confirmed the formation of AgNPs showing the diffraction peaks of the face-centered cubic structure of the metallic silver phase (JCPDS card No. 87-0717), at 2θ 38.1, 44.2, 64.4, and 77.4 ° respectively representing (111), (200), (220), and (311) planes. AgCur shows also the presence of $NaNO_3$ as reaction coproduct formed by the sodium of NaOH and the nitrate anion of $AgNO_3$, represented by diffraction peaks at 2θ 29.3, 31.9, and 47.9 °. The crystallite size, calculated by Scherrer's equation using the main Ag diffraction peak (111), is 7.9 nm in the case of AgCur, while it is smaller for AgCur_Cas, 4.6 nm. Since from TEM images the two samples showed comparable size with slightly smaller AgCur_Cas population, it is possible to assume that casein push the synthesis towards smaller sized coherently scattering crystalline domains, obtaining more likely polycrystalline nanoparticles.[100,101,102,103]

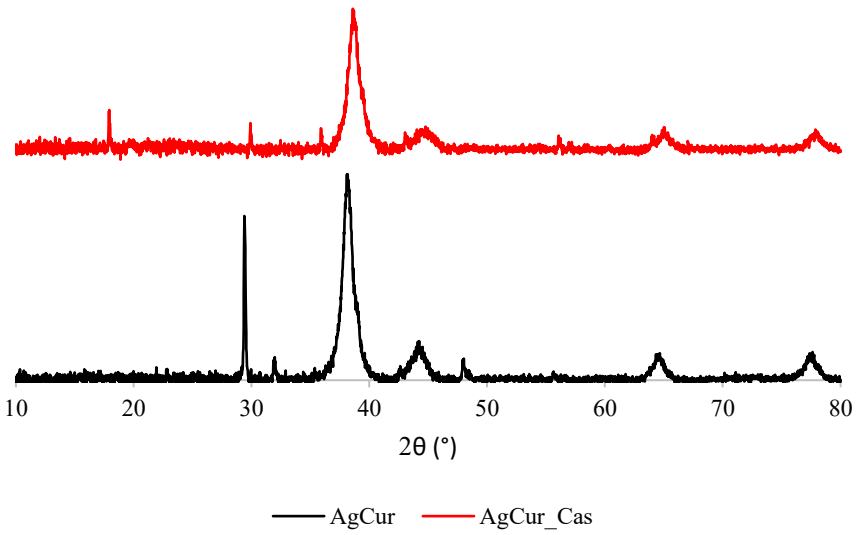


*Figure 32 – XRD spectra comparison of AgCur and AgCur_Cas. The samples show the typical face-centered cubic pattern of metallic silver.*

***Hydrodynamic diameter*** – The colloidal properties of all the synthesized variants of curcumin capped silver nanoparticles were analyzed. Curcumin is a relatively small molecule but due to the reduced solubility in water tens to form large aggregates, as it is possible to see by the hydrodynamic diameter reported in Table 17 for the blank samples Cur, Cur_A, Cur_B, Cur_C, Cur_D, and Cur_Cas. In this case, curcumin capped AgNPs have smaller dimensions respect to

the blanks, in fact the coordination of the organic shell on the surface of the AgNPs gives hydrodynamic size of about 100 nm with a polydisperse population. AgCur_A, characterized by a reduced amount of curcumin, was already identified by the UV-Vis spectrum and the Ag conversion as a problematic composition, it is confirmed also by DLS analysis, where micrometric aggregates are detected in a highly polydisperse population. Casein seems to contribute to generate a smaller coordination sphere surrounding AgNPs.

*Table 17 – Average hydrodynamic diameter and polydispersity index determined by DLS of curcumin-capped AgNPs and their blanks.*

| Sample | Average hydrodynamic diameter (nm) | PDI |
|---|---|---|
| AgCur | 106.5 ± 0.6 | 0.278 ± 0.006 |
| AgCur_A | 2921 ± 475 | 1.000 ± 0.000 |
| AgCur_B | 93.0 ± 0.8 | 0.390 ± 0.008 |
| AgCur_C | 45.5 ± 0.4 | 0.437 ± 0.004 |
| AgCur_D | 86.6 ± 0.9 | 0.502 ± 0.034 |
| AgCur_Cas | 61 ± 3 | 0.447 ± 0.050 |
| Cur | 406 ± 159 | 0.820 ± 0.165 |
| Cur_A | 1108 ± 464 | 0.810 ± 0.160 |
| Cur_B | 406 ± 126 | 0.472 ± 0.038 |
| Cur_C | 248 ± 45 | 0.471 ± 0.053 |
| Cur_D | 349 ± 41 | 0.431 ± 0.023 |
| Cur_Cas | 3172 ± 919 | 1.000 ± 0.000 |

***Zeta potential*** – ELS analysis underlines the negative charge attributed to these AgNPs from the curcumin coating, as it is possible to see in Table 18. All the samples and the blanks demonstrate elevated zeta potential absolute value, considering that above ±30 mV the colloidal suspension may be considered stable. Samples range from -37 to -57 mV and blanks from -28 to -55 mV. This suggest a good electrostatic repulsion between nanoparticles, but it is observed a not excellent stability during the long-term storing of these sample. A little sedimentation occurs, this is due to the limited solubility of curcumin in water environment.

*Table 18 – Zeta potential and pH of curcumin-capped AgNPs and their blanks.*

| Sample | Zeta potential (mV) | pH |
|---|---|---|
| AgCur | -38.9 ± 0.3 | 9.00 |
| AgCur_A | -37 ± 1 | 5.44 |
| AgCur_B | -47.0 ± 0.8 | 7.13 |
| AgCur_C | -53.6 ± 0.7 | 10.60 |
| AgCur_D | -56.9 ± 0.9 | 11.18 |
| AgCur_Cas | -40 ± 1 | 8.30 |
| Cur | -28 ± 1 | 10.60 |
| Cur_A | -51 ± 4 | 9.36 |
| Cur_B | -55 ± 2 | 9.45 |
| Cur_C | -53 ± 2 | 11.36 |
| Cur_D | -37 ± 4 | 11.64 |
| Cur_Cas | -49 ± 5 | 9.91 |

The titration of the zeta potential as function of the pH helps in the determination of the pH range of stability of the synthesized NPs, and so the pH interval where the products may be exploited. As it is recorded for the zeta potential single points above, the titrations of different compositions have similar behavior, except for AgCur_A that shows less negative values of zeta potential in the pH interval explored (data not reported). The general trend of the samples is similar to the one of curcumin and casein alone, stable at neutral and basic pH, then the surface charge is neutralized moving towards strongly acidic environments.

### 3.2.3. Sodium surfactin-capped silver nanoparticles

Sodium surfactin, whose molecular structure is shown in Figure 33, is an amphiphilic cyclic lipopeptide made of a hydrophilic oligopeptide ring and a hydrophobic fatty acid chain. The peptide polar ring is constituted by the following amino acids: glutamic acid, leucine, valine, and aspartic acid, chained as follows L-Glu, L-Leu, D-Leu, L-Val, L-Asp, D-Leu, and L-Leu.[132] The hydrophobic phase, derived from the fatty acid, is typically an iso-dodecyl carbon chain. Sodium surfactin chemical structure, $C_{53}H_{93}N_7NaO_{13}$, is completed by a sodium atom, for a total molecular weight of 1059.3 g·mol$^{-1}$.[133,134]

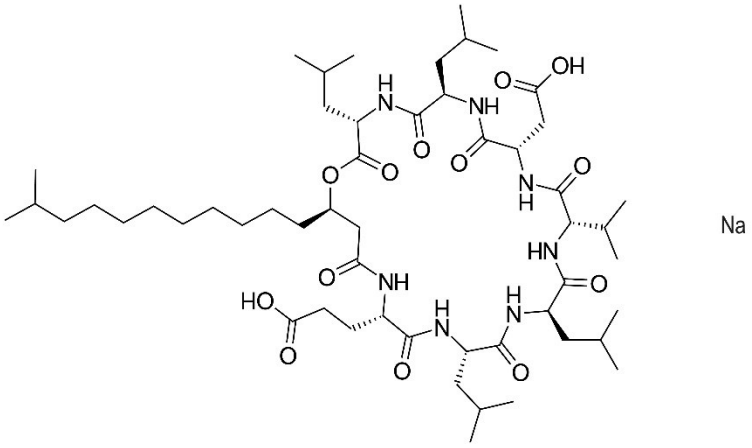


*Figure 33 – Sodium surfactin molecular structure.*

Sodium surfactin, as suggested by the name of the compound, is a surfactant (***surf**ace-**act**ive-**a**g**ent***). The amphiphilic structure allows to decrease the surface or interfacial tension between two phases.[135] In the aqueous phase these compounds tend naturally to form aggregates commonly named micelles. Micelles are constituted by an external layer where the hydrophilic heads are in contacts with the water, and by an internal core where the hydrophobic tails are confined. A schematic representation of a micelle is reported in Figure 34, but depending on the surfactant chemical structure they can create micelles of different shape and size, such as spherical, cylindrical, bilayer, and other arrangements. Other external important parameters influencing the shape of micelles are pH, temperature, and salinity of the solution, together with the concentration of surfactant.[136]

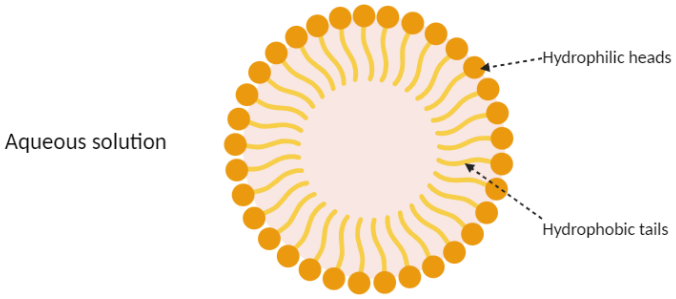


*Figure 34 – Typical micellar structure exposing the hydrophilic heads to the external aqueous environment and secluding the hydrophobic tails in the internal core.*

Each surfactant is characterized by its own critical micelle concentration which is the minimal concentration of surfactant molecules dispersed in water to initiate the micelles formation. As well as for the morphology of the micelles, the critical micelle concentration mostly depends on the molecular structure of the surfactant and on the aqueous environment physical characteristics such as pH, temperature, and salinity. In particular, sodium surfactin is an interesting surfactant thanks to the low value of critical micelle concentration 9.4 μM, this is positive since it means it's able to create micellar structures already at low concentrations.[137]Also, it's able to reduces the water surface tension from 72 $mN \cdot m^{-1}$ to 27 $mN \cdot m^{-1}$, in a concentration of 20 μM.[138] Moreover, sodium surfactin it has been attributed antifungal, antimicrobial, antiviral, antitumoral, and insecticidal.[139] Biocidal activity mechanisms of the molecule are characterized by a complex pattern, typically starting from the destabilization of the bilayer membrane stability and perturbing the cellular integrity.[140,141] Sodium surfactin acts rapidly on the membrane permeability, leading to the leakage of vesicle contents to the external medium, then it follows the contribution to several intracellular biological processes.[142] Regarding the antiviral properties of sodium surfactin, it is especially active against enveloped viruses, since it acts directly on the lipid envelope structures of the pathogen. The amphiphilic structure is a key factor that contributes to nonspecific detergent activity that disintegrate viruses. Sodium surfactin may represent an efficient tool for virus inactivation and prevention against virus infection.[143,144]
Sodium surfactin belongs to a subclass of surfactants, namely biosurfactants, these molecules can be synthesized by microorganisms as secondary metabolites with promising surfactant properties. Biosurfactants are secreted in the extracellular periphery or attached to the cell surface, their synthesis depends on environmental parameters such as pH, oxygen and nutrient availability. Such substances have attracted attention for a variety of applications in different industrial sectors due to their high structural diversity and beneficial properties, such as the

production under controlled conditions, a wide spectrum of physical and chemical properties, and additional benefits such as antimicrobial activity, presumably low toxicity and high biodegradability.[145] In particular, sodium surfactin is synthesized by the bacterial strain *Bacillus subtilis*, which activates surviving strategies such as antibiotic production, sporulation, and enzyme synthesis when found in nutrient deficiency. Among these enzymes, non-ribosomal peptide synthases are responsible for the synthesis of the peptide ring that through lipo-initiation process incorporates the lipid chain to obtain the amphiphilic structure of sodium surfactin.[146]
Biological systems such as bacteria, fungi, and algae or other products such as plant extracts have demonstrated their capabilities in the synthesis of nanoparticles.[147,148,149] The major complication related to the implementation of these solutions is due to the slower reaction rate, leading to very long reaction times between 24-120 h. This, combined to a more complex nanoparticles separation hinder biosynthesis in gaining ground as a viable solution in the industry.[150,151] Biosurfactants may be an interesting alternative to be used in the synthesis of metallic nanoparticles (MeNPs), silver nanoparticles (AgNPs) are especially targeted in the antimicrobial field. Biosurfactant molecules can act as capping and stabilizing agent for the newly formed MeNPs. The presence of biosurfactant on the surface of the particles avoid their excessive growth and potential aggregation and agglomerations processes that would lead to colloidal instability and sedimentation. Whether the interaction between the organic stabilizer and the metal particle is possible and to what degree depends on the nature of the biosurfactant (ionic, non-ionic, polymeric…) and the particle. These syntheses represent an easier alternative to other biological systems driven synthesis. In addition, biosurfactant capped silver nanoparticles have been reported in literature to show promising antimicrobial and cytotoxic properties, highlighting a synergistic effect that leads to a better antimicrobial activity respect to nanoparticles and biosurfactants alone.[152]

***Design of experiment*** – Sodium surfactin is used as capping agent in the green synthesis of silver nanoparticles pursuing a synergistic effect able to enhance the antimicrobial properties of the product. The synthesis is performed at room temperature in aqueous environment, in this way the energy consumption is minimized and the use of harmful organic solvents is avoided.
The most important parameters for this synthesis process were identified as the reagents molar ratios, respectively sodium surfactin and sodium hydroxide related to silver, Sur/Ag and NaOH/Ag. Thanks to a DoE these two variables were deeply explored, the resulting points in the bidimensional space confined by the axes Sur/Ag and NaOH/Ag are represented in the graph in Figure 35.

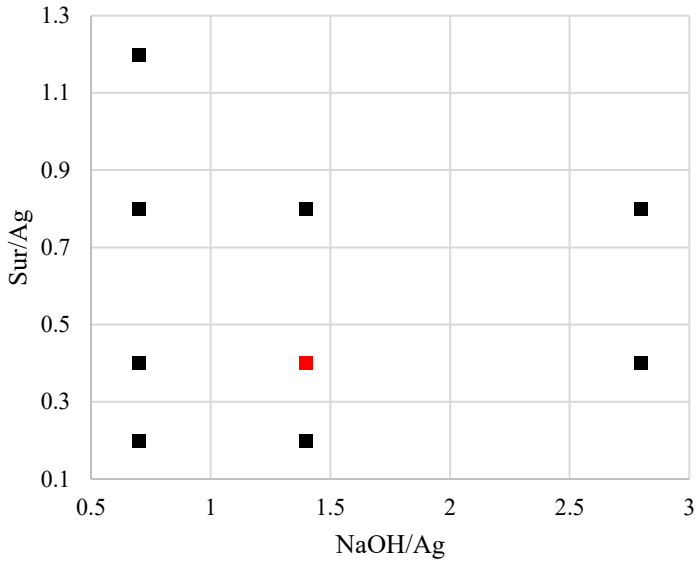


*Figure 35 – Design of experiment assessed to optimize the reagent molar ratios (Sur/Ag and NaOH/Ag) of the AgNPs synthesis performed using sodium surfactin as capping agent. In red is reported the most promising composition (AgSur_05), in black the composition of the other samples.*

A total of 15 synthesis conditions were tested, excluding 6 synthesis where less or non-relevant parameters were tested 9 points are reported in Figure 35, it is reported in red the most promising composition labeled AgSur_05. The composition of the cited synthesis is reported in the following Table 19:

*Table 19 – Sodium surfactin-capped silver nanoparticles composition and reagent molar ratios.*

| Sample | Sur/Ag molar ratio | NaOH/Ag molar ratio |
|---|---|---|
| AgSur_03 | 0.2 | 0.7 |
| AgSur_04 | 0.4 | 0.7 |
| AgSur_05 | 0.4 | 1.4 |
| AgSur_06 | 0.2 | 1.4 |
| AgSur_07 | 0.8 | 1.4 |
| AgSur_08 | 0.8 | 0.7 |
| AgSur_09 | 0.4 | 2.8 |
| AgSur_10 | 0.8 | 2.8 |
| AgSur_15 | 1.2 | 0.7 |

Other non-reported synthesis implied the addition of a secondary capping agent like polyvinylpyrrolidone (PVP), working at 70 °C whit microwave heating, or using a different silver concentration. These parameters showed no benefits for the synthetic process.

***UV-Vis spectroscopy*** – Sodium surfactin capped silver nanoparticles exhibits a different UV-Vis absorption spectrum respect to the classic AgNPs, the sample's spectra are represented in Figure 36. The surface plasmon resonance peak is not centered at 400-420 nm, but it is observed a blu-shift towards UV region, with a maximum at about 320-330 nm. This may be caused by the synthesis of very small nanoparticles or by the presence of other species different than the only $Ag^0$.

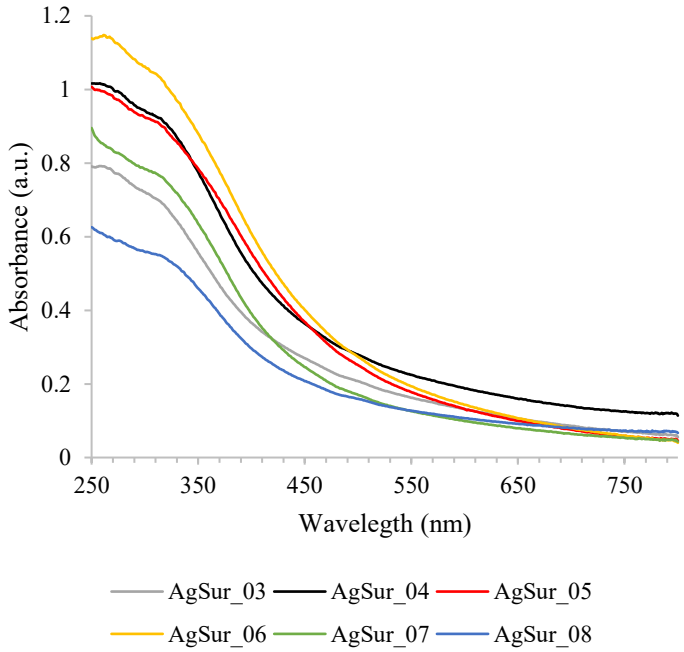


*Figure 36 – UV-Vis absorption spectra comparison of the synthesized AgSur samples: AgSur_03, AgSur_04, AgSur_05, AgSur_06, AgSur_06, AgSur_07, and AgSur_08. All the AgSur compositions did not present the typical SPR absorption peak of AgNPs centered at 400-420 nm. A blue-shift phenomenon occurred shifting the peak towards 320-330 nm.*

The UV-Vis absorption of sodium surfactin is reported in the graph in Figure 37, where the surfactant has been analyzed in different conditions, as powder, water suspension, and as blank replicating the conditions of the syntheses. The trend is similar for all the conditions testes, no absorption is observed in the visible and near UV range, but an important absorption is registered at wavelength < 250 nm. Maximum absorption peaks at 210-220 nm correspond with surfactin typical peptide bond absorption.[153] Furthermore, some emission phenomena happen in the range

270-320 nm for the powder sample. Theoretically there should not be interferences generated from sodium surfactin in the AgSur samples UV-Vis absorption spectra.

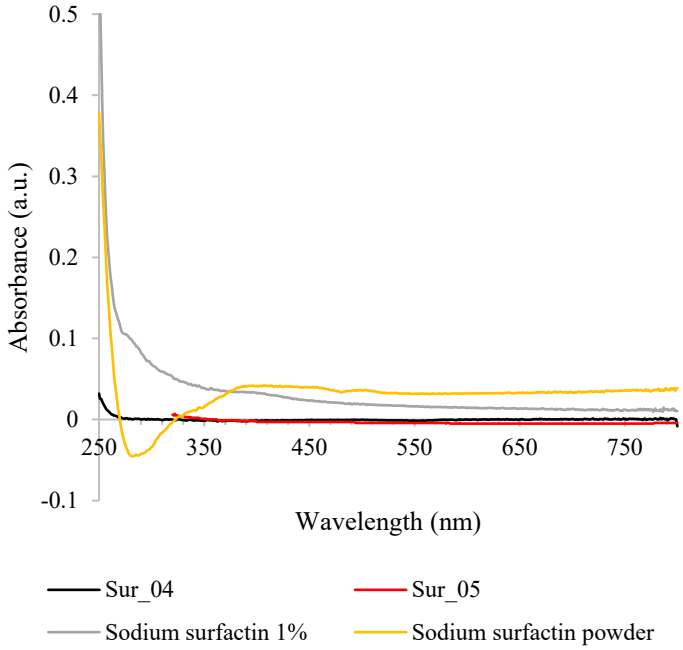


*Figure 37 – Sodium surfactin blanks Sur_04 and Sur_05, sodium surfactin 1% solution, and sodium surfactin powder UV-Vis absorption spectra comparison. Relevant absorption at wavelength < 250 nm.*

*Table 20 – Total silver concentration and $Ag^+$ conversion of sodium surfactin-capped AgNPs, determined by ICP-OES.*

| Sample | Total Ag concentration ($mg \cdot L^{-1}$) | $Ag^+$ conversion (%) |
|---|---|---|
| AgSur_03 | 5269 ± 28 | 98.60 ± 0.02 |
| AgSur_04 | 5232 ± 42 | 99.04 ± 0.02 |
| AgSur_05 | 5317 ± 37 | 99.98 ± 0.01 |
| AgSur_06 | 5268 ± 27 | 99.98 ± 0.01 |
| AgSur_07 | 5397 ± 29 | 99.98 ± 0.01 |
| AgSur_08 | 5276 ± 26 | 99.24 ± 0.02 |
| AgSur_09 | 3131 ± 16 | 99.98 ± 0.01 |
| AgSur_10 | 5698 ± 33 | 99.92 ± 0.01 |
| AgSur_15 | 4528 ± 41 | 99.93 ± 0.03 |

***Silver quantification by ICP-OES*** – The quantification of the total silver and the conversion of the silver cation performed by ICP-OES reports silver concentration aligned with the theoretical

value of 5000 mg·L$^{-1}$ and always a quantitative (6 samples with conversion > 99.9 %) or nearly quantitative (3 samples with conversion > 98.5 %). Results are explicated in Table 20.

***Transmission electron microscopy*** – TEM investigations were focused on the most promising samples, namely AgSur_04 and AgSur_05, these first discrimination was based on the stability of the samples. AgSur_04 and AgSur_05 were selected because they showed no precipitation after a week stored at 4 °C in dark conditions. They share the same Sur/Ag molar ratio, 0.4 which is an intermediate value of the DoE, lower ratios lead to unstable suspension and for higher load, sodium surfactin gives aggregation and poorer results in the synthesis. AgSur_04 and AgSur_05 differ for the NaOH/Ag molar ratio, they have the two lowest amounts of NaOH, ratio 0.7 AgSur_04 and 1.4 AgSur_05. AgSur_04 HAADF-STEM images, reported in Figure 38, reveal crystalline AgNPs with very small particle size, ranging from 1 to 4 nm. They are well dispersed on the support carbon film. These images were used for statistical size analysis measuring the major and minor axis of each particle. SAED diffraction pattern and the relative rotational average show that all rings can be indexed as silver lattice planes. The sharp spots are produced by the larger particle or agglomerates, while the diffuse rings are due to the NPs having size ranging from 1-2 nm.

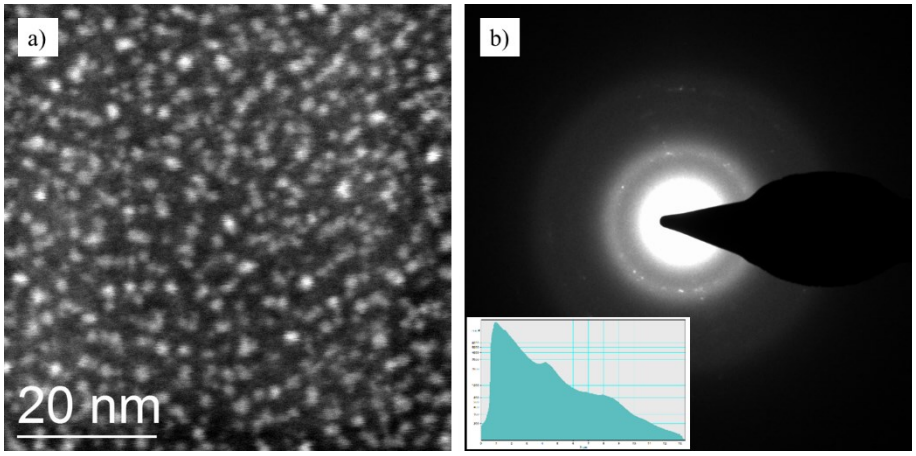


*Figure 38 – a) HAADF-STEM image of AgSur_04 used for the particles size statistical analysis showing particles size ranging from 1-4 nm. b) SAED image of AgCur showing the diffraction pattern of crystalline metallic silver lattice planes.*

Together with small NPs, HAADF-STEM images represented in Figure 39, report larger agglomerates with sizes in the range from 20 to 150 nm. These images were used for statistical size analysis measuring the long and short axis of each agglomerate.

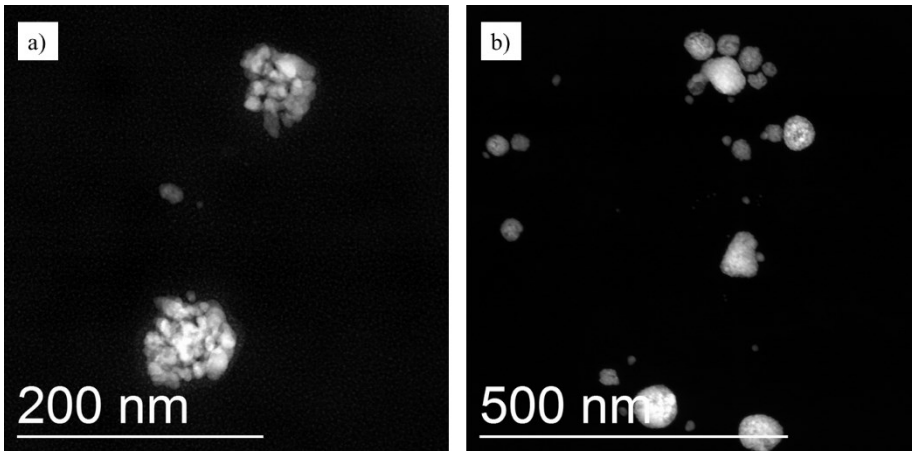


*Figure 39 – a) and b) HAADF-STEM images of AgSur_04 agglomerates used for the size statistical analysis showing aggregates size ranging from 20-150 nm.*

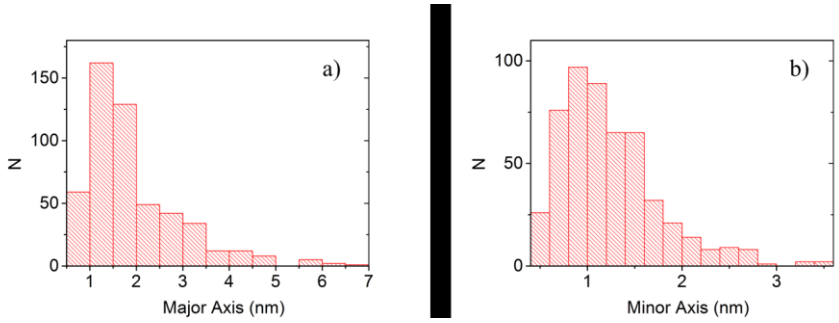


*Figure 40 – Size distribution statistical analysis of the dimensions of the sample AgSur_04: a) major axis population distribution 1.9 ± 0.2 nm; b) minor axis population distribution 1.2 ± 0.2 nm. The diameter measurements are reported with a confidence interval of 99%.*

The size of 515 small NPs in different images was measured, the statistical distribution is reported in Figure 40, the long axis estimated mean value is 1.9 ± 0.2 nm and short axis 1.2 ± 0.2 nm with a confidence interval of 99 %. The size of 74 agglomerates in different images was measured and the long axis estimated mean value is 45 ± 10 nm and short axis 34 ± 8 nm with a confidence interval of 99 %.

Similar morphology was observed for AgSur_05 whose HAADF-STEM images, reported in Figure 41, show small and crystalline AgNPs with size ranging from 0.5 to 3 nm. They are well dispersed on the support carbon film. These images were used for statistical size analysis measuring the major and minor axis of each particle. SAED diffraction pattern and the relative rotational average in Figure 41 reveal that all rings can be indexed as silver lattice planes. The sharp spots are produced by the larger particle or agglomerates, while the diffuse rings are due to the NPs having size ranging from 1-2 nm.

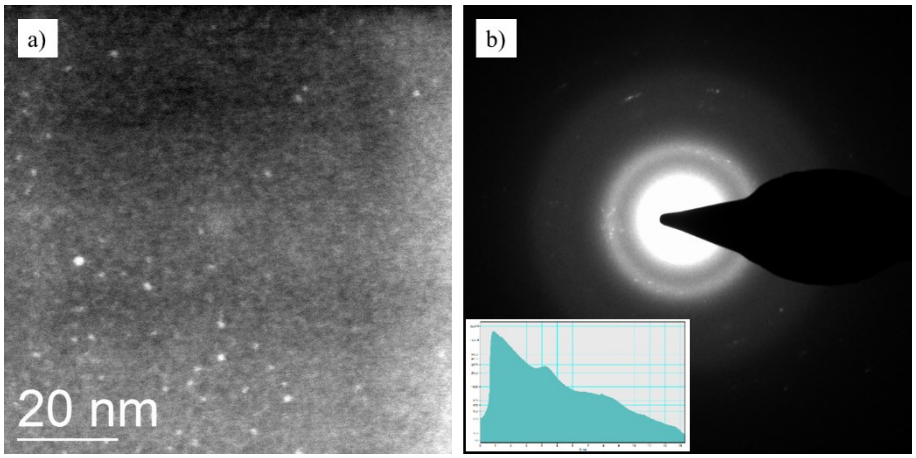


*Figure 41 – a) HAADF-STEM image of AgSur_05 used for the particles size statistical analysis showing particles size ranging from 0.5-3 nm. b) SAED image of AgCur showing the diffraction pattern of crystalline metallic silver lattice planes.*

AgSur_05 HAADF-STEM images in Figure 42 represent the larger agglomerates with size ranging from 20 to 150 nm. These images were used for statistical size analysis measuring the long and short axis of each particle.

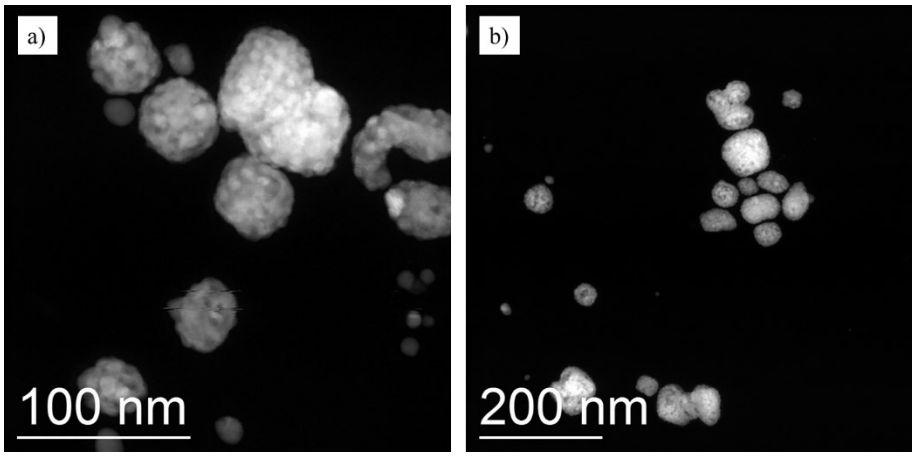


*Figure 42 – a) and b) HAADF-STEM images of AgSur_05 agglomerates used for the size statistical analysis showing aggregates size ranging from 20-150 nm.*

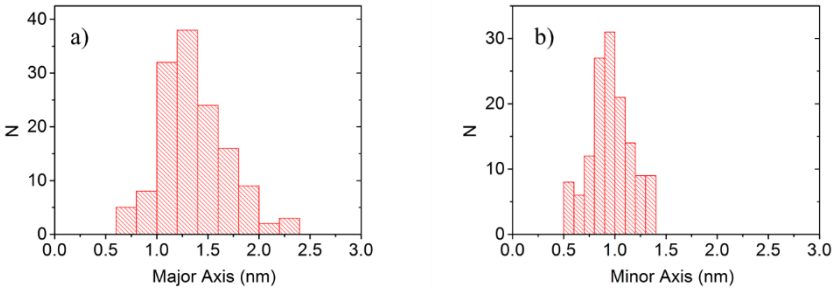


*Figure 43 – Size distribution statistical analysis of the dimensions of the sample AgSur_05: a) major axis population distribution 1.4 ± 0.2 nm; b) minor axis population distribution 1.0 ± 0.2 nm. The diameter measurements are reported with a confidence interval of 99%.*

The size of 137 small NPs in different images were measured and the long axis estimated mean value 1.4 ± 0.2 nm, and the short axis 1.0 ± 0.2 nm, with a confidence interval of 99% (Figure 43).

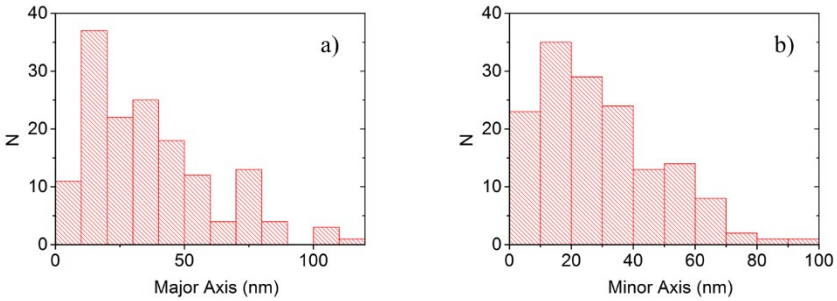


*Figure 44 – Size distribution statistical analysis of the aggregates observed for the sample AgSur_05: a) major axis population distribution 37 ± 6 nm; b) minor axis population distribution 29 ± 5 nm. The diameter measurements are reported with a confidence interval of 99%.*

The size of 150 agglomerates in different images were measured resulting in a long axis estimated mean value of 37 ± 6 nm and a short axis 29 ± 5 nm with a 99% confidence interval (Figure 44).

***X-ray diffraction spectroscopy*** – XRD spectra revealed a more complicated situation respect the desired metallic AgNPs composition. As it is possible to see in Figure 45, AgSur_04 and AgSur_05 exhibit several other peaks beside the FCC silver pattern. The predominant undesired byproducts obtained were identified mostly as carbonate phases: silver carbonate and silver sodium carbonate. Sodium nitrate was also present as a reaction coproduct generated by sodium from sodium hydroxide and the nitrate counterion of the silver nitrate precursor. Sodium

surfactin powder was analyzed and the characteristic amorphous wide band centered about 20 ° was detected. These results reveal that even if the conversion of the silver precursor is quantitative, the yield in silver nanoparticles is compromised by byproducts formation for these syntheses.

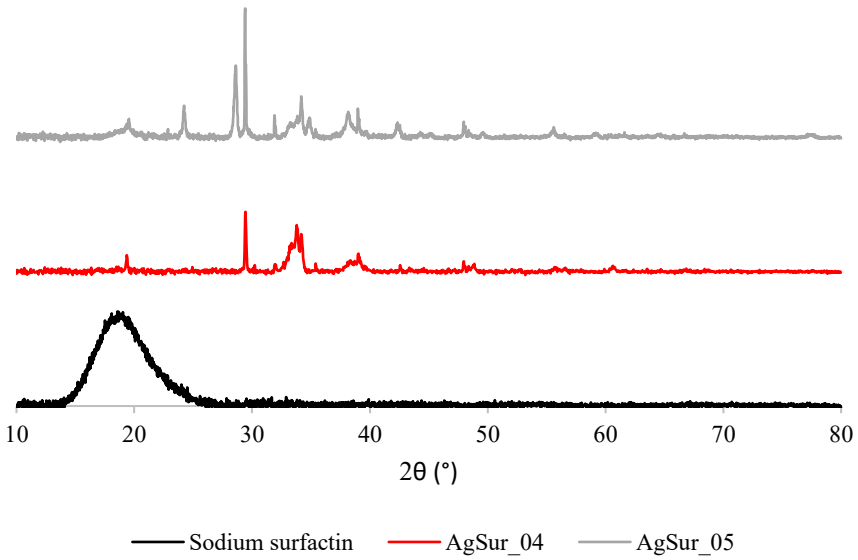


*Figure 45 – XRD spectra comparison of sodium surfactin powder, AgSur_04, and AgSur_05. Sodium surfactin shows the amorphous diffraction band, while the AgNPs-containing samples show the typical face-centered cubic pattern of metallic silver coupled with silver carbonate phases.*

***Hydrodynamic diameter*** – The DLS technique revealed an average hydrodynamic diameter mostly comprised in the range 120-150 nm, with a PDI suggesting relatively monodisperse populations, as reported in Table 21. There are not particular trends to highlight, with the exception of the samples AgSur_09 and AgSur_10 where the higher amount of NaOH (molar ratio NaOH/Ag 2.8) used leads to larger hydrodynamic diameters, higher PDI, and the precipitation of the unstable product. It may be due to an excessive growth of the AgNPs or to coagulation phenomenon. On the other side, also AgSur_15 exhibit a hydrodynamic diameter larger than the rest of the samples, and the peculiarity of this synthesis is the highest load of sodium surfactin (Sur/Ag molar ratio 1.2), probably leading to a larger organic shell surrounding the NPs. The blanks of the two most promising samples, Sur_04 and Sur_05, show large particles probably generated by micellar and supra-micellar structures of sodium surfactin in basic environment, with a larger sized population for AgSur_05.

*Table 21 – Average hydrodynamic diameter and polydispersity index of sodium surfactin-capped AgNPs and their blanks.*

| Sample | Average hydrodynamic diameter (nm) | PDI |
|---|---|---|
| AgSur_03 | 140.3 ± 0.7 | 0.173 ± 0.009 |
| AgSur_04 | 140 ± 4 | 0.238 ± 0.023 |
| AgSur_05 | 145.9 ± 0.8 | 0.150 ± 0.006 |
| AgSur_06 | 131.7 ± 0.6 | 0.118 ± 0.012 |
| AgSur_07 | 121.8 ± 0.7 | 0.130 ± 0.008 |
| AgSur_08 | 152.0 ± 0.7 | 0.133 ± 0.02 |
| AgSur_09 | 840 ± 100 | 0.688 ± 0.128 |
| AgSur_10 | 810 ± 25 | 0.526 ± 0.068 |
| AgSur_15 | 207 ± 4 | 0.251 ± 0.019 |
| Sur_04 | 1156 ± 285 | 0.734 ± 0.065 |
| Sur_05 | 4031 ± 2222 | 0.338 ± 0.042 |

The population distribution in terms of hydrodynamic diameter, represented in Figure 46, confirms what discussed, most of the samples have a nearly superimposable monodisperse and monomodal distribution eventually with some larger aggregates. AgSur_15 shows a slightly larger population, while AgSur_09 and AgSur_10 have a completely different behavior in terms of both average size and distribution.

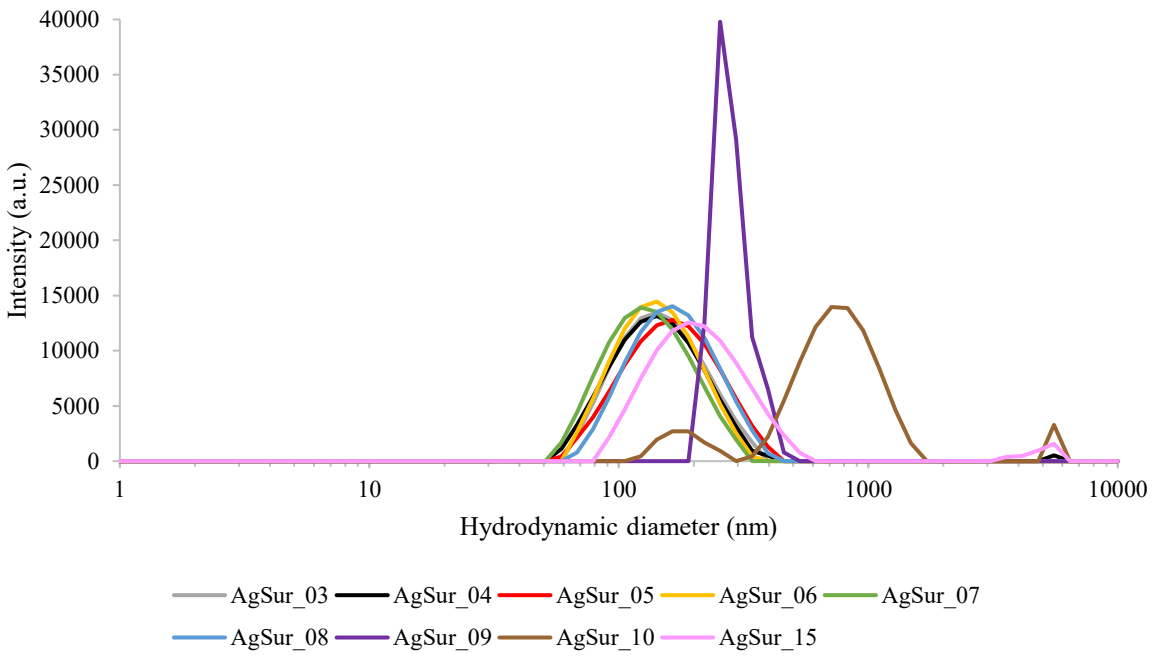


*Figure 46 – Hydrodynamic diameter population distribution determined by DLS analysis of the samples: AgSur_03, AgSur_04, AgSur_05, AgSur_06, AgSur_07, AgSur_08, AgSur_09, AgSur_10, and AgSur_15.*

***Zeta potential*** – Sodium surfactin as capping agent is able to confer strong negative charge to the nanoparticles, the zeta potential measurements reported in Table 22, highlight extremely stable suspension thanks to zeta potential values in the range from -40 to -48 mV. This demonstrate how the sodium surfactin can stabilize the colloidal suspensions thanks to the electrostatic repulsion.

Another information gathered from the titration of the zeta potential as a function of the pH, is related to the sodium surfactin coverage of the nanoparticles. In fact, along all the pH intervals studied in Figure 47, the two selected samples, AgSur_04 and AgSur_08 have similar behavior to the sodium surfactin alone. Confirming the creation of a surface layer on the Ag core fulfilling capping and stabilizing agent requirements and purposes. The isoelectric point resulted to be ≈ 2.9 for AgSur_04, and ≈ 1.8 for AgSur_08 and the sodium surfactin dispersed in Milli-Q water.

*Table 22 – Zeta potential and pH of sodium surfactin-capped AgNPs, their blanks, and sodium surfactin solution.*

| Sample | Zeta potential | pH |
|---|---|---|
| AgSur_03 | -40 ± 1 | 9.38 |
| AgSur_04 | -47 ± 3 | 8.86 |
| AgSur_05 | -46.9 ± 0.3 | 9.60 |
| AgSur_06 | -44.0 ± 0.4 | 9.97 |
| AgSur_07 | -46 ± 1 | 9.77 |
| AgSur_08 | -48 ± 1 | 8.84 |
| AgSur_09 | -47 ± 2 | 9.75 |
| AgSur_10 | -45.8 ± 0.7 | 10.33 |
| AgSur_15 | -48.3 ± 0.9 | 8.52 |
| Sur_04 | -15 ± 4 | 10.32 |
| Sur_05 | -35 ± 2 | 10.94 |
| Sodium surfactin | -38 ± 6 | 5.90 |

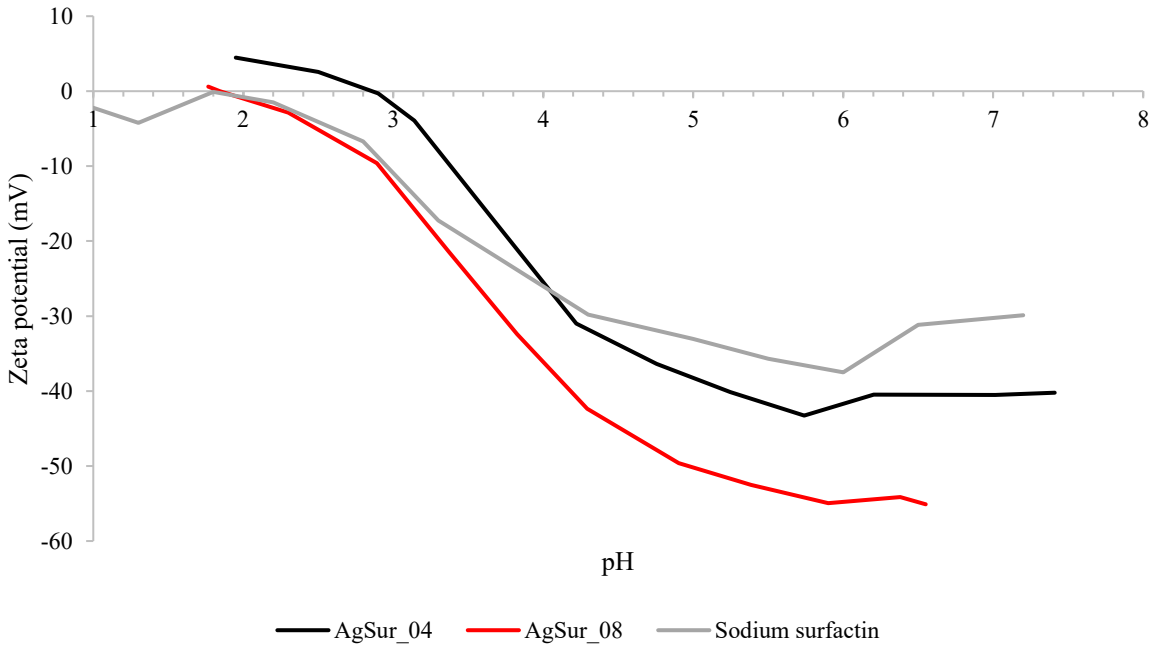


*Figure 47 – Zeta potential titrations as function of the pH of the samples AgSur_04, AgSur_08, and sodium surfactin.*

### 3.2.4. Antimicrobial activity of the designer silver nanoparticles

The antimicrobial tests were carried out by external laboratories either as project partners or subcontractors, in particular, antibacterial tests were performed by certified laboratories of CNR-STIIMA (Biella, Italy) and Chimicambiente (Vicenza, Italy), while antiviral tests were assessed by Università degli Studi di Milano La Statale (Milano, Italy).

The several design variants of the three differently coated types of AgNPs were studied in term of antibacterial activity against *Escherichia coli* Gram-negative and *Staphylococcus aureus* Gram-positive bacteria, and in terms of antiviral activity against SARS-CoV-2 representing enveloped viruses and BK-polyomavirus representing non-enveloped ones. In this way it was possible to perform a detailed screening of the performance of the various samples produced, ranking the most promising materials for future field applications.

***Antibacterial activity*** – Antibacterial tests were carried out in compliance with UNI EN 1040:2005 standardized method "Quantitative suspension test for the evaluation of basic bactericidal activity of chemical disinfectants and antiseptics" against *Escherichia coli* (ATCC 10536) and *Staphylococcus aureus* (ATCC 6538). For AgHEC and AgCur variants, the AgNPs concentration range 10-0.1 $mg \cdot L^{-1}$ was studied, then the most promising samples were tested at higher concentration, 50 $mg \cdot L^{-1}$. In Table 23 are reported AgHEC results and in Table 24 the ones related to AgCur samples.

*Table 23 – Antibacterial activity results against E. coli and S. aureus of AgHEC samples and their blanks. The results are expressed as logarithmic bacterial reduction as function of the silver concentration ($mg \cdot L^{-1}$).*

| Sample | *Escherichia coli* | | | | *Staphylococcus aureus* | | | |
|---|---|---|---|---|---|---|---|---|
| | 10 $mg \cdot L^{-1}$ | 1 $mg \cdot L^{-1}$ | 0.5 $mg \cdot L^{-1}$ | 0.1 $mg \cdot L^{-1}$ | 10 $mg \cdot L^{-1}$ | 1 $mg \cdot L^{-1}$ | 0.5 $mg \cdot L^{-1}$ | 0.1 $mg \cdot L^{-1}$ |
| AgHEC_5.5_2.8 | 1.19 | < 0.3 | < 0.3 | < 0.3 | 0.62 | < 0.3 | < 0.3 | < 0.3 |
| AgHEC_6.4_1.4 | 2.23 | 0.68 | 0.48 | < 0.3 | 4.86 | 3.56 | 1.51 | < 0.3 |
| AgHEC_6.4_3.7 | 1.35 | 0.56 | < 0.3 | < 0.3 | 0.60 | < 0.3 | < 0.3 | < 0.3 |
| AgHEC_2.8_1.4 | 1.15 | < 0.3 | < 0.3 | < 0.3 | 1.65 | < 0.3 | < 0.3 | < 0.3 |
| AgHEC_2.8_2.8 | 1.82 | 0.47 | < 0.3 | < 0.3 | 0.43 | < 0.3 | < 0.3 | < 0.3 |
| AgHEC_2.8_3.7 | 1.85 | 0.51 | < 0.3 | < 0.3 | 1.48 | < 0.3 | < 0.3 | < 0.3 |
| HEC_5.5_2.8 | 1.43 | 0.90 | 0.70 | < 0.3 | < 0.3 | < 0.3 | < 0.3 | < 0.3 |
| HEC_6.4_1.4 | 1.55 | 0.98 | 0.69 | < 0.3 | < 0.3 | < 0.3 | < 0.3 | < 0.3 |
| HEC_6.4_3.7 | 1.39 | 0.85 | 0.60 | < 0.3 | < 0.3 | < 0.3 | < 0.3 | < 0.3 |
| HEC_2.8_1.4 | 1.39 | < 0.3 | < 0.3 | < 0.3 | < 0.3 | < 0.3 | < 0.3 | < 0.3 |
| HEC_2.8_2.8 | 1.65 | 0.61 | < 0.3 | < 0.3 | < 0.3 | < 0.3 | < 0.3 | < 0.3 |
| HEC_2.8_3.7 | 1.75 | 1.11 | 0.80 | < 0.3 | 1.08 | 0.41 | < 0.3 | < 0.3 |

*Table 24 – Antibacterial activity results against E. coli and S. aureus of AgCur samples and their blanks. The results are expressed as logarithmic bacterial reduction as function of the silver concentration ($mg \cdot L^{-1}$).*

| Sample | *Escherichia coli* | | | | *Staphylococcus aureus* | | | |
|---|---|---|---|---|---|---|---|---|
| | 10 $mg \cdot L^{-1}$ | 1 $mg \cdot L^{-1}$ | 0.5 $mg \cdot L^{-1}$ | 0.1 $mg \cdot L^{-1}$ | 10 $mg \cdot L^{-1}$ | 1 $mg \cdot L^{-1}$ | 0.5 $mg \cdot L^{-1}$ | 0.1 $mg \cdot L^{-1}$ |
| AgCur | 2.38 | 0.59 | < 0.3 | < 0.3 | 4.56 | < 0.3 | < 0.3 | < 0.3 |
| AgCur_Cas | 3.11 | 0.59 | < 0.3 | < 0.3 | 4.48 | 0.65 | < 0.3 | < 0.3 |
| Cur | 0.36 | < 0.3 | < 0.3 | < 0.3 | 0.38 | < 0.3 | < 0.3 | < 0.3 |
| Cur_Cas | < 0.3 | < 0.3 | < 0.3 | < 0.3 | 0.36 | < 0.3 | < 0.3 | < 0.3 |

The tests carried out against *E. coli* and *S. aureus* identified AgHEC_6.4_1.4, AgCur, and AgCur_Cas as the most active antibacterial AgNPs compositions. In fact, at Ag concentration of 10 mg·L$^{-1}$, they exhibited respectively a logarithmic reduction of 2.23, 2.38, and 3.11 against *E. coli*, and 4.86, 4.56, and 4.48 against *S. aureus* (logarithmic reduction: 1 log = 90%, 2 log = 99%, 3 log = 99.9%...). To better evaluate these samples, they were tested at higher concentration, 50 mg·L$^{-1}$, results are reported in Table 25. It is noteworthy, that *S. aureus* resulted more susceptible to the selected AgNPs, but on the other side, hydroxyethyl cellulose based blanks exhibit a relevant activity against *E. coli*. One of the main differences between Gram-negative bacteria like *E. coli* and Gram-positive bacteria like *S. aureus* stems from the thickness of the peptidoglycan layer in the cell wall. Gram-negative bacteria have a thinner layer included between an inner and an outer cell membrane, resulting in a higher susceptibility of *E. coli* with respect to the positively charged quaternary ammonium functionalities of hydroxyethyl cellulose biopolymer. On the other side, Gram-positive bacteria have a thicker peptidoglycan layer, but typically they result more receptive to agents targeting the cell wall, like antibiotics, and in this case for *S. aureus* could be AgNPs and $Ag^+$ ions, and this is due to the missing outer membrane.[154]

*Table 25 – Antibacterial activity results at higher silver concentration (50 mg·L$^{-1}$) of AgHEC_6.4_1.4, AgCur, and AgCur_Cas against E. coli and S. aureus. The results are expressed as logarithmic bacterial reduction.*

| **Sample** | ***Escherichia coli*** | ***Staphylococcus aureus*** |
|---|---|---|
| | 50 mg·L$^{-1}$ | 50 mg·L$^{-1}$ |
| AgHEC_6.4_1.4 | > 5.45 | 4.64 |
| AgCur | 4.66 | 4.44 |
| AgCur_Cas | 5.02 | 4.80 |

Results related to higher concentrated tests reported in Table 25 highlight an excellent antibacterial activity of the selected variants. Comparable logarithmic reduction values were obtained against *S. aureus*, while against *E. coli* AgHEC_6.4_1.4 stands as the most active composition. In these conditions, at a concentration of 50 mg·L$^{-1}$, it reached the higher detectable value for the test with a logarithmic reduction greater than 5.45.

The antibacterial results collected were transposed to graphs in Figure 48 representing the activity against *E. coli* of AgHEC_5.5_2.8, AgHEC_6.4_1.4, AgCur, and AgCur_Cas, and in Figure 49 the same samples against *S. aureus*. The initial AgHEC_5.5_2.8 composition is less active respect to the subsequently developed variants that exhibit similar concentration-

dependent behaviors. In particular, AgHEC_6.4_1.4 resulted to be strongly active against Gram-positive bacteria, here represented by *S. aureus*, even at low concentrations, 0.5 and 1 mg·L$^{-1}$.

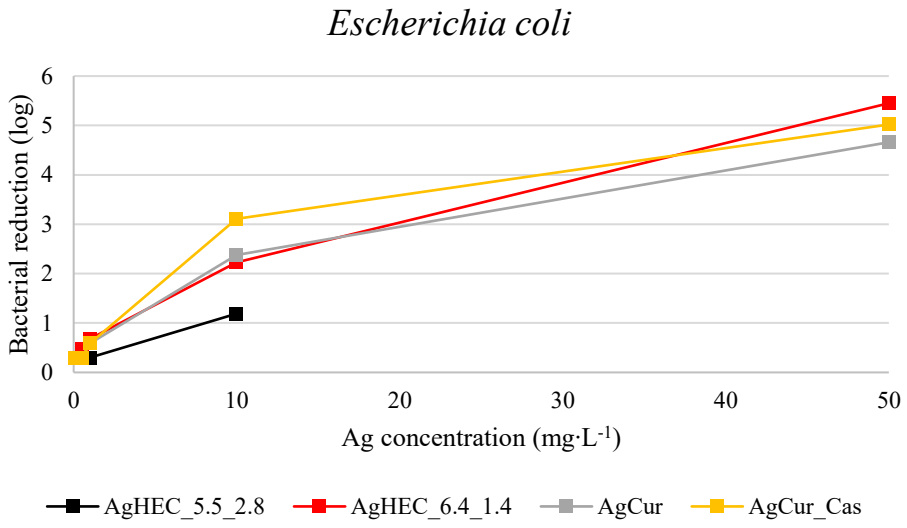


*Figure 48 – Antibacterial activity of AgHEC_5.5_2.8, AgHEC_6.4_1.4, AgCur, and AgCur_Cas against E. coli. The results are expressed as logarithmic bacterial reduction as function of the silver concentration (mg·L$^{-1}$).*

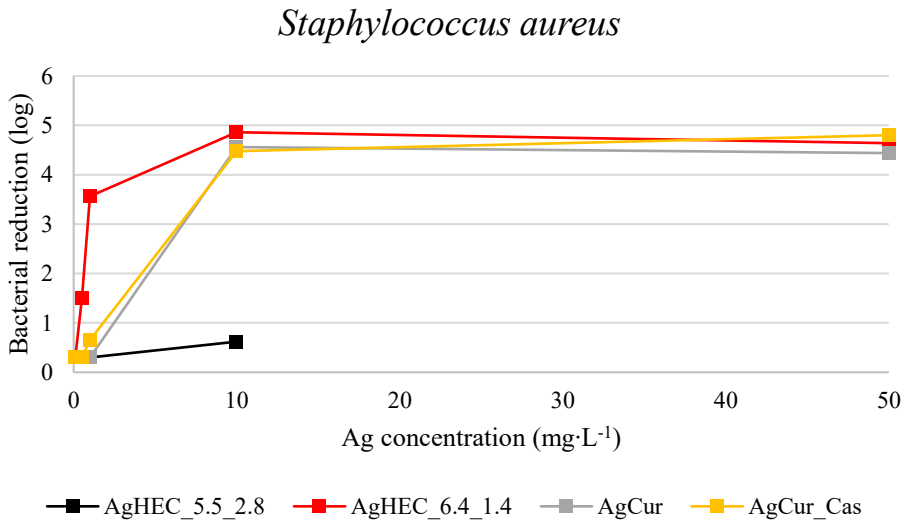


*Figure 49 – Antibacterial activity of AgHEC_5.5_2.8, AgHEC_6.4_1.4, AgCur, and AgCur_Cas against S. aureus. The results are expressed as logarithmic bacterial reduction as function of the silver concentration (mg·L$^{-1}$).*

The last variant analyzed is AgSur_04, these sodium surfactin capped silver nanoparticles revealed very small TEM size, with estimated long axis mean value of 1.9 ± 0.2 nm and short axis 1.2 ± 0.2 nm. This particle size is very promising for the antimicrobial applications. Antibacterial results, reported in Table 26, show a concertation dependent behavior against *S.*

*aureus* with excellent bacterial reduction of 3.15 log already at 10 mg·L$^{-1}$, and an activity above the detection limit against *E. coli* for all the concentration range explored, 100-10 mg·L$^{-1}$. These AgNPs are an interesting option for the antimicrobial application, thanks to *S. aureus* reduction comparable with the other selected variants, and an exceptional activity against *E. coli*. In this case, the blank constituted by the sodium surfactin basic solution is not particularly active against *S. aureus*.

*Table 26 – Antibacterial activity of AgSur_04 and its blank against E. coli and S. aureus. The results are expressed as logarithmic bacterial reduction as function of the silver concentration (mg·L$^{-1}$).*

| **Sample** | ***Escherichia coli*** | | | ***Staphylococcus aureus*** | | |
|---|---|---|---|---|---|---|
| | 100 mg·L$^{-1}$ | 50 mg·L$^{-1}$ | 10 mg·L$^{-1}$ | 100 mg·L$^{-1}$ | 50 mg·L$^{-1}$ | 10 mg·L$^{-1}$ |
| AgSur_04 | > 5.53 | > 5.53 | > 5.53 | > 5.49 | 4.01 | 3.15 |
| Sur_04 | n.d. | n.d. | n.d. | 0.39 | 0.10 | 0.02 |

***Antiviral activity*** – The antiviral testing activity has been performed by the Università degli Studi di Milano La Statale (UNIMI). The results here reported were collected within the @CNR research project SanoSIL.

***Cytotoxicity assay of AgCur on Vero E6 cells*** – Cell cytotoxicity was evaluated by monitoring the effect of AgNPs and their blanks on Vero E6 cells. Cell viability was measured by MTT assay. The percentage of viable cells was calculated using untreated cells as control (100% viability) using the formula reported in Equation 2.[155]

$$\frac{(\text{Sample absorbance} - \text{Cell free sample blank})}{\text{Mean media control absorbance}} \cdot 100 \qquad \text{Equation 2}$$

The 50% cytotoxic concentration ($CC_{50}$) causing 50% reduction of Vero E6 cells viability with respect to untreated control cells are reported in Table 27. From these *in-vitro* assay AgCur resulted to have minimal cytotoxic effects with an outstanding 50 % cytotoxic concentration of 629.7 $mg \cdot L^{-1}$, if compared with other drugs used for the treatment of malaria and investigated in the application against SARS-CoV-2, such as chloroquine which has a $CC_{50}$ of 30.5 $mg \cdot L^{-1}$, this is a very promising result for human applications.[156,157]

*Table 27 – 50% cytotoxic concentration ($CC_{50}$) of AgCur and its blank.*

| | **Sample** | **$CC_{50}$ ($mg \cdot L^{-1}$)** |
|---|---|---|
| AgCur-based nanoforms | AgCur | 629.7 |
| | Cur blank | > 2500 |

***Evaluation of the antiviral activity against SARS-CoV-2 Omicron BA.2 variant of AgCur by RT-qPCR*** – Vero E6 cells were infected with SARS-CoV-2 Omicron BA.2 variant, SARS-CoV-2 was selected to represent the class of enveloped viruses, and also because of his relevance in the latest years. The quantification of SARS-CoV-2 copy numbers in cell supernatant was evaluated via specific real time quantitative polymerase chain reaction (RT-qPCR) of the N1 gene. The $IC_{50}$ value was extrapolated as the concentration inducing a 50% inhibition of viral replication. The antiviral activity was evaluated for AgNPs and their blanks. AgCur showed the ability to suppress SARS-CoV-2 replication, with a dose-dependent activity, as reported in Figure 50, AgCur $IC_{50}$ was 8.3 $mg \cdot L^{-1}$. A nearly quantitative viral replication inhibition (0.09%) was registered for an AgCur concentration of 50 $mg \cdot L^{-1}$.

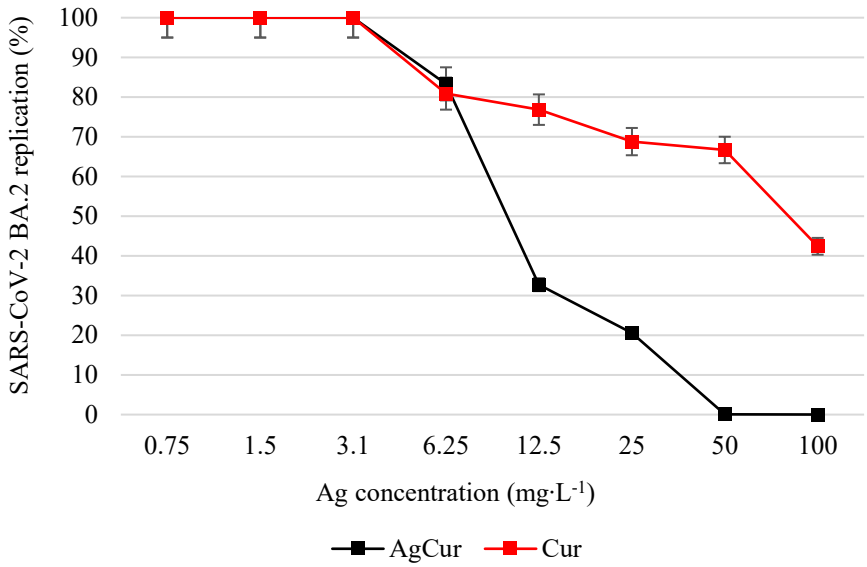


*Figure 50 – Antiviral activity of AgCur and its blank Cur against SARS-CoV-2 BA.2 variant. The results are expressed as percentage of the viral replication as function of the silver concentration (mg·L$^{-1}$).*

The selectivity index (SI) calculated as the ratio between $CC_{50}$ and $IC_{50}$ represents an important non-dimensional parameter to evaluated the safe and effective dose range for bioactive compounds. A higher SI value indicates a larger concentration window for safe *in-vivo* viral infections treatments. During drugs screening a SI value of 10 is a requirement for further development of the product.[158] AgCur demonstrated outstanding SI with a value of 75.9. In Figure 51 are superimposed the cytotoxicity and antiviral results of AgCur. Chloroquine, tested as positive control against SARS-CoV-2 had a SI of 8.5. While the curcumin alone, without AgNPs demonstrated very low cytotoxicity ($CC_{50}$ > 2500 mg·L$^{-1}$) but also a reduced antiviral activity ($IC_{50}$ 50-100 mg·L$^{-1}$) resulting in a SI > 25.

Curcumin is the primary polyphenolic compound found in turmeric and it has garnered considerable interest due to its various and biological properties, including antioxidant, antimicrobial, and anti-inflammatory effects.[159] In particular, the antioxidant and anti-inflammatory characteristics of curcumin could potentially reduce the cytotoxicity of curcumin-capped AgNPs. While its intrinsic antiviral activity could establish synergistic effects enhancing the antiviral action of silver nanophases.

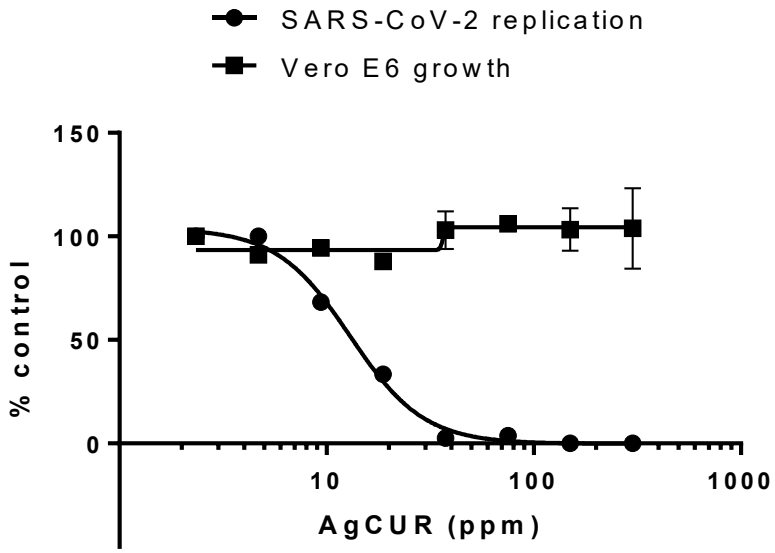


*Figure 51 – Cytotoxicity on Vero E6 cells and viral activity against SARS-CoV-2 BA.2 variant of AgCur. The results are expressed as % of Vero E6 cells growth and SARS-CoV-2 BA.2 replication as function of the silver concentration (mg·L$^{-1}$). The graph represents the mean of 3 different experiments in triplicate. The viral load data were normalized versus untreated infected controls. The curves fitting was obtained by non-linear regression analysis using a four-parameter logistic method (software GraphPadPrism 6). The $CC_{50}$ causing 50% reduction of Vero E6 cells viability with respect to untreated control cells was determined using Gene5 software, while the $IC_{50}$ value was extrapolated as the concentration that induced 50% inhibition of viral replication.*

***Evaluation of virucide activity against SARS-CoV-2 Omicron BA.2 variant of AgCur by plaque assay*** – The virucide activity against SARS-CoV-2 Omicron BA.2 variant was determined by plaque assay to confirm AgCur antiviral properties, Table 28. A quantitative viral suppression was obtained at a silver concentration of 75 mg·L$^{-1}$. For the second AgCur batch tested it was obtained a 50 mg·L$^{-1}$.

*Table 28 – Virucide activity against SARS-CoV-2 Omicron BA.2 of AgCur and its blank, determined by plaque assay.*

| **Sample** | **Mean PFU·mL$^{-1}$ (% of SARS-CoV-2 infectivity compared to untreated infected cells)** | | | | |
|---|---|---|---|---|---|
| | *Untreated infected cells* | *6.5 mg·L$^{-1}$* | *25 mg·L$^{-1}$* | *50 mg·L$^{-1}$* | *100 mg·L$^{-1}$* |
| AgCur | 67.25 (100.00%) | 52.25 (78.07%) | 18.25 (27.14%) | 2.00 (2.97%) | 0.00 (0.00%) |
| Cur | 67.25 (100.00%) | 52.50 (78.06%) | 51.00 (75.83%) | 50.25 (74.72%) | 26.25 (39.03%) |

***Evaluation of the antiviral activity against SARS-CoV-2 Omicron BA.2 variant of Argotone drug*** – Argotone is a silver containing drug recognized by the Italian Medicines Agency (Agenzia Italiana del Farmaco AIFA) used for its antiseptic and nasal decongestant actions. Argotone active ingredients are silver proteinate (1 %wt) and ephedrine chloro-hydrate (0.9 %wt), other ingredients are water, sodium chloride and sodium thiosulphate.[160] Argotone has been used as commercial benchmark comparison for the antiviral tests against SARS-CoV-2 Omicron BA.2 variant.

The cytotoxicity evaluated by MTT assay resulted in a $CC_{50}$ of 9.3 $mg \cdot L^{-1}$. The antiviral activity against SARS-CoV-2 BA.2 was evaluated by RT-qPCR, the results are reported in Figure 52 and the $IC_{50}$ was 1.80 $mg \cdot L^{-1}$. The virucidal activity was evaluated by plaque assay confirmed the results of the antiviral assay, the results are reported in Figure 52. The selectivity index calculated for Argotone resulted 5.2, the value is significantly lower than the one obtained by AgCur SI 75.9. This comparison confirmed the promising properties of AgCur against SARS-CoV-2 Omicron BA.2 variant.

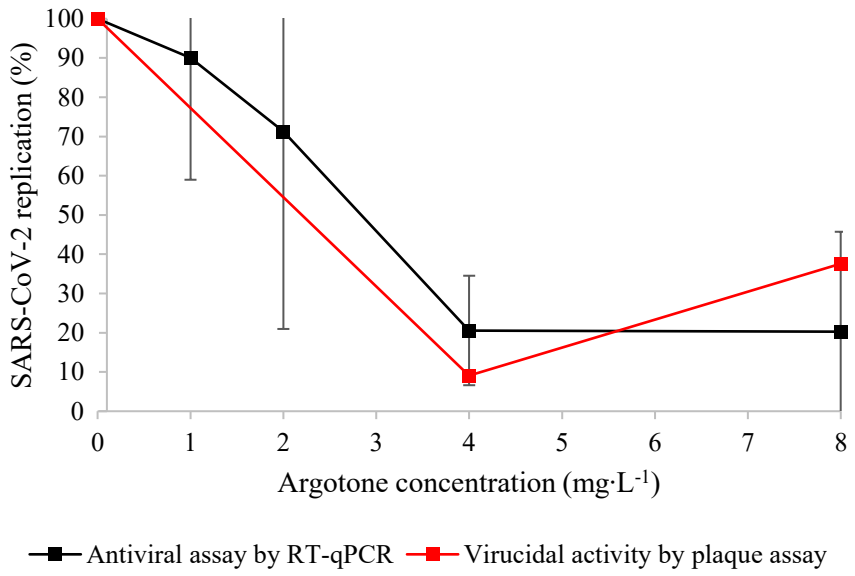


*Figure 52 – Antiviral and virucidal activity against SARS-CoV-2 BA.2 variant of Argotone drug. The results are expressed as viral replication percentage as function of the drug concentration ($mg \cdot L^{-1}$).*

***Evaluation of the antiviral activity against SARS-CoV-2 original variant of AgNPs by RT-qPCR*** – SARS-CoV-2 original variant was successfully isolated from a nasal swab. AgHEC_5.5_2.8, AgHEC_2.8_2.8, AgCur, and AgCur_Cas antiviral activity results obtained by RT-qPCR are reported in the graph in Figure 53 expressed as mean % of SARS-CoV-2 replication compared to the infected untreated cells.

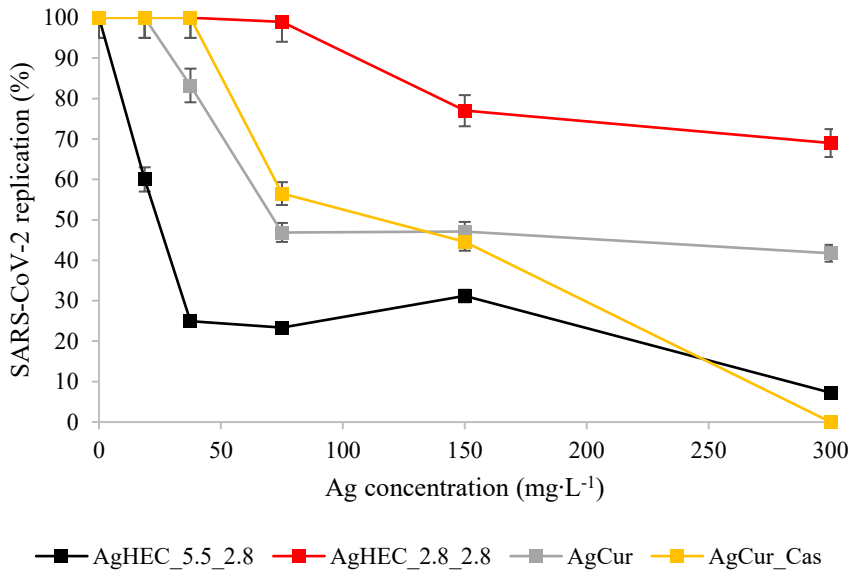


*Figure 53 – Antiviral activity against SARS-CoV-2 original variant of AgHEC_5.5_2.8, AgHEC_2.8_2.8, AgCur, and AgCur_Cas. The results are expressed as percentage of the viral replication as function of the silver concentration. The inhibition of SARS-CoV-2 replication was obtained in-vitro using the pre-treated virus with AgNPs to infect the cells. The results were obtained employing SARS-CoV-2 N1 gene RT-qPCR on RNA isolated from the supernatants of treated infected cells.*

*Table 29 – Inhibition concentration of SARS-CoV-2 ($IC_{50}$), cytotoxic concentration on Vero E6 cells ($CC_{50}$), and selectivity index (SI) of cellulose, curcumin, and sodium surfactin-capped AgNPs and their blanks.*

| | **Sample** | **$IC_{50}$ ($mg \cdot L^{-1}$)** | **$CC_{50}$ ($mg \cdot L^{-1}$)** | **SI** |
|---|---|---|---|---|
| AgHEC-based nanoforms | AgHEC_5.5_2.8 | 12.4 | 275.5 | 22.2 |
| | HEC_5.5_2.8 blank | n.d. | > 200 | n.d. |
| | AgHEC_2.8_2.8 | > 300 | 191.1 | < 0.6 |
| AgCur-based nanoforms | AgCur | 66.3 | 629.7 | 9.5 |
| | Cur blank | 50-100 | > 2500 | > 250 |
| | AgCur_Cas | 109 | > 300 | n.d. |
| AgSur-based nanoforms | AgSur_04 | n.d. | 4.05 | n.d. |
| | Sur_04 | n.d. | > 200 | n.d. |
| | AgSur_05 | n.d. | 2.34 | n.d. |
| Reference drug | Chloroquine | 3.6 | 30.5 | 8.5 |

The antiviral activity expressed as $IC_{50}$, the cytotoxicity expressed as $CC_{50}$ and the selectivity index SI of the studied samples (AgHEC_5.5_2.8, AgHEC_2.8_2.8, AgCur, and AgCur_Cas)

against SARS-CoV-2, are summarized in Table 29, together with the chloroquine information to be used as comparison.

Comparing the AgCur antiviral results against SARS-CoV-2 original variant ($IC_{50}$ 66.3 $mg \cdot L^{-1}$) with the previous test against SARS-CoV-2 Omicron BA.2 variant ($IC_{50}$ 8.3 $mg \cdot L^{-1}$), AgCur demonstrated a better antiviral activity against the Omicron variant which is the one still circulating and concerning the World Health Organization.[161]

Based on RT-qPCR virus replication data it was possible to rank the tested AgNPs against SARS-CoV-2 original variant based on their $IC_{50}$, the concentration inhibiting 50% of the viral replication: AgHEC_5.5_2.8 ($IC_{50}$ 12.4 $mg \cdot L^{-1}$), AgCur ($IC_{50}$ 66.3 $mg \cdot L^{-1}$), AgCur_Cas ($IC_{50}$ 109 $mg \cdot L^{-1}$), and AgHEC_2.8_2.8 ($IC_{50}$ > 300 $mg \cdot L^{-1}$).

Hydroxyethyl cellulose-capped AgHEC_5.5_2.8 sample had higher activity against SARS-CoV-2 original variant ($IC_{50}$ 12.4 $mg \cdot L^{-1}$) respect to the curcumin compositions AgCur ($IC_{50}$ 66.3 $mg \cdot L^{-1}$) and AgCur_Cas ($IC_{50}$ 109 $mg \cdot L^{-1}$).

The reduced cytotoxicity of the curcumin coating improved the safety profile largely increasing the $CC_{50}$ respect to the cellulose-coated samples. The most relevant physicochemical difference between the two capping agents is the zeta potential, which is positive for cellulose-capped AgNPs and negative for curcumin-capped AgNPs. It is recognized in literature that positive charged nanoparticles can better interact with the negative charged cells' phospholipidic membrane favouring their uptake by the biological milieu and subsequently demonstrating higher cytotoxicity than anionic nanoparticles.[162,163]

Both AgCur and AgHEC_5.5_2.8 offer a better selectivity index respect to chloroquine, demonstrating their viability in the treatment of SARS-CoV-2. Curcumin-based NPs offer a safer approach with their minimal cytotoxic effects, hydroxyethyl cellulose based NPs have higher activity requiring a lesser dose. Both of these paths lead to an improvement in the selectivity index of the sample.

It was not possible to test the antiviral activity of sodium surfactin-capped nanoparticles because of the high cytotoxicity against the model Vero E6 cells ($CC_{50}$ 2-4 $mg \cdot L^{-1}$). Even if these nanoparticles exhibit negative charge as well as curcumin-coated AgNPs, they are characterized by important cytotoxicity effects probably due to the biosurfactant effect of sodium surfactin promoting the cell membrane lysis.

Since AgSur variants were very active against bacteria, these materials may be studied in application involving limited or better no kind of human exposure, avoiding accidental release in the environment.

***AgNPs activity against non-enveloped virus: BK polyomavirus*** – AgCur, AgCur_Cas, and AgHEC_5.5_2.8 were tested against BK polyomavirus. No activity was observed at the different AgNPs concentrations tested, BK polyomavirus replication was always ≥ 100% (data not shown). An antiviral mechanism hyphtesis was proposed with AgNPs exerting their activity against the viral envelope, that is not present in the BK polyomavirus, but it is a component of the SARS-CoV-2 virion.

***Hypothesis on the AgNPs antiviral activity mechanism*** – The genome of SARS-CoV-2, a protein enveloped virus, produces structural, nonstructural, and accessory proteins, all of which are crucial for the virus's replication process. As represented in Figure 54, the primary targets for antiviral action are the spike protein, the 3C-like protease (3CLpro), the papain-like cysteine protease (PLpro), and the RNA-dependent RNA polymerase (RdRp).[164,165,166,167]

***Main antiviral targets***

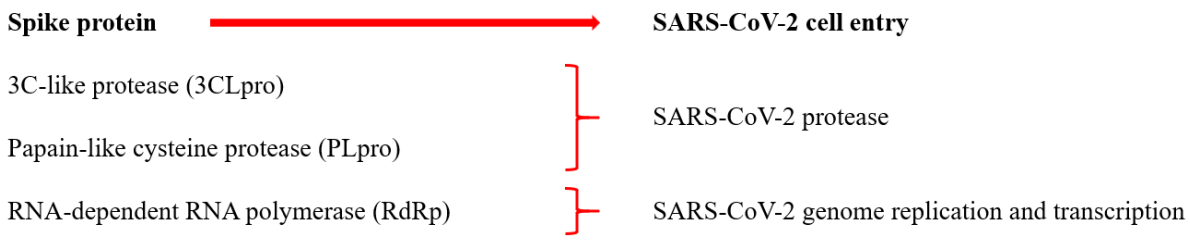


*Figure 54 – Scheme representing the main antiviral targets to prevent and cure SARS-CoV-2 infections.*

The antiviral activity of AgNPs was assessed by two opposite testing procedures:

- *Pre-inoculum*. First the virus is incubated with AgNPs at room temperature, then it is used to infect the cells.
- *Post-inoculum*. Firs the cells are infected by the virus, incubated at 37 °C, and subsequently treated by AgNPs.

The two testing procedures are schematized in Figure 55, where it is possible to see how they were used to assess the antiviral activity of AgNPs against SARS-CoV-2. AgNPs exhibited antiviral activity only if tested following the pre-inoculum methodology, otherwise chloroquine and other antiviral drugs were effective following the post-inoculum procedure. AgNPs different behavior observed between the two testing methodology suggests an interaction of AgNPs with the protein viral envelope of SARS-CoV-2, inhibiting its attachment to cells' receptors, preventing virus cell entry.

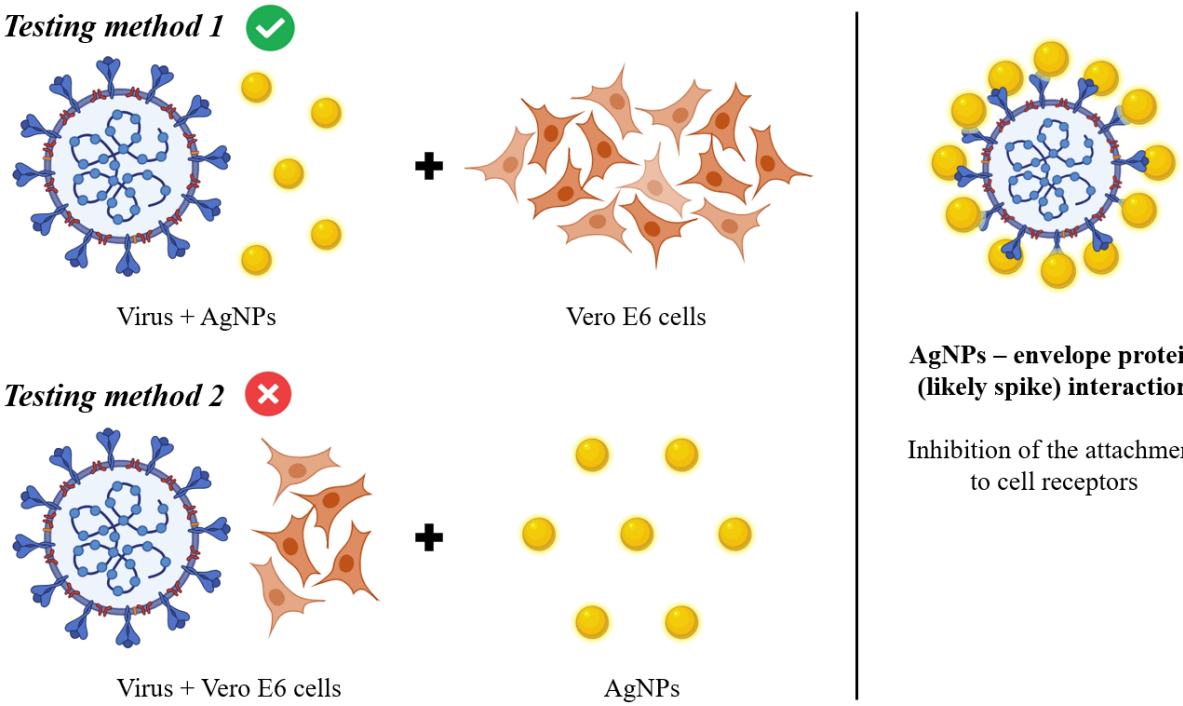


*Figure 55 – Testing methods implemented to study the antiviral mechanism of AgNPs against SARS-CoV-2. Testing method 1: pre-inoculum procedure where the virus is incubated with AgNPs before the cells' infection. Testing method 2: post-inoculum procedure where the AgNPs treatment is performed on the infected cells. Only the testing method 1 demonstrated good antiviral activity favoring the hypothesis of an inhibition action performed by AgNPs against SARS-CoV-2 cells' infection.*

AgNPs tested against BK polyomavirus, a non-enveloped virus, didn't exhibit any antiviral properties for both testing methods, as schematized in Figure 56. This result further supports the theory that the action mechanism of AgNPs is dependent on their interaction with the protein envelope of the virus (spike protein).

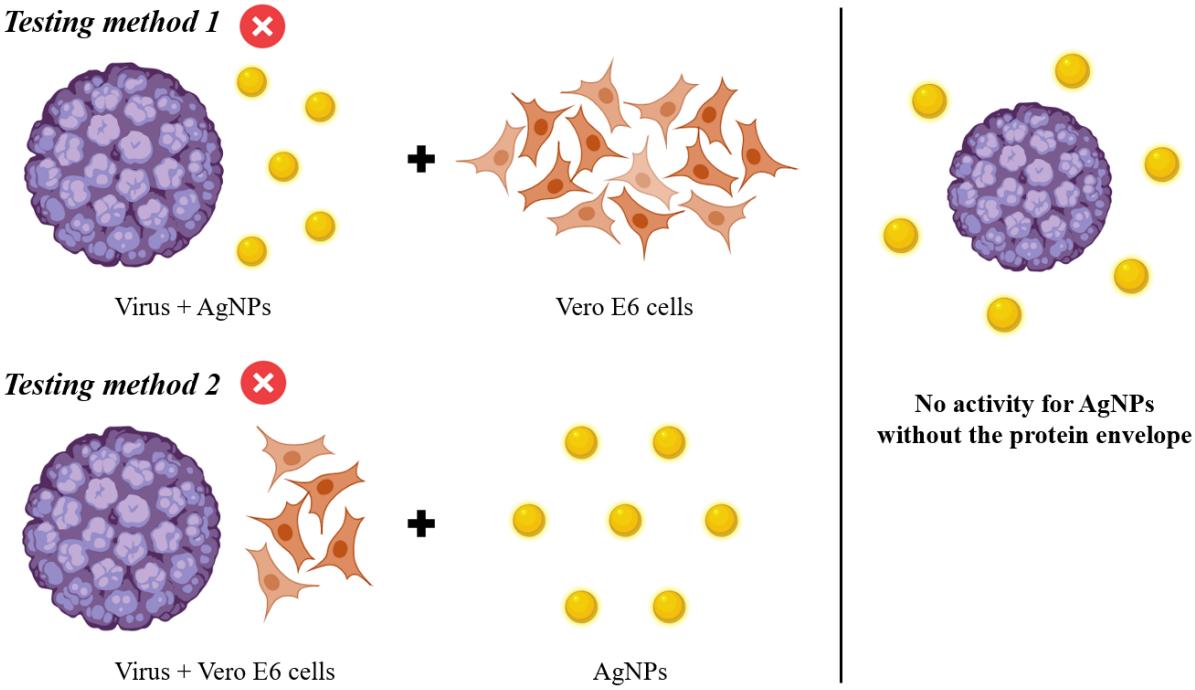


*Figure 56 – Testing methods implemented to study the antiviral mechanism of AgNPs against BK polyomavirus. Testing method 1: pre-inoculum procedure where the virus is incubated with AgNPs before the cells' infection. Testing method 2: post-inoculum procedure where the AgNPs treatment is performed on the infected cells. AgNPs demonstrated no antiviral activity against BK polyomavirus which lacks of an externa protein envelope, favoring the hypothesis that the antiviral mechanism of AgNPs involves an interaction with the viral envelope inhibiting the attachment to cells' receptors.*

***Conclusions*** – The antiviral results can be summarized as follow:

- The antiviral tests against SARS-CoV-2 Omicron BA.2 variant demonstrated different AgNPs mechanisms of action against bacteria (AgHEC_6.4_1.4 was the best performing sample) and viruses. In fact, AgCur showed excellent antiviral performance coupled with an outstanding selectivity index (SI 75.9), associated to a large safe and effective dose window, if compared to chloroquine drug used as positive control (SI 8.5).
- AgCur demonstrated to be the lowest cytotoxic silver nanoform tested and the most active one against SARS-CoV-2 Omicron BA.2 variant, resulting a very promising option for antiviral applications. The excellent antiviral activity and low cytotoxicity of this compound is probably due to the antiviral and antioxidant properties of curcumin, establishing synergistic effects with AgNPs.
- The antiviral testing procedure adopted and the different results collected for enveloped and non-enveloped viruses suggested an interaction of AgNPs with protein envelope of the viruses, in particular for SARS-CoV-2 it is the spike protein. In this way the interaction with the cell receptors is inhibited preventing the infection.

- The test performed on SARS-CoV-2 original variant allowed the activity comparison between different AgNPs samples. In this case, AgCur demonstrated reduced activity compared to the Omicron BA.2 variant with a selectivity index of 9.5, while better performances were recorded for AgHEC_5.5_2.8 with a selectivity index of 22.2.

### 3.2.5. Dissolution of AgHEC in relevant media

Human and environmental exposure are fundamental parameters to be considered during a material safety profile assessment. To determine possible real exposure scenario for human toxicity and environmental eco-toxicity studies, different dissolution tests were assessed.[168]

***Human exposure*** – To perform a toxicity study it is important to know reliable exposure doses and which silver compounds are present. Materials and in particular nanomaterials, may undergo transformation processes once they enter the human body. Thanks to *in vitro* acellular dissolution assays it is possible to study these processes using simulated biological fluid, and then better understand and eventually predict the *in vivo* behavior. This kind of tests allow to estimate the bio-persistence and bio-availability of the nanomaterial, helping the study of its distribution within the organism, its potential acute and long-term toxicity, and also the pathogenicity.[169] Several protocols have been published to simulate different *in vivo* scenarios. AgHEC_5.5_2.8 was selected as sample for dissolution tests, it underwent two different protocols:

- Synthetic sweat (sodium chloride 0.5 %wt, lactic acid 0.1 %wt, and urea 0.1 %wt water solution regulated to pH 4.5 with 1 M ammonium hydroxide), 1 and 24 hours exposure at 32 °C, testing Ag 10 and 50 $mg \cdot L^{-1}$. The fluid has been identified to simulate the dissolution into human sweat, relevant for dermal exposure studies.
- DMEM (Dulbecco's Modified Eagle Medium) loaded with a 10 %wt FBS (fetal bovine serum), 1 and 24 hours exposure at 37 °C, testing Ag 10 and 50 $mg \cdot L^{-1}$. The fluid represents a frequently used cell media and has been identified to simulate the biological environment and better support the in-vitro toxicological experiments.

After the dissolution tests, AgNPs were filtered away by ultracentrifugation (cut-off 10 kDa) and dissolved $Ag^+$ ions were quantified analyzing by ICP-OES the filtered medium after the acidic digestion. Results are expressed as percentage of $Ag^+$ released respect to the starting AgNPs amount.

In Table 30 are reported synthetic sweat results and in Table 31 DMEM+FBS results. In general, it was observed limited dissolution for both protocols, slightly higher in synthetic sweat. It is really interesting to note that there was no proportionality in the $Ag^+$ concentration detected by ICP-OES and the starting Ag concentration, but rather there was an inverse proportionality with the dissolution ratio and the starting concentration. This means that moving from a starting Ag concentration of 10 $mg \cdot L^{-1}$ to 50 $mg \cdot L^{-1}$, the $Ag^+$ concentration detected was similar, but the calculated dissolution rate as $Ag^+/Ag_{tot}$ results to be about one fifth. It is possible to assume that it is due to a sort of saturation of the media, limiting the silver dissolution. This suggest that the

instauration of equilibria may play a relevant role in real field scenarios. Furthermore, over time moving from 1 hour to 24 hours, it was observed a reduced dissolution rate, this is counterintuitive and may be due to aggregation phenomenon.

Other supplementary information is reported in Table 30 and Table 31, such as the hydrodynamic diameter, the zeta potential and the pH of tested samples. In particular, synthetic sweat composition and acidic pH lead towards positively slightly positively charged particles with larger detected hydrodynamic diameter. It is the opposite for DMEM+FBS, where the biological environmental and basic pH lead to slightly negative particles with smaller hydrodynamic diameters.

In conclusion, AgHEC_5.5_2.8 resulted stable to the tested dissolution protocols.

*Table 30 – AgHEC_5.5_2.8 dissolution test in synthetic sweat.*

| ***AgHEC_5.5_2.8 dissolution test in synthetic sweat*** | | | | | |
|---|---|---|---|---|---|
| **$Ag^+/Ag_{tot}$ (%)** | **Time (h)** | **Ag initial conc. ($mg \cdot L^{-1}$)** | **Size (nm)** | **Zeta potential (mV)** | **pH** |
| 6.2 | 1 | 10 | 176 | 4.8 | 4.5 |
| 4.3 | 24 | 10 | 253 | 0.6 | 4.5 |
| 0.9 | 1 | 50 | 266 | 0.7 | 4.8 |
| 0.6 | 24 | 50 | 267 | 0.4 | 4.9 |

*Table 31 – AgHEC_5.5_2.8 dissolution test in synthetic DMEM+FBS.*

| ***AgHEC_5.5_2.8 dissolution test in DMEM+FBS*** | | | | | |
|---|---|---|---|---|---|
| **$Ag^+/Ag_{tot}$ (%)** | **Time (h)** | **Ag initial conc. ($mg \cdot L^{-1}$)** | **Size (nm)** | **Zeta potential (mV)** | **pH** |
| 0.8 | 1 | 10 | 45.6 | -4.0 | 8.4 |
| 0.7 | 24 | 10 | 93 | -2.0 | 8.7 |
| 0.2 | 1 | 50 | 70 | -1.9 | 8.4 |
| 0.2 | 24 | 50 | 68.4 | -1.7 | 8.7 |

To study the respiratory exposure after the possible inhalation of these nanophases, two other simulating fluids were tested. The most relevant were selected as: simulated lung lining fluid (LLF) which covers the respiratory tract, and phagolysosomal simulated fluid (PSF) which represent the uptake of alveolar macrophages. It is important to consider that lungs are not static systems, ions liberated from nanomaterials are usually transported elsewhere. So, in a static

system it is possible to encounter saturation problems that are not typically present in real *in vivo* scenarios, beside that they have shown good predictivity.[170]

These dissolution assays were assessed following the ISO/TR19057:2017(E) guidelines. The PSF media was prepared according to a literature procedure, omitting alkylbenzyldimethylammonium chloride as potential interferent, Table 32.[171] The LLF media preparing procedure is described in the ISO document and different literature study, Table 33.[172,173] Briefly, the protocol adopted for both media is:

- Erlenmeyer flask containing 100 mL of biological fluid and an Ag initial concentration of 1 $mg \cdot L^{-1}$. The samples are placed in an orbital shaker at 37 °C and 180 rpm, after 5 minutes of equilibration, the sampling starts by selecting as time points 0, 1, 24, and 48 hours.

At time points 4 mL aliquots were taken for ICP-MS quantification of Ag, total silver was determined by acidic digesting the aliquot, while the dissolved fraction was assessed by previously filtering the aliquots by ultracentrifugation (40 min, 4000 rpm, 20 °C, and 3kDa). Silver dissolution data were associated with DLS, ELS, and pH measurements.

*Table 32 – Simulated lung lining fluid composition.*

| **Lung lining fluid (pH 7.4)** | |
|---|---|
| *Component* | *Concentration ($mg \cdot L^{-1}$)* |
| $MgCl_2 \cdot 6H_2O$ | 212 |
| NaCl | 6415 |
| $CaCl_2 \cdot 2H_2O$ | 255 |
| $Na_2SO_4$ | 79 |
| $Na_2HPO_4$ | 148 |
| $NaHCO_3$ | 2703 |
| $C_4H_4Na_2O_6 \cdot 2H_2O$ (sodium tartrate dihydrate) | 180 |
| $HOC(COONa)(CH_2COONa)_2 \cdot 2H_2O$ (trisodium citrate dihydrate) | 180 |
| $C_3H_5NaO_3$ (sodium lactate) | 175 |
| $C_3H_3NaO_3$ (sodium pyruvate) | 172 |
| $NH_2CH_2COOH$ (glycine) | 118 |

*Table 33 – Phagolysosomal simulated fluid composition.*

| **Phagolysosomal simulated fluid (pH 4.5)** | |
|---|---|
| *Component* | *Concentration ($mg \cdot L^{-1}$)* |
| NaCl | 6650 |
| $Na_2HPO_4$ | 142 |
| $Na_2SO_4$ | 71 |
| $CaCl_2 \cdot 2H_2O$ | 29 |
| $NH_2CH_2COOH$ (glycine) | 405 |
| $C_8H_5O_4K$ (potassium hydrogen phthalate) | 4085 |

Three samples were selected for this study: AgHEC_5.5_2.8, considered as reference starting material, and AgHEC_6.4_1.4 and AgCur, two different variants subsequently developed. The results collected are summarized in the following graphs. In Figure 57 is reported the evolution of pH as function of time, in Figure 58 the zeta potential, in Figure 59 the hydrodynamic diameter, in Figure 60 the polydispersity index, and finally in Figure 61 the dissolution rate.

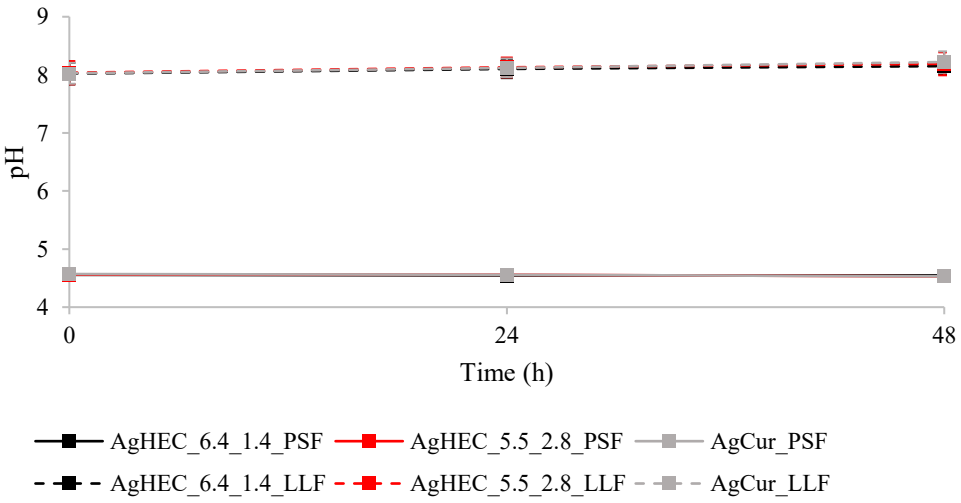


*Figure 57 – 48 hours pH monitoring of AgHEC_6.4_1.4, AgHEC_5.5_2.8, and AgCur dispersed in phagolysosomal simulated fluid (PSF) and simulated lung lining fluid (LLF).*

The pHs imposed by the simulating media are preserved for the whole duration of the experiments, Figure 57. PSF is about 4.6 and LLF about 8.1, they are slightly higher than the theoretical ones (4.5 for PSF and 7.4 for LLF), probably due to the presence of the silver nanoparticles, which are basic colloidal suspension.

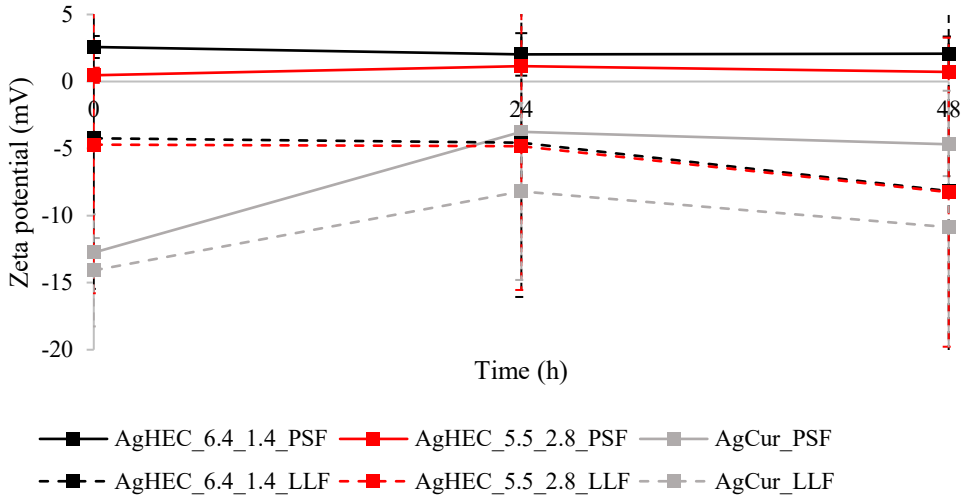


*Figure 58 – 48 hours zeta potential monitoring of AgHEC_6.4_1.4, AgHEC_5.5_2.8, and AgCur dispersed in phagolysosomal simulated fluid (PSF) and simulated lung lining fluid (LLF).*

The zeta potential gives indirect information regarding the colloidal stability of the nanoparticles, in fact higher zeta potential absolute values represent stronger electrostatic repulsion. In general, absolute zeta potential values above ±30 mV are defined enough to grant electrostatic stability to the suspension.[174] This parameter is strongly affected by the pH since it depends by the ions and counterions surrounding the particle shell. In general, the absolute values of the samples in these simulated media is not high enough to ensure good electrostatic stability, in particular for AgHEC_5.5_2.8 and AgHEC_6.4_1.4 with values close to 0 mV, Figure 58. Their zeta potential remains more or less constant during the 48 hours test. On the other side, AgCur shows a significative decrease of zeta potential already at 24 hours, this may imply an increasing instability over time, and a possible deterioration of the curcumin coating surrounding the nanoparticles. Most of the cellular membranes are usually negatively charged, so the zeta potential can play an important role in the membrane permeation and typically positively charged particles demonstrate higher toxicity levels associated with the membrane disruption.[175]

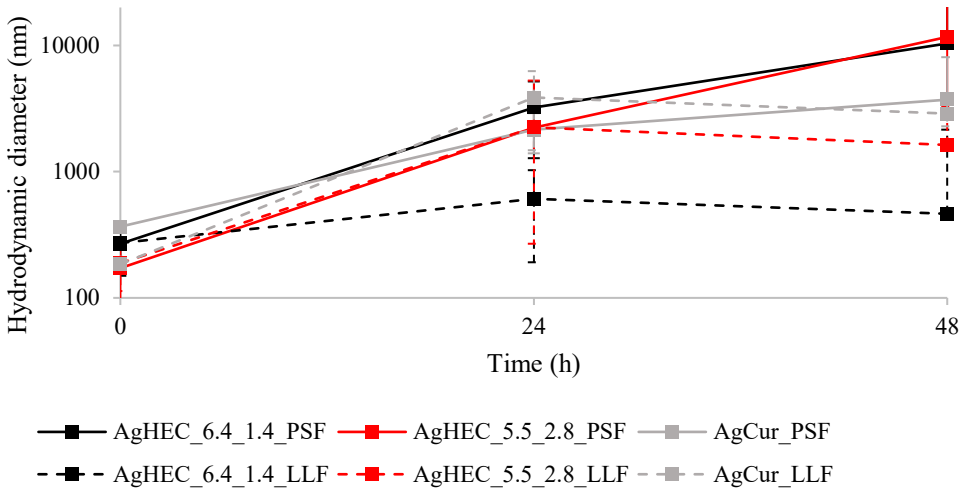


*Figure 59 – 48 hours hydrodynamic diameter monitoring of AgHEC_6.4_1.4, AgHEC_5.5_2.8, and AgCur dispersed in phagolysosomal simulated fluid (PSF) and simulated lung lining fluid (LLF).*

The hydrodynamic diameter trend represents an unstable condition for the samples in both biological simulated environments, Figure 59. In fact, it is possible to observe relevant aggregation phenomena leading to coarse micrometric aggregates. PSF seems to accentuate this phenomenon leading to larger aggregates for all samples. The differences between PSF and LLF are more visible for quaternary hydroxyethyl cellulose capped samples AgHEC_5.5_2.8 and AgHEC_6.4_1.4, while the 48 hours hydrodynamic diameter of AgCur is similar in the two media.

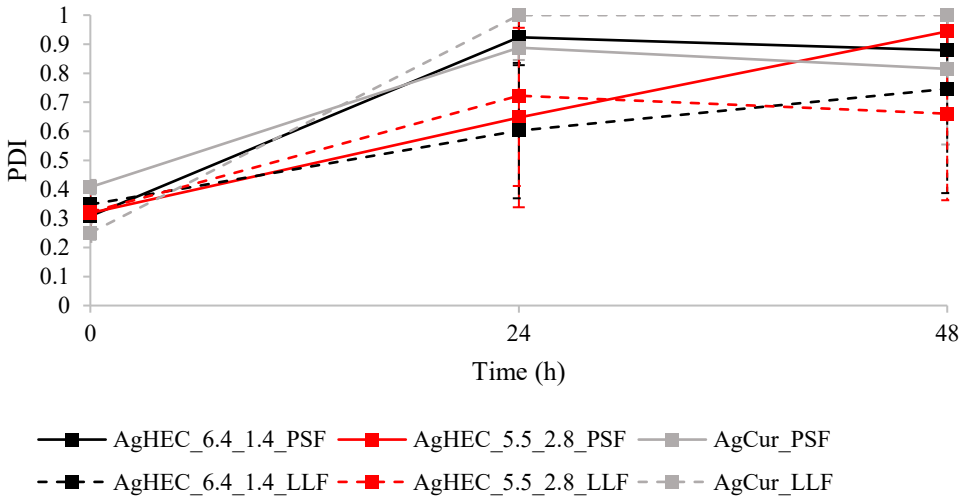


*Figure 60 – 48 hours polydispersity index (PDI) monitoring of AgHEC_6.4_1.4, AgHEC_5.5_2.8, and AgCur dispersed in phagolysosomal simulated fluid (PSF) and simulated lung lining fluid (LLF).*

The polydispersity index results reported in Figure 60 are according to the hydrodynamic diameter. Already at 24 hours the populations show high polydispersity level, confirming uncontrolled aggregation phenomena. As well as the hydrodynamic diameter, PSF is affecting in a stronger way HEC-based samples, while AgCur reveal an opposite trend.

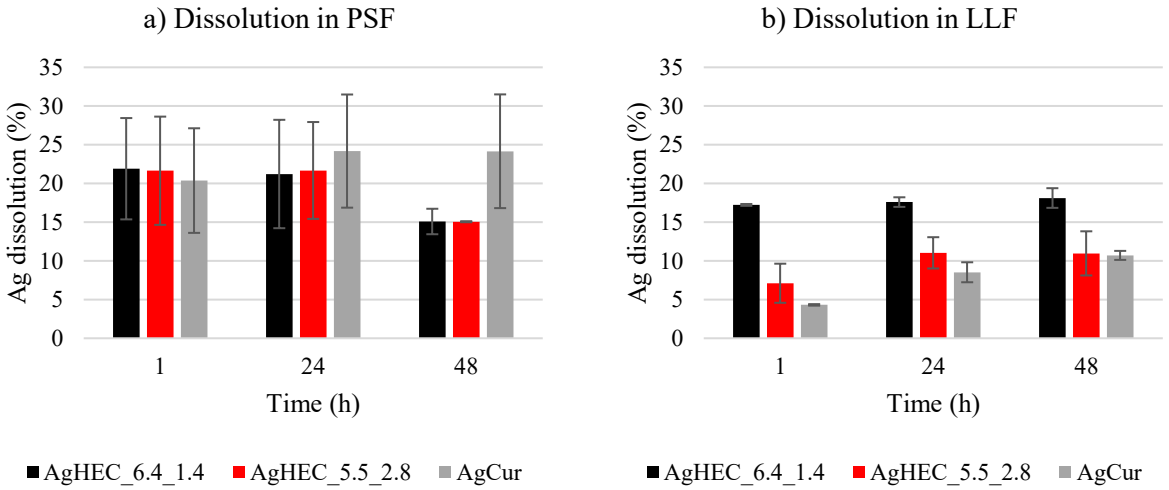


*Figure 61 – 48 hours silver dissolution rate monitoring of AgHEC_6.4_1.4, AgHEC_5.5_2.8, and AgCur dispersed in: a) phagolysosomal simulated fluid (PSF) and b) simulated lung lining fluid (LLF).*

For what concerns the dissolution rate of these nanomaterials, results reported in Figure 61 highlight important differences between the two tested media, PSF and LLF. In the PSF case, there aren't relevant differences among AgNPs variants tested at 1 and 24 hours. At 48 hours there is a distinguished behavior of HEC coated particles, the dissolution rate drops significantly from ≈ 21% at 24 hours to ≈ 15%. At 48 hours, strong aggregation phenomena occurred for HEC coated samples in PSF, as confirmed by DLS analysis, the hydrodynamic diameter reaches values larger than 10 µm, so it is likely to observe precipitation and sedimentation, reducing this way the silver cations available for the dissolution. The LLF case is different, first it is possible to see a lesser dissolution rate for all samples, then the 3 materials exhibit different Ag dissolutions. AgHEC_6.4_1.4 shows larger $Ag^{+}$ release with a 17-18% dissolution, it is followed by AgHEC_5.5_2.8 with an increasing release during the 48 hours from 7% to about 11%, an then AgCur results to be more stable in this environment thanks to the more negative zeta potential with a progressive release of about 4% at 1 hour till 11% at 48 hours. Based on these results it is possible to classify tested materials as quickly dissolving nanomaterials.

These tests were operated at low silver concentration, 1 $mg \cdot L^{-1}$, because working at higher concentrations would have accentuated the main problem of static dissolution assays, the

saturation of the solution that would lead to and underestimation of the material solubility. Recently, some European funded project such as Gov4Nano (*Meeting the need of nanotechnology*) and PATROLS (Physiologically Anchored Tools for Realistic nanOmateriaL hazard aSsessment) worked this topic, stressing creating and improving guidelines for the dissolution test of nanomaterials in biological fluids.[176,177] They also remarked the importance of the study and characterization of agglomeration and dispersion phenomenon affecting dissolution assays.

***Environmental exposure*** – To perform eco-toxicity studies it is fundamental to know silver concentrations and forms. As well as for human exposure dissolution tests, two protocols were tested on AgHEC_5.5_2.8:

- Soil media, exposure time 1, 5, 28, and 56 days, under static conditions at 20 °C. AgNPs were tested at 10, 100, and 1000 $mg \cdot L^{-1}$.
- ISO media, exposure time 1, 5, 28, and 56 days, under static conditions at 20 °C. AgNPs were tested at 10, 100, and 1000 $mg \cdot L^{-1}$.

After the dissolution tests, AgNPs were filtered away by ultracentrifugation (cut-off 10 kDa) and dissolved $Ag^+$ ions were quantified analyzing by ICP-OES the filtered medium after the acidic digestion. Results are expressed as concentration of $Ag^+$ released as function of time.

Results obtained with Soil media are reported in the graph in Figure 62, while the ones with ISO media in the graph in Figure 63. These tests demonstrated the high stability of AgHEC_5.5_2.8 in these environments, in fact the $Ag^+$ dissolved concentration is very limited in both scenarios. Even strongly increasing the starting silver concentration (1000 $mg \cdot L^{-1}$), there aren't relevant dissolution behaviors, the Ag+ concentration remains largely below 0.7 $mg \cdot L^{-1}$ for all the samples, and in ISO media even below 0.05 $mg \cdot L^{-1}$. These results represent important stability of AgHEC_5.5_2.8 in these simulated environments, probably shifting the main problem of the accidental release of these nanophases in the environment from the dissolution of silver ions to the potential accumulation of silver nanoparticles.

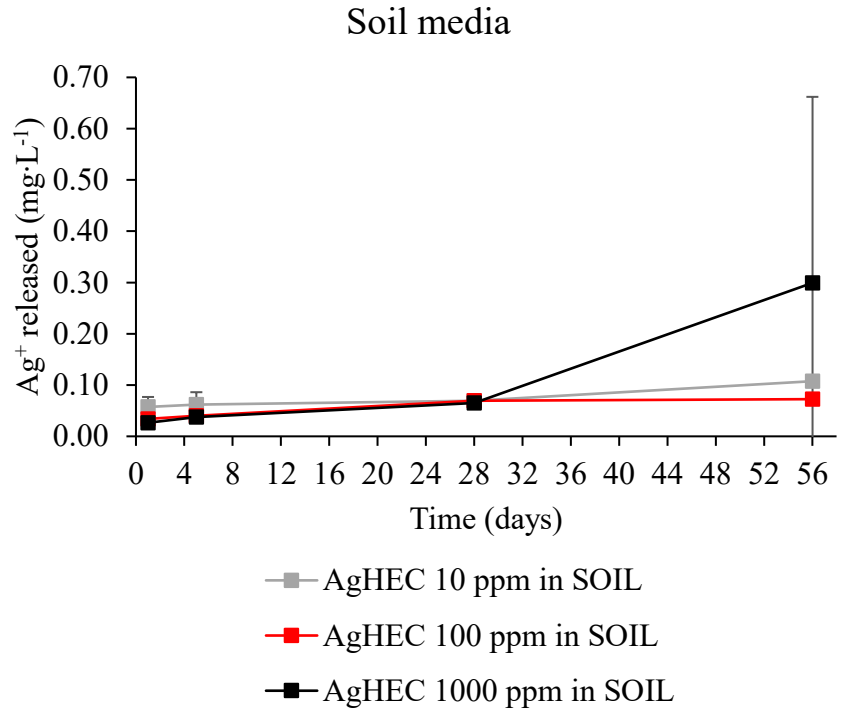


*Figure 62 – 56 days silver dissolution rate monitoring of AgHEC_5.5_2.8 dispersed in soil media at three concentrations: 10, 100, and 100 ppm.*

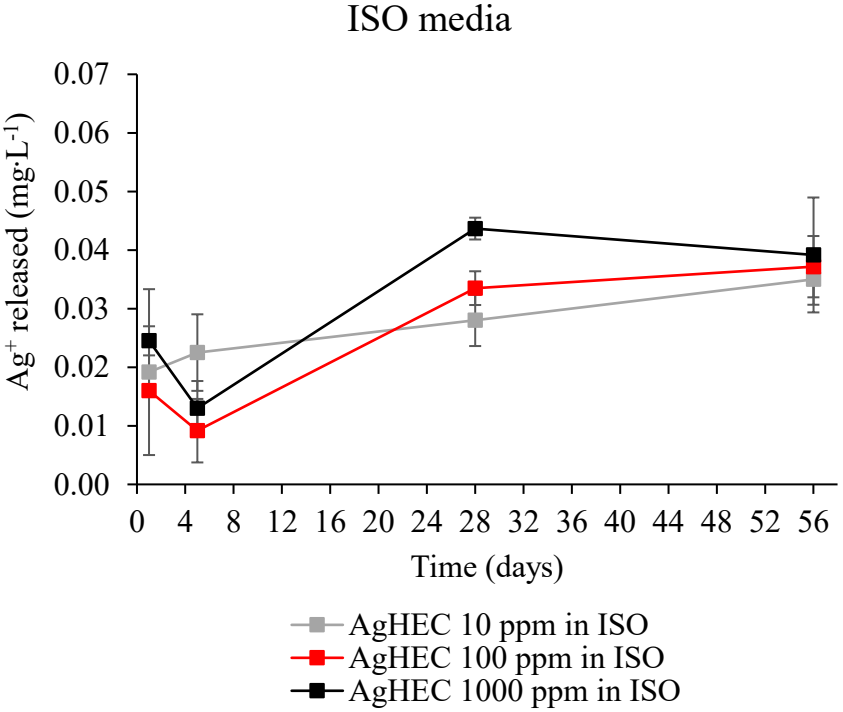


*Figure 63 – 56 days silver dissolution rate monitoring of AgHEC_5.5_2.8 dispersed in ISO media at three concentrations: 10, 100, and 100 ppm.*

### 3.2.6. Additional physical and chemical properties of synthesized silver nanoparticles

In a point of view of an improvement of the technology readiness level (TRL) of these materials, which could be represented by the implementation in a device or a large-scale application of the products, some secondary importance physical properties of the colloidal suspension were studied, which are usually ignored at laboratory scale research.

***Density*** – The density of the synthesized colloidal suspension was determined by weighting a known volume. In general, it was possible to state with good approximation that the density of the sample prepared is close to water density 0.998 $g \cdot mL^{-1}$ at 20 °C.[178] The concentrated sol (≈ 0.5 %wt in Ag) measured density at ≈ 20 °C resulted to be 1.014 $g \cdot mL^{-1}$ for AgHEC_5.5_2.8, 1.020 $g \cdot mL^{-1}$ for AgHEC_6.4_1.4, and 0.990 $g \cdot mL^{-1}$ for AgCur. A similar situation is observed for the samples diluted 1:100 in volume. In this case the density is even closer to the one of the Milli-Q water which resulted to be experimentally 1.000 $g \cdot mL^{-1}$. It resulted to be 1.006 $g \cdot mL^{-1}$ for AgHEC_5.5_2.8, 1.008 $g \cdot mL^{-1}$ for AgHEC_2.8_1.4, 1.008 $g \cdot mL^{-1}$ for AgHEC_2.8_2.8, 1.006 $g \cdot mL^{-1}$ for AgCur, and 1.012 $g \cdot mL^{-1}$ for AgCur_Cas. It has been established that the difference in samples density with respect to water density can be considered negligible. Therefore, it has been approximated to 1.000 $g \cdot mL^{-1}$ in the calculation for dilutions, characterizations and tests carried out.

***Surface tension*** – The surface tension of AgHEC_5.5_2.8 sample at different concentrations was studied thanks to a DSA30S (Krüss) optical tensiometer using the pendant drop method. The average parameters of the measurements are here reported: temperature 27.2 °C, drop volume 25 µL, B factor 0.6, and average area 43 $mm^2$. The results reported in Table 34 show a concentration dependent behavior, the surface tension increases with the dilution of the sample.

*Table 34 – Surface tension measurements of AgHEC_5.5_2.8 at different silver concentrations.*

| Sample | Concentration (%wt) | Surface tension ($mN \cdot m^{-1}$) |
|---|---|---|
| AgHEC_5.5_2.8 | 0.5 | 63.8 ± 0.3 |
| AgHEC_5.5_2.8 | 0.125 | 62.9 ± 0.3 |
| AgHEC_5.5_2.8 | 0.1 | 65.3 ± 0.2 |
| AgHEC_5.5_2.8 | 0.01 | 66.8 ± 0.3 |
| AgHEC_5.5_2.8 | 0.005 | 66 ± 1 |

AgHEC_5.5_2.8 has a lower surface tension respect to water, 72.8 $mN \cdot m^{-1}$ at 20°C.[179] The higher the dilution is, the closer the surface tension of AgHEC_5.5_2.8 is to the one of water. The synthesis influences several parameters that can interfere with this property, the pH, the presence of dissolved ions, and dispersed nanoparticles, together with the quaternized hydroxyethyl cellulose biopolymer. This slight variation can affect wetting and capillarity.

***Viscosity*** – AgHEC_5.5_2.8 and AgHEC_6.4_1.4 were selected for a viscosity study. Quaternized hydroxyethyl cellulose based nanoparticles demonstrated a relevant increase in viscosity during the synthesis, in particular composition with higher biopolymer content showed the highest viscosity, as for example AgHEC_6.4_1.4. On the other hand, AgCur and AgSur nanoparticles presented lower viscosity, closer to the one of water, so they weren't considered for this analysis. Freshly synthesized AgHEC_5.5_2.8 and AgHEC_6.4_1.4 viscosity temporal evolution was monitored with a rotational rheometer C-VOR 120 (Bohlin Instruments), working at 25 °C and with a shear rate of 0.1 $s^{-1}$. The monitoring started before the 48 hours aging included in the synthesis process, from 0 to 8 hours the viscosity was measured every 1.5 hours, then for the first 3 days it was measured once per day. Finally, the last points were measured after a long term storing in dark conditions at 4 °C, up to 22 months. Results are reported in Figure 64.

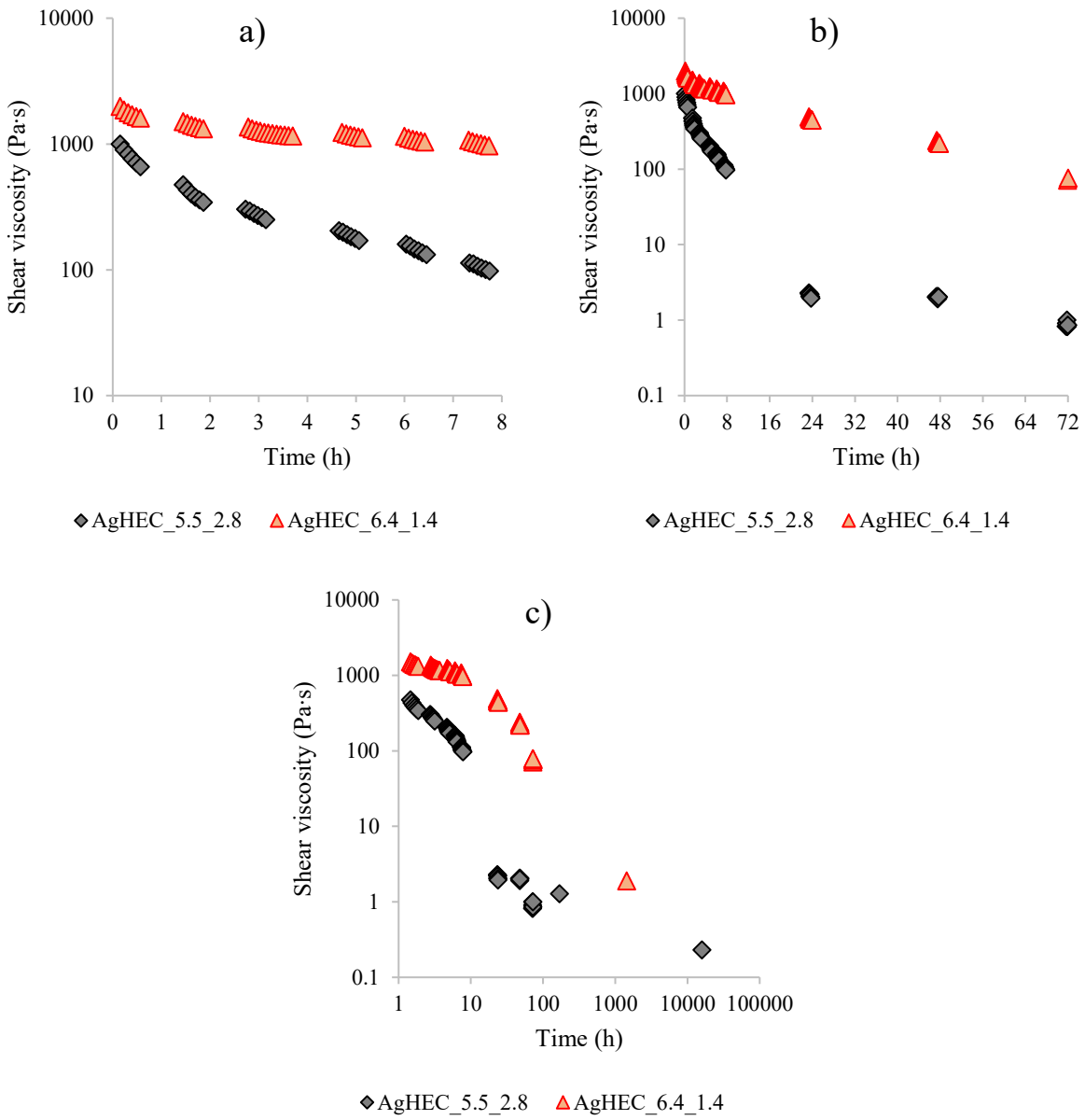


*Figure 64 – Viscosity of the samples AgHEC_5.5_2.8 and AgHEC_6.4_1.4 at a silver concentration of 5000 mg·L$^{-1}$. Time evolution of the viscosity after the synthesis: a) 0-8 hours; b) 0-72 hours; c) 0-22 months.*

It was possible to observe a viscosity decreasing trend overtime. AgHEC_6.4_1.4, the composition with higher amount of capping agent (HEC), showed higher viscosity and a slower reduction. Immediately after the synthesis, AgHEC_5.5_2.8 has a viscosity of 997 Pa·s, that decreases to 97 Pa·s after 8 hours, it reaches 1 Pa·s after 3 days, no relevant variations are observed after one week, and finally decreases to 0.2 Pa·s after 22 months. AgHEC_6.4_1.4 starts from 1986 Pa·s, it drops to 968 Pa·s within 8 hours, to 79 Pa·s after 3 days, and finally to 2 Pa·s after 2 months. Even after the aging period the sample's viscosity was several order of magnitude higher respects to the viscosity of water which is $8.9 \cdot 10^{-4}$ Pa·s at 25 °C and 1 atm.[180]

The viscosity of the samples diluted 1:100 in weight was also measured. This information may be interesting for the physicochemical characterization assessed on the diluted suspension and also for the application of these material which occurs in a diluted form and not with the concentrated suspension. The viscosity of 1:100 diluted AgHEC_5.5_2.8 is $1.82 \cdot 10^{-3}$ Pa·s and $1.93 \cdot 10^{-3}$ Pa·s for AgHEC_6.4_1.4. Even at this dilution it is about the double of water's viscosity.

The strong increase in viscosity obtained during the synthesis of hydroxyethyl cellulose capped silver nanoparticles may have some implications in the synthesis itself. Immediately after the addition of the last reagent, namely the sodium hydroxide solution, the sample turn from whitish to dark brown and the viscosity increase enormously. The high viscosity can influence the kinetic of the process slowing the diffusion of silver cation, in fact 48 hours aging are required for reaction completeness. Also, higher viscosity composition such as AgHE_6.4_1.4 may favors the development of smaller sized nanoparticles acting on the nucleation-growth rates equilibrium. Furthermore, in a more applicative way of thinking, the viscosity may influence the thickness of an eventual coating to be deposited, the production of a spray through a nozzle, and other experimental parameters. So, it is important to consider this property of the material and also to evaluate possible dilution factor to reach the requirements for the desire application.

## 3.3. Conclusions

In this chapter were described the synthesis of antimicrobial silver nanoparticles performed by implementing the Safe and Sustainable by Design guidelines to produce effective materials minimizing the impact on human and environmental health. Three different capping agents were used, obtaining three main classes of silver nanoparticles:

- Quaternized hydroxyethyl cellulose is a biopolymer obtained by addition of positively charged quaternary ammonium functionalities on the main hydroxyethyl cellulose chain. It is a bioderived molecule with intrinsic antimicrobial properties, that grants both electrostatic and steric stabilization to the colloidal nanoparticles.
- Curcumin it is a natural derived organic molecule extracted from *Curcuma longa* that possesses several intrinsic beneficial properties, like antimicrobial activity and therapeutic effects. It is a negatively charged molecule that can be used as a capping agent for negatively charged silver nanoparticles.
- Sodium surfactin is a biosurfactant produced by bacterial metabolism, it possesses the typical properties of surfactant, and the micellar structures generated by its dispersion in water can be used as microreactors. The structure is a cyclic lipopeptide, it is negatively charged and possesses sodium as a counterion. The surfactant activity can enhance the antimicrobial activity of silver nanoparticles helping the pathogens' membrane lysis.

For each class a design of experiment was developed considering the main variables impacting the physicochemical and functional properties of the final product. A full set of variants was produced and characterized finding correlations between composition, physicochemical properties, and antimicrobial activity.

HEC capped AgNPs possess positive zeta potential, while Cur- and Sur-capped AgNPs are characterized by negative zeta potential. This allows to study of different interaction with cells and pathogens, also confers different stability and durability of the product. TEM images revealed spheroidal nanoparticles with average size comprised in the range 12-18 nm for AgHEC and AgCur variants, while smaller sized distribution was obtained for AgSur where the average diameter is 1-2 nm, for AgSur it was also observed a larger population constituted by aggregates of size 29-45 nm. Smaller particles exhibit higher activities thanks to the higher surface/volume ratio, this is helpful as antimicrobial agent as well as in catalysis or other applications. Sodium surfactin capped AgNPs have a smaller size, but XRD measurements revealed a non-quantitative selectivity towards metallic silver phase, in fact silver carbonate phases were identified as undesired byproducts. So, even if the exploitation of sodium surfactin micelles as template agent

for the synthesis of AgNPs may be a promising solution for the production ultra-small particles, the reaction condition should be further optimized to increase the selectivity of the process. On the other side, excellent results were obtained using hydroxyethyl cellulose and curcumin.

Once the full set of variants was produced and characterized at colloidal level (UV-Vis absorption, hydrodynamic diameter, PDI, zeta potential, Ag concentration and conversion by ICP-OES, TEM, and XRD), a reduced roster of sample was selected for the antimicrobial study. The selection was based on the most promising physicochemical properties and stability of the colloidal suspensions. For HEC, AgHEC_6.4_1.4 and AgHEC_5.5_2.8 demonstrated smaller sized TEM average diameter, as well as quantitative conversion of silver precursor, they displayed long-term stability and shelf-life. For Cur, AgCur and AgCur_Cas resulted to be the most stable and reproducible samples, with comparable TEM size with HEC capped AgNPs. Finally, for Sur, AgSur _04 and AgSur_05 were the most stable suspensions with smaller hydrodynamic diameter, so they were chosen for the antimicrobial tests.

The antimicrobial tests were divided in:

- Antibacterial tests, *E. coli* was studied as representative of Gram-negative bacteria and *S. aureus* for Gram-positive.
- Antiviral tests, SARS-CoV-2 was used as model for enveloped viruses and BK polyomavirus for the non-enveloped.

From the antibacterial tests AgHEC_6.4_1.4, AgCur and AgSur_04 emerged as the most active variants against both Gram-negative and Gram-positive bacteria. *S. aureus* demonstrated higher susceptibility towards AgHEC_6.4_1.4 and AgCur, while *E. coli* toward AgSur_04. In this case, the different coating and composition reflected into a different antibacterial activity. The samples showed concentration dependent behavior reaching excellent activity (up to 2-5 log bacterial reduction) at 10 $mg \cdot L^{-1}$.

Antiviral tests highlighted an important information related to the possible antiviral mechanism of action of AgNPs. In fact, all the tested samples showed good activity against SARS-CoV-2 but no activity was registered against BK polyomavirus. This led to the assumption that these AgNPs interact with the viral envelope to display their antiviral activity. It was not possible to test AgSur samples due to their high cytotoxicity. HEC and Cur based composition showed promising antiviral activity with a concentration dependent behavior, reaching $IC_{50}$ values comparable to chloroquine a commercial drug (AgHEC_5.5_2.8 $IC_{50}$ = 12.4, AgCur $IC_{50}$ = 66.3, and chloroquine $IC_{50}$ = 3.6). AgHEC demonstrated higher activity at low concentration respect to AgCur, but the minimal cytotoxic effects of AgCur allows a wider concentration range for a safe and effective use (AgHEC_5.5_2.8 $CC_{50}$ = 275.5, AgCur $CC_{50}$ = 629.7, and chloroquine

$CC_{50}$ = 30.5), represented by greater selectivity indexes respect to chloroquine (AgHEC_5.5_2.8 SI = 22.2, AgCur SI = 10.4, and chloroquine SI = 8.5).

Summarizing it is possible to say that three different capping agents were exploited for the development of Safe and Sustainable by Design synthesis of antimicrobial silver nanoparticles. Each capping agents leaded to specific physicochemical and functional properties that may be useful in different application fields. For example, negatively charge curcumin capped silver nanoparticles may be implemented in antimicrobial agents for direct human contact because of the negligible cytotoxicity, while other variants such as sodium surfactin capped silver nanoparticles may find application for the preparation of antimicrobial surfaces or materials that does not imply human exposure, finally quaternized hydroxyethyl cellulose capped silver nanoparticles have an external positively charged biopolymeric layer that may favor interaction with different substrates and exhibit different interaction with the biological environment.

## 3.4. Experimental section

Hereafter are reported the experimental procedures for the synthesis of the studied silver nanoparticles. Specifically, hydroxyethyl cellulose capped silver nanoparticles, curcumin capped silver nanoparticles and sodium surfactin capped silver nanoparticles.

Syntheses are followed by the main techniques, instrumentations, and parameters adopted for the physicochemical characterization of the colloidal suspension obtained.

Finally, are reported the antimicrobial, both antibacterial and antiviral, tests used for the evaluation of the activity of the samples.

### 3.4.1. Synthesis of hydroxyethyl cellulose capped silver nanoparticles

The AgNPs synthesis starts from silver nitrate (CAS Number 7761-88-8) from Sigma-Aldrich (Product Number 209139, purity ≥ 99.0 %) as silver precursor. First, quaternized hydroxyethyl cellulose (CAS Number 68610-92-4, SoftCAT Polymer SL-30 from The Dow Chemical Company) is dispersed in Milli-Q water (electrical resistivity ≥ 18.2 MΩ·cm at 25 °C and a total organic carbon, TOC, value below 5 ppb) by mechanical stirring, 300 rpm, at room temperature (25 °C). Subsequently, 0.2 M $AgNO_3$ solution is mixed to the polymer suspension by mechanical stirring, 300 rpm. Finally, to activate the reduction reaction of silver ions to metallic silver, 1 M NaOH solution is added to the batch mechanically stirred, 300 rpm. Sodium hydroxide (CAS Number 1310-73-2) anhydrous pellets purchased from Sigma-Aldrich (Product Number S5881, purity ≥ 98 %) was used as basic initiator of the reaction. Immediately after the NaOH addition the suspension color change from off-white to brown and the viscosity increases noticeably, the stirring speed is increased to 500 rpm for 5 minutes. After that, the product is aged by storing it in dark conditions at room temperature for 48 hours promoting the total silver conversion and the gel reorganization into a lower viscosity highly concentrated suspension (5000 $mg \cdot L^{-1}$). The synthesis is finished and the product can be stored at 4 °C in dark conditions up to 1 year.

A typical synthesis of HEC coated AgNPs (AgHEC) is conducted at room temperature processing 500 mL of sample to obtain a theoretical final concentration of silver of 0.5 %wt. With this purpose, 24.51 g of HEC are dispersed in 305 mL of Milli-Q water, first 125 mL of 0.2 M $AgNO_3$, and then 70 mL of 1 M NaOH are added to the suspension.

### 3.4.2. Synthesis of curcumin capped silver nanoparticles

AgCur syntheses were executed using silver nitrate (CAS Number 7761-88-8) from Sigma-Aldrich (Product Number 209139, purity ≥ 99.0 %) as silver precursor, sodium hydroxide (CAS Number 1310-73-2) from Sigma-Aldrich (Product Number S5881, purity ≥ 98 %) as basic initiator of the reaction, and curcumin (CAS Number 458-37-7) from Sigma-Aldrich (Product Number C1386, purity ≥ 65 %) as reducing and capping agent. The synthesis is performed at 70 °C thanks to microwave heating (Microsynth Plus, Milestone) with reflux.[181]

A typical synthesis of AgCur involves a volume of 170 mL with a theoretical silver concentration of 0.5 %wt. 0.5511 g of curcumin are dissolved in 150 mL of 0.089 M NaOH solution. Within the microwave oven, the reaction mix, kept under magnetic stirring, is heated up to 70 °C with a heating ramp of 5 minutes and a maximum power of 300 W. Once the set point temperature is reached, 20 mL of 0.44 M $AgNO_3$ are added and the reaction mix is stirred at 70 °C for 2 minutes with a maximum power of 150 W. The reaction is quenched in an ice bath and the product can be stored at 4 °C in dark conditions for up to 6 months.

Further investigations have been carried out, hydroalcoholic mixture in different water-ethanol (ethanol CAS Number 64-17-5 from Sigma Aldrich Product Number 32221-M, purity ≥ 99.8 %) ratios were used as reaction environment to favor the difficult solubilization of curcumin in water, and additional capping agent were tested such as polyvinylpyrrolidone (CAS Number 9003-39-8 from Sigma-Aldrich Product Number 234257, average molecular weight ≈ 29000) or casein hydrolysate (CAS Number 91079-40-2 from Sigma-Aldrich Product Number 22090), in particular casein micelles can form fluorescent complex with curcumin which could be useful to track the NPs during the application and characterization.

### 3.4.3. Synthesis of sodium surfactin capped silver nanoparticles

The synthesis of sodium surfactin capped silver nanoparticles (AgSur) was carried out using (CAS Number 7761-88-8) from Sigma-Aldrich (Product Number 209139, purity ≥ 99.0 %) as silver precursor, sodium hydroxide (CAS Number 1310-73-2) from Sigma-Aldrich (Product Number S5881, purity ≥ 98 %) as basic initiator of the reaction, and sodium surfactin was provided by AmbrosiaLab, a research spinoff of the University of Ferrara, (white to off-white powder, purity ≥ 99.0 %) as capping agent. The syntheses were performed at room temperature, under magnetic stirring, and using Milli-Q water as reaction environment.

A typical synthesis of AgSur involves a volume of 30 mL with a theoretical silver concentration of 0.5 %wt. 0.6 g of sodium surfactin are dispersed in 25.95 mL of Milli-Q water under magnetic stirring (300 rpm). Subsequently 1.05 mL of 1 M NaOH are added. Finally, 3 mL of 0.5 M $AgNO_3$ solution are added to the reaction mixture, the suspension immediately changes color from transparent to brown, revealing the formation of AgNPs. The batch is stirred for 10 minutes, then the reaction is finished and the product can be stored in dark conditions at 4 °C for up to 3 months.

### 3.4.4. Physicochemical characterization of silver nanoparticles

The most important colloidal parameter monitored for the samples synthesized are: hydrodynamic diameter, zeta potential, pH, UV-Vis adsorption, silver total and ionic form concentrations, crystalline structure and size by XRD, and particle size by TEM.

***Hydrodynamic diameter*** – The measurement of the hydrodynamic diameter was performed by through dynamic light scattering (DLS) technique. DLS is based on the scattering of a monochromatic and coherent light source, laser, that invest a colloidal suspension. It is a non-destructive and non-invasive technique based on the assumption that the speed of each particle subject to random Brownian motion is correlated to their dimensions. Smaller particles move faster and bigger particles are slower. The instrument considers the diameter of the whole kinetic unit in motion, including the particles, eventual species adsorbed on the surface such as stabilizing agents, and the surrounding coordination sphere. The electrical double layer surrounding the particles is susceptible to the ionic strength of the media, a high conductivity induces a shrinkage of the double layer which reflects to a smaller hydrodynamic diameter and vice versa.

The theoretical fundaments of the technique are temporal correlation functions, where the correlation decays over time due to the particles motion. The correlation decrease exponentially until there is no correlation at all between the starting and final state. As said, smaller particles move faster and the correlation decays faster, vice versa for larger particles. Since the instrument analyze the diffusion of the particles, it is possible to calculate the hydrodynamic diameter ($\varphi_h$) from the Stokes-Einstein equation, Equation 3, using the translational diffusion coefficient (D) measured, knowing the Boltzmann's constant (k), temperature (T), and the viscosity ($\eta$).[182]

$$\varphi_h = \frac{k \cdot T}{3 \cdot \pi \cdot \eta \cdot D} \qquad \text{Equation 3}$$

The used instrument was the Zetasizer Nano ZSP (Malvern Panalytical) equipped with MPT-2 multipurpose titrator and vacuum degasser accessories. The instrument operates with an incident laser characterized by a wavelength of 633 nm and it detects the back-scattered radiation at a working angle of 173 °, in this way multiple scattering problems are avoided or limited. The range of detection moves from 0.4 nm to 10 μm. Analysis were conducted at 25 °C, in aqueous media, water viscosity 0.8872 cP, and refractive index 1.330. The parameter adopted for silver nanoparticles are: refractive index 1.520 and absorption coefficient 0.1.

The typical sample was diluted 1:100 by weight in Milli-Q water, starting from the reaction product which is a concentrated suspension of silver nanoparticles ≈ 0.5 %wt in silver that correspond to ≈ 5000 $mg \cdot L^{-1}$, obtaining a final concentration in silver of ≈ 50 $mg \cdot L^{-1}$.
Hydrodynamic diameter average value and distribution profile were assessed, together with the polydispersity index (PDI). PDI ranges from 0-1 values where 0 corresponds to a perfectly uniform and monodispersed sample and 1 to a highly polydisperse sample. General polydispersity ranges are reported in the Table 35.[183]

*Table 35 – Polydispersity index range correspondence with the polydispersity classification.*

| Polydispersity index range | Polydispersity classification |
|---|---|
| < 0.2 | Monodisperse |
| 0.2-0.6 | Moderate polydispersity |
| > 0.6 | High polydispersity |

***Zeta potential*** – The zeta potential is the electrical potential measured at the slipping plane of the electrical double layer surrounding particles in colloidal suspensions. It represents the electrical potential at the interface between the ions and molecules attached to the surface and the mobile fluid. Zeta potential is an important indicator of the colloidal stability, the higher is its absolute value the stronger is the electrostatic repulsion between particles leading to a better stability. In the following Table 36 are reported the typical stability labels associated with the zeta potential values.[184]

*Table 36 – Zeta potential ranges correspondence to the electrostatic stabilization of the colloidal suspension.*

| Zeta potential range (mV) | Stability behavior |
|---|---|
| 0 to ± 5 | Rapid coagulation or flocculation |
| ± 10 to ± 30 | Incipient stability |
| ± 30 to ± 40 | Moderate stability |
| ± 40 to ± 60 | Good stability |
| > ± 60 | Excellent stability |

Zeta potential is measured via electrophoretic light scattering (ELS), the working principles are the same as for the dynamic light scattering, but in this case particles motion is due to the application of an electric field instead of being the random Brownian motion. Electrophoretic mobility ($U_e$) is monitored similarly to the diffusion coefficient for DLS, then, thanks to the

Henry equation, reported as Equation 4, it is correlated to the zeta potential (Z), the dielectric constant (ε), the viscosity (η), and the Henry function (f[ka]).[185]

$$U_e = \frac{2 \cdot \varepsilon \cdot Z \cdot f[ka]}{3 \cdot \eta} \qquad \text{Equation 4}$$

The used instrument was the Zetasizer Nano ZSP (Malvern Panalytical) equipped with MPT-2 multipurpose titrator and vacuum degasser accessories. The instrument operates with an incident laser characterized by a wavelength of 633 nm and it detects the back-scattered radiation at a working angle of 173 °, in this way multiple scattering problems are avoided or limited. Analysis were conducted at 25 °C, in aqueous media, water viscosity 0.8872 cP, refractive index 1.330, and dielectric constant 78.5. The parameter adopted for silver nanoparticles are: refractive index 1.520 and absorption coefficient 0.1. For f[ka] Smoluchowski model was adopted.
The typical sample was diluted 1:100 by weight in Milli-Q water, starting from the reaction product which is a concentrated suspension of silver nanoparticles ≈ 0.5 %wt in silver that correspond to ≈ 5000 mg·L$^{-1}$, obtaining a final concentration in silver of ≈ 50 mg·L$^{-1}$. Thanks to the automatic titrator it was possible to perform zeta potential titration as pH function, to assess the stability of colloidal samples at different pH and to identify the isoelectric point (IEP) which is the pH value that correspond to zeta potential 0.00 mV and the maximum of instability of the system. Titration required about 10 mL of sample diluted ≈ 50 mg·L$^{-1}$ and were performed using 0.1 M and 0.01 M HCl for acidic titrations or 0.1 M and 0.01 M NaOH for basic titrations. The pH was constantly monitored with the instrument's pH-meter MV 114-SC SEN 0106.

***UV-Vis spectroscopy*** – To analyze the typical absorption peak of silver nanoparticles in the visible region around 400 nm, a Lambda 750 spectrophotometer (PerkinElmer) was used. Silver nanoparticles absorb in visible due to surface plasmon resonance (SPR) phenomenon, variation in size and morphology may influence the shape and maximum of the absorption peak.
UV-Vis spectroscopy was used after syntheses to verify whether silver nanoparticles were obtained or not. To avoid detector saturation, reaction products ≈ 0.5 %wt in silver were diluted from 1:100 to 1:800 by weight in Milli-Q water. Absorbance measures were conducted in a wavelength range explored of 250-800 nm, with a measuring step of 1 nm.

***Nanoparticle and ionic silver fractions quantification by ICP-OES*** – Inductively coupled plasma – optical emission spectroscopy (ICP-OES) was used for the quantification of the

concentration of silver in the post-reaction products. The instrument, Agilent 5100 ICP-OES with mounted the autosampler Agilent SPS 3 (Agilent Technologies), uses argon plasma powered by a 27 MHz radio frequency generator, reaching temperature up to 6000-10000 °C. Working at high temperature, elements present in the samples have enough energy to reach exited states, when electrons drop back to the ground state a specific wavelength energy emission occurs. Each element has its own characteristic spectrum collected by as spectrometer in the range 170-800 nm, in the case of silver the wavelength analyzed are: 224.641, 241.318, 328.068, and 338.289 nm. The last two wavelength reported, 328 and 338 nm, are the strongest signal for silver and are the most reliable since they are easier to be recognized from the background or interferences. To assess a quantitative analysis, a calibration curve is required, a typical calibration curve for silver is prepared starting from the certified reference material ICP standard 1000 $mg \cdot L^{-1}$ Ag in 2 %wt $HNO_3$ (CPAchem) and diluted to 100, 10, 1, and 0.1 $mg \cdot L^{-1}$. The internal calibration verification (ICV) is prepared at the same concentration as the samples to be analyzed, usually 5 $mg \cdot L^{-1}$, starting from the certified reference material multielement standard solution 5 for ICP (Sigma-Aldrich) 10 $mg \cdot L^{-1}$ Ag in 10 %wt $HNO_3$ matrix. Blank, not containing the analyte, ICV, and the calibration curve are prepared using the same matrix as the sample and the same digestion protocol. For the silver quantification, samples were diluted 1:1000 by weight reaching a concentration of about 5 $mg \cdot L^{-1}$, then they were acidic digested adding a 10 %v/v of ≥ 65 %wt $HNO_3$ (Sigma-Aldrich) and a 10 %v/v of 30 %wt $H_2O_2$ (Sigma-Aldrich), for example to a 10 mL volume of sample were added 1 mL of $HNO_3$ and 1 mL of $H_2O_2$. Sodium surfactin capped silver nanoparticles (AgSur) require a specific digestion protocol, a microwave-assisted acidic digestion was used of these samples. 0.5 mL of sample were treated with 2 mL of ≥ 65 %wt $HNO_3$ (Sigma-Aldrich) and a 1 mL of 30 %wt $H_2O_2$ (Sigma-Aldrich) and then placed in the microwave digestion platform Multiwave 5000 (Anton Paar) to undergo the following temperature profile, also reported in the graph in Figure 65: starting from room temperature it takes 5 minutes to reach 120 °C, samples stays at 120 °C for 2 minutes, then during a 10 minutes ramp they reach 210 °C, finally there is an isotherm segment at 210 °C for 15 minutes, after that the samples are cooled at room temperature.

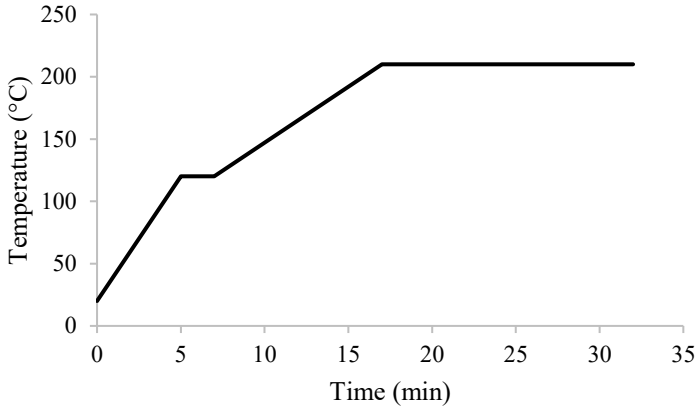


*Figure 65 – Microwave thermal profile of the microwave-assisted acidic digestion of sodium surfactin-capped nanoparticles as pretreatment of the ICP-OES analysis.*

Total silver concentration was assessed on the samples diluted 1:1000 by weight. The silver ionic fraction was determined removing AgNPs by filtration. Samples diluted 1:100 by weight were filtered by Amicon Ultra-15 centrifugal filter (Millipore) with a filtering membrane of regenerated cellulose and a 10 kDa molecular weight cut-off (MWCO) also labeled as nominal molecular weight limit (NMWL). The filtration is performed via centrifugation 4500 rpm, 45 minutes, and 20 °C using a Centrisart G-16C (Sartorius). AgNPs are retained by the filtering membrane, while the aqueous media and dissolved silver ions pass through, filtered aliquot were digested as previously described before being analyzed by ICP-OES.

***Crystalline structure and size by XRD spectroscopy*** – The instrument used for the determination of the x-ray diffraction (XRD) pattern of the nanoparticles synthesized is the D8 ADVANCE (Bruker) operating in 2θ mode and using a copper target (Cu Kα, λ = 0.15406 nm). The selected working conditions are 10-80 ° 2θ range, acquiring the signal every 0.02 ° step, and acquisition time of 0.5 seconds. The phase recognition qualitative analysis is based on the Bragg's law, which is reported in Equation 5, it correlates the distance d between successive lattice planes of the sample, the wavelength of the incident radiation λ comparable to atomic spacings in the lattice, the glancing angle θ where the reflection is possible, and the diffraction order n which is a positive natural number. The diffraction pattern is the result of the collection of the intensity of the scattered radiation as function of the scattered angle.[186]

$$n \cdot \lambda = 2 \cdot d \cdot \sin\theta \qquad \text{Equation 5}$$

The estimation of the crystallite size from the XRD spectrum was performed applying Scherrer's equation, reported as Equation 6. In Scherrer's equation, τ is the average size of the crystallite which may be smaller or equal to the particle size, K is a shape factor, usually it assumes value of about 0.9 for spheroidal particles, λ is the wavelength of the incident x-rays, β represent the full width at half maximum (FWHM) of the analyzed peak, and θ is the Bragg angle.[187]

$$\tau = \frac{K \cdot \lambda}{\beta \cdot \cos\theta} \qquad \text{Equation 6}$$

To analyze the colloidal suspensions, a thin and homogeneous layer of silver nanoparticles was deposited by drop-casting on a glass substrate. Depending on the viscosity of the sample, concentrated ≈ 5000 mg·L$^{-1}$ or diluted ≈ 500 mg·L$^{-1}$ suspension were deposited. Droplets were dried in oven at 70 °C, if the coating was not thick or homogenous enough, the drop-casting process was repeated 2-5 times.

***Particle size by TEM*** – Morphological evaluation and particle size determination were assessed by transmission electron microscopy (TEM) using a Tecnai F20 (FEI) microscope operating at 200 keV. The instrument is equipped with an energy dispersive x-ray spectroscopy (EDX) micro-analysis and the scanning transmission electron microscopy (STEM) accessories. The TEM images were taken in phase contrast mode, high-resolution transmission electron microscopy (HRTEM), and selected area electron diffraction (SAED). STEM pictures were recorded using a high angle annular dark field (HAADF) detector.
The sample preparation involves a solution dilution 1:100 in volume in Milli-Q water and sonication for 10 minutes, then the sample is deposited on a holey carbon film supported copper grid. The preparation was then dried at 80 °C.

### 3.4.5. Functional characterization of silver nanoparticles

***Antibacterial tests in sol phase*** – Sol phase antibacterial tests were carried out by the certified laboratory Chimicambiente (Vicenza, Italy) in compliance with UNI EN 1040:2005 standardized method "Quantitative suspension test for the evaluation of basic bactericidal activity of chemical disinfectants and antiseptics" against *Escherichia coli* (ATCC 10536) and *Staphylococcus aureus* (ATCC 6538). Incubation temperature 37 °C, test temperature 20 ± 1 °C, and contact time 24 hours. For these samples, 4 dilutions were considered in the concentration range 10-0.05 $mg \cdot L^{-1}$. The most effective samples were explored at 50 $mg \cdot L^{-1}$ as well. Each result is the average of three independent measurements. Blanks solutions were considered as comparison. Results were expressed as logarithmic bacterial viability reduction.

***Antiviral tests in sol phase*** – The antiviral tests on silver nanoparticles and their blanks were performed by the Università degli Studi di Milano La Statale.
SARS-CoV-2 was isolated from 500 µl of a COVID19 patient's nasal-pharyngeal swab, added to Vero E6 cells at 80% confluence. The inoculum was removed after a 3 hours incubation at 37 °C with 5% $CO_2$ and the cells were incubated at 37 °C, 5% $CO_2$, for 72 hours, when cytopathic effects (CPE) were evident. The quantification of viral replication numbers in the cell supernatant was evaluated via SARS-CoV-2 specific quantitative real-time polymerase chain reaction RT-qPCR.[188] The SARS-CoV-2 titer was determined by plaque assay, using dilution factors ranging from $10^1$ to $10^9$. The sequencing of the complete genome was performed and submitted to Gen Bank. The virus was used at a multiplicity of infection (MOI) of 0.05 in subsequent experiments.

***Vero E6 cells SARS-CoV-2 infection*** – Vero E6 cells were seeded into 96-well plates at a density of $1.3 \cdot 10^4$ cells·well$^{-1}$ and were incubated for 24 hours at 37 °C and 5% $CO_2$. Cells were then infected with SARS-CoV-2 at a multiplicity of infection (MOI) of 0.05 (1000 PFU·well$^{-1}$) and incubated for 2 hours at 37 °C and 5% $CO_2$. Virus inoculum was removed and infected the cells were incubated in a medium for 48 hours at 37 °C and 5% $CO_2$.

***Vero E6 cells BK polyomavirus infection*** – The cells were infected using $10^8$ virions corresponding to $4 \cdot 10^6$ virus DNA copies·mL$^{-1}$ (calculated by means of RT-PCR) of BK polyomavirus archetype (WW) strain stock, purchased at ATCC® (VR-837). The day before the infection, $1.3 \cdot 10^4$ cells were plated in a six well plate. On day 0, the cells (which reached 70% confluence) were washed twice with Dulbecco's phosphate-buffered saline w/o calcium and magnesium (DPBS; Euroclone, Italy). Then the virus stock, diluted with specific serum-free culture medium, was added to the flask. The cells were held at 37 °C for 90 minutes. Then, the inoculum was removed, the cells were washed with DPBS to eliminate the unbound virus, and the complete medium was added and the infection lasted 72 hours, at 37 °C and 5% $CO_2$.

***Vero E6 cells infected by virus previously treated by AgNPs*** – To verify the mechanism of antiviral activity of the compounds: The virus, at a MOI of 0.05, was incubated for 1 h in presence of different concentrations of AgNPs suspensions, and then added to the cell monolayer for 2 hours at 37 °C and 5% $CO_2$. After the removal of the virus inoculum, a complete medium was added to the cells, that were incubated for 48 hours at 37 °C and 5% $CO_2$. The test was performed in triplicate.

***Evaluation of the antiviral and virucidal activity of AgNPs suspensions*** – The quantification of the viral copy numbers in the cell supernatant was evaluated via specific quantitative real-time polymerase chain reaction RT-qPCR, targeting the N1 SARS-CoV-2 gene, or the VP1 BK polyomavirus gene after the isolation of RNA for SARS-CoV-2 or DNA for BK polyomavirus from the cell supernatants.[188] Results were expressed as the percentage of viral replication, compared to the infected untreated cells (100%). The virucidal activity of AgNPs suspensions was evaluated by Plaque Reduction Assay. Vero E6 cells were seeded in six-well plates (400.000 cells·well$^{-1}$) for 24 hours at 37°C. Viral particles were treated with different concentration of AgNPs for 1h, and then added to the wells for 2 hours at 37°C. After removal of virus inoculum, the cells were overlaid with 0.3% agarose dissolved in cell medium at 37°C for 48 hours. Cells were fixed with 4% formaldehyde solution, and following the overlay medium removal, were stained with methylene blue to visualize plaques in the confluent cell monolayer. The plaques were counted and the results were reported as PFU·mL$^{-1}$ and as percentage of virus replication, compared to untreated infected cells.

***Evaluation of cytotoxic concentration ($CC_{50}$), inhibition concentration ($IC_{50}$) and selectivity index (SI) of selected AgNPs*** – For the cytotoxicity assay, cells were seeded into 96-well plates at concentration of $1 \cdot 10^4$ cells·well$^{-1}$. After 24 hours of incubation, the cells were treated with serial 2-fold dilutions of AgNPs suspensions in duplicate. After incubation for 48 hours at 37 °C and 5% $CO_2$, cell viability was measured by MTT assay. The percentage of viable cells was calculated using untreated cells as control (100% viability) using the formula reported in Equation 7.[155]

$$\frac{(\text{Sample absorbance} - \text{Cell free sample blank})}{\text{Mean media control absorbance}} \cdot 100 \qquad \text{Equation 7}$$

The morphological changes of Vero E6 cells were also observed by light microscopy. The 50% cytotoxic concentration ($CC_{50}$) causing 50% reduction of Vero E6 cells viability with respect to untreated control cells was determined using Gene5 software. The 50% antiviral activity ($IC_{50}$) causing 50% reduction of SARS-CoV-2 replication with respect to untreated control infected cells was determined using Gene5 software. The Selectivity Index was calculated as $CC_{50} \cdot IC_{50}^{-1}$ ratio.

## 3.5. References


49. Salleh A, Naomi R, Utami ND, Mohammad AW, Mahmoudi E, Mustafa N, Fauzi MB. The Potential of Silver Nanoparticles for Antiviral and Antibacterial Applications: A Mechanism of Action. Nanomaterials (Basel). 2020 Aug 9;10(8):1566. doi: 10.3390/nano10081566. PMID: 32784939; PMCID: PMC7466543.
50. Devnarain N, Osman N, Fasiku VO, et al. Intrinsic stimuli-responsive nanocarriers for smart drug delivery of antibacterial agents—An in-depth review of the last two decades. WIREs Nanomed Nanobiotechnol. 2021; 13:e1664. https://doi.org/10.1002/wnan.1664
51. Motta, G.; Gualtieri, M.; Saibene, M.; Bengalli, R.; Brigliadori, A.; Carrière, M.; Mantecca, P. Preliminary Toxicological Analysis in a Safe-by-Design and Adverse Outcome Pathway-Driven Approach on Different Silver Nanoparticles: Assessment of Acute Responses in A549 Cells. Toxics 2023, 11, 195. https://doi.org/10.3390/toxics11020195.
52. Zielińska, A.; Costa, B.; Ferreira, M.V.; Miguéis, D.; Louros, J.M.S.; Durazzo, A.; Lucarini, M.; Eder, P.; V. Chaud, M.; Morsink, M.; et al. Nanotoxicology and Nanosafety: Safety-by-Design and Testing at a Glance. Int. J. Environ. Res. Public Health 2020, 17, 4657. https://doi.org/10.3390/ijerph17134657.
53. Sánchez-López, E.; Gomes, D.; Esteruelas, G.; Bonilla, L.; Lopez-Machado, A.L.; Galindo, R.; Cano, A.; Espina, M.; Ettcheto, M.; Camins, A.; et al. Metal-Based Nanoparticles as Antimicrobial Agents: An Overview. Nanomaterials 2020, 10, 292. https://doi.org/10.3390/nano10020292.
54. C.A. Ottoni, M.C. Lima Neto, P. Léo, B.D. Ortolan, E. Barbieri, A.O. De Souza, Environmental impact of biogenic silver nanoparticles in soil and aquatic organisms, Chemosphere, Volume 239, 2020, 124698, ISSN 0045-6535, https://doi.org/10.1016/j.chemosphere.2019.124698.
55. Teixeira, M.C.; Carbone, C.; Sousa, M.C.; Espina, M.; Garcia, M.L.; Sanchez-Lopez, E.; Souto, E.B. Nanomedicines for the Delivery of Antimicrobial Peptides (AMPs). Nanomaterials 2020, 10, 560. https://doi.org/10.3390/nano10030560.
56. Franci G, Falanga A, Galdiero S, Palomba L, Rai M, Morelli G, Galdiero M. Silver nanoparticles as potential antibacterial agents. Molecules. 2015 May 18;20(5):8856-74. doi: 10.3390/molecules20058856. PMID: 25993417; PMCID: PMC6272636.
57. Stefania Marin et al. Applications and Toxicity of Silver Nanoparticles: A Recent Review. Volume 15, Issue 16, 2015, 1596-1604. DOI: 10.2174/1568026615666150414142209.

58. Diniz, F.R.; Maia, R.C.A.P.; de Andrade, L.R.M.; Andrade, L.N.; Vinicius Chaud, M.; da Silva, C.F.; Corrêa, C.B.; de Albuquerque Junior, R.L.C.; Pereira da Costa, L.; Shin, S.R.; et al. Silver Nanoparticles-Composing Alginate/Gelatine Hydrogel Improves Wound Healing In Vivo. Nanomaterials 2020, 10, 390. https://doi.org/10.3390/nano10020390.

59. Hissae Yassue-Cordeiro, P.; Henrique Zandonai, C.; Pereira Genesi, B.; Santos Lopes, P.; Sanchez-Lopez, E.; Luisa Garcia, M.; Regina Camargo Fernandes-Machado, N.; Severino, P.; B. Souto, E.; Ferreira da Silva, C. Development of Chitosan/Silver Sulfadiazine/Zeolite Composite Films for Wound Dressing. Pharmaceutics 2019, 11, 535. https://doi.org/10.3390/pharmaceutics11100535.

60. Gustavo P. Barbosa, Henrique S. Debone, Patrícia Severino, Eliana B. Souto, Classius F. da Silva, Design and characterization of chitosan/zeolite composite films — Effect of zeolite type and zeolite dose on the film properties, Materials Science and Engineering: C, Volume 60, 2016, Pages 246-254, ISSN 0928-4931, https://doi.org/10.1016/j.msec.2015.11.034.

61. Liuya Wei, Jingran Lu, Huizhong Xu, Atish Patel, Zhe-Sheng Chen, Guofang Chen, Silver nanoparticles: synthesis, properties, and therapeutic applications, Drug Discovery Today, Volume 20, Issue 5, 2015, Pages 595-601, ISSN 1359-6446, https://doi.org/10.1016/j.drudis.2014.11.014.

62. Zielińska A, Costa B, Ferreira MV, Miguéis D, Louros JMS, Durazzo A, Lucarini M, Eder P, Chaud MV, Morsink M, Willemen N, Severino P, Santini A, Souto EB. Nanotoxicology and Nanosafety: Safety-By-Design and Testing at a Glance. Int J Environ Res Public Health. 2020 Jun 28;17(13):4657. doi: 10.3390/ijerph17134657. PMID: 32605255; PMCID: PMC7369733.

63. Loiseau A, Asila V, Boitel-Aullen G, Lam M, Salmain M, Boujday S. Silver-Based Plasmonic Nanoparticles for and Their Use in Biosensing. Biosensors (Basel). 2019 Jun 10;9(2):78. doi: 10.3390/bios9020078. PMID: 31185689; PMCID: PMC6627098.

64. Bryan Calderón-Jiménez et al, Silver Nanoparticles: Technological Advances, Societal Impacts, and Metrological Challenges. Front. Chem., 21 February 2017, Sec. Green and Sustainable Chemistry, Volume 5 – 2017. https://doi.org/10.3389/fchem.2017.00006.

65. Liao, C.; Li, Y.; Tjong, S.C. Bactericidal and Cytotoxic Properties of Silver Nanoparticles. Int. J. Mol. Sci. 2019, 20, 449. https://doi.org/10.3390/ijms20020449.

66. Zielińska A, Costa B, Ferreira MV, Miguéis D, Louros JMS, Durazzo A, Lucarini M, Eder P, Chaud MV, Morsink M, Willemen N, Severino P, Santini A, Souto EB. Nanotoxicology and Nanosafety: Safety-By-Design and Testing at a Glance. Int J Environ

Res Public Health. 2020 Jun 28;17(13):4657. doi: 10.3390/ijerph17134657. PMID: 32605255; PMCID: PMC7369733.

67. Ge L, Li Q, Wang M, Ouyang J, Li X, Xing MM. Nanosilver particles in medical applications: synthesis, performance, and toxicity. Int J Nanomedicine. 2014 May 16;9:2399-407. doi: 10.2147/IJN.S55015. PMID: 24876773; PMCID: PMC4037247.
68. Tang S, Zheng J. Antibacterial Activity of Silver Nanoparticles: Structural Effects. Adv Healthc Mater. 2018 Jul;7(13):e1701503. doi: 10.1002/adhm.201701503. Epub 2018 May 29. PMID: 29808627.
69. Morones JR, Elechiguerra JL, Camacho A, Holt K, Kouri JB, Ramírez JT, Yacaman MJ. The bactericidal effect of silver nanoparticles. Nanotechnology. 2005 Oct;16(10):2346-53. doi: 10.1088/0957-4484/16/10/059. Epub 2005 Aug 26. PMID: 20818017.
70. Almatroudi, Ahmad. "Silver nanoparticles: synthesis, characterisation and biomedical applications" Open Life Sciences, vol. 15, no. 1, 2020, pp. 819-839. https://doi.org/10.1515/biol-2020-0094.
71. Salleh A, Naomi R, Utami ND, Mohammad AW, Mahmoudi E, Mustafa N, Fauzi MB. The Potential of Silver Nanoparticles for Antiviral and Antibacterial Applications: A Mechanism of Action. Nanomaterials (Basel). 2020 Aug 9;10(8):1566. doi: 10.3390/nano10081566. PMID: 32784939; PMCID: PMC7466543.
72. Marassi V, Di Cristo L, Smith SGJ, Ortelli S, Blosi M, Costa AL, Reschiglian P, Volkov Y, Prina-Mello A. Silver nanoparticles as a medical device in healthcare settings: a five-step approach for candidate screening of coating agents. R Soc Open Sci. 2018 Jan 31;5(1):171113. doi: 10.1098/rsos.171113. PMID: 29410826; PMCID: PMC5792903.
73. Suresh Kumar Kailasa, Dharaben J. Joshi, Mehul R. Kateshiya, Janardhan Reddy Koduru, Naved I. Malek, Review on the biomedical and sensing applications of nanomaterial-incorporated hydrogels, Materials Today Chemistry, Volume 23, 2022, 100746, ISSN 2468-5194, https://doi.org/10.1016/j.mtchem.2021.100746.
74. Navajas, A.; Uriarte, L.; Gandía, L.M. Application of Eco-Design and Life Cycle Assessment Standards for Environmental Impact Reduction of an Industrial Product. Sustainability 2017, 9, 1724. https://doi.org/10.3390/su9101724.
75. Khan, N., Jhariya, M.K., Raj, A., Banerjee, A., Meena, R.S. (2021). Soil Carbon Stock and Sequestration: Implications for Climate Change Adaptation and Mitigation. In: Jhariya, M.K., Meena, R.S., Banerjee, A. (eds) Ecological Intensification of Natural Resources for Sustainable Agriculture . Springer, Singapore. https://doi.org/10.1007/978-981-33-4203-3_13.

76. Krishna N. Ganesh et al. Green Chemistry: A Framework for a Sustainable Future. Environ. Sci. Technol. Lett. 2021, 8, 7, 487–491. https://doi.org/10.1021/acs.estlett.1c00434.
77. Sharma, S.K., & Mudhoo, A. (Eds.). (2010). Green Chemistry for Environmental Sustainability (1st ed.). CRC Press. https://doi.org/10.1201/EBK1439824733.
78. Abdussalam-Mohammed, W., Ali, A.Q., & Errayes, A.O. (2020). Green Chemistry: Principles, Applications, and Disadvantages. Chemical Methodologies.
79. Transforming our world: the 2030 Agenda for Sustainable Development. https://sustainabledevelopment.un.org/content/documents/21252030%20Agenda%20for%20Sustainable%20Development%20web.pdf?source=patrick.net.
80. Siddi Marco. The European Green Deal: Asseasing its current state and future implementation. 2020. https://hdl.handle.net/11584/313484.
81. Vanýsek, Petr. "ELECTROCHEMICAL SERIES." (2010).
82. Tang S, Zheng J. Antibacterial Activity of Silver Nanoparticles: Structural Effects. Adv Healthc Mater. 2018 Jul;7(13):e1701503. doi: 10.1002/adhm.201701503. Epub 2018 May 29. PMID: 29808627.
83. Chen L, Liang J. An overview of functional nanoparticles as novel emerging antiviral therapeutic agents. Mater Sci Eng C Mater Biol Appl. 2020 Jul;112:110924. doi: 10.1016/j.msec.2020.110924. Epub 2020 Apr 6. PMID: 32409074; PMCID: PMC7195146.
84. Ke-Xin Huang, Ling-Yue Zhou, Jia-Qi Chen, Na Peng, Hong-Xiang Chen, Hua-Zhi Gu, Tao Zou, Applications and perspectives of quaternized cellulose, chitin and chitosan: A review, International Journal of Biological Macromolecules, Volume 242, Part 3, 2023, 124990, ISSN 0141-8130, https://doi.org/10.1016/j.ijbiomac.2023.124990.
85. Ilya Shlar et al. The mode of antimicrobial action of curcumin depends on the delivery system: monolithic nanoparticles vs. supramolecular inclusion complex. RSC Adv., 2017,7, 42559-42569. https://doi.org/10.1039/C7RA07303H.
86. Cheng Zhen, Xian-Feng Ge, Yi-Ting Lu, Wen-Zheng Liu. Chemical structure, properties and potential applications of surfactin, as well as advanced strategies for improving its microbial production[J]. AIMS Microbiology, 2023, 9(2): 195-217. doi: 10.3934/microbiol.2023012.
87. Chen X, Lu Y, Shan M, Zhao H, Lu Z, Lu Y. A mini-review: mechanism of antimicrobial action and application of surfactin. World J Microbiol Biotechnol. 2022 Jun 20;38(8):143. doi: 10.1007/s11274-022-03323-3. PMID: 35718798.

88. A. L. Costa, M.Blosi, WO 2016125070A1- Process for the preparation of nanoparticles of noble metals in hydrogel and nanoparticles thus obtained.
89. Technologies, Products, and Product Development for the Personal Care Industry, Amerchol Corporation (a subsidiary of The Dow Chemical Company), Form No. 324-00009-0405 AMS, April 2005.
90. Amerchol web site: Products Functional Overview: Conditioning Polymers: http://www.dow.com/ucc/amerchol/overview/con_poly.htm.
91. SoftCAT™ Polymer SX-400H Safety Data Sheet, Dow Chemical Company Ltd., June 26, 2007.
92. SoftCAT SX Conditioning Polymers, Amerchol Corporation (a subsidiary of The Dow Chemical Company), Form No. 324-00265-0407 AMS, April 2007.
93. Alfei S, Schito AM. Positively Charged Polymers as Promising Devices against Multidrug Resistant Gram-Negative Bacteria: A Review. Polymers (Basel). 2020 May 23;12(5):1195. doi: 10.3390/polym12051195. PMID: 32456255; PMCID: PMC7285334.
94. Susmila Aparna Gaddam et al, Efficient and robust biofabrication of silver nanoparticles by cassia alata leaf extract and their antimicrobial activity, J Nanostruct Chem (2014) 4:82, DOI 10.1007/s40097-014-0082-5.
95. J. J. Mock, M. Barbic, D. R. Smith, D. A. Schultz, S. Schultz; Shape effects in plasmon resonance of individual colloidal silver nanoparticles. J. Chem. Phys. 15 April 2002; 116 (15): 6755–6759. https://doi.org/10.1063/1.1462610.
96. Panacek A, Kvítek L, Prucek R, Kolar M, Vecerova R, Pizúrova N, Sharma VK, Nevecna T, Zboril R. Silver colloid nanoparticles: synthesis, characterization, and their antibacterial activity. J Phys Chem B. 2006 Aug 24;110(33):16248-53. doi: 10.1021/jp063826h. PMID: 16913750.
97. Zoya Zaheer, Rafiuddin, Silver nanoparticles to self-assembled films: Green synthesis and characterization, Colloids and Surfaces B: Biointerfaces, Volume 90, 2012, Pages 48-52, ISSN 0927-7765, https://doi.org/10.1016/j.colsurfb.2011.09.037.
98. Gopinath, K., Gowri, S. & Arumugam, A. Phytosynthesis of silver nanoparticles using Pterocarpus santalinus leaf extract and their antibacterial properties. J Nanostruct Chem 3, 68 (2013). https://doi.org/10.1186/2193-8865-3-68.
99. Jizhuang Wang et al. ChemInform Abstract: Photochemical Conversion of AgCl Nanocubes to Hybrid AgCl-Ag Nanoparticles with High Activity and Long-Term Stability Towards Photocatalytic Degradation of Organic Dyes. Canadian Journal of Chemistry 90(10):858-864. DOI: 10.1139/v2012-079.

100. Stefanos Mourdikoudis et al. Characterization techniques for nanoparticles: comparison and complementarity upon studying nanoparticle properties. Nanoscale, 2018,10, 12871-12934. https://doi.org/10.1039/C8NR02278J.

101. Holger Borchert et al. Determination of Nanocrystal Sizes: A Comparison of TEM, SAXS, and XRD Studies of Highly Monodisperse $CoPt_3$ Particles. Langmuir 2005, 21, 5, 1931–1936. https://doi.org/10.1021/la0477183.

102. Nadzeya Khinevich, Domantas Peckus, Asta Tamulevičienė, Gerda Klimaitė, Joel Henzie, Tomas Tamulevičius, Sigitas Tamulevičius, Size and crystallinity effect on the ultrafast optical response of chemically synthesized silver nanoparticles, Journal of Materiomics, 2023, ISSN 2352-8478, https://doi.org/10.1016/j.jmat.2023.08.009.

103. Zheng J, Ding Y, Tian B, Wang ZL, Zhuang X. Luminescent and Raman active silver nanoparticles with polycrystalline structure. J Am Chem Soc. 2008 Aug 13;130(32):10472-3. doi: 10.1021/ja803302p. Epub 2008 Jul 18. PMID: 18636722; PMCID: PMC2645914.

104. Li Yixuan, Majjid A. Qaria, Sethupathy Sivasamy, Sun Jianzhong, Zhu Daochen, Curcumin production and bioavailability: A comprehensive review of curcumin extraction, synthesis, biotransformation and delivery systems, Industrial Crops and Products, Volume 172, 2021, 114050, ISSN 0926-6690, https://doi.org/10.1016/j.indcrop.2021.114050.

105. Stati G, Rossi F, Trakoolwilaiwan T, Tung LD, Mourdikoudis S, Thanh NTK, Di Pietro R. Development and Characterization of Curcumin-Silver Nanoparticles as a Promising Formulation to Test on Human Pterygium-Derived Keratinocytes. Molecules. 2022 Jan 3;27(1):282. doi: 10.3390/molecules27010282. PMID: 35011514; PMCID: PMC8746426.

106. Dai, C.; Lin, J.; Li, H.; Shen, Z.; Wang, Y.; Velkov, T.; Shen, J. The Natural Product Curcumin as an Antibacterial Agent: Current Achievements and Problems. Antioxidants 2022, 11, 459. https://doi.org/10.3390/antiox11030459.

107. Morão LG, Polaquini CR, Kopacz M, Torrezan GS, Ayusso GM, Dilarri G, Cavalca LB, Zielińska A, Scheffers DJ, Regasini LO, Ferreira H. A simplified curcumin targets the membrane of Bacillus subtilis. Microbiologyopen. 2019 Apr;8(4):e00683. doi: 10.1002/mbo3.683. Epub 2018 Jul 26. PMID: 30051597; PMCID: PMC6460283.

108. Varshney GK, Saini RK, Gupta PK, Das K. Effect of curcumin on the diffusion kinetics of a hemicyanine dye, LDS-698, across a lipid bilayer probed by second harmonic spectroscopy. Langmuir. 2013 Mar 5;29(9):2912-8. doi: 10.1021/la304778d. Epub 2013

Feb 20. PMID: 23391287.

109. Deryabin D, Galadzhieva A, Kosyan D, Duskaev G. Plant-Derived Inhibitors of AHL-Mediated Quorum Sensing in Bacteria: Modes of Action. Int J Mol Sci. 2019 Nov 8;20(22):5588. doi: 10.3390/ijms20225588. PMID: 31717364; PMCID: PMC6888686.
110. Brackman G, Coenye T. Quorum sensing inhibitors as anti-biofilm agents. Curr Pharm Des. 2015;21(1):5-11. doi: 10.2174/1381612820666140905114627. PMID: 25189863.
111. Ding T, Li T, Li J. Impact of curcumin liposomes with anti-quorum sensing properties against foodborne pathogens Aeromonas hydrophila and Serratia grimesii. Microb Pathog. 2018 Sep;122:137-143. doi: 10.1016/j.micpath.2018.06.009. Epub 2018 Jun 7. PMID: 29885365.
112. Marisol Porto Rocha, Mariana Sousa Santos, Paôlla Layanna Fernandes Rodrigues, Thalita Santos Dantas Araújo, Janeide Muritiba de Oliveira, Luciano Pereira Rosa, Vanderlei Salvador Bagnato, Francine Cristina da Silva, Photodynamic therapry with curcumin in the reduction of enterococcus faecalis biofilm in bone cavity: rMicrobiological and spectral fluorescense analysis, Photodiagnosis and Photodynamic Therapy, Volume 33, 2021, 102084, ISSN 1572-1000, https://doi.org/10.1016/j.pdpdt.2020.102084.
113. Santos CA, Lima EMF, Franco BDGM, Pinto UM. Exploring Phenolic Compounds as Quorum Sensing Inhibitors in Foodborne Bacteria. Front Microbiol. 2021 Sep 14;12:735931. doi: 10.3389/fmicb.2021.735931. PMID: 34594318; PMCID: PMC8477669.
114. Yadav, S., Singh, A.K., Agrahari, A.K. et al. Making of water soluble curcumin to potentiate conventional antimicrobials by inducing apoptosis-like phenomena among drug-resistant bacteria. Sci Rep 10, 14204 (2020). https://doi.org/10.1038/s41598-020-70921-2.
115. Rai D, Singh JK, Roy N, Panda D. Curcumin inhibits FtsZ assembly: an attractive mechanism for its antibacterial activity. Biochem J. 2008 Feb 15;410(1):147-55. doi: 10.1042/BJ20070891. PMID: 17953519.
116. Du S, Lutkenhaus J. At the Heart of Bacterial Cytokinesis: The Z Ring. Trends Microbiol. 2019 Sep;27(9):781-791. doi: 10.1016/j.tim.2019.04.011. Epub 2019 Jun 3. PMID: 31171437; PMCID: PMC6831097.
117. Zheng D, Huang C, Huang H, Zhao Y, Khan MRU, Zhao H, Huang L. Antibacterial Mechanism of Curcumin: A Review. Chem Biodivers. 2020 Aug;17(8):e2000171. doi: 10.1002/cbdv.202000171. Epub 2020 Jul 27. PMID: 32533635.

118. Ghasemi M, Khorsandi K, Kianmehr Z. Photodynamic inactivation with curcumin and silver nanoparticles hinders Pseudomonas aeruginosa planktonic and biofilm formation: evaluation of glutathione peroxidase activity and ROS production. World J Microbiol Biotechnol. 2021 Aug 11;37(9):149. doi: 10.1007/s11274-021-03104-4. PMID: 34379214.

119. Belenky P, Ye JD, Porter CB, Cohen NR, Lobritz MA, Ferrante T, Jain S, Korry BJ, Schwarz EG, Walker GC, Collins JJ. Bactericidal Antibiotics Induce Toxic Metabolic Perturbations that Lead to Cellular Damage. Cell Rep. 2015 Nov 3;13(5):968-80. doi: 10.1016/j.celrep.2015.09.059. Epub 2015 Oct 22. PMID: 26565910; PMCID: PMC4648786.

120. Sandhya A. Marathe et al. Differential Modulation of Intracellular Survival of Cytosolic and Vacuolar Pathogens by Curcumin. Antimicrobial Agents and Chemotherapy 2012 Volume 56 Number 11 p. 5555–5567.

121. Marambio-Jones, C., Hoek, E.M.V. A review of the antibacterial effects of silver nanomaterials and potential implications for human health and the environment. J Nanopart Res 12, 1531–1551 (2010). https://doi.org/10.1007/s11051-010-9900-y.

122. Yang XX, Li CM, Huang CZ. Curcumin modified silver nanoparticles for highly efficient inhibition of respiratory syncytial virus infection. Nanoscale. 2016 Feb 7;8(5):3040-8. doi: 10.1039/c5nr07918g. PMID: 26781043.

123. Hussain, Y.; Alam, W.; Ullah, H.; Dacrema, M.; Daglia, M.; Khan, H.; Arciola, C.R. Antimicrobial Potential of Curcumin: Therapeutic Potential and Challenges to Clinical Applications. Antibiotics 2022, 11, 322. https://doi.org/10.3390/antibiotics11030322.

124. Yana Manolova, Vera Deneva, Liudmil Antonov, Elena Drakalska, Denitsa Momekova, Nikolay Lambov, The effect of the water on the curcumin tautomerism: A quantitative approach, Spectrochimica Acta Part A: Molecular and Biomolecular Spectroscopy, Volume 132, 2014, Pages 815-820, ISSN 1386-1425, https://doi.org/10.1016/j.saa.2014.05.096.

125. Li Yixuan, Majjid A. Qaria, Sethupathy Sivasamy, Sun Jianzhong, Zhu Daochen, Curcumin production and bioavailability: A comprehensive review of curcumin extraction, synthesis, biotransformation and delivery systems, Industrial Crops and Products, Volume 172, 2021, 114050, ISSN 0926-6690, https://doi.org/10.1016/j.indcrop.2021.114050.

126. Abhishek Gupta et al. Synthesis of Silver Nanoparticles Using Curcumin-Cyclodextrins Loaded into Bacterial Cellulose-Based Hydrogels for Wound Dressing Applications.

Biomacromolecules 2020, 21, 5, 1802–1811. https://doi.org/10.1021/acs.biomac.9b01724.

127. Abhishek Sahu et al. Fluorescence Study of the Curcumin−Casein Micelle Complexation and Its Application as a Drug Nanocarrier to Cancer Cells. Biomacromolecules 2008, 9, 10, 2905–2912. https://doi.org/10.1021/bm800683f.
128. Kotha RR, Luthria DL. Curcumin: Biological, Pharmaceutical, Nutraceutical, and Analytical Aspects. Molecules. 2019 Aug 13;24(16):2930. doi: 10.3390/molecules24162930. PMID: 31412624; PMCID: PMC6720683.
129. Mondal S, Ghosh S, Moulik SP. Stability of curcumin in different solvent and solution media: UV-visible and steady-state fluorescence spectral study. J Photochem Photobiol B. 2016 May;158:212-8. doi: 10.1016/j.jphotobiol.2016.03.004. Epub 2016 Mar 6. PMID: 26985735.
130. Vamshi Krishna Rapalli, Vedhant Kaul, Srividya Gorantla, Tejashree Waghule, Sunil Kumar Dubey, Murali Monohar Pandey, Gautam Singhvi, UV Spectrophotometric method for characterization of curcumin loaded nanostructured lipid nanocarriers in simulated conditions: Method development, in-vitro and ex-vivo applications in topical delivery, Spectrochimica Acta Part A: Molecular and Biomolecular Spectroscopy, Volume 224, 2020, 117392, ISSN 1386-1425, https://doi.org/10.1016/j.saa.2019.117392.
131. Piyali Chatterjee et al. Tautomers and Rotamers of Curcumin: A Combined UV Spectroscopy, High-Performance Liquid Chromatography, Ion Mobility Mass Spectrometry, and Electronic Structure Theory Study. J. Phys. Chem. A 2022, 126, 10, 1591–1604. https://doi.org/10.1021/acs.jpca.1c08612.
132. Bonmatin JM, Laprévote O, Peypoux F. Diversity among microbial cyclic lipopeptides: iturins and surfactins. Activity-structure relationships to design new bioactive agents. Comb Chem High Throughput Screen. 2003 Sep;6(6):541-56. doi: 10.2174/138620703106298716. PMID: 14529379.
133. Chen, Wei-Chuan et al. “Applications of a lipopeptide biosurfactant, surfactin, produced by microorganisms.” Biochemical Engineering Journal 103 (2015): 158-169.
134. Théatre A, Cano-Prieto C, Bartolini M, Laurin Y, Deleu M, Niehren J, Fida T, Gerbinet S, Alanjary M, Medema MH, Léonard A, Lins L, Arabolaza A, Gramajo H, Gross H, Jacques P. The Surfactin-Like Lipopeptides From Bacillus spp.: Natural Biodiversity and Synthetic Biology for a Broader Application Range. Front Bioeng Biotechnol. 2021 Mar 2;9:623701. doi: 10.3389/fbioe.2021.623701. PMID: 33738277; PMCID: PMC7960918.
135. Christopher FC, Ponnusamy SK, Ganesan JJ, Ramamurthy R. Investigating the prospects

of bacterial biosurfactants for metal nanoparticle synthesis - a comprehensive review. IET Nanobiotechnol. 2019 May;13(3):243-249. doi: 10.1049/iet-nbt.2018.5184. PMID: 31053685; PMCID: PMC8676648.

136. Y. Nakama, Chapter 15 - Surfactants, Editor(s): Kazutami Sakamoto, Robert Y. Lochhead, Howard I. Maibach, Yuji Yamashita, Cosmetic Science and Technology, Elsevier, 2017, Pages 231-244, ISBN 9780128020050, https://doi.org/10.1016/B978-0-12-802005-0.00015-X.
137. Yutaka Ishigami, Mohamad Osman, Hisae Nakahara, Yoh Sano, Ryo Ishiguro, Mutsuo Matsumoto, Significance of β-sheet formation for micellization and surface adsorption of surfactin, Colloids and Surfaces B: Biointerfaces, Volume 4, Issue 6, 1995, Pages 341-348, ISSN 0927-7765, https://doi.org/10.1016/0927-7765(94)01183-6.
138. Yeh MS, Wei YH, Chang JS. Enhanced production of surfactin from Bacillus subtilis by addition of solid carriers. Biotechnol Prog. 2005 Jul-Aug;21(4):1329-34. doi: 10.1021/bp050040c. PMID: 16080719.
139. Nikhil S. Shaligram et al. Surfactin–A Review on Biosynthesis, Fermentation, Purification and Applications. 2010, Food Technology and Biotechnology, 48(2).
140. Seydlová, G., Svobodová, J. Review of surfactin chemical properties and the potential biomedical applications. cent.eur.j.med 3, 123–133 (2008). https://doi.org/10.2478/s11536-008-0002-5.
141. Carrillo C, Teruel JA, Aranda FJ, Ortiz A. Molecular mechanism of membrane permeabilization by the peptide antibiotic surfactin. Biochim Biophys Acta. 2003 Apr 1;1611(1-2):91-7. doi: 10.1016/s0005-2736(03)00029-4. PMID: 12659949.
142. Santos, Vanessa Santana Vieira et al. “Toxicity and applications of surfactin for health and environmental biotechnology.” Journal of Toxicology and Environmental Health, Part B 21 (2018): 382 - 399.
143. Kracht M, Rokos H, Ozel M, Kowall M, Pauli G, Vater J. Antiviral and hemolytic activities of surfactin isoforms and their methyl ester derivatives. J Antibiot (Tokyo). 1999 Jul;52(7):613-9. doi: 10.7164/antibiotics.52.613. PMID: 10513840.
144. Vollenbroich D, Ozel M, Vater J, Kamp RM, Pauli G. Mechanism of inactivation of enveloped viruses by the biosurfactant surfactin from Bacillus subtilis. Biologicals. 1997 Sep;25(3):289-97. doi: 10.1006/biol.1997.0099. PMID: 9324997.
145. Peypoux F, Bonmatin JM, Wallach J. Recent trends in the biochemistry of surfactin. Appl Microbiol Biotechnol. 1999 May;51(5):553-63. doi: 10.1007/s002530051432. PMID: 10390813.

146. Chen, Wei-Chuan et al. “Applications of a lipopeptide biosurfactant, surfactin, produced by microorganisms.” Biochemical Engineering Journal 103 (2015): 158-169.
147. A. Satyanarayana Reddy, Chien-Yen Chen, Simon C. Baker, Chien-Cheng Chen, Jiin-Shuh Jean, Cheng-Wei Fan, Hau-Ren Chen, Jung-Chen Wang, Synthesis of silver nanoparticles using surfactin: A biosurfactant as stabilizing agent, Materials Letters, Volume 63, Issue 15, 2009, Pages 1227-1230, ISSN 0167-577X, https://doi.org/10.1016/j.matlet.2009.02.028.
148. Absar Ahmad, Priyabrata Mukherjee, Satyajyoti Senapati, Deendayal Mandal, M.Islam Khan, Rajiv Kumar, Murali Sastry, Extracellular biosynthesis of silver nanoparticles using the fungus Fusarium oxysporum, Colloids and Surfaces B: Biointerfaces, Volume 28, Issue 4, 2003, Pages 313-318, ISSN 0927-7765, https://doi.org/10.1016/S0927-7765(02)00174-1.
149. Klaus-Joerger T, Joerger R, Olsson E, Granqvist C. Bacteria as workers in the living factory: metal-accumulating bacteria and their potential for materials science. Trends Biotechnol. 2001 Jan;19(1):15-20. doi: 10.1016/s0167-7799(00)01514-6. PMID: 11146098.
150. Najitha Banu, A., Balasubramanian, C. & Moorthi, P.V. Biosynthesis of silver nanoparticles using Bacillus thuringiensis against dengue vector, Aedes aegypti (Diptera: Culicidae). Parasitol Res 113, 311–316 (2014). https://doi.org/10.1007/s00436-013-3656-0.
151. Shankar SS, Rai A, Ankamwar B, Singh A, Ahmad A, Sastry M. Biological synthesis of triangular gold nanoprisms. Nat Mater. 2004 Jul;3(7):482-8. doi: 10.1038/nmat1152. Epub 2004 Jun 20. PMID: 15208703.
152. Christopher FC, Ponnusamy SK, Ganesan JJ, Ramamurthy R. Investigating the prospects of bacterial biosurfactants for metal nanoparticle synthesis - a comprehensive review. IET Nanobiotechnol. 2019 May;13(3):243-249. doi: 10.1049/iet-nbt.2018.5184. PMID: 31053685; PMCID: PMC8676648.
153. Meena, K.R., Dhiman, R., Singh, K. et al. Purification and identification of a surfactin biosurfactant and engine oil degradation by Bacillus velezensis KLP2016. Microb Cell Fact 20, 26 (2021). https://doi.org/10.1186/s12934-021-01519-0.
154. Woese CR. Bacterial evolution. Microbiol Rev. 1987 Jun;51(2):221-71. doi: 10.1128/mr.51.2.221-271.1987. PMID: 2439888; PMCID: PMC373105.
155. Woese CR. Bacterial evolution. Microbiol Rev. 1987 Jun;51(2):221-71. doi: 10.1128/mr.51.2.221-271.1987. PMID: 2439888; PMCID: PMC373105.

156. Devaux CA, Rolain JM, Colson P, Raoult D. New insights on the antiviral effects of chloroquine against coronavirus: what to expect for COVID-19? Int J Antimicrob Agents. 2020 May;55(5):105938. doi: 10.1016/j.ijantimicag.2020.105938. Epub 2020 Mar 12. PMID: 32171740; PMCID: PMC7118659.

157. A. L. Costa et al. Eco design for Ag-based solutions against SARS-CoV-2 and E. coli. Environ. Sci.: Nano, 2022,9, 4295-4304. DOI https://doi.org/10.1039/D2EN00178K.

158. Cushnie, T.P.T., Cushnie, B., Echeverría, J. et al. Bioprospecting for Antibacterial Drugs: a Multidisciplinary Perspective on Natural Product Source Material, Bioassay Selection and Avoidable Pitfalls. Pharm Res 37, 125 (2020). https://doi.org/10.1007/s11095-020-02849-1.

159. Moghadamtousi SZ, Kadir HA, Hassandarvish P, Tajik H, Abubakar S, Zandi K. A review on antibacterial, antiviral, and antifungal activity of curcumin. Biomed Res Int. 2014;2014:186864. doi: 10.1155/2014/186864. Epub 2014 Apr 29. PMID: 24877064; PMCID: PMC4022204.

160. https://farmaci.agenziafarmaco.gov.it/aifa/servlet/PdfDownloadServlet?pdfFileName=footer_000015_003950_FI.pdf&retry=0&sys=m0b1l3.

161. https://www.who.int/en/activities/tracking-SARS-CoV-2-variants/

162. Anju Manuja, Balvinder Kumar, Rajesh Kumar, Dharvi Chhabra, Mayukh Ghosh, Mayank Manuja, Basanti Brar, Yash Pal, B.N. Tripathi, Minakshi Prasad, Metal/metal oxide nanoparticles: Toxicity concerns associated with their physical state and remediation for biomedical applications, Toxicology Reports, Volume 8, 2021, Pages 1970-1978, ISSN 2214-7500, https://doi.org/10.1016/j.toxrep.2021.11.020.

163. Hainan Sun et al. Cytotoxicity-Related Bioeffects Induced by Nanoparticles: The Role of Surface Chemistry. Front. Bioeng. Biotechnol., Sec. Nanobiotechnology Volume 7 - 2019 https://doi.org/10.3389/fbioe.2019.00414.

164. Sun J, He WT, Wang L, Lai A, Ji X, Zhai X, Li G, Suchard MA, Tian J, Zhou J, Veit M, Su S. COVID-19: Epidemiology, Evolution, and Cross-Disciplinary Perspectives. Trends Mol Med. 2020 May;26(5):483-495. doi: 10.1016/j.molmed.2020.02.008. Epub 2020 Mar 21. PMID: 32359479; PMCID: PMC7118693.

165. Du L, He Y, Zhou Y, Liu S, Zheng BJ, Jiang S. The spike protein of SARS-CoV--a target for vaccine and therapeutic development. Nat Rev Microbiol. 2009 Mar;7(3):226-36. doi: 10.1038/nrmicro2090. Epub 2009 Feb 9. PMID: 19198616; PMCID: PMC2750777.

166. Walls AC, Park YJ, Tortorici MA, Wall A, McGuire AT, Veesler D. Structure, Function,

and Antigenicity of the SARS-CoV-2 Spike Glycoprotein. Cell. 2020 Dec 10;183(6):1735. doi: 10.1016/j.cell.2020.11.032. Erratum for: Cell. 2020 Apr 16;181(2):281-292.e6. PMID: 33306958; PMCID: PMC7833104.

167. Lu R, Zhao X, Li J, Niu P, Yang B, Wu H, Wang W, Song H, Huang B, Zhu N, Bi Y, Ma X, Zhan F, Wang L, Hu T, Zhou H, Hu Z, Zhou W, Zhao L, Chen J, Meng Y, Wang J, Lin Y, Yuan J, Xie Z, Ma J, Liu WJ, Wang D, Xu W, Holmes EC, Gao GF, Wu G, Chen W, Shi W, Tan W. Genomic characterisation and epidemiology of 2019 novel coronavirus: implications for virus origins and receptor binding. Lancet. 2020 Feb 22;395(10224):565-574. doi: 10.1016/S0140-6736(20)30251-8. Epub 2020 Jan 30. PMID: 32007145; PMCID: PMC7159086.
168. D. Gardini, M. Blosi, S. Ortelli, C. Delpivo, O. Bussolati, M.G. Bianchi, M. Allegri, E. Bergamaschi, A.L. Costa, Nanosilver: An innovative paradigm to promote its safe and active use, NanoImpact, Volume 11, 2018, Pages 128-135, ISSN 2452-0748, https://doi.org/10.1016/j.impact.2018.06.003.
169. Innes E, Yiu HHP, McLean P, Brown W, Boyles M. Simulated biological fluids - a systematic review of their biological relevance and use in relation to inhalation toxicology of particles and fibres. Crit Rev Toxicol. 2021 Mar;51(3):217-248. doi: 10.1080/10408444.2021.1903386. Epub 2021 Apr 27. PMID: 33905298.
170. Avramescu ML, Rasmussen PE, Chénier M, Gardner HD. Influence of pH, particle size and crystal form on dissolution behaviour of engineered nanomaterials. Environ Sci Pollut Res Int. 2017 Jan;24(2):1553-1564. doi: 10.1007/s11356-016-7932-2. Epub 2016 Oct 26. PMID: 27785722; PMCID: PMC5306302.
171. Stefaniak AB, Guilmette RA, Day GA, Hoover MD, Breysse PN, Scripsick RC. Characterization of phagolysosomal simulant fluid for study of beryllium aerosol particle dissolution. Toxicol In Vitro. 2005 Feb;19(1):123-34. doi: 10.1016/j.tiv.2004.08.001. PMID: 15582363.
172. Takaya, Mitsutoshi et al. “Dissolution of functional materials and rare earth oxides into pseudo alveolar fluid.” Industrial health 44 4 (2006): 639-44.
173. Innes E, Yiu HHP, McLean P, Brown W, Boyles M. Simulated biological fluids - a systematic review of their biological relevance and use in relation to inhalation toxicology of particles and fibres. Crit Rev Toxicol. 2021 Mar;51(3):217-248. doi: 10.1080/10408444.2021.1903386. Epub 2021 Apr 27. PMID: 33905298.
174. Lowry, Gregory Victor et al. “Guidance to improve the scientific value of zeta-potential measurements in nanoEHS.” Environmental science. Nano 3 (2016): 953-965.

175. Clogston JD, Patri AK. Zeta potential measurement. Methods Mol Biol. 2011;697:63-70. doi: 10.1007/978-1-60327-198-1_6. PMID: 21116954.
176. https://www.gov4nano.eu/
177. https://www.patrols-h2020.eu/
178. M. Tanaka et al, Recommended table for the density of water between 0 °C and 40 °C based on recent experimental reports, 2001 Metrologia 38 301. DOI 10.1088/0026-1394/38/4/3.
179. Shen G. Campbell biology (edited by Lisa Urry, Michael Cain, Steven Wasserman, Peter Minorsky and Jane Reece). J Biol Res (Thessalon). 2020 Dec 9;27(1):19. doi: 10.1186/s40709-020-00127-0. PMID: 33298185; PMCID: PMC7727124.
180. CRC Handbook of Chemistry and Physics, 84th Edition Edited by David R. Lide (National Institute of Standards and Technology). J. Am. Chem. Soc. 2004, 126, 5, 1586. https://doi.org/10.1021/ja0336372.
181. Blosi, M.; Albonetti, S.; Dondi, M.; Baldi, G.; Barzanti, A.; Bitossi, M. Process for Preparing Stable Suspensions of Metal Nanoparticles and the Stable Colloidal Suspensions Obtained Thereby. European Patent Office EP2403636A2, 10 March 2010.
182. Frank Babick, Chapter 3.2.1 - Dynamic light scattering (DLS), Editor(s): Vasile-Dan Hodoroaba, Wolfgang E.S. Unger, Alexander G. Shard, In Micro and Nano Technologies, Characterization of Nanoparticles, Elsevier, 2020, Pages 137-172, ISBN 9780128141823, https://doi.org/10.1016/B978-0-12-814182-3.00010-9.
183. Rituraj Borah, Sammy W. Verbruggen, Effect of size distribution, skewness and roughness on the optical properties of colloidal plasmonic nanoparticles, Colloids and Surfaces A: Physicochemical and Engineering Aspects, Volume 640, 2022, 128521, ISSN 0927-7757, https://doi.org/10.1016/j.colsurfa.2022.128521.
184. Ajeet Kumar, Chandra Kumar Dixit, 3 - Methods for characterization of nanoparticles, Editor(s): Surendra Nimesh, Ramesh Chandra, Nidhi Gupta, Advances in Nanomedicine for the Delivery of Therapeutic Nucleic Acids, Woodhead Publishing, 2017, Pages 43-58, ISBN 9780081005576, https://doi.org/10.1016/B978-0-08-100557-6.00003-1.
185. Ohshima, H. (2013). Zeta Potential. In: Tadros, T. (eds) Encyclopedia of Colloid and Interface Science. Springer, Berlin, Heidelberg. https://doi.org/10.1007/978-3-642-20665-8_162
186. M. Dudley, X.R. Huang, X-ray Topography, Editor(s): K.H. Jürgen Buschow, Robert W. Cahn, Merton C. Flemings, Bernhard Ilschner, Edward J. Kramer, Subhash Mahajan, Patrick Veyssière, Encyclopedia of Materials: Science and Technology, Elsevier, 2001,

Pages 9813-9825, ISBN 9780080431529, https://doi.org/10.1016/B0-08-043152-6/01780-0.

187. Holzwarth, U., Gibson, N. The Scherrer equation versus the 'Debye-Scherrer equation'. Nature Nanotech 6, 534 (2011). https://doi.org/10.1038/nnano.2011.145.

188. World Health Organization, WHO. Coronavirus disease (COVID-19) technical guidance: Laboratory testing for 2019-nCoV in humans. US CDC Real-time RT-PCR Panel for Detection 2019-Novel Coronavirus (28 January 2020). Available at: https://www.fda.gov/media/134922/download [last access 20 March 2020

# Chapter 4

## *Production of nano-enabled products implementing antimicrobial silver nanoparticles on different substrates*

Part of the content of this chapter has been published as G. Motta et. al. “Preliminary Toxicological Analysis in a Safe-by-Design and Adverse Outcome Pathway-Driven Approach on Different Silver Nanoparticles: Assessment of Acute Responses in A549 Cells” Toxics 2023, 11, 195.

## 4.1. Antimicrobial nano-enabled products implementing silver nanoparticles

The recent outbreak of the SARS-CoV-2 pandemic has attracted the attention of the academic and scientific world. In fact, the latest years an important increase in the number of studies in the field of fighting and prevention of pathogens infection has been registered.[189,190,191] Several strategies have been proposed over the years to address this issue, among various antibacterial and antiviral strategies, nanotechnology demonstrated to have the capability to be an important pillar in this research field.[192] Several emerging nanoparticles have been reported to exhibit excellent efficacy against bacteria and viruses. In particular, silver nanoparticles are the most studied for this application.[157,193]

The main obstacle impeding the large-scale implementation of silver nanoparticles and nanomaterials in general as antimicrobial remedy is the difficult safety and sustainability assessment of these materials.[193] For this reason, the first phase of this work was focused on the development of safe and sustainable by design syntheses of silver nanoparticles. The colloidal suspensions obtained have been widely characterized and tested in terms of antimicrobial properties. The next step in the life cycle involves the implementation of the developed AgNPs variants into nano-enabled products exploitable in everyday life.


*Figure 66 – Implementation of the Safe and Sustainable by Design (SSbD) synthesis of AgNPs into nano-enabled products. The case studies proposed for the implementation of the antimicrobial AgNPs are: textiles for gowns and facemasks, paper for highly circulating documents, polymeric films for packaging, and freeze-dried products for nasal spray.*

Nanophases manufacturing raises important questions related to their safety profile, inhalation, dermal contact, as well as ingestion may all be possible workers exposure routes. Exposures levels and limit thresholds have to be defined in order to establish the process safety, eventually studying alternatives to mitigate the risks.[193,194,195] In this chapter dip-coating, spray-coating, and roll-to-roll printing will be investigated as manufacturing processes to implement AgNPs into antimicrobial nano-enabled products based on textiles and paper substrates. Also, biopolymeric films and freeze-dried biopolymeric scaffolds will be used as embedding matrixes for the nanophases. The nano-enabled products presented in this chapter are summarized in the scheme in Figure 66.

The manufacturing process choices should be a compromise between the final product performances and the safety profile. The nano-enabled products use phase stage is a key point to study the human exposure and the environmental nanophases release. To better understand the transformation of the AgNPs and their fate, dissolution studies and use phase simulation tests are fundamental to determine the durability of the product as well as the risks for humans and environment. Toxicity and ecotoxicity evaluations are based on the exposure levels and routes, so these simulating tests are the base for the risk assessment. In this chapter, different tests were applied based on the final product application, such as antimicrobial textiles washing cycles and abrasion or antimicrobial paper washing, dissolution, and crumpling. Another key point in the life cycle assessment is the end of life, considering the final disposal of the product and the eventual accumulation of nanophases into the environment and forms of life, as well as the dissolution of ions or the transformations occurring to the nanomaterial. A scheme of the life cycle is reported in Figure 67, the highlighted phases will be explored in this chapter.

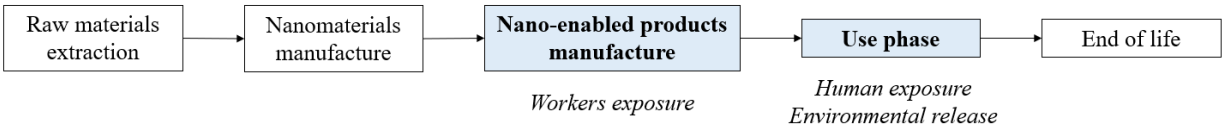


*Figure 67 – Scheme of the life cycle stages of nanomaterials implementation into nano-enabled products. Focus on the manufacturing and use phase stages.*

### 4.1.1. Antimicrobial textiles

Nanotechnology and nanosafety necessitate improvements in the evaluation of the risk-benefit profile of nanoproducts and nanoprocesses. A full life cycle assessment is particularly required for this kind of materials, because every life cycle step can strongly affect the safety and sustainability of the product. Starting from the nanomaterial synthesis design options it is possible to control the final product properties, affecting its functionality, durability, and human and environmental exposure and risks. Synthesis design variables should be carefully selected to develop the desired properties. The European Commission promoted Safe and Sustainable by Design approaches within several European funded projects. These frameworks focus on the design and re-design of nanophases to deliver safer and more sustainable products preserving, and when it is possible, improving their activity. These projects' goal is to define general Safe and Sustainable by Design guidelines and regulations to help future manufacturer in the decision-making process aimed at the development of new nanoproduct and nanoprocesses. To make important steps in this direction, it is not only the synthesis step that should be considered, but also the manufacturing of the nanomaterials into nano-enabled products, the use phase, and the end of life. The manufacturing step is mostly focused on workers exposure in the working site, inhalation and dermal exposure routes usually are the most investigated scenarios. At this stage the design of the manufacturing process should consider the performance of the material as well as the workers safety and the sustainability in terms of both environmental and economical sustainability. The use phase is mostly targeted to the consumer exposure and the environmental release. Minimizing the potential toxicity of the material and the acute toxicity concentration exposure is the main objective. To reach this goal it is important to control the nano-enabled product stability, nanomaterials release, and the toxicity profile of the released phases. Finally, the difficulty in the recycling of these materials contributes to another hot topic regarding nano-enabled products, their end of life. It is important to study the persistency and the transformations of the nanomaterials.

The design of new product and processes or the re-design of already existing technologies is one of the most promising solution in this field. Considering the whole product life cycle since the very beginning of its design developing the safest and most sustainable variant could be the best option for the nanomaterial's world. To shift from iterative to predictive design it is fundamental the help of informatic tools and artificial intelligence implementation. At the moment, several European funded projects like ASINA are working in this direction. The implementation of iterative-predictive hybrid case studies for the design of nanoproducts and nanoprocesses is

being used for the construction of useful databases. The collected results will be implemented into informatic platforms to help future nanomaterials designer in their decisions.

The activities here described, focused on the nanomaterials and nano-enabled products development, are part of the European Project ASINA – Anticipating Safety Issues at the Design Stage of NAno Product Development – within the European Program H2020-NMBP-TO-IND-2018-2020, TOPIC: NMBP-15-2019: Safe by design, from science to regulation: metrics and main sectors (RIA).

***ASINA Project*** – The project has the ambition to promote consistent, applicable and scientifically sound Safe-by-Design nano-practices, considering all nano-enabled products design dimensions: functionality, production technologies, safety, environmental sustainability, cost effectiveness and regulatory requirements, in line with research responsible innovation policy. The expected impacts of the project are the implementation of Safe-by-design tools at an early stage of nanomaterial development, improving workplaces quality minimizing risk level, mitigate the exposure due to the release of NMs from products which should be monitored by low-cost techniques, increased industrial competitiveness, and impact on human health, environment, and regulations.[48]

The project is structured in two value chains:

- Value chain 1 is focused on antimicrobial and depolluting coatings applied on two main case studies: photocatalytic filters and illumination systems based on titanium dioxide nanoparticles coating, and antimicrobial textiles based on silver nanoparticles coating.
- Value chain 2 studies nanostructured capsules delivering active phases in cosmetics, two products of interest were identified in antiaging skin care cream and antibacterial hand cream.

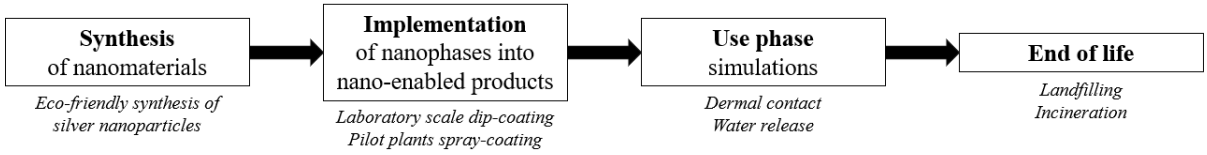


*Figure 68 – Scheme of the product life cycle stages studied within the European project ASINA.*

This chapter describes the progress done in value chain 1 in the implementation of silver nanoparticles as coating of antimicrobial textiles. Starting from the synthesis of the nanomaterial, passing through its implementation into the nano-enabled product and finally studying the use

phase of the product in terms of performances and silver release to simulate human exposure and environmental impact. The main life cycle steps studied in the project are described in the scheme in Figure 68.

***Antimicrobial textiles*** – The textile industry is one of the main fields that could benefit from the recent advance in nanotechnology, in fact the global market projection for nano-enabled textiles is to increase form 4.61 billion dollars in 2021 to 13.83 billion dollars in 2026.[196] In fact, textiles are used for a large variety of applications such as clothes, furniture, bio-medical equipment, and water filtration.[197,198,199,200,201] Antimicrobial property of silver nanoparticles is of the most appreciated features of functional textiles, especially in the medical field where antimicrobial medical coats or equipment may play a relevant role, and also in the sportive outfit reducing bacterial and fungal infection, preventing unpleasant odors, and maybe saving some water and energy for washing.[202] This makes silver nanoparticles coated textile an excellent case study for the development of industrial safe and sustainable by design nano-practices. There are several ways to incorporate AgNPs into textiles, different fabric substrates to implement, and differently synthesized AgNPs. All of these factors influence the stability of the coating, the silver release during the lifespan of the product, also various use phase and disposal scenarios should be taken into consideration for a detailed evaluation of human and environmental exposure.[203] The exposure scenarios are present at all life cycle phases of the product, including initial synthesis, manufacturing, usage phase and disposal.[204] Life cycle assessment (LCA) methods are required to determine the potential risks of AgNPs and nano-enabled textiles related to human and environmental health, and their sustainability.[205]

It has been demonstrated that some physicochemical properties of AgNPs play an important role in the antimicrobial activity of the product, for example the size of the nanoparticle is crucial, but also the shape, surface charge and chemistry, an eventual coating or capping agent, the agglomeration degree, and dissolution rate.[206] AgNPs most active fraction is the one with diameter less than 10 nm.[207] In fact, the surface/volume aspect ratio is one of the main controlling factor of the dissolution rate of NPs, $Ag^+$ ion released can easily interact with bacterial membrane disrupting the cell wall, and this may be considered one of the main antimicrobial mechanisms of silver.[208] Also the direct contact between bacterial cell and AgNPs may cause the membrane disruption leading to cellular contents leaks and cell death.[209]

***Results and discussion***

***Synthesis of silver nanoparticles*** – Considering the importance of the properties of silver nanoparticles and the role played by the capping agent, the project started studying the synthesis of the nanomaterial. Quaternized hydroxyethyl cellulose and curcumin were selected as capping agents for the desired AgNPs. The synthesis, physicochemical characterization, and functional tests of these materials are described in Chapter 3. The design of experiment built for both AgHEC and AgCur, resulted in a composition optimization process that led to the selection of AgHEC_5.5_2.8 and AgHEC_6.4_1.4 variants for hydroxyethyl cellulose, and AgCur for curcumin capped nanoparticles. AgHEC_5.5_2.8 and AgCur are what were defined the standard composition respectively for the two capping agent, AgHEC_5.5_2.8 may be considered a starting and reference point for all the consideration, AgHEC_6.4_1.4 is the composition that exhibited the highest antimicrobial activity, while AgCur is an alternative composition that show very different properties: extremely low cytotoxicity, negative surface charge (opposite respect the positively charged HEC based variants), and smaller hydrodynamic diameter. The set of AgNPs variants of interest is defined as AgHEC_5.5_2.8, AgHEC_6.4_1.4, and AgCur, the syntheses produce about 5000 $mg \cdot L^{-1}$ silver concentrated suspension, that where properly diluted for the coating application at about 1000 $mg \cdot L^{-1}$ and 500 $mg \cdot L^{-1}$. These three solutions were implemented in the production of antimicrobial textiles.

***Implementation of AgNPs into nano-enabled products*** – The substrate of interest is medical grade polyester fabric, which could represent a real application of the nano-enabled product in the medical field. The production process passed through laboratory scale test exploiting dip-coating technique for the coating deposition, subsequently it was up-scaled to pilot-plants facilities where spray-coating was the best solution for to increase the productivity. The silver load deposited on the samples was assessed by ICP-OES analysis, the antibacterial activity of the nano-enabled products was tested, and simulation of the use phase were performed thanks to specific test to reproduce the silver release and the human exposure, after these aging tests the durability of the coating was monitored evaluating once again the Ag content and the antibacterial activity. In order to assess a complete comparison of the different solution tested identifying benefits and problematics related to the 3 AgNPs variants, dip-coating and spray-coating, and the activation with plasma, the ICP-OES and antimicrobial tests performed on fresh and aged samples will be reported and compared based on their categories. Substrate plasma treatment was tested to activate the textile surface to improve AgNPs adhesion, theoretically achieving a higher silver load and a better washing fastness.

***Laboratory scale dip-coating*** – In Table 37 are reported the samples produced by dip-coating, the deposition conditions and the total silver load assessed by ICP-OES expressed as milligram of silver per gram of fabric. From these first results emerged a correlation between the silver concentration of the deposited suspension and the silver load on the fabric. The blank shows a non-relevant silver content, 2 to 3 orders of magnitude lower than the coated samples. The most interesting information is the affinity of the different variant for the polyester substrate and the influence of the plasma on this parameter.[210] Without plasma activation, AgCur exhibits the highest silver load, followed by the HEC-capped nanoparticles, with AgHEC_5.5_2.8 showing a little higher silver load compared to AgHEC_6.4_1.4. Comparing the plasma-treated substrates, the silver load results leveled among the three samples. HEC-based NPs load results unaffected by the plasma, while a detrimental effect manifests for AgCur, reducing the silver deposited, this is particularly evident with the 1000 $mg \cdot L^{-1}$ suspensions. In general, it is possible to state that AgCur shows better affinity for the substrate, the plasma activation has demonstrated no benefits, and higher Ag sol concentration leads to higher Ag load in the coating.

*Table 37 – AgNPs dip-coated textiles, sample preparation conditions, and silver load assessed by ICP-OES.*

| Dip-coating AgNPs variant | Ag sol concentration ($mg \cdot L^{-1}$) | Plasma activation | Ag coating load ($mg \cdot g^{-1}$) |
|---|---|---|---|
| Blank | 0 | No | 0.001 ± n.d. |
| AgCur | 500 | No | 0.50 ± 0.02 |
| AgHEC_6.4_1.4 | 500 | No | 0.330 ± 0.008 |
| AgHEC_5.5_2.8 | 500 | No | 0.39 ± 0.04 |
| AgCur | 500 | Yes | 0.4 ± 0.1 |
| AgHEC_6.4_1.4 | 500 | Yes | 0.37 ± 0.03 |
| AgHEC_5.5_2.8 | 500 | Yes | 0.4 ± 0.1 |
| AgCur | 1000 | No | 1.4 ± 0.2 |
| AgHEC_6.4_1.4 | 1000 | No | 0.622 ± 0.002 |
| AgHEC_5.5_2.8 | 1000 | No | 0.79 ± 0.06 |
| AgCur | 1000 | Yes | 0.7 ± 0.3 |
| AgHEC_6.4_1.4 | 1000 | Yes | 0.66 ± 0.05 |
| AgHEC_5.5_2.8 | 1000 | Yes | 0.7 ± 0.2 |

***Use phase simulation on dip-coated samples, washing tests*** – To simulate the use phase of these materials, the prepared samples underwent washing machine and soft abrasion test. In this way, the environmental impact of the silver release in the washing water was evaluated together with the human dermal contact exposure. Briefly, the washing test aims to evaluate the silver released from textiles in the washing water, simulating the use phase of the coated polyester NEPs. The results collected from the washing test are summarized in the following graphs, where it is possible to see in Figure 69 the silver release of washing cycle 1, in Figure 71 washing cycle 5, and in Figure 72 washing cycle 10. The samples are labeled using the NPs composition (AgCur, AgHEC_5.5_2.8, or AgHEC_6.4_1.4), followed by the concentration of the silver suspension used for the dip-coating (500 or 1000 mg·L$^{-1}$), and the letter "P" in the case of plasma activated substrates.

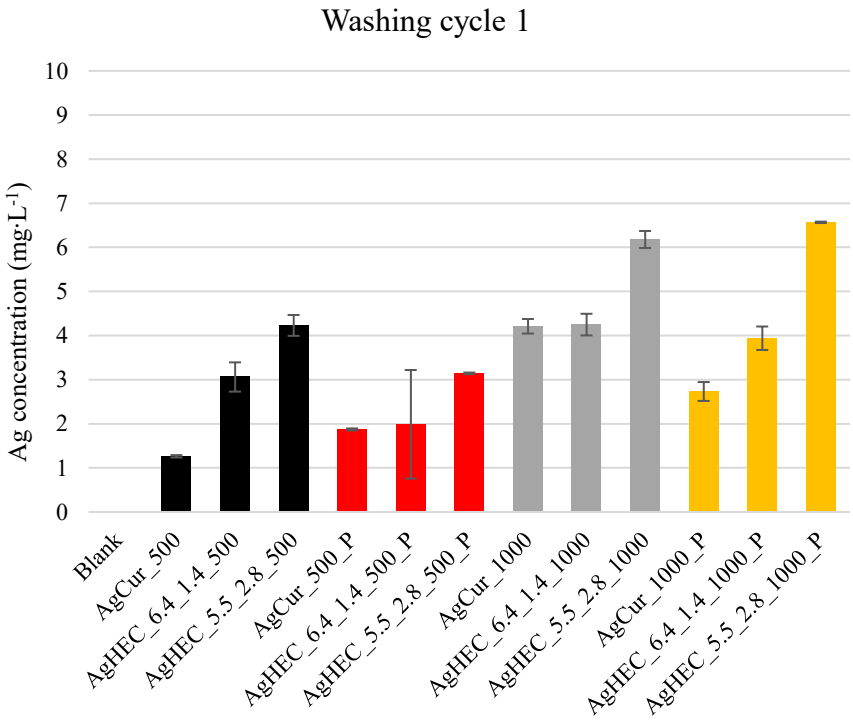


*Figure 69 – Concentration of the silver released after the first washing cycle of the medical-grade polyester textiles dip-coated by AgCur, AgHEC_6.4_1.4, or AgHEC_5.5_2.8 at a silver concentration of 500 or 1000 mg·L$^{-1}$, studying the effect of the activation of the fabric substrate thanks to a plasma pre-treatment (P).*

The ICP-MS detected concentrations of silver released by the fabrics after washing cycle 1 are reported in the graph in Figure 69, where it is possible to see that for all the conditions, 500 or 1000 mg·L$^{-1}$, the sample AgHEC_5.5_2.8 is the one exhibiting the highest release. It is followed by AgHEC_6.4_1.4, while AgCur shows higher washing fastness with the lower release

detected. This confirms the greater affinity of AgCur for the medical grade polyester used as substrate, in fact, it is the composition that gives the highest silver load by dip-coating and the one that demonstrates better washing fastness. Both the composition derived from the standard product AgHEC_5.5_2.8 reveal better behavior with respect to the starting point. This means that the optimization of the composition thanks to the DoE, leading to AgHEC_6.4_1.4, and the substitution of HEC as a capping agent with curcumin improved the applicability of the coating for the desired application in the production of antimicrobial textiles.

For the antimicrobial textile case study, the washing resistance is a key parameter to evaluate the durability and reusability of the nano-enabled products. Several factors contribute to improve NPs attachment to the textile, such as the textile-AgNPs interaction mostly determined by the capping agent, the stability of the AgNPs and the dissolution resulting in $Ag^+$ cation release, and the interaction of the detergent or washing environment with AgNPs, moreover binder additives may be implemented to improve the attachment. In this specific case, it is possible that the higher amount of capping agent in AgHEC_6.4_1.4 compared to AgHEC_5.5_2.8 increases the AgNPs stability reducing the dissolution induced by the washing test. In the case of AgCur, there may be different phenomena favoring the washing fastness of this sample. Curcumin used as capping agent confers negative zeta potential to AgNPs, it is the opposite for HEC-coated samples, this could lead to a better grafting on the textile fibers constituted by medical grade polyester. Furthermore, as reported in Table 38, the detergent used during the washing tests create a negatively charged environment which is less likely to interact with negative AgCur nanoparticles. The different contributes result into an overall better washing fastness of the AgCur-coated textiles.[211,212,213,214]

For what concerns the plasma activation, there aren't clear trends that allow to establish its advantages on the washing fastness. At low Ag concentration (500 $mg \cdot L^{-1}$) the plasma activation seems to help the grafting of AgHEC_6.4_1.4 and AgHEC_5.5_2.8, reducing the silver release, and the opposite for AgCur. At higher concentrations (1000 $mg \cdot L^{-1}$) there aren't relevant differences for AgHEC_6.4_1.4 and AgHEC_5.5_2.8, while improving the attachment of AgCur. However, these considerations may be not particularly relevant and resulting from experimental fluctuations.

The washing waters collected after the washing cycle 1 were analyzed to check the physicochemical properties of the AgNPs released. Table 38 highlights that these results are strongly affected by the presence of detergent in the solutions, in fact, the zeta potential of the samples results always negative, even for quaternized hydroxyethyl cellulose capped AgNPs, usually positively charged. The average resulting charge detected by the instrument is more

negative for AgCur and the blank respect to AgHEC variants, this is due to the intrinsic HEC charge. Moreover, some textile microfibers were detected, this affects the hydrodynamic diameter and polydispersity measurements. HEC based compositions preserve more their original behavior while curcumin shows larger particles and incremented polydispersity, comparable values with the blank. This difference, observed for washing 1, may be justified by because both HEC based AgNPs show higher silver release, liberating more NPs that can be detected by the instrument. While the slower silver release promoted by AgCur leads to a behavior similar to the blank.

*Table 38 – Colloidal characterization of the washing water of blank, AgHEC_5.5_2.8, AgHEC_6.4_1.4, and AgCur after the first washing cycle: zeta potential, hydrodynamic diameter and polydispersity index.*

| Sample | Zeta potential (mV) | Hydrodynamic diameter (nm) | PDI |
|---|---|---|---|
| Blank | -43 ± 3 | 1902 ± 818 | 0.841 ± 0.276 |
| AgHEC_5.5_2.8 | -23 ± 5 | 199 ± 238 | 0.378 ±0.174 |
| AgHEC_6.4_1.4 | -24 ± 3 | 646 ± 970 | 0.594 ± 0.402 |
| AgCur | -45 ± 3 | 1836 ± 1514 | 0.827 ± 0.166 |

The microfibers generated during the washing cycles were collected by filtration on paper filter (≈ 20 μm) to be further investigated, such as for cytotoxicity tests. SEM images of the fibers isolated from AgHEC_5.5_2.8 are reported in Figure 70.

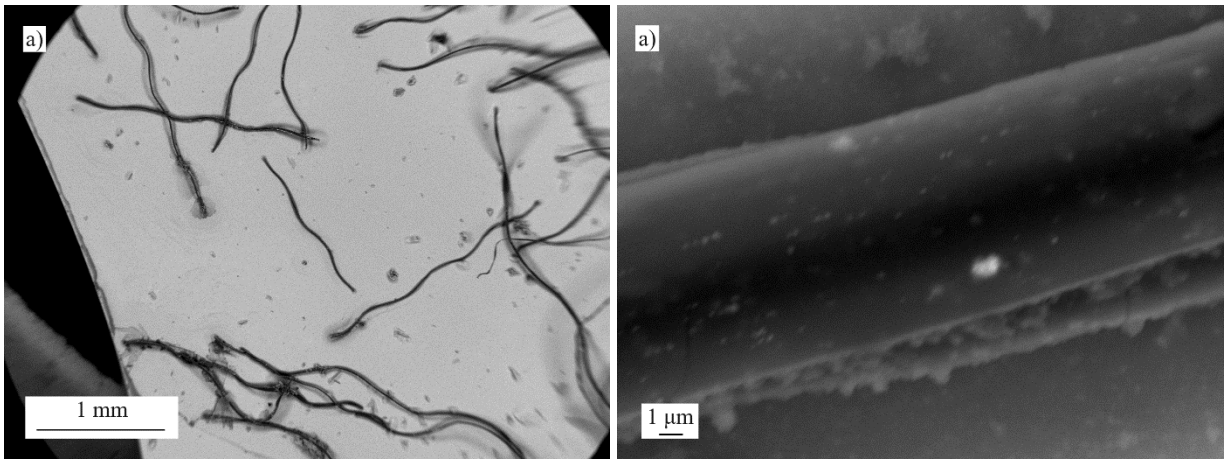


*Figure 70 – SEM images of the fibers collected in the washing waters of the first washing cycle of the sample AgHEC_5.5_2.8. a) panoramic image of the microfibers collected; b) detailed view of the microfiber surface.*

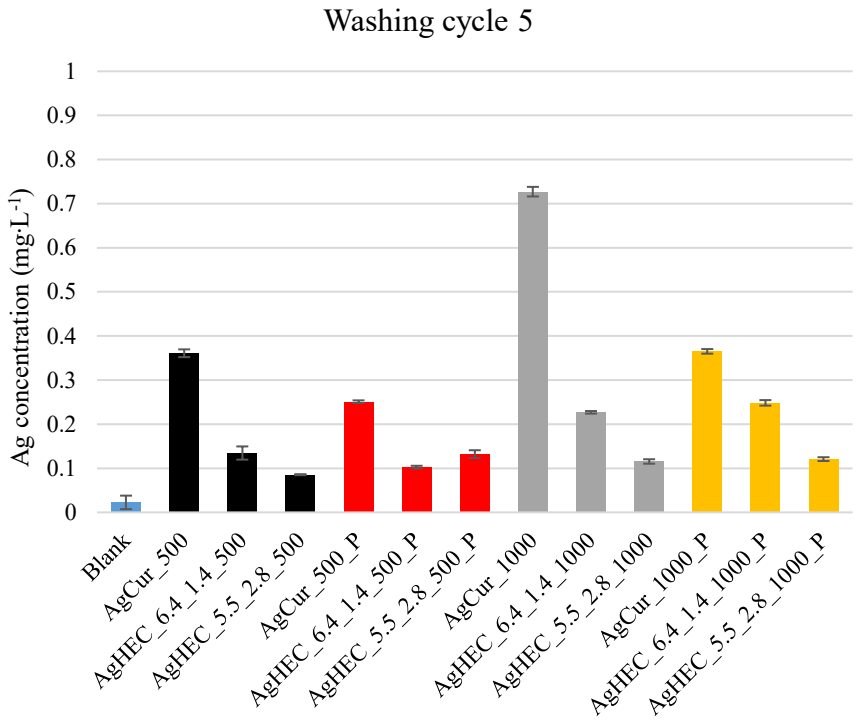


*Figure 71 – Concentration of the silver released after the fifth washing cycle of the medical-grade polyester textiles dip-coated by AgCur, AgHEC_6.4_1.4, or AgHEC_5.5_2.8 at a silver concentration of 500 or 1000 mg·L$^{-1}$, studying the effect of the activation of the fabric substrate thanks to a plasma pre-treatment (P).*

After 5 washing cycles, Figure 71, the silver release is reduced by one order of magnitude, because the weakly attached nanoparticles were removed during the first washing and the total load remaining on the substrate is lesser. In this case the trend is reversed respect washing 1, in fact, this time is AgCur the samples with higher release and AgHEC_5.5_2.8 the lesser released. This is likely to happen because AgCur is the sample with the highest load of silver, starting with a higher amount and having released less during the first washings, the opposite happens for AgHEC_5.5_2.8.

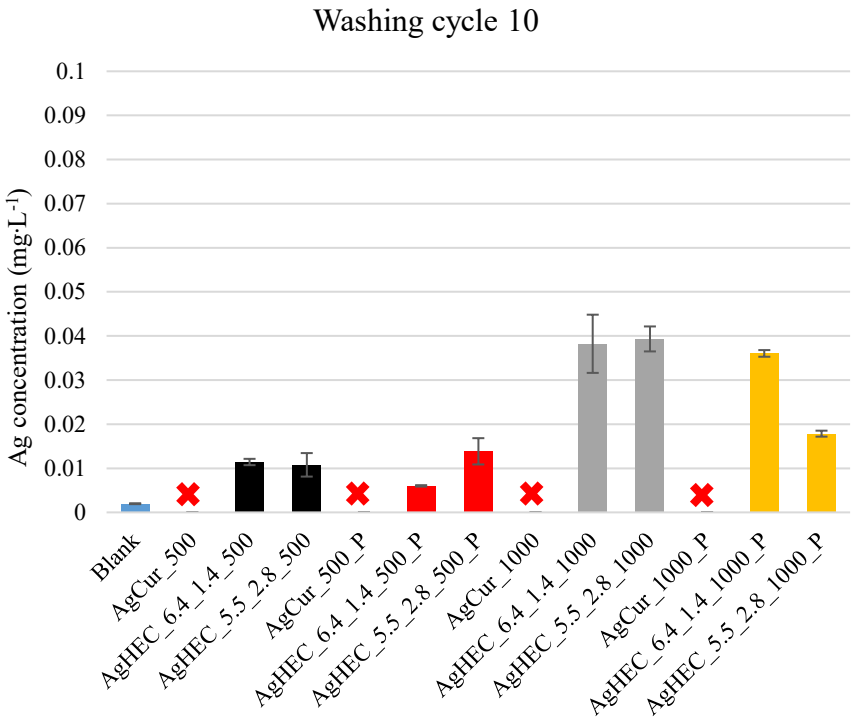


*Figure 72 – Concentration of the silver released after the tenth washing cycle of the medical-grade polyester textiles dip-coated by AgCur, AgHEC_6.4_1.4, or AgHEC_5.5_2.8 at a silver concentration of 500 or 1000 mg·L$^{-1}$, studying the effect of the activation of the fabric substrate thanks to a plasma pre-treatment (P).*

Washing cycle 10 silver release represented in graph in Figure 72, highlights another reduction of one order of magnitude. The limited amount of silver grafted on the fabric is the strongest attached, leading to lower release rate. In these samples the differences between 500 and 1000 mg·L$^{-1}$ can be better appreciated. AgCur coated fabrics were not analyzed after washing 10. Summarizing, AgCur gives a more durable coating with a slower silver release rate, AgHEC_5.5_2.8 is the variant with the worst washing fastness. Plasma-treated samples didn't' show impressive benefits. The higher silver load granted by dip-coating with 1000 mg·L$^{-1}$ Ag concentrated suspension grants better washing resistance.

***Use phase simulation on dip-coated samples, soft abrasion test*** – ICP-MS results on the standard cotton textiles used for the textile-skin dermal contact simulation represent the silver released by soft abrasion test and were normalized for the exposed surface of the substrate. The tip diameter of 16 mm corresponds to a tip surface of about 2 cm$^2$, that is scans the sample for a length of 10 cm. With good approximation it is possible to consider a fabric-scanned surface of 18 cm$^2$. The Ag concentration detected by ICP-OES expressed in micrograms of silver per liter of solution (ppb) was normalized for the scanned surface (18 cm$^2$), resulting in a final value of

silver concentration released per fabric surface area (ppb·cm$^{-2}$). Samples are labeled the same way as for washing tests, results are reported in Figure 73 and Figure 74 respectively for dip-coating Ag concentrations 500 and 1000 mg·L$^{-1}$.

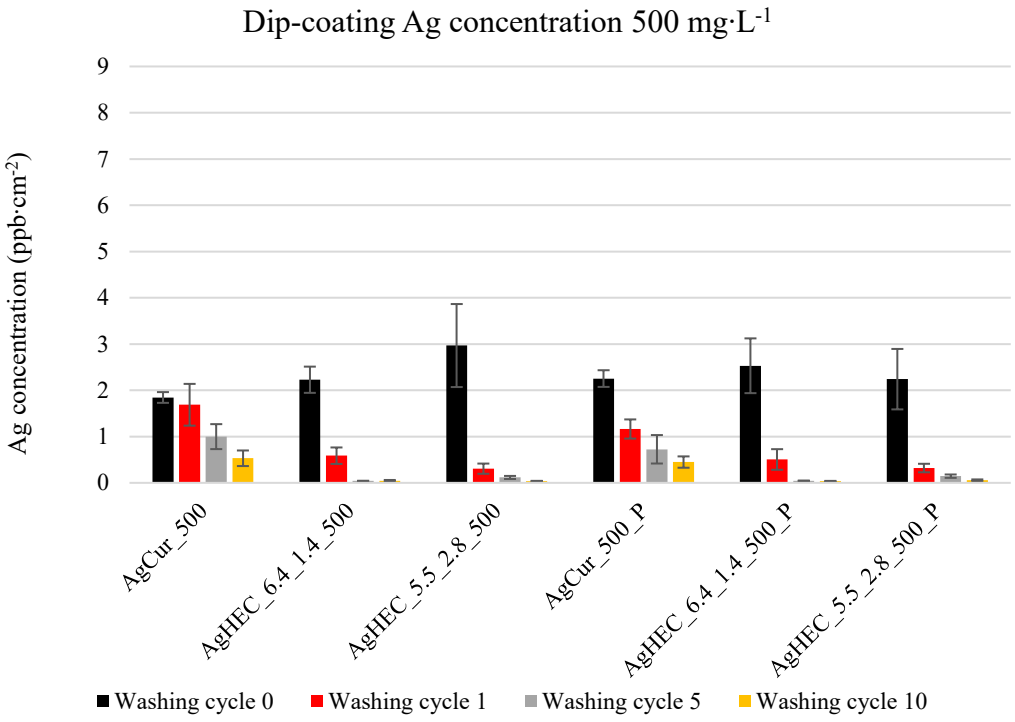


*Figure 73 – Soft abrasion test results of the textiles dip-coated by AgCur, AgHEC_6.4_1.4, and AgHEC_5.5_2.8 at a silver concentration of 500 mg·L$^{-1}$, evaluating the effect of the pre-treatment by plasma activation (P) on the pristine material and after washing cycle 1, 5 and 10. The amount of silver released by the coated textiles during the abrasion test is reported as silver concentration released normalized by the textile surface scanned (ppb·cm$^{-2}$).*

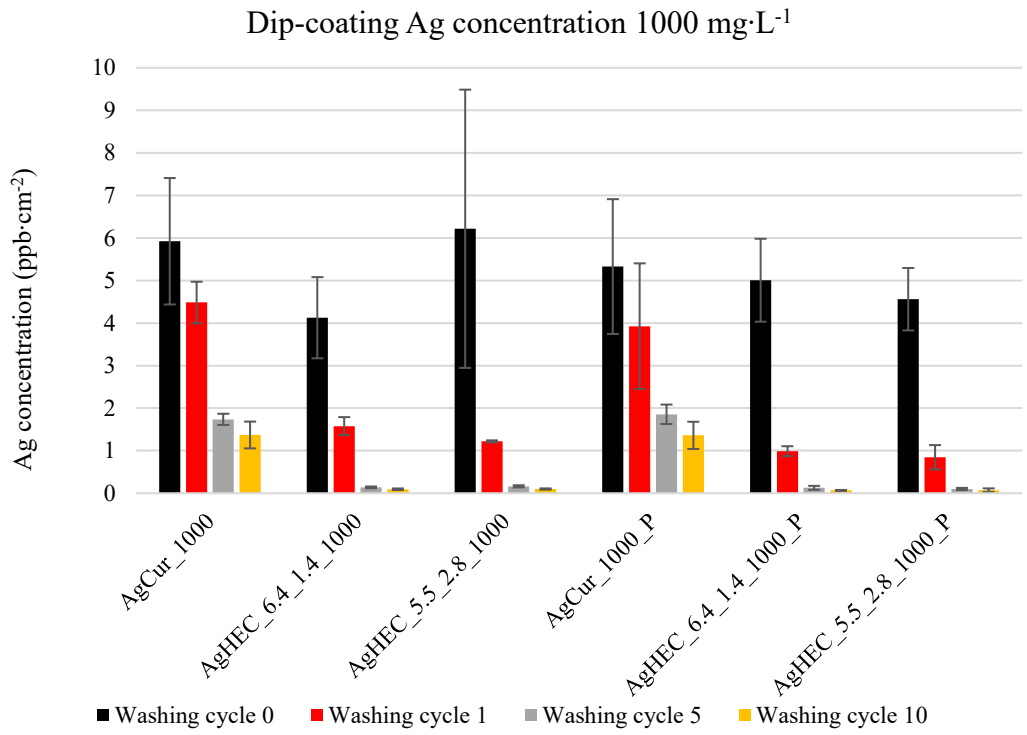


*Figure 74 – Soft abrasion test results of the textiles dip-coated by AgCur, AgHEC_6.4_1.4, and AgHEC_5.5_2.8 at a silver concentration of 1000 mg·L$^{-1}$, evaluating the effect of the pre-treatment by plasma activation (P) on the pristine material and after washing cycle 1, 5 and 10. The amount of silver released by the coated textiles during the abrasion test is reported as silver concentration released normalized by the textile surface scanned (ppb·cm$^{-2}$).*

As it is possible to see comparing the graphs in Figure 73 and Figure 74, a higher Ag concentration employed during the dip-coating determines a higher Ag load in the coating, and subsequently is translated into a higher release during the dermal contact simulation. This means that is necessary to find the most active and less cytotoxic formulation, in order to reduce the required amount of AgNPs in the antimicrobial coating. In this way the human exposure and the environmental release are minimized. The graphs highlight a strong effect of the washing cycles on the soft abrasion test, washing away the coating reduce the amount of silver available for the human exposure, in fact moving from 0 to 10 washing cycles there is a huge difference in silver released. As it is possible to see, HEC based formulation release most of the silver during the first washing cycle, while AgCur has a more gradual behavior with a more durable coating and most likely also a more durable antimicrobial activity. As for previous tests, the plasma treatment seems to not influence the attachment of AgNPs.

***Pilot plant spray-coating*** – During the second spray-coating campaign, several conditions were tested for each silver variant (AgHEC_5.5_2.8, AgHEC_6.4_1.4, and AgCur), all the samples were coated applying a 1000 $mg \cdot L^{-1}$ suspension, in Table 39 are reported the process parameters.

*Table 39 – Spray-coating parameters set-up for the different sample prepared (A, B, C, C_plasma, D, and E): spray flow rate, conveyor belt speed, and plasma activation.*

| Code | Spray flow rate ($mL \cdot min^{-1}$) | Conveyor belt speed ($m \cdot min^{-1}$) | Plasma activation |
|---|---|---|---|
| **A** | 60 | 6 | No |
| B | 80 | 6 | No |
| C | 60 | 4 | No |
| C_plasma | 60 | 4 | Yes |
| D | 80 | 4 | No |
| E | 60 | 2 | No |

The total silver amount loaded by spray-coating on the fabrics was assessed by ICP-OES and it is expressed as milligrams of silver per gram of textile in Table 40. Moving from treatment labeled as A towards E, a faster flow rate and slower conveyor belt speed involve an increasing silver load. The plasma activation does not determine any relevant changes in silver load for all three variants applied. These values were used to estimate the Ag dose applied in the antibacterial tests, and to calculate the silver released percentage during the washing simulations.

*Table 40 – Silver load on spray-coated samples by AgCur, AgHEC_6.4_1.4, and AgHEC_5.5_2.8, assessed by ICP-OES.*

| Spray-coated sample | Ag coating load ($mg \cdot g^{-1}$) |
|---|---|
| Blank | n.d. |
| AgCur_A | 0.057 ± 0.002 |
| AgCur_B | 0.10 ± 0.01 |
| AgCur_C | 0.10 ± 0.01 |
| AgCur_C_plasma | 0.08 ± 0.01 |
| AgCur_D | 0.131 ± 0.002 |
| AgCur_E | 0.151 ± 0.001 |
| AgHEC_6.4_1.4_A | 0.08 ± 0.01 |
| AgHEC_6.4_1.4_B | 0.084 ± 0.003 |
| AgHEC_6.4_1.4_C | 0.106 ± 0.003 |
| AgHEC_6.4_1.4_C_plasma | 0.103 ± 0.006 |
| AgHEC_6.4_1.4_D | 0.125 ± 0.006 |
| AgHEC_6.4_1.4_E | 0.18 ± 0.03 |
| AgHEC_5.5_2.8_A | 0.052 ± 0.002 |
| AgHEC_5.5_2.8_B | 0.08 ± 0.01 |
| AgHEC_5.5_2.8_C | 0.09 ± 0.05 |
| AgHEC_5.5_2.8_C_plasma | 0.10 ± 0.02 |
| AgHEC_5.5_2.8_D | 0.11 ± 0.02 |
| AgHEC_5.5_2.8_E | 0.244 ± 0.002 |

***Use phase simulation on spray-coated samples: washing tests*** – In the following Figure 75, are reported the results obtained by the washing simulation of 1 washing cycle. The applied protocol led to a silver release in the range of 0.1-4 $mg \cdot L^{-1}$, in particular, curcumin-capped silver nanoparticles confirm a better washing fastness compared to the cellulose-capped counterpart. In fact, AgCur Ag release is lower for all the spray-coating tested conditions. For the standard HEC variant AgHEC_5.5_2.8, only 3 deposition conditions (C, C_plasma, and D) were tested, and on average they showed the highest release. These first results on spray-coating samples seem to confirm what was observed previously for dip-coated ones. AgCur has the better washing fastness, followed by AgHEC_6.4_1.4, and the worst performance is exhibited by AgHEC_5.5_2.8. The plasma treatment does not provide any improvement, C and C_plasma treatments reveal no relevant differences for the 3 variants. The increasing silver load from

treatment A to E reflects into the same trend in terms of silver release during the washing simulation, higher Ag load imply higher Ag release.

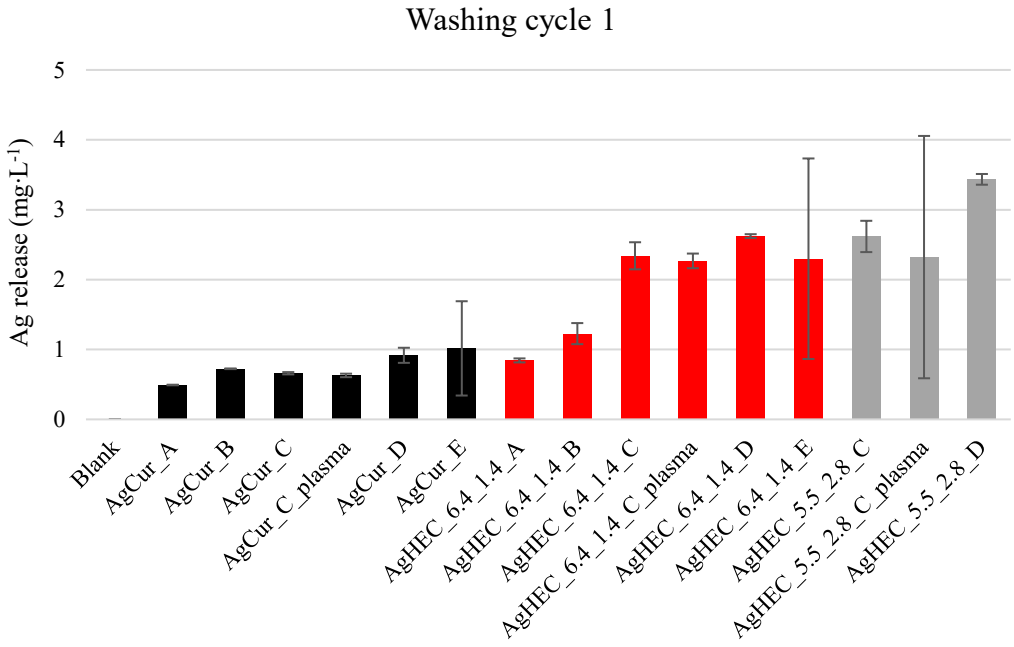


*Figure 75 – Concentration of the silver released after the first washing cycle of the medical-grade polyester textiles spray-coated by AgCur, AgHEC_6.4_1.4, or AgHEC_5.5_2.8 at a silver concentration of 1000 mg·L$^{-1}$ using different deposition conditions (A, B, C, C_plasma, D, and E), studying the effect of the activation of the fabric substrate thanks to a plasma pre-treatment (plasma).*

The results corresponding to 5 washing cycles are reported in Figure 76, the trend correlating the silver load and the silver release is confirmed, also the plasma activation is still unaffecting the results. The variants ranking is inverted, in this case AgHEC_5.5_2.8 releases less Ag and AgCur the greatest amount. This behavior was already observed for the dip-coated samples, AgCur stronger attachment to the fabric determines better washing fastness and a gradual Ag release, while the HEC based variants release most of the silver during the firsts washing cycles. In general, the difference between the Ag released concentration detected is one order of magnitude lower for washing 5 than washing 1.

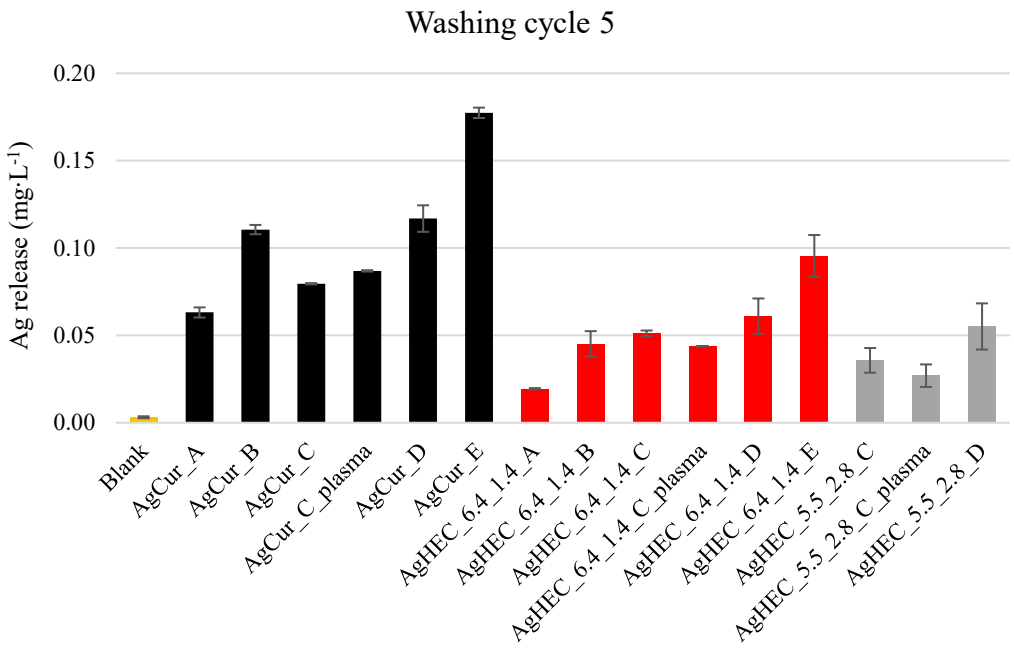


*Figure 76 – Concentration of the silver released after the fifth washing cycle of the medical-grade polyester textiles spray-coated by AgCur, AgHEC_6.4_1.4, or AgHEC_5.5_2.8 at a silver concentration of 1000 mg·L$^{-1}$ using different deposition conditions (A, B, C, C_plasma, D, and E), studying the effect of the activation of the fabric substrate thanks to a plasma pre-treatment (plasma).*

Another order of magnitude drop is observed in the Ag released concentration passing from washing 5 to washing 10. Even after 10 washing cycles, Figure 77, AgCur shows significantly higher Ag release respect to the HEC based variants, with a silver load-dependent behavior still well observable. In conclusion, it is possible to state that the most promising solution for this application is the AgCur variant based on the washing fastness, the most important information will be provided by antimicrobial test. The plasma activation is ineffective for these samples, and the initial silver load requires a balance between coating activity, resistance, and silver release.

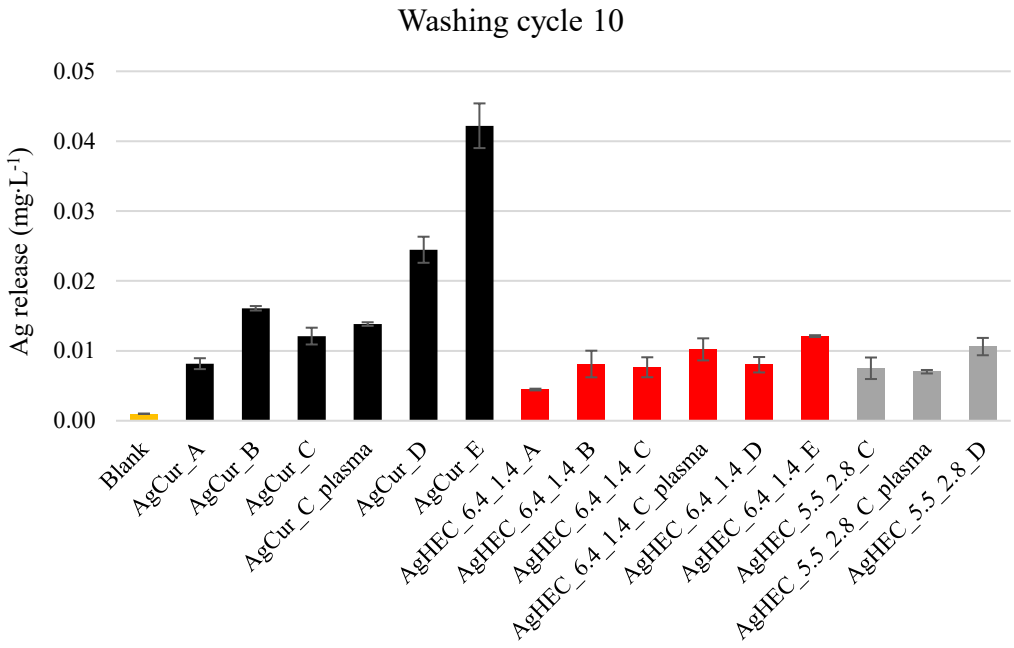


*Figure 77 – Concentration of the silver released after the tenth washing cycle of the medical-grade polyester textiles spray-coated by AgCur, AgHEC_6.4_1.4, or AgHEC_5.5_2.8 at a silver concentration of 1000 mg·L$^{-1}$ using different deposition conditions (A, B, C, C_plasma, D, and E), studying the effect of the activation of the fabric substrate thanks to a plasma pre-treatment (plasma).*

The silver released after washing cycle 1, 5, and 10 was compared with the initial silver load in the coatings. The percentage released of the total silver was calculated and the results are summarized in Table 41 and represented in the graphs in Figure 78.

*Table 41 – Silver release from AgCur, AgHEC_6.4_1.4, and AgHEC_5.5_2.8 spray-coated textiles after washing 1, 5, 10, and the total cumulative value, assessed by ICP-MS.*

| Spray-coated sample | Washing 1 Ag release (%) | Washing 5 Ag release (%) | Washing 10 Ag release (%) | Total Ag release (%) |
|---|---|---|---|---|
| AgCur_A | 43.46 | 5.57 | 0.72 | 49.76 |
| AgCur_B | 37.63 | 5.74 | 0.84 | 44.21 |
| AgCur_C | 32.37 | 3.90 | 0.59 | 36.87 |
| AgCur_C_plasma | 41.13 | 5.68 | 0.90 | 47.71 |
| AgCur_D | 35.15 | 4.48 | 0.94 | 40.56 |
| AgCur_E | 33.75 | 5.89 | 1.40 | 41.05 |
| AgHEC_6.4_1.4_A | 55.07 | 1.27 | 0.29 | 56.63 |
| AgHEC_6.4_1.4_B | 75.33 | 2.77 | 0.50 | 78.60 |
| AgHEC_6.4_1.4_C | > 100* | AgHEC_5.5_2.82.49 | 0.37 | > 100* |
| AgHEC_6.4_1.4_C_plasma | > 100* | 2.15 | 0.50 | > 100* |
| AgHEC_6.4_1.4_D | > 100* | 2.46 | 0.32 | > 100* |
| AgHEC_6.4_1.4_E | 65.05 | 2.70 | 0.34 | 68.10 |
| _C | > 100* | 2.04 | 0.43 | > 100* |
| AgHEC_5.5_2.8_C_plasma | > 100* | 1.44 | 0.37 | > 100* |
| AgHEC_5.5_2.8_D | > 100* | 2.63 | 0.51 | > 100* |

**Marked values resulted slightly higher than the theoretical 100 %, probably meaning that some inhomogeneties in the coating led to analyzed differently Ag loaded pieces of fabrics for the total Ag load repsect to the washing tests*

AgCur variant confirmed its better washing resistance and gradual silver release during the following washing cycles. About 35-40 % of starting silver is released during the first washing cycle, 5 % during the fifth, and 1 % during the tenth. AgHEC_6.4_1.4 spray-coating conditions A, B, and E revealed a higher release, 55-75 %, while for both AgHEC_6.4_1.4 and AgHEC_5.5_2.8, treatments C, C_plasma, and D demonstrated an anomalous behavior, with a nearly quantitative silver release during the first washing cycle, as if the coating was not strongly attached to the fabric substrate. HEC-based NPs have lower release after washing 5, 1-2 %, and even lower after washing 10, less than 0.5 %, confirming that most of the coating is detached during the first washings.

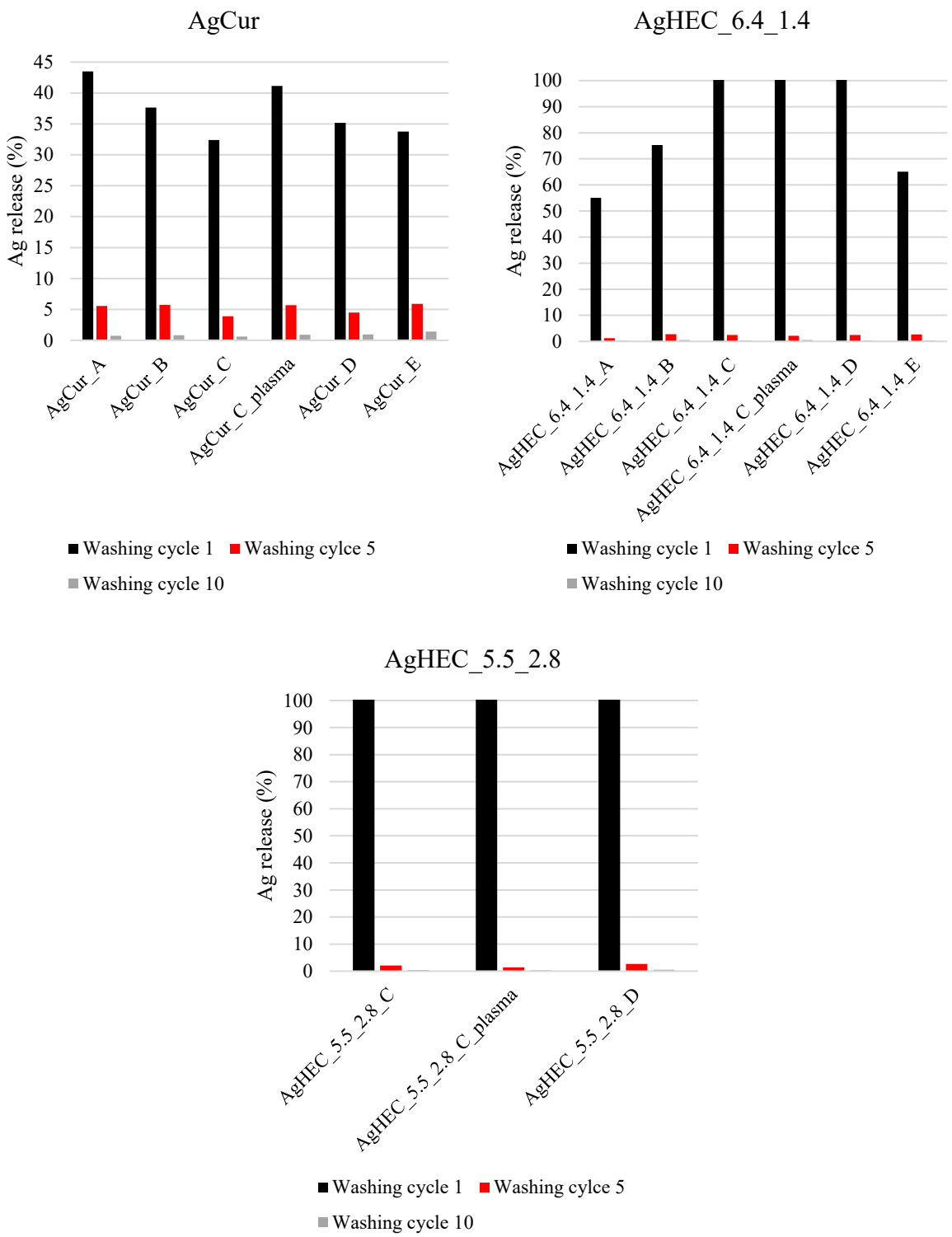


*Figure 78 – Percentage of the silver released respect to the initial load on the textiles spray-coated by AgCur, AgHEC_6.4_1.4, or AgHEC_5.5_2.8 with different spraying conditions (A, B, C, C_plasma, D, and E).*

Figure 79 reports SEM images of AgCur_D fabric after the first washing cycle. There aren't relevant damages on the textile, and it is possible to see deposited matter on the fibers. Even if about 35% of the initial silver Ag was released, from EDX analysis it was possible to confirm

the presence of silver, but the coating was less homogenous than the starting unwashed material, in fact after washing cycle 1 there were some regions where it was more difficult to detect the silver signal.

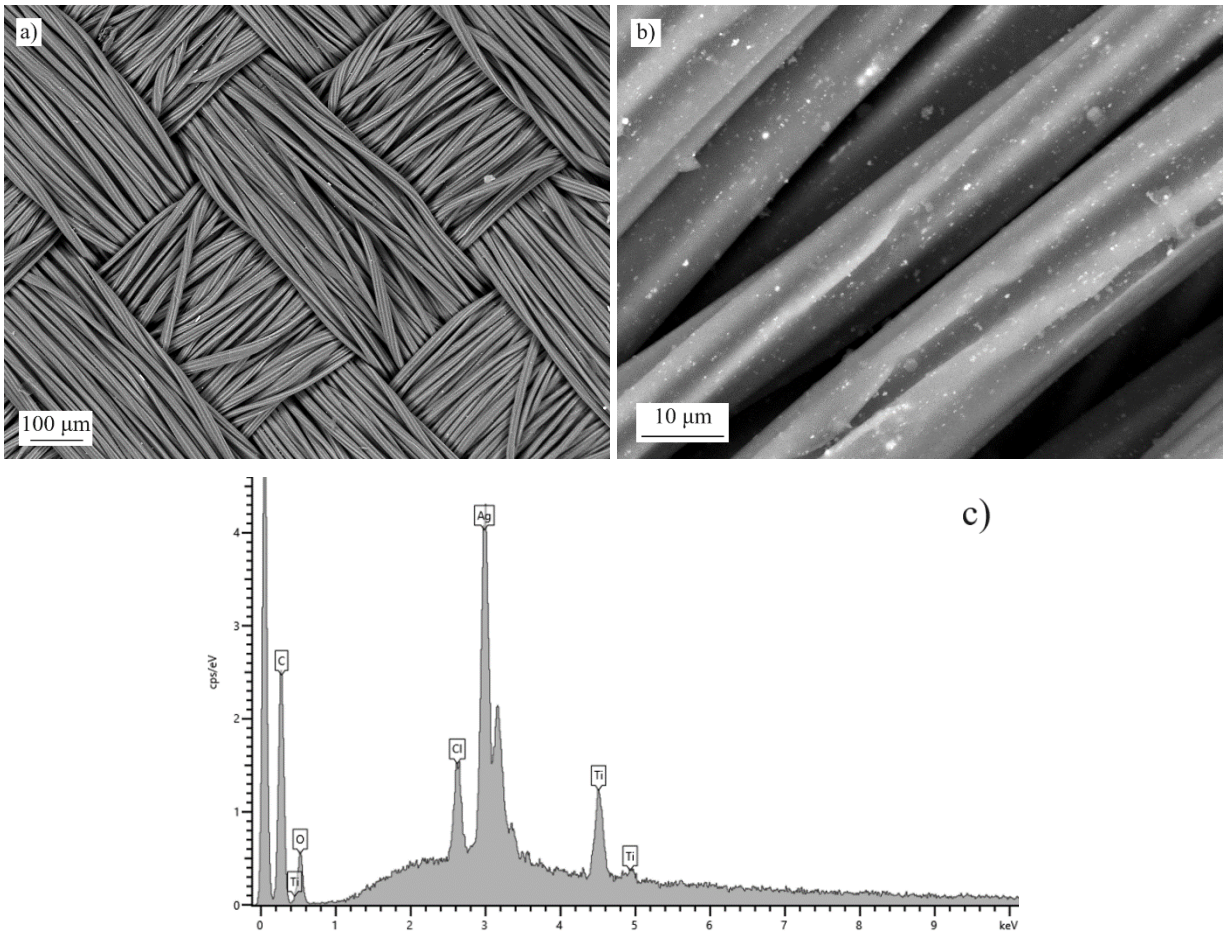


*Figure 79 – a) and b) SEM images of the spray-coated textiles by AgCur_D after the first washing cycle; c) EDX spectrum of the AgCur_D sample after the first washing cycle confirming the presence of silver as textile coating.*

***Use phase simulation on spray-coated samples, soft abrasion test*** – The dermal contact simulation performed by soft abrasion test confirms the results of washing tests. In fact, by the graphs represented in Figure 80, Figure 81, and Figure 82, repectively for AgCur, AgHEC_6.4_1.4, and AgHEC_5.5_2.8, it is possible to correlate washing and abrasion tests trends. The results are expressed as the concentration of silver released ($\mu g \cdot L^{-1}$ or ppb) detected by ICP-MS, normalized by the surface of fabric scanned during the test. The measurements were performed on fresh coated samples, and after washing cycle 1, and 10. As for previous results, the increasing initial silver load is also reflected in a higher release during abrasion, which also implies a higher human exposure during the use phase. This trend can be clearly observed in AgCur for all 3 sets of data, fresh, washing 1, and washing 10 (Figure 80), while for

AgHEC_6.4_1.4 can be better appreciated only for the firsts 2 sets (Figure 81). AgHEC_5.5_2.8 has a reduced roster, so it is difficult to elaborate these kind of behaviors (Figure 82). As further confirmation, AgCur has a gradual release behavior, granting a more durable antimicrobial effect of the coating, while HEC capped AgNPs tend to be released faster during both the washing cycles and also the abrasion tests. As it is possible to notice by comparing graphs in Figure 80 and Figure 81, the silver release during the abrasion on unwashed fabrics results about 50 % higher for AgHEC_6.4_1.4 than for AgCur. So, AgCur not only shows improved washing fastness but also abrasion resistance. This combination provides a more durable coating, and a longer time-diluted human exposure since there is not a massive release in the first stages of the use phase.

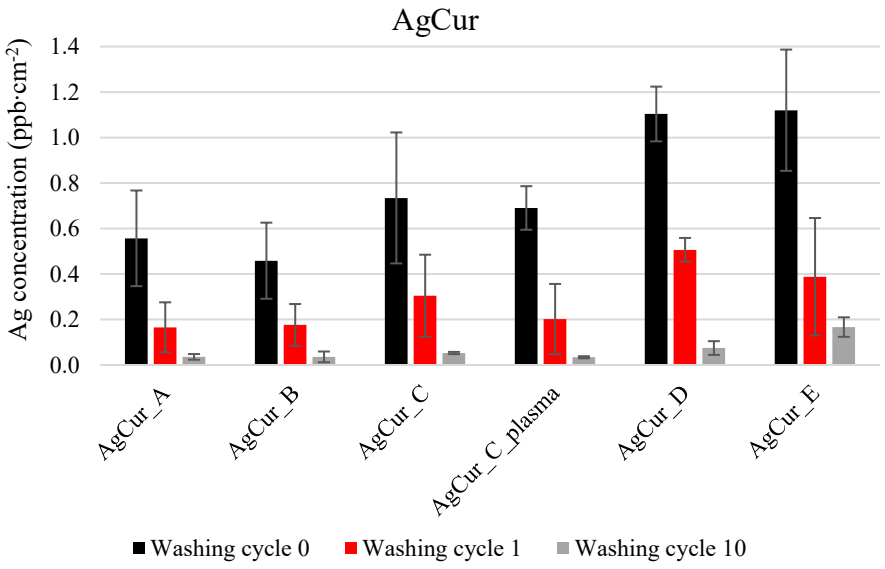


*Figure 80 – Soft abrasion test results of the textiles spray-coated by AgCur at a silver concentration of 1000 mg·L$^{-1}$, evaluating the different spray-coating conditions (A, B, C, C_plasma, D, and E) on the pristine material and after washing cycle 1 and 10. The amount of silver released by the coated textiles during the abrasion test is reported as silver concentration released normalized by the textile surface scanned (ppb·cm$^{-2}$).*

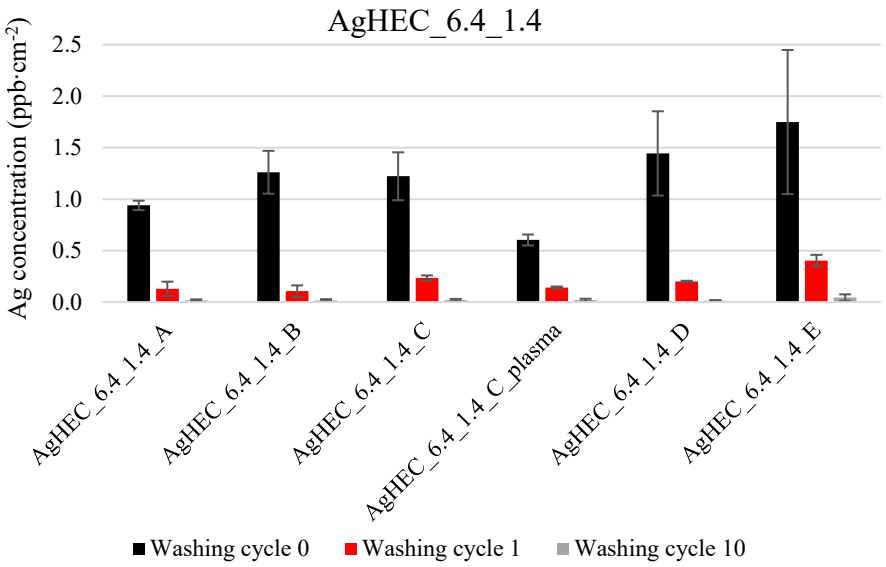


*Figure 81 – Soft abrasion test results of the textiles spray-coated by AgHEC_6.4_1.4 at a silver concentration of 1000 mg·L$^{-1}$, evaluating the different spray-coating conditions (A, B, C, C_plasma, D, and E) on the pristine material and after washing cycle 1 and 10. The amount of silver released by the coated textiles during the abrasion test is reported as silver concentration released normalized by the textile surface scanned (ppb·cm$^{-2}$).*

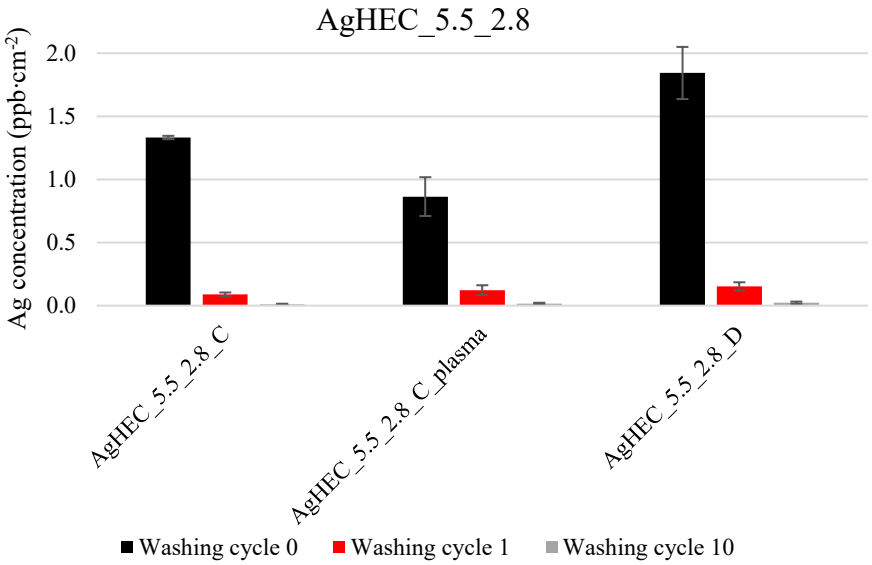


*Figure 82 – Soft abrasion test results of the textiles spray-coated by AgHEC_5.5_2.8 at a silver concentration of 1000 mg·L$^{-1}$, evaluating the different spray-coating conditions (C, C_plasma, and D) on the pristine material and after washing cycle 1 and 10. The amount of silver released by the coated textiles during the abrasion test is reported as silver concentration released normalized by the textile surface scanned (ppb·cm$^{-2}$).*

***Antibacterial test*** – The antimicrobial activity of the coated textiles was evaluated against *E. coli* Gram-negative and *S. aureus* Gram-positive bacteria. To simulate the use phase, the antibacterial

activity was assessed on pristine coated textile and after 1, 5, 10, and 15 washing cycles. In this way it, is possible to determine if the silver amount remaining attached after washing the coated fabric is enough to grant antimicrobial properties to the nano-enabled product.

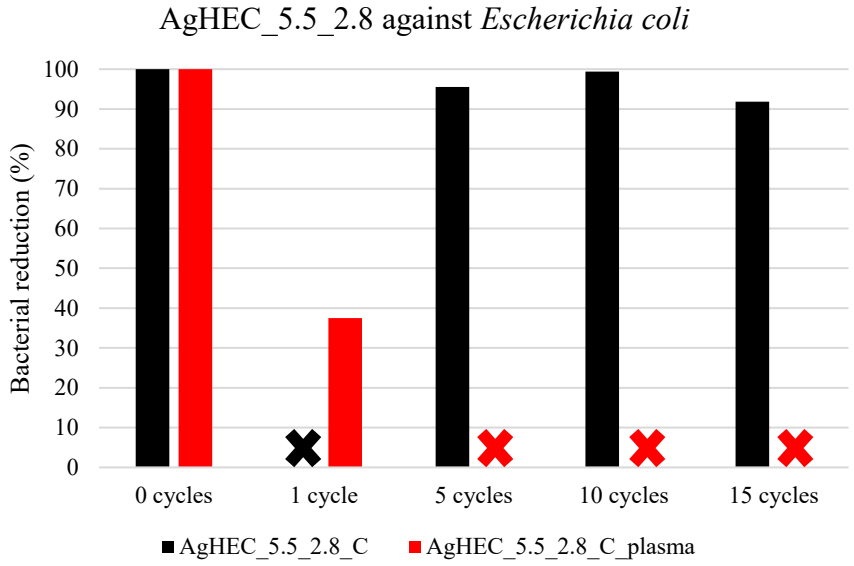


*Figure 83 – Antibacterial activity of AgHEC_5.5_2.8_C and AgHEC_5.5_2.8_C_plasma spray-coated textiles against E. coli. The tests were performed on the pristine materials and after washing cycle 1, 5, 10, and 15. Cross-marked results were not assessed.*

The washing test results previously reported, demonstrated different behavior depending on the capping agent. Curcumin based AgNPs give a gradual release over consecutive washing cycles, while quaternized hydroxyethyl cellulose based AgNPs show larger release during the first washing cycle. It is expected that these behaviors influence the antimicrobial properties of the products. As reported in the graph in Figure 83, tests assessed on AgHEC_5.5_2.8 against *E. coli*, using two different deposition conditions (C and C_plasma), demonstrated different trends depending on the plasma activation. In fact, the same deposition parameters were used to produce the two samples, the only difference is related to a plasma activation of the textile substrate for C_plasma. The plasma highlighted a detrimental effect on the performances, both the samples start with a 100 % bacterial reduction as pristine, but the plasma-activated counterpart (AgHEC_5.5_2.8_C_plamsa) demonstrates an important drop of performance already after the first washing cycle, while the equivalent sample non-treated with plasma preserve excellent antimicrobial properties even after 15 washing cycles, confirming a bacterial reduction over 90%. From these first results it is possible to state a detrimental effect of the plasma treatment on the washing fastness of the antimicrobial coating.

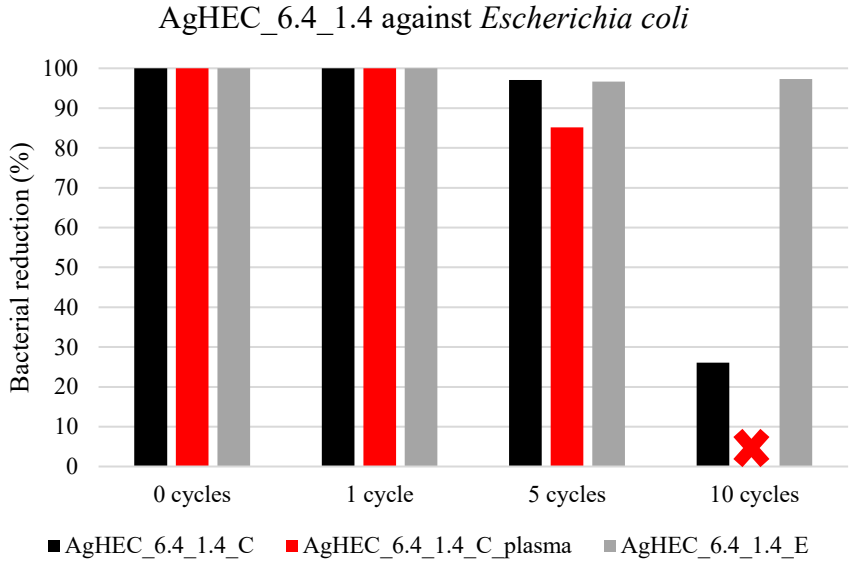


*Figure 84 – Antibacterial activity of AgHEC_6.4_1.4_C, AgHEC_6.4_1.4_C_plasma, and AgHEC_6.4_1.4_E spray-coated textiles against E. coli. The tests were performed on the pristine materials and after washing cycle 1, 5, and 10. Cross-marked results were not assessed.*

For AgHEC_6.4_1.4 three deposition conditions were tested, C and C_plasma were chosen for the evaluate the effect of plasma activation on this variant, while the condition E is the one that grants the higher silver load, the collected results are reported in Figure 84. AgHEC_6.4_1.4 has demonstrated to be the most active AgNPs variant tested against pathogens, in these tests exhibited for all the deposition conditions excellent antibacterial activity, with a quantitative depletion of *E. coli* (100 % bacterial reduction), as pristine coating and after the first washing cycle. After 5 washing cycles there is a slight decrease of performance with comparable results for samples C and E, while the same way as for AgHEC_5.5_2.8, the sample that underwent plasma activation (C_plasma) shows a faster deterioration of the coating, with consequent loss of antimicrobial activity. After 10 washing cycles, treatment E, the one with the highest silver load, preserves excellent antibacterial activity, while lower silver loaded sample C exhibits an important decrease in performance. From these tests the counterproductive effect of the plasma treatment is confirmed, and treatments with higher silver load grant more durable antimicrobial coatings.

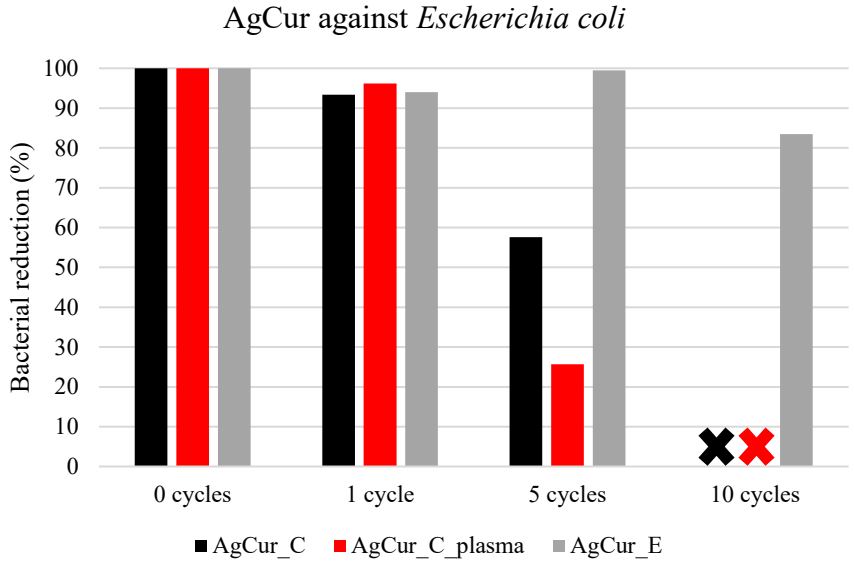


*Figure 85 – Antibacterial activity of AgCur_C, AgCur_C_plasma, and AgCur_E spray-coated textiles against E. coli. The tests were performed on the pristine materials and after washing cycle 1, 5, and 10. Cross-marked results were not assessed.*

Samples treated the same way as AgHEC_6.4_1.4 were tested for AgCur (C, C_plasma, and E), the results are reported in Figure 85. The same trends were observed, but in this case the activity is slightly reduced already after the first washing cycle homogenously for the three deposition conditions. Summarizing, the plasma treated sample (C_plasma) shows the worst performance after 5 washing cycles and the treatment with the highest silver load (E) grants the most durable coating in terms of antimicrobial properties.

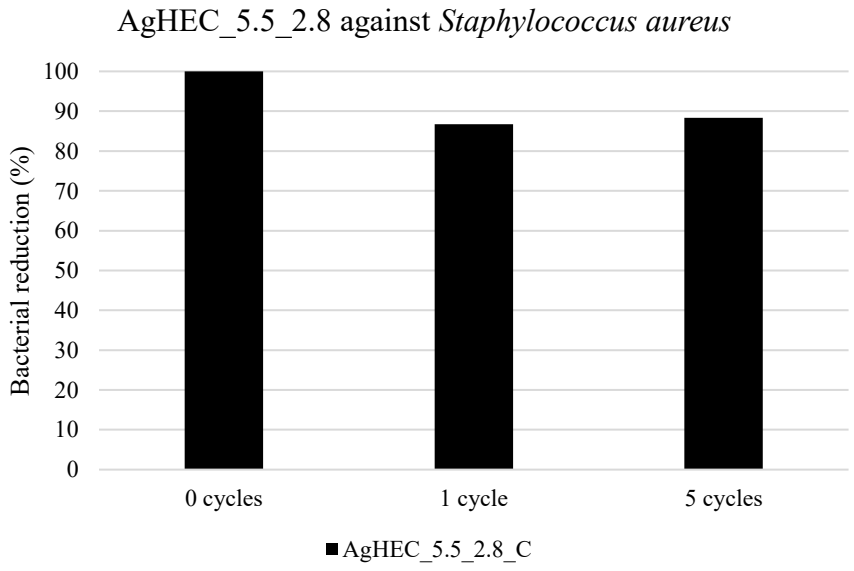


*Figure 86 – Antibacterial activity of AgHEC_5.5_2.8_C spray-coated textile against S. aureus. The tests were performed on the pristine materials and after washing cycle 1 and 5.*

Finally, the samples were tested against the Gram-positive *S. aureus* bacterium. All the pristine samples tested demonstrated excellent antibacterial activity with a 100 % bacterial reduction for AgHEC_5.5_2.8_C_plasma, AgHEC_6.4_1.4_C_plasma, AgHEC_6.4_1.4_E, AgCur_C, AgCur_C_plasma, and AgCur_E, and 99.5 % bacterial reduction for AgHEC_6.4_1.4_C. The sample AgHEC_5.5_2.8_C was selected for the study of the antibacterial activity after few washing cycles, results are reported in Figure 86. As it is possible to see, there is a slight depletion of performance, but after 5 washing cycles, it demonstrates still 88.3 % *S. aureus* reduction. AgHEC_5.5_2.8 demonstrated to produce an antibacterial coating active against both Gram-negative and Gram-positive bacteria with considerable washing fastness also with a lower silver load (deposition condition C respect to E).

To summarize the results of these antibacterial tests, AgHEC_6.4_1.4 resulted as the most active and durable coating when deposited with a high silver load (spray-coating condition E) even if from the washing test it resulted in a large amount of silver released already from the first cycle. Even AgCur exhibits excellent antibacterial activity and considerable washing fastness when deposited with a high silver load. AgHEC_5.5_2.8 demonstrated good antibacterial properties and durable coating already with a lower silver load (spray-coating condition C)

***Conclusions***

The project aimed to the development of Safe-by-Design strategies, alternatives, and procedures to be later translated into guidelines for future nanoproducts and nanoprocesses. The results here described were focused on the antimicrobial textiles case study, where silver nanoparticles were implemented in medical grade polyester fabrics. To achieve the goal different synthesis strategies were applied, modifying reagents molar ratios to enhance the antimicrobial activity of the product, or substituting the capping agent to confer different surface properties. In this perspective, AgHEC_5.5_2.8 and AgHEC_6.4_1.4 quaternized hydroxyethyl cellulose-capped silver nanoparticles, and AgCur curcumin-capped silver nanoparticles were studied as coating for the antimicrobial textiles. AgNPs suspension physicochemical and functional properties suggested AgHEC_6.4_1.4 as the most active solution associated with excellent performance of AgCur together with a reduced cytotoxicity. Nanophases processing and implementation into nano-enabled products passed through laboratory scale tests exploiting dip-coating technique, to subsequently scale-up to pilot plants equipped with spray-coater machines. The experimental conditions allowed to reach a higher silver load in the product obtained by dip-coating compared to spray-coating. The performed tests highlighted AgCur as the most durable coating, exhibiting the highest attachment to the fabric and the best washing fastness and abrasion resistance. While HEC capped variants showed high Ag release already from the first washing cycle, AgCur demonstrated a gradual release over repeated washing cycles. Higher silver load treatments resulted in more durable coatings for both dip-coated and spray-coated samples, and the plasma activation of the substrate before the coating production didn't show any benefit. For what concerns the antimicrobial coating similar trends were observed. All pristine samples pointed out quantitative or nearly quantitative antibacterial activity against both Gram-negative and Gram-positive bacteria. The plasma activation was detrimental to the antibacterial activity assessed after the washing cycles, and treatments granting higher silver load ensured more durable coatings. At high Ag load AgHEC_6.4_1.4 resulted as the most active and durable coating. AgHEC_5.5_2.8 showed an excellent preservation of the antimicrobial properties after washing already at medium Ag load treatments. AgCur, which is the variant promoting the best grafting, washing fastness, and abrasion resistance, ensures excellent antibacterial activity but compared to AgHEC_6.4_1.4 also has a higher performance loss after washing.

Based on the needs it is possible to select dip- or spray-coating, the former promoting higher silver load and the latter more suitable for tailored large scale production. The tested design alternatives promoted several improvements if compared to the starting AgNPs synthesis, in terms of antimicrobial activity, cytotoxicity, or coating activity and durability.

***Experimental part: antimicrobial textiles***

***Dip-coating*** – Laboratory scale samples production started from the preparation of the substrate. Medical grade polyester fabric was cut into 5·12 $cm^2$ rectangular pieces, then to favor the coating gripping they were washed with Milli-Q water and soap by sonication for 20 minutes, then 3 times with only Milli-Q water and 5 minutes of ultrasound, finally they were rinsed 3 times with Milli-Q water. Fabrics were dried at room temperature overnight before the coating deposition. In order to improve the performance of the product and to favor the adhesion of AgNPs on the fabric, samples number was duplicated and half of them was pre-treated with plasma activation with a 200 W treatment for 2 minutes immediately before the dip-coating. The selected samples were AgHEC_5.5_2.8, AgHEC_6.4_1.4, and AgCur, with the corresponding blank suspensions HEC_5.5_2.8, HEC_6.4_1.4, and Cur. Two concentrations were tested, 1000 $mg \cdot L^{-1}$ and 500 $mg \cdot L^{-1}$ concentrated silver baths were used to dip of fabric to obtain different silver load on the coating, and subsequently better antimicrobial properties and coating resistance and stability. The coating deposition was obtained by 3 minutes immersion time and followed by the removal of the exceeding suspension squeezing the samples with the help of two rollers. The dip-coating was followed by a thermal treatment at 80 °C for 10 minutes to dry the fabric and consolidate the coating. The entire process is schematized in Figure 87. The untreated washed fabric was used as reference for the analysis.

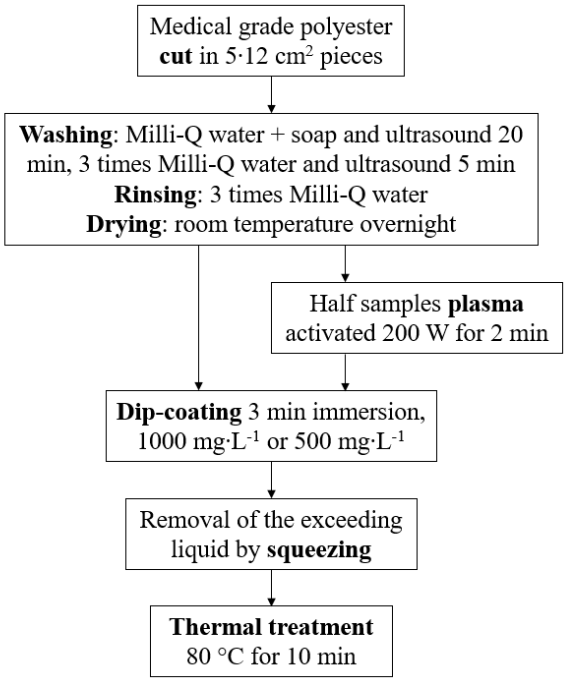


*Figure 87 – Schematic procedure for the preparation of AgNPs dip-coated antimicrobial textiles.*

***Spray-coating*** – A first spray-coating campaign was carried out at pilot plants scale focused on finding optimal spraying conditions and to correlate this information to the activity and durability of the coating. In this case only AgHEC_5.5_2.8 and its blank HEC_5.5_2.8 were used as coating agents at the two selected concentrations 1000 mg·L$^{-1}$ and 500 mg·L$^{-1}$. About 2 m$^2$ fabrics could be processed in continuous thanks to the productive line where automated rolls moved the samples from the plasma pre-treatment surface activation, to the spraying chamber, and finally through the oven for the final drying and consolidation of the coating at 80 °C. Rolls speed could be regulated independently to select the duration of each step. For these samples the spray flow rate was tested at 200 and 400 mL·min$^{-1}$, to achieve different silver load and properties.

A second pilot plant spray-coating campaign was conducted in another pre-industrial plant implementing all the three silver variants selected AgHEC_5.5_2.8, AgHEC_6.4_1.4, and AgCur. In this case only the 1000 mg·L$^{-1}$ silver concentration was considered and a shorter 80 °C thermal treatment was used, for a better consolidation a second 80 °C for 10 minutes thermal treatment is suggested for these samples. For each variant, 6 samples were produced varying the spray flow rate (60 and 80 mL·min$^{-1}$), the conveyor belt speed (2, 4, and 6 m·min$^{-1}$), and just one sample for each AgNPs composition was produced implementing the plasma activation. Both smaller (21·30 cm$^2$) and longer (tens of meter) fabrics were used for the production of nano-enabled products.

During these field tests a worker exposure monitoring campaign were assessed evaluating the particulate matter released during the whole days of experimental activities. The scheme of the spray-coating process is represented in Figure 88.

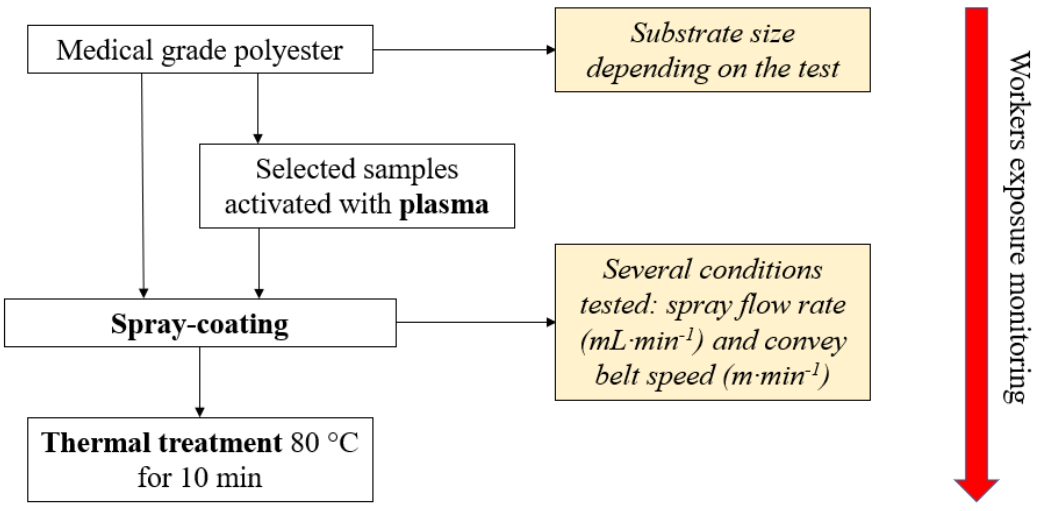


*Figure 88 – Schematic procedure for the preparation of AgNPs spray-coated antimicrobial textiles.*

***Washing test***s – Tests were conducted following the "ISO 105-C06 (A1S) for color fastness to domestic and commercial laundering (2010)" with a lab washing machine (Linitest Plus, Atlas Electrical Device); 30 minutes, 40 °C, motor speed 40 ± 1 rpm, stainless steel vessels (75 ± 5 mm diameter, 125 ± 10 mm height, 550 ± 50 mL)) and a washing solution of 4 ± 0.01 $g \cdot L^{-1}$ ECE Color Fastness Test Detergent 77 in deionized water (pH 10) and ten stainless steel ball (Ø = 0.6 cm) to simulate the mechanical energy applied by friction to the textiles. Five pieces of textile were cut with an area of 40 $cm^2$ per piece and stacked in the vessel. A volume of 150 mL of washing solution, preheated at 40 °C, was added to the vessel, together with the steel balls and the textiles. After the washing process, the washing water was collected and the textiles were rinsed one by one dipping them three times in 100 mL of deionized water. Once this step was finished, the water was renewed to avoid the accumulation of silver. Finally, the textiles were dried overnight at room temperature. To study the form and size of the NPs released, the washing water was filtered from textile fibers (pore size 20 µm) and stored for electron microscopy characterization (TEM and SEM) and silver quantification by using ICP-MS. Tests were conducted by repeating washing cycles 0 (untreated), 1, 5 and 10 times on the same pieces of textile to evaluate the washing fastness.

***Soft abrasion test*** – The soft abrasion test to simulate textile-skin contact was based on an adaptation of "ISO 105 X12:2016 - Part X12: Colour fastness to rubbing". The test was performed using a crock meter (302-P, JBA). The equipment applies a low-energy wearing (9 N) on a 10 cm long surface by a cylindric tip (ø = 16 mm) covered with a cotton tissue. 40 $cm^2$ cut textiles used for washing cycles were attached by double face tape into the dedicated spot for the rubbing. A cotton napkin was impregnated with 5 drops of a simulated sweat solution buffered with ammonium hydroxide to pH 6.5, before covering the crock-meter tip. A total of 10 rubbing cycles (1 $second \cdot cycle^{-1}$) were done, triplicates were performed to unwashed textiles (0 cycles) and washed textiles after 1, 5 and 10 washing cycles. Characterization was performed on the rubbered textiles (remaining NM concentration) and the cotton tissue (NM release receiving compartment) using ICP-MS and SEM techniques.

### 4.1.2. Antimicrobial paper

This chapter describes a tiered approach aimed at the implementation of active nanophases in paper-based nano-enabled products (NEPs). In particular, antimicrobial silver nanoparticles were used to produce antibacterial and antiviral coatings. First, a screening of the physicochemical and antimicrobial properties of several AgNPs synthesis was assessed in order to select the most promising alternatives. The selected variants were implemented as coating and the obtained nano-enabled products were tested in terms of antimicrobial properties, coating durability, aesthetical properties, and user safety. Subsequently, the scale-up of the process was performed moving from laboratory scale dip-coating of small paper substrates towards pre-industrial trials carried out by roll-to-roll printing incrementing the size of the samples and the overall productivity of the process. A conceptual map of the project is represented in Figure 89.

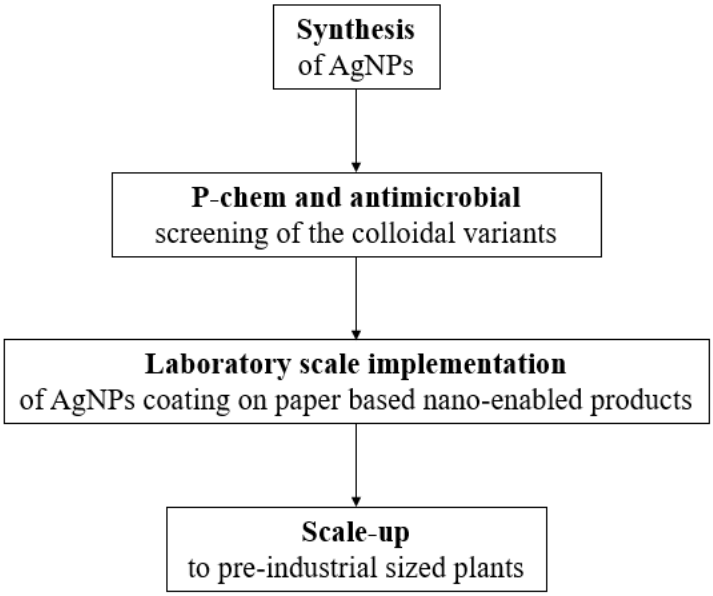


*Figure 89 – Schematic concept map of the preparation of paper-based antimicrobial nano-enabled products.*

***Colloidal level screening of the most promising solutions***

The eco-friendly and easily scalable syntheses of silver nanoparticles based on quaternized hydroxyethyl cellulose (AgHEC) and curcumin (AgCur), were implemented in the production of antimicrobial paper. The scope is to apply an antimicrobial and durable nanocoating on paper-based materials with high circulation rate to reduce the transmission of pathogens, like viruses and bacteria.

***Physicochemical characterization of sols*** – Both quaternized hydroxyethyl cellulose (HEC) and curcumin (Cur) are benign regents with intrinsic antimicrobial properties that have been used as reducing and stabilizing agents during the synthesis of AgNPs. A set of 12 variants, described in Table 42, was selected as a starting point for the investigations. Each product was studied by changing the main synthesis parameters: reagent molar ratios, reaction temperature, solvent composition, or adding new components such as casein or chitosan.

These syntheses were deeply explored and their optimization is described in Chapter 3. Briefly, widespread physicochemical characterization allowed to evaluate the quality of the prepared suspensions. A key aspect to promote an optimal deposition is a good colloidal stability, for quaternized hydroxyethyl cellulose capped nanoparticles the stability was granted only for molar ratios HEC/Ag 2.8 or greater. AgHEC exhibited positive surface charge thanks to the quaternary ammonium functionalities, while AgCur is negative, the two opposite charged particles offer the possibility to investigate different biological interactions with pathogen. TEM analysis showed spheroidal nanoparticles with average diameter in the range 10-20 nm. Based on the physicochemical properties and the stability, some variants were selected for the antimicrobial tests against both bacteria and viruses.

*Table 42 – Description of the set of 12 AgNPs variants proposed for this study.*

| Sample | Ag concentration ($mg \cdot L^{-1}$) | Description |
|---|---|---|
| AgHEC_5.5_2.8 | 5000 | Quaternized hydroxyethyl cellulose AgNPs, standard molar ratios: HEC/Ag 5.5, NaOH/Ag 2.8 |
| AgHEC_1.4_2.8 | 5000 | Quaternized hydroxyethyl cellulose AgNPs, molar ratios HEC/Ag 1.4, NaOH/Ag 2.8 |
| AgHEC_2.8_1.4 | 5000 | Quaternized hydroxyethyl cellulose AgNPs, molar ratios HEC/Ag 2.8, NaOH/Ag 1.4 |
| AgHEC_2.8_2.8 | 5000 | Quaternized hydroxyethyl cellulose AgNPs, molar ratios HEC/Ag 2.8, NaOH/Ag 2.8 |
| AgHEC_6.4_1.4 | 5000 | Quaternized hydroxyethyl cellulose AgNPs, molar ratios HEC/Ag 6.4, NaOH/Ag 1.4 |
| AgHEC+Chit 1:1 | 2500 | AgHEC_5.5_2.8 mixed with chitosan* in weight ratio 1:1 |
| AgHEC+Chit 1:2 | 1700 | AgHEC_5.5_2.8 mixed with chitosan* in weight ratio 1:2 |
| AgHEC+Chit 2:1 | 3300 | AgHEC_5.5_2.8 mixed with chitosan* in weight ratio 2:1 |
| AgCur | 5000 | Curcumin capped AgNPs |
| AgCur_Cas | 5000 | Curcumin and casein capped AgNPs |
| AgCur_EtOH | 5000 | Curcumin capped AgNPs synthesized in ethanol at room temperature |
| AgCur_EtOH_70 | 5000 | Curcumin capped AgNPs synthesized in ethanol at 70 °C |

**Chitosan (CAS Number 9012-76-4) Sigma-Aldrich (Product Number C3646), dispersed in a 1 %wt solution of acetic acid (CAS Number 64-19-7) Sigma Aldrich (Product Number 695092)*

***Antimicrobial test in sol*** – Antibacterial and antiviral results together with the cytotoxicity of the colloidal AgNPs suspensions are reported in Chapter 3.2.4. Briefly, AgHEC_6.4_1.4 emerged as the most active sample against both Gram-negative *E. coli* and Gram-positive *S. aureus* bacteria, ensuring 99.99-99.999% bacterial reduction tested at 50 $mg \cdot L^{-1}$. AgCur as well exhibited excellent antibacterial properties ensuring 99.99% bacterial reduction tested at 50 $mg \cdot L^{-1}$. Moreover, AgCur demonstrated minimal *in-vitro* cytotoxic effects on Vero E6 cells with

a $CC_{50}$ of 629.7 $mg \cdot L^{-1}$. AgCur pointed out excellent antiviral activity against SARS-CoV-2 Omicron BA.2 variant resulting in an outstanding selectivity index of 75.9.

***Laboratory scale production of nano-enabled products by dip-coating***

Based on physicochemical and functional results, a reduced set of 7 AgNPs variants was selected for the implementation as antimicrobial coating. These 7 samples and their corresponding blank solution (same composition but Ag 0 $mg \cdot L^{-1}$) were deposited by dip-coating on paper substrates simulating paper-based materials with high circulation rate at 3 different concentrations 1000, 500, and 100 $mg \cdot L^{-1}$. In a further selection step, only 5 variants were deposited at two dilutions, 100 and 50 $mg \cdot L^{-1}$, and the resulting products were tested in terms of antibacterial and antiviral activity in order to find the minimum effective concentration. In parallel, physicochemical characterizations were carried out on the same samples: colorimetric performance evaluation via CIELAB parameters comparison before and after the coating deposition, coating homogeneity by electron microscopy coupled with energy dispersive x-ray spectroscopy (FESEM-EDX), ICP-OES quantification of the Ag deposited, and $Ag^{+}$ ion release from the coated substrates once exposed to relevant simulating fluid for the use phase. A schematic illustration of the variant selection process is reported in Figure 90.

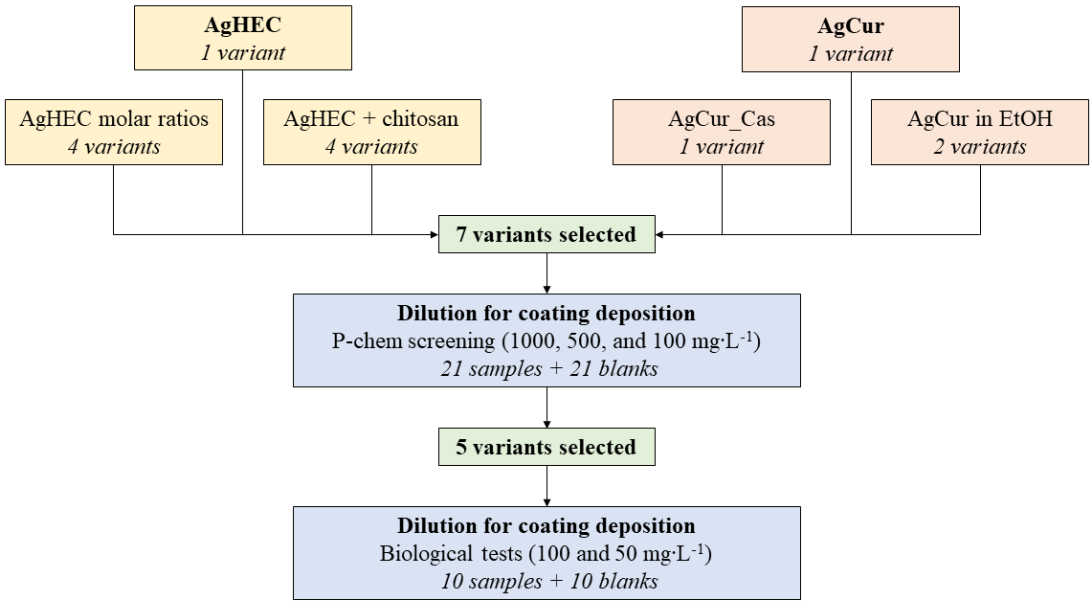


*Figure 90 – Schematic workflow describing the quaternized hydroxyethyl cellulose- and curcumin-based AgNPs variants selection process for the dip-coating depositions.*

During the first laboratory scale trials, the dip-coating technique was selected to deposit a thin layer of nanoparticles on the substrates, freshly dip-coated samples are represented in Figure 91.

*Figure 91 – Image representing the dip-coating deposition of AgNPs on paper substrates at different silver concentrations.*

***Colorimetric evaluation*** – For a real application of this technology, it is important to evaluate the quality of the coating in terms of homogeneity and aesthetical performance. A higher sample concentration leads toward a stronger yellow coloration due to the typical yellow color of AgNPs. A colorimetric evaluation was assessed by analyzing the CIELAB coordinates of the untreated paper and the coated samples. CIELAB coordinates were applied to provide a solid color descriptor involving 3 parameters: lightness, red-green color axis "a", and yellow-blue axis "b". While ΔE is the calculated total color variation. Table 43 reports the colorimetric parameter of the different paper-based samples produced at different concentrations.

As expected, the main colorimetric variation occurred along "b" axis, this parameter shifted toward positive values due to the typical yellow color of AgNPs, smaller variations toward red were detected for "a" axis and a negative delta was observed for the lightness "L". By analyzing ΔE values, the curcumin-based coatings determined smaller variations than hydroxyethyl cellulose-based ones, despite the curcumin orange color. Decreasing the HEC load in samples AgHEC_2.8_2.8 and AgHEC_2.8_1.4 provided a ΔE reduction. Casein was responsible of a brownish shade in AgCur_Cas samples, while AgHEC_2.8_1.4 turned grey, due to particles coarsening and microscopic precipitation, consistent phenomenon with the redshifted UV-Vis resonance band and with the reduced reaction yield. In general, higher diluted suspension (100 $mg \cdot L^{-1}$) led to a lower Ag load on the paper and so a limited color variation of the final product, as it is possible to see in Figure 92.

*Table 43 – Colorimetric analysis results of the paper substrates coated with the selected AgNPs variants at 3 different concentrations: 100, 500, and 1000 mg·L$^{-1}$. The results are reported as difference (Δ) respect to the untreated paper substrate.*

| **100 mg·L$^{-1}$ samples** | **ΔL** | **Δa** | **Δb** | **ΔE** |
|---|---|---|---|---|
| AgHEC_5.5_2.8 | -3.77 | -0.01 | 12.42 | 12.98 |
| AgCur | -2.89 | 0.48 | 7.74 | 8.28 |
| AgCur_Cas | -3.55 | 1.30 | 8.00 | 8.85 |
| AgHEC_2.8_2.8 | -2.94 | -0.57 | 11.00 | 11.40 |
| AgHEC_2.8_1.4 | -3.34 | -0.16 | 5.20 | 6.18 |
| AgCur_EtOH | -2.71 | -0.10 | 8.70 | 9.11 |
| AgCur_EtOH_70 | -2.82 | -0.28 | 9.11 | 9.54 |
| **500 mg·L$^{-1}$ samples** | **ΔL** | **Δa** | **Δb** | **ΔE** |
| AgHEC_5.5_2.8 | -10.71 | 3.37 | 31.22 | 33.17 |
| AgCur | -10.81 | 5.28 | 20.87 | 24.09 |
| AgCur_Cas | -9.30 | 4.61 | 13.42 | 16.96 |
| AgHEC_2.8_2.8 | -8.66 | 2.07 | 24.17 | 25.76 |
| AgHEC_2.8_1.4 | -14.78 | 0.50 | 12.10 | 19.11 |
| AgCur_EtOH | -10.49 | 5.01 | 21.20 | 24.17 |
| AgCur_EtOH_70 | -10.06 | 3.53 | 22.76 | 25.14 |
| **1000 mg·L$^{-1}$ samples** | **ΔL** | **Δa** | **Δb** | **ΔE** |
| AgHEC_5.5_2.8 | -17.53 | 8.34 | 42.70 | 46.90 |
| AgCur | -17.23 | 9.51 | 23.84 | 30.91 |
| AgCur_Cas | -14.74 | 6.93 | 14.32 | 21.69 |
| AgHEC_2.8_2.8 | -15.05 | 6.36 | 29.27 | 33.52 |
| AgHEC_2.8_1.4 | -24.59 | 5.15 | 21.31 | 32.94 |
| AgCur_EtOH | -16.85 | 8.84 | 26.33 | 32.49 |
| AgCur_EtOH_70 | -17.43 | 8.95 | 26.46 | 32.93 |

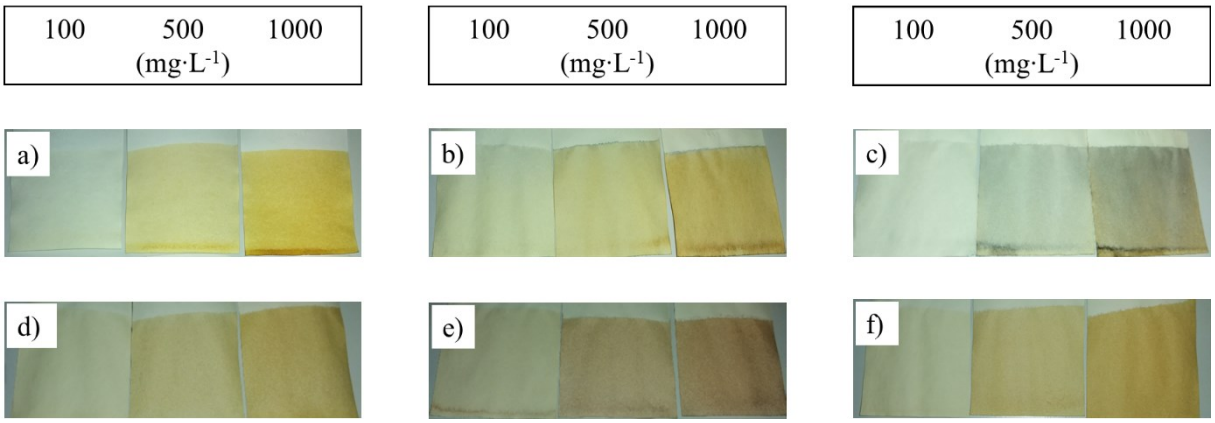


*Figure 92 – Paper substrates dip-coated by AgNPs at a concentration of 100, 500, or 1000 mg·L$^{-1}$. a) AgHEC_5.5_2.8; b) AgHEC_2.8_2.8; c) AgHEC_2.8_1.4; d) AgCur; e) AgCur_Cas; and f) AgCur_EtOH.*

This project aims to identify the most active AgNPs and optimal Ag content to achieve the best compromise between color variation and antimicrobial activity. For this reason, latest steps focused on 5 variants implemented the most diluted sol concentrations: 100 and 50 mg·L$^{-1}$.
AgHEC+Chit samples were prepared to mitigate the yellow color determined by AgHEC diluting the suspension with chitosan, which is a transparent biopolymer with intrinsic antimicrobial properties. The final diluted Ag concentration is 50 mg·L$^{-1}$, the lowest tested. The colorimetric values are reported in Table 44, there is a slight reduction in terms of ΔE, about 4 points, this may be a good result, but the information has to be combined with antibacterial and antiviral results to understand if the coupling of chitosan with AgNPs brings the desired advantages.

*Table 44 – Colorimetric analysis results of the paper substrates coated with the AgNPs variants containing chitosan in different weight ratio at a concentration of 50 mg·L$^{-1}$. The results are reported as difference (Δ) respect to the untreated paper substrate.*

| **50 mg·L$^{-1}$ samples** | ΔL | Δa | Δb | ΔE |
|---|---|---|---|---|
| AgHEC+Chit 1:1 | -3.13 | 1.47 | 8.56 | 9.23 |
| AgHEC+Chit 1:2 | -3.04 | 1.53 | 8.39 | 9.06 |
| AgHEC+Chit 2:1 | -3.42 | 1.44 | 8.09 | 8.90 |

***Silver load quantification*** – The quantification of the silver deposited on the coated samples have been performed by ICP-OES. To investigate the capabilities of different nanoparticles to coat the paper substrate adopted, a set of AgHEC_5.5_2.8, AgHEC_2.8_2.8, and AgCur at different concentrations was acidic digested, filtered, and then analyzed. Results are reported in Table 45 as milligrams of Ag detected per gram of coated paper digested.

*Table 45 – Quantification of the silver load deposited on the paper substrates assessed by ICP-OES.*

| Sample | Ag sol concentration ($mg \cdot L^{-1}$) | Ag deposited ($mg \cdot g^{-1}$) |
|---|---|---|
| Blank (untreated paper) | 0 | 0.008 ± 0.006 |
| AgHEC_5.5_2.8 | 100 | 0.1143 ± 0.0001 |
| AgHEC_5.5_2.8 | 500 | 0.0909 ± 0.0004 |
| AgHEC_5.5_2.8 | 1000 | 0.886 ± 0.009 |
| AgHEC_2.8_2.8 | 1000 | 0.311 ± 0.002 |
| AgCur | 100 | 0.063 ± 0.003 |
| AgCur | 500 | 0.057 ± 0.002 |
| AgCur | 1000 | 0.043 ± 0.003 |

The untreated paper confirms not to have silver, the detected value is comparable with the associated error and close to the detection limit of the instrument. AgHEC_5.5_2.8 showed comparable Ag load at the two lower concentrations (100 and 500 $mg \cdot L^{-1}$), about 0.1 $mg \cdot g^{-1}$. This behavior is in slight contrast with the colorimetric data which evidenced a more linear correlation between the sol concentration and the coated paper color. Potentially, some deviation may be due to sample manipulation during digestion and filtration steps. An important increase in silver content is detected for AgHEC_5.5_2.8 1000 $mg \cdot L^{-1}$ reaching about 0.9 $mg \cdot g^{-1}$. AgHEC_2.8_2.8 applied at 1000 $mg \cdot L^{-1}$ determined a silver load about 0.3 $mg \cdot g^{-1}$, lesser than AgHEC_5.5_2.8 at the same concentration, probably because sample AgHEC_2.8_2.8 contains a halved amount of cellulose, which may play a key role in the coating attachment mechanisms. Apparently, AgCur coated samples highlighted a silver loading behavior not dependent on AgCur sol concentration. All AgCur samples contained about 0.05 $mg \cdot g^{-1}$. For AgCur, as well as for AgHEC_5.5_2.8, these data are not well aligned with the colorimetric values. Anyway, data collected pointed out a general higher affinity of AgHEC than AgCur for the paper substrate, condition probably stemmed from the presence of hydroxyethyl cellulose, acting as grafting additive toward the paper for AgHEC samples.

***Electron microscopy morphology and coating distribution evaluation*** – To investigate the morphology and the distribution of the coatings, the samples were observed by field emission electron microscope coupled with an energy dispersive x-ray probe (FESEM-EDX). The identification of AgNPs by FESEM was very difficult due to the embedding in the organic

capping agent and the deposition on the fibrous matrix, but the silver presence was confirmed by EDX spectra. All the coated samples were analyzed but the ones coated with the highest concentrated suspension (1000 mg·L$^{-1}$) gave more appreciable results, revealing the presence of AgNPs covering the cellulose fibers. As example are reported the untreated paper substrate (Figure 93), and the samples coated with AgHEC_5.5_2.8 500 mg·L$^{-1}$ (Figure 94 and Figure 95), and AgCur 1000 mg·L$^{-1}$ (Figure 96).

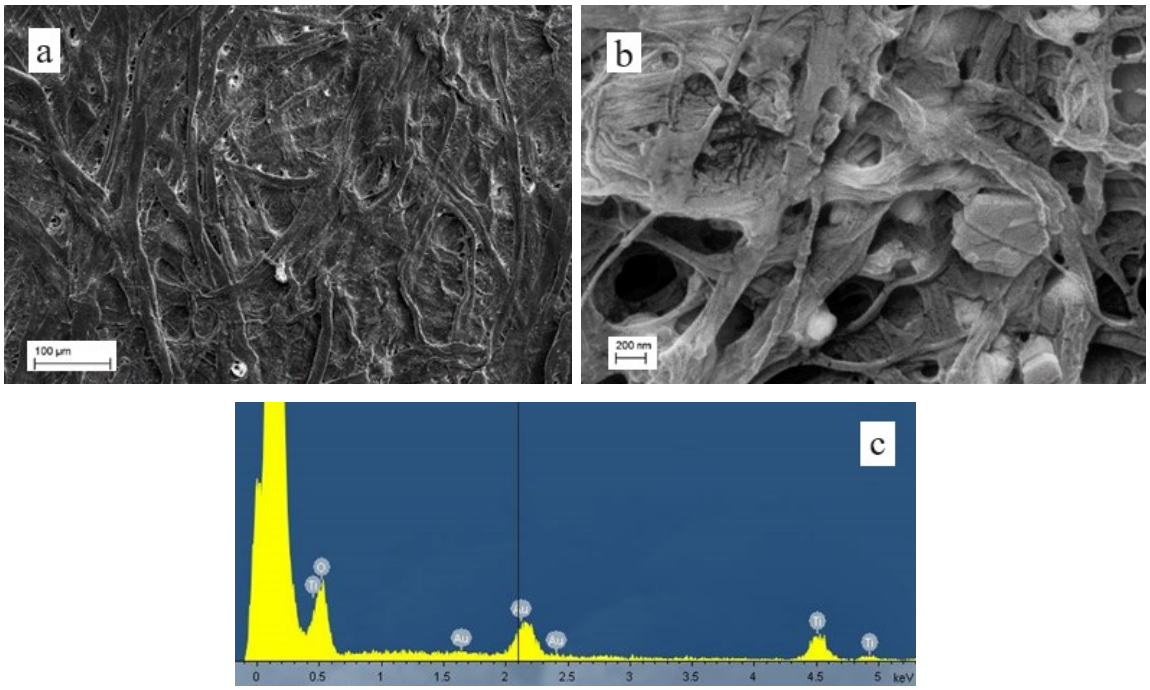


*Figure 93 – Uncoated paper substrates: a) and b) SEM images; c) EDX spectrum.*

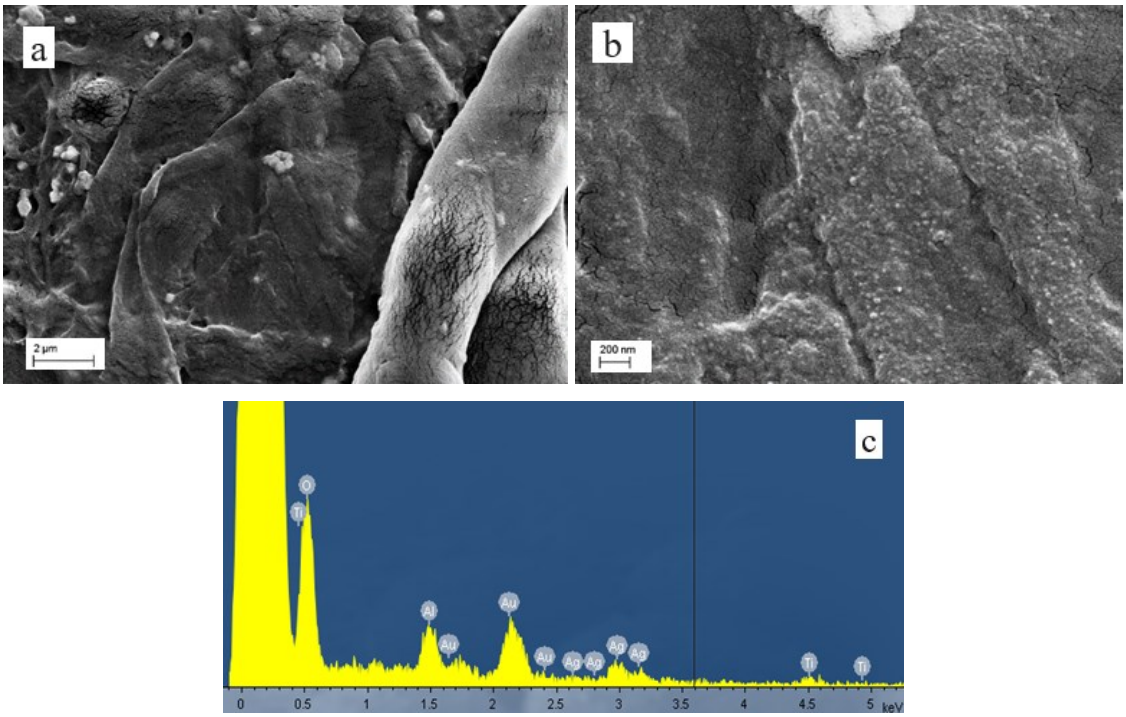


*Figure 94 – Sample coated by AgHEC_5.5_2.8 at a silver concentration of 500 mg·L$^{-1}$: a) and b) SEM images; c) EDX spectrum.*

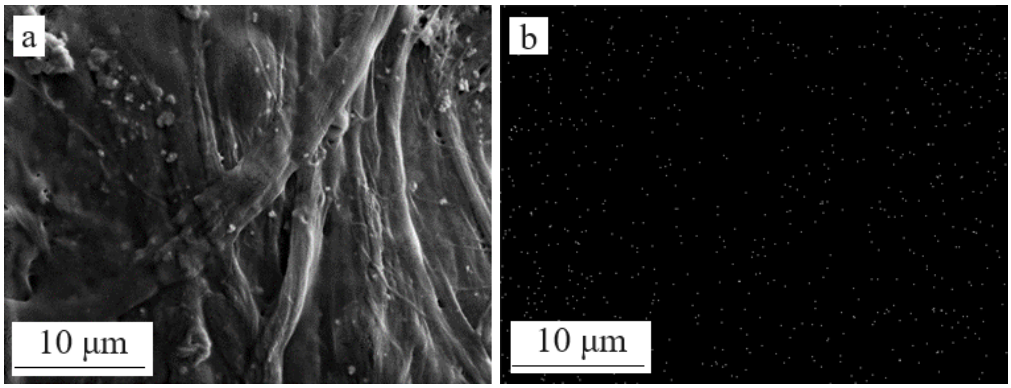


*Figure 95 – Sample coated by AgHEC_5.5_2.8 at a silver concentration of 500 mg·L$^{-1}$: a) SEM image; c) corresponding EDX silver distribution map.*

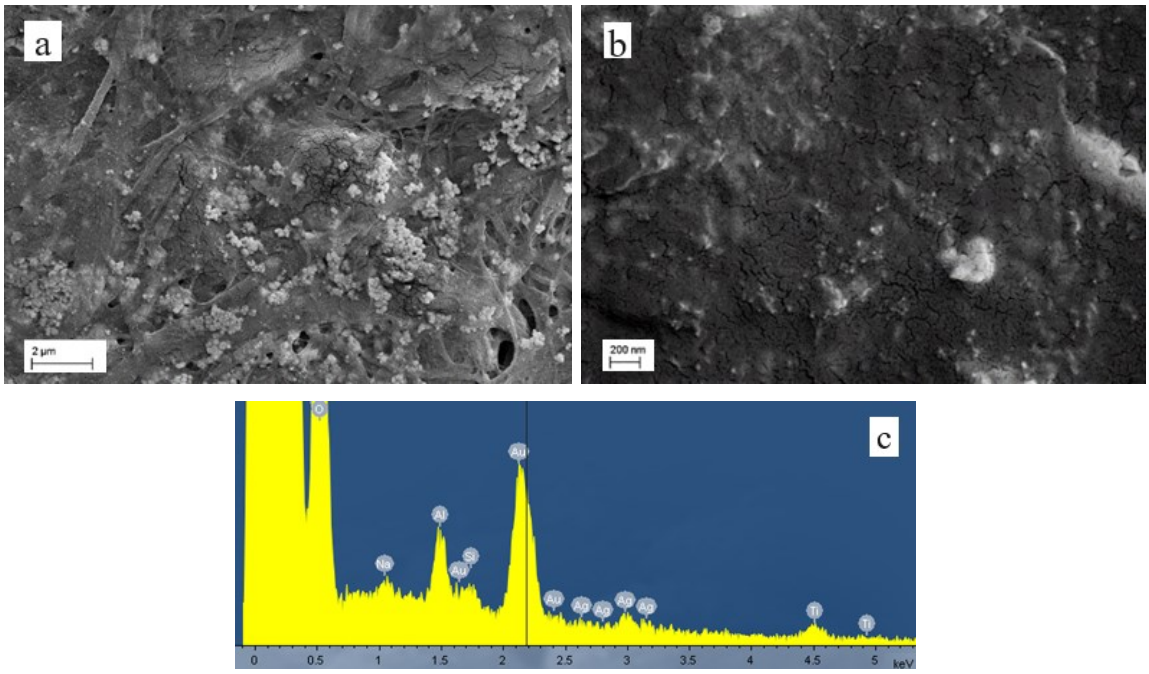


*Figure 96 – Sample coated by AgCur at a silver concentration of 1000 mg·L$^{-1}$: a) and b) SEM images; c) EDX spectrum.*

Uncoated samples (Figure 93) highlighted the typical fibrous microstructure of cellulosic paper, the EDX showed the presence of Au sputtered on the sample to increase its conductibility, Ti was also observed, probably under $TiO_2$ form to enhance paper's brightness. The samples coated by AgHEC_5.5_2.8 500 mg·L$^{-1}$ (Figure 94) showed the presence of the coating on the fibers, highlighted by some cracks on the surface, probably produced during the rapid water evaporation occurred during the heating treatment of the hydroxyethyl cellulose matrix or by the electron beam susceptibility of the hydroxyethyl cellulose embedding agent. The images collected at higher magnifications evidenced the presence of well dispersed white dots covering the fibers and consistent in size and shape with AgNPs. EDX spectra and maps (Figure 95) collected on different areas of the sample confirmed the presence of Ag homogenously distributed on the paper surface. The same situation was observed on AgCur 1000 mg·L$^{-1}$ coated sample (Figure 96).

***Dissolution test*** – To collect some preliminary information regarding the safety of these materials, the use phase was simulated thanks to silver dissolution tests. The selected substrate is the sample coated by 500 mg·L$^{-1}$ AgHEC_5.5_2.8 and its blank (HEC without AgNPs). As relevant medium for the user exposure assessment of these paper-based materials with high circulation rate, synthetic sweat (32 °C) was selected and water (25 °C) was used as comparison of interest. It is worth mentioning that the applied conditions were very severe, due to both the

long exposure time and the synthetic sweat acidic pH (≈ 4.5). However, the results shown in Table 46 reveal Ag release about 5 % of the starting load for both water and synthetic sweat environment. This is a promising result proving a good adhesion of nanoparticles to the substrate with a very limited release and reduced correlated risks for the user. The Ag released ($mg \cdot L^{-1}$) is the value detected by the instrument, while the (%) is calculated on the starting mass of coated paper tested and its correspondent Ag load. No meaningful release was detected for the blank, while the two environment, Milli-Q water and synthetic sweat, gave similar results for AgHEC_5.5_2.8.

*Table 46 – Dissolution test in Milli-Q water and synthetic sweat. Assessment of the silver dissolved and released from the samples by ICP-OES.*

| Sample | Medium | Ag released ($mg \cdot L^{-1}$) | Ag released (%) |
|---|---|---|---|
| HEC_5.5_2.8 | Milli-Q water | $0.5 \cdot 10^{-5} \pm 1 \cdot 10^{-5}$ | n.d. |
| AgHEC_5.5_2.8 | Milli-Q water | $9 \cdot 10^{-3} \pm 4 \cdot 10^{-3}$ | 5.6 |
| HEC_5.5_2.8 | Synthetic sweat | 0 | n.d. |
| AgHEC_5.5_2.8 | Synthetic sweat | $10 \cdot 10^{-3} \pm 3 \cdot 10^{-3}$ | 4.5 |

***Antiviral test on coated paper*** – Based on the physicochemical and antimicrobial properties of the colloidal suspensions, and the additional characterization on these first nano-enabled products obtained by laboratory scale dip-coating, attentions were focused on AgHEC_6.4_1.4 and AgCur since they are among the most antimicrobial formulations and promising solutions, together with the standard AgHEC_5.5_2.8 composition and the composite with chitosan AgHEC+Chit 1:2 and AgHEC+Chit 2:1. Despite the good antimicrobial properties, AgCur_Cas coating was excluded due to the strong brow color transferred to the product. 50 and 100 $mg \cdot L^{-1}$ were considered as reference concentration for the deposition with some concentrated test at 500 $mg \cdot L^{-1}$. In the end, the best compromise between antimicrobial activity and aesthetical properties is the coating obtained by the 100 $mg \cdot L^{-1}$ suspensions.

All the antiviral tests on coatings were carried out by considering the untreated paper as reference. The main difficult faced assessing the antiviral activity stemmed from the identification of significant differences between treated and not treated samples. In fact, for long contact times (1, 2, and 3 hours) treated and not treated samples gave comparable results, probably due to the natural virus weakening under air exposure and adsorption on the paper substrate, not properly calculated by the textile ISO procedure. At 1 hour it was observed an 89.2

% virus inhibition for the untreated sample, and comparable values for the other samples: AgHEC_5.5_2.8 88.0 %, AgHEC_6.4_1.4 92.9 %, AgCur 95.0 %, AgHEC+Chit 2:1 79.6 %, and AgHEC+Chit 1:2 97.6 %. For this reason, the most promising samples were tested at shorter contact times (15 and 30 minutes) which allowed the identification of differences between treated and not treated samples. The data shown in Figure 97 point out relevant differences between not treated and treated samples only for short contact times (< 60 minutes). AgHEC_5.5_2.8 (50 $mg \cdot L^{-1}$) resulted the most effective at the shortest contact time, with a virus inhibition of 92-95%. AgHEC_6.4_1.4 and AgCur (100 $mg \cdot L^{-1}$) evidenced an effect at 30 minutes, with a good inhibition percentage of 82-85%.

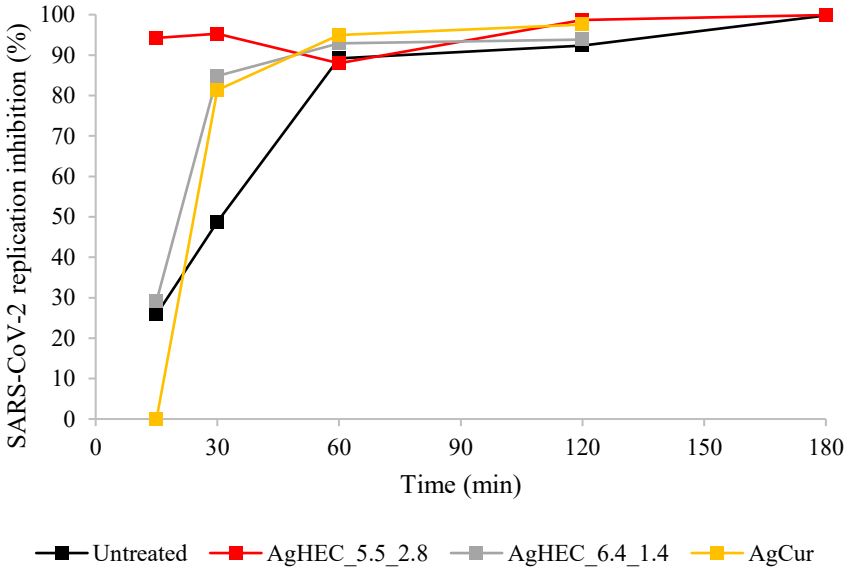


*Figure 97 – Antiviral activity against SARS-CoV-2 of the untreated paper substrate and AgHEC_5.5_2.8, AgHEC_6.4_1.4, and AgCur dip-coated samples. The results are expressed as percentage of the viral replication inhibition as function of the exposure time.*

***Antibacterial test on coated paper*** - From the antibacterial test in suspension AgHEC_6.4_1.4 and AgCur were the most interesting solutions. Moving from a suspension to a coating the NPs activity may decrease due to the reduced mobility. The results, summarized in Table 47, reveal that only AgHEC_6.4_1.4 deposited at 100 $mg \cdot L^{-1}$ is able to reach an almost complete bacterial depletion against both *E. coli* and *S. aureus*. Due to the limited mobility of NPs, the main antimicrobial mechanism may be the $Ag^{+}$ ion release and probably AgHEC_6.4_1.4 is the most active composition. In general, AgNPs have demonstrated to be more active against *E. coli* rather than *S. aureus*, HEC based NPs show stronger antibacterial properties, and the coupling with chitosan did not reveal any improvement.

*Table 47 – Antibacterial activity of the AgNPs dip-coated paper-based nano-enabled products against E. coli and S. aureus.*

| **Sample** | **Deposited Ag concentration ($mg \cdot L^{-1}$)** | **Bacterial reduction (%)** | |
|---|---|---|---|
| | | *E. coli* | *S. aureus* |
| Untreated | 0 | 0 | 0 |
| AgHEC_5.5_2.8 | 50 | 69 ± 5 | n.d. |
| AgHEC_5.5_2.8 | 100 | 78 ± 15 | n.d. |
| AgHEC_6.4_1.4 | 50 | 90 ± 8 | 89 ± 5 |
| AgHEC_6.4_1.4 | 100 | 99.7 ± 0.9 | 97.3 ± 0.7 |
| AgCur | 50 | 19 ± 7 | n.d. |
| AgCur | 100 | 24 ± 8 | n.d. |
| AgHEC+Chit 2:1 | 100 | 61 ± 6 | n.d. |
| AgHEC+Chit 1:2 | 100 | 68 ± 7 | n.d. |

***Stress test and use phase simulation*** – The coating durability is a key parameter for the implementation of the technology in a real application. A full set of relevant aging treatment protocols was considered, two tests were selected as most meaningful for the final application: crumpling and washing machine. Other interesting treatments were the mechanical abrasion from glass balls and the chemical resistance after NaClO attack. In this way, the manipulation and the water/sweat resistance of these paper-based materials with high circulation rate was studied, comparing the antimicrobial performance before and after the aging treatments. AgHEC_6.4_1.4 and AgCur coating obtained from 100 $mg \cdot L^{-1}$ suspensions were studied against *E. coli* bacteria, and SARS-CoV-2 virus. Antibacterial results are summarized in Table 48.

*Table 48 – Evaluation of the coating durability and antibacterial activity against E. coli of the samples that underwent the stress test (crumpling or washing machine).*

| **Sample** | **Deposited Ag concentration ($mg \cdot L^{-1}$)** | ***E. coli* reduction (%)** | |
|---|---|---|---|
| | | Crumpling | Washing machine |
| Untreated | 0 | 0 | 0 |
| Untreated aged | 0 | 0 | 0 |
| AgHEC_6.4_1.4 | 100 | 99 | 64 |
| AgCur | 100 | 56 | 56 |

AgHEC_6.4_1.4 was confirmed the most active coating against bacteria, ensuring a complete *E. coli* depletion after crumpling treatment and a 64 % abatement after the more severe washing machine test. AgCur highlighted an unexpected improved activity if compared with fresh sample, probably due a not homogeneous distribution of nanomaterial or to a kind of activation induced by the aging treatments. No antibacterial activity was observed for the untreated sample before and after the aging tests.

Antiviral results evidenced an emphasized adsorption, observed on aged uncoated samples as well for the aged coated ones. For these samples the relevant adsorption leads to a difficult discrimination between adsorption and antiviral contributes, even at the shortest contact times, as it is possible to see in the graphs in Figure 98.

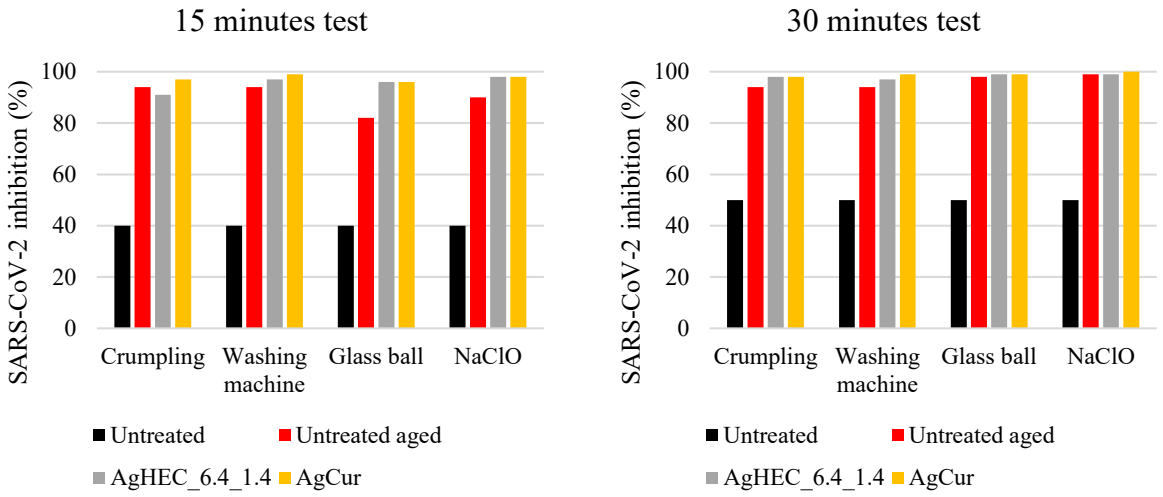


*Figure 98 - Virucidal activity against SARS-CoV-2 of untreated pristine paper used as reference, untreated aged paper, AgHEC_6.4_1.4, and AgCur aged samples. Four different aging procedure were tested: crumpling, washing machine, glass ball, and NaClO. SARS-CoV-2 stock solution was applied on 2·2 cm$^2$ pieces of paper and recovered after the indicated exposure times. The residual virus titer was assessed via limiting dilution assay. Results are reported as percentage viral inhibition.*

Untreated samples showed only the natural viral inhibition due to air exposition, while untreated aged samples demonstrated higher activity, comparable with AgHEC_6.4_1.4 and AgCur. In general, coated samples showed higher activity respect to the untreated aged samples, even if the differences were small. Still, it is difficult to discriminate between virus adsorption on the substrate and the real antiviral effect.

***Scale-up to pre-industrial level roll-to-roll printing***

The coating based on AgHEC_6.4_1.4 100 $mg \cdot L^{-1}$ was the best candidate in terms of antimicrobial activity, both antiviral and antibacterial, and durability, so it was selected for the pre-industrial trials. 100 L of AgHEC_6.4_1.4 100 $mg \cdot L^{-1}$ were produced diluting 50 times 2 L of the synthesis product AgHEC_6.4_1.4 5000 $mg \cdot L^{-1}$. The typical laboratory scale synthesis involves volumes ranging from 30-100 mL, for the scale-up 5 replicas of 500 mL synthesis were produced. Each batch, as well as the final mixed product, was characterized to ensure the process reproducibility at higher volumes. In fact, upscaling the synthetic process of nanomaterials could imply some variations of the physicochemical features due to the establishment of new nucleation/growth equilibria that can occur passing to larger synthesis volumes. The results collected at this stage were consistent with the standard synthesis in terms of hydrodynamic diameter, polydispersity index, zeta potential, pH, Ag concentration and conversion, XRD spectrum and crystallite size, and UV-Vis absorption. These characterizations are widely described in Chapter 3. If at laboratory scale viscosity may be a secondary parameter, moving to industrial scale it can be a relevant information to allow the best working conditions. The starting product is several orders of magnitude more viscous than water, but the diluted sample reach viscosity values comparable with water, about $2 \cdot 10^{-3}$ Pa·s diluted 100 times. Even at this dilution it is about the double of water's viscosity, but it caused no complications for the implementation in the industrial plant.

For large scale production, the post-deposition thermal curing temperature it is a key parameter for the energy consumption and feasibility of the entire process. 10 minutes thermal treatment at 90 or 120 °C were tested, 90 °C is the typical temperature adopted during the project, but a higher temperature could ensure a better durability of the product. Colorimetric analysis was used to discriminate the different effect of the curing temperature on the product. The untreated substrate was used as reference and the ΔE color difference in the CIELAB color space was calculated. No differences were detected for both the AgHEC_6.4_1.4 100 $mg \cdot L^{-1}$ coated samples and the blanks only coated with the capping agent, between paper cured at 90 or 120 °C, Figure 99. Since the two treatments seems to give similar results, the lower temperature (90 °C) more cost-effective one may be suggested for the scale-up.

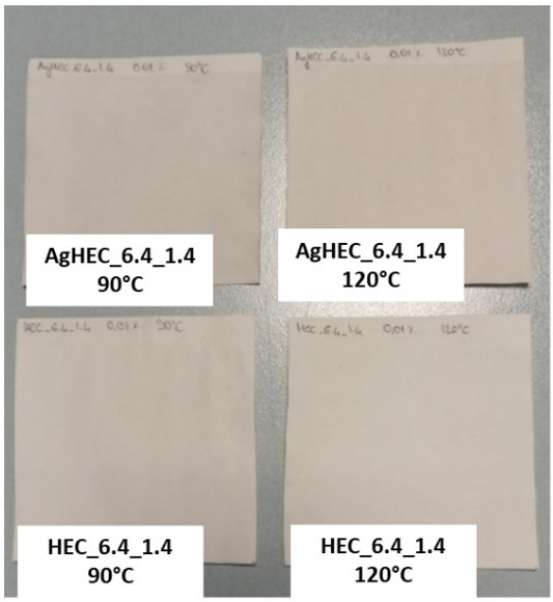


*Figure 99 – Comparison of the thermal treatment temperatures (90 °C vs 120 °C) effects on AgHEC_6.4_1.4 and its blank HEC_6.4_1.4.*

The coating did not induce any color and gloss changes in the sheets. This characteristic is of paramount importance, since it demonstrates that the coating does not influence the visual appearance of the product. However, the absence of measurable optical variations makes difficult the inline control of the coating process. Tarnished sheets showed negligible traces of humidity, therefore, no persistent waving on the paper or sticking was observed. These results were confirmed by absence of issues in the stacking of the sheets.

***Coating homogeneity evaluation by ICP-OES and colorimetric analysis*** – The coating load was estimated weighting stacks of 20 sheets before the deposition and after the final curing. Results suggested an estimated load of about 0.445 $g \cdot m^{-2}$, this value takes into consideration all the coating with the capping agent, not only the AgNPs, moreover this estimation may be affected by the presence of some humidity. The precise quantification of Ag in the coating was performed by ICP-OES. To determine the homogeneity of Ag distribution, the paper sheets were divided in 5 columns and 8 rows, 5 points were selected, represented in black in Figure 100, to cover center, sides and corners of the sheet. Reproducibility of the treatment was evaluated analyzing several sheets.

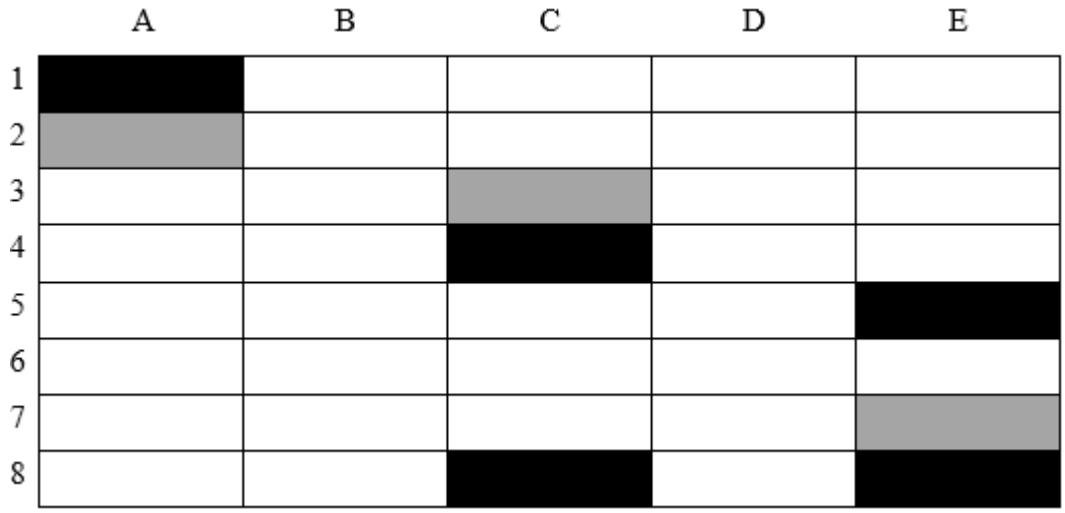


*Figure 100 – Schematic representation of the division of the paper sheets coated by roll-to-roll printing. In black are highlighted the pieces selected for the quantification of the silver load by ICP-OES and in grey the pieces selected for the colorimetric study.*

In Table 49 are reported the average results on 4 different sheets classified in base of the position on the sheet.

*Table 49 – Assessment of the silver load on the roll-to-roll coated samples by ICP-OES. The silver concentration was evaluated in different region of the paper sheet to evaluate the homogeneity of the coating.*

| **Sample position** | **Ag load ($\mu g_{Ag} \cdot g_{paper}^{-1}$)** | **Deviation from the average (%)** |
|---|---|---|
| A1 | 0.75 ± 0.09 | 3.6 |
| C4 | 0.75 ± 0.05 | 3.6 |
| E5 | 0.71 ± 0.09 | -0.4 |
| C8 | 0.71 ± 0.05 | -0.4 |
| E8 | 0.65 ± 0.06 | -6.4 |
| Average | 0.71 ± 0.04 | 0 |

The analyzed samples revealed a silver load ranging from 0.65 to 0.75 micrograms of Ag per gram of coated paper. The little value of the standard deviation reflects a good reproducibility among different sheets while the calculated deviation from the average reflects a trend where the right side of the sheets results to have a lower silver load respect to the left side and the center of the sheet. Variations largely less than 10 % still represent a good enough homogeneity in the coating distribution for the desired application.

The Ag load achieved by the industrial scale roll-to-roll technology (≈ 0.7 $\mu g \cdot g^{-1}$) is strongly lower, about 20-fold, than the amount applied at laboratory scale by dip-coating (≈ 20 $\mu g \cdot g^{-1}$). The antimicrobial performance will determine if a higher Ag concentration is needed to ensure the roll-to-roll deposited coatings activity.

Concluding, the roll-to-roll technology ensures coating homogeneity within the surface of the same sheet, and reproducibility among different sheets. The data suggested a smaller amount of Ag in the right region of the samples.

A colorimetric analysis was performed on these products in the 3 positions represented in grey in Figure 100, close to the samples analyzed by ICP-OES. An untreated sheet was used as reference. The ΔE color variation calculated in the CIELAB space is negligible for all the position and samples, with an average value ranging from 0.5 to 0.7. This result is aligned with the little amount of silver detected by ICP-OES in the coating.

***Conclusions***

12 variants of Ag-based nanosuspensions were prepared using ecofriendly and easily scalable methods. The 5 most promising variants were selected based on physicochemical and antimicrobial features. Sol-phase antibacterial tests highlighted the synergistic effect of HEC coupled with AgNPs. AgHEC_6.4_1.4 exhibited the highest antibacterial activity. HEC- and Cur-based AgNPs confirmed excellent antiviral activity against SARS-CoV-2 and an optimal selectivity index ensuring a wide safe and efficient concentration range.

Paper substrates were coated through dip-coating deposition and thermally treated at 90°C for 10 minutes. The yellow color typical of AgNPs strongly affected the paper color at the highest deposition concentration, as assessed by the colorimetric evaluation, therefore the identification of the minimum antimicrobial concentration will play a key role to optimize the material. FESEM-EDX analyses highlighted the presence of Ag on the surface, homogeneously distributed on the cellulosic fibers. Using ICP-OES measurements Ag deposited on the substrates was quantified and HEC seemed to favor the nanoparticles attachment on paper substrates. AgHEC_6.4_1.4 and AgCur coatings ensured good antibacterial and antiviral activities combined with an acceptable durability. The deposition of 100 $mg \cdot L^{-1}$ AgNPs suspensions is the optimal compromise between antimicrobial activity, durability and aesthetical features of the products. During the pre-industrial trials AgHEC_6.4_1.4 coating was successfully upscaled resulting in the preparation of 100 L at a concentration of 100 $mg \cdot L^{-1}$ of AgNPs. The batch-to-batch reproducibility was ensured by verifying the physicochemical properties of the upscaled suspensions. The quantification of the Ag amount in the coating by means of ICP-OES highlighted a very good reproducibility among the different sheets, however by sampling different zones of a same paper sheets some trends were observed. Roll-to-roll technique provided a drastically reduced amount Ag ($\approx 0.7\ \mu g \cdot g^{-1}$) compared to the dip-coating ($\approx 14\ \mu g \cdot g^{-1}$) promoting a detrimental effect on the antibacterial feature. Since the higher Ag load in the dip-coating samples is aesthetically acceptable, it will be possible for future trials to increase the concentration of the Ag suspension to enable higher Ag load by roll-to-roll application as well.

***Experimental part***

In this section are described the testing protocols for the antimicrobial performance in sol and as coating, characterization methods such as colorimetric, ICP-OES, and FESEM-EDX analysis, and finally the experimental dip-coating and roll-to-roll-printing procedures.

***Laboratory scale dip-coating*** – The dip-coater is a machine that allows the production of coating by substrate immersion in the coating agent bath at controlled speed. The custom model created by Aurel S.p.A. allows pre-industrial scale deposition, regulating immersion-withdraw speed and the soaking time, granting excellent reproducibility. For the deposition of AgNPs on paper substrates, experimental parameters were optimized as follows: dipping and withdrawing speed 2 $mm \cdot s^{-1}$, soaking time 5 s, and the successive thermal treatment is performed at 90 °C for 10 minutes in a static oven. 7 samples and their corresponding blank solution (same composition but Ag 0 $mg \cdot L^{-1}$) were deposited by dip-coating on paper substrates simulating paper-based materials with high circulation rate at 3 different concentrations 1000, 500, and 100 $mg \cdot L^{-1}$. In a further selection step, only 5 variants were deposited at two dilutions, 100 and 50 $mg \cdot L^{-1}$.

***Pre-industrial scale roll-to-roll printing*** – For the pre-industrialization trial a specific roll-to-roll printing machine was opportunely configured for printing water-based solutions. An 80 L external reservoir has been prepared and two flexo-plates with a layout covering the whole paper sheet were implemented in the printing unit. This trial involved the production of 4000 paper sheets. Before starting, the cleaning routine of the machine was performed, first the instrument was rinsed with a specific solvent, then washed 3-4 times with demineralized water, at the end of the production campaign the machine was washed once again with demineralized water. To startup the machine, configure sheet format, and printing parameters, 2500 blank sheets were used, then 500 sheets were coated and weighted to determine the varnish load, which was about 1.0 $g \cdot m^{-2}$. For the tests, 4000 sheets were varnished at a speed of 7000 $sheets \cdot h^{-1}$, the product was first UV cured reaching a temperature of 35-45 °C, then moved to an oven for the thermal treatment, 10 minutes at 90 °C.

***Silver quantification*** – Inductively coupled plasma – optical emission spectroscopy (ICP-OES) was used for the quantification of silver during different stage of the project. First, for the determination of the concentration of colloidal suspensions to be applied as coating, then the silver loaded as coating on paper substrates, finally for the dissolution test to quantify the concertation of silver released. The analyses were conducted thanks to an Agilent 5100 ICP-OES

with mounted the autosampler Agilent SPS 3 (Agilent Technologies). Before the analysis, the suspensions (the starting colloidal suspension used for the coating production and also the simulating fluid containing dissolved $Ag^+$ cations from the dissolution tests) were acidic digested using ≥ 65 %wt $HNO_3$ (Sigma-Aldrich) and 30 %wt $H_2O_2$ (Sigma-Aldrich), while the quantification of Ag on coated paper was assessed preparing the samples for the analysis by microwave assisted acidic digestion treated with ≥ 65 %wt $HNO_3$ (Sigma-Aldrich) and 30 %wt $H_2O_2$ (Sigma-Aldrich), not digested solid fibers were removed by filtration, alternatively the selected paper pieces were weighted and cut into smaller parts, then soaked in a mixture of 2 mL of 65 %wt $HNO_3$, 2 mL of 30 %wt $H_2O_2$, and 2 mL of Milli-Q water, 3 minutes per side.

***Dissolution test*** - The samples were soaked in 5 mL of liquid medium for 3 hours in static condition, then they were removed and the liquid phase was analyzed by ICP-OES to assess the Ag release. The selected simulating fluid for the dissolution test are simulated sweat and Milli-Q water, they were selected in order to mimic a real application of these nano-enabled products.

***Electron microscopy FESEM-EDX*** – Field emission scanning electron microscopy (FESEM) was used coupled with energy dispersive x-ray spectroscopy (EDX) to study the morphology and the surface of the coated products, and also the silver distribution on the coating. FESEM images allowed the morphological study of substrate and coating. EDX allowed the evaluation of the silver distribution over the surface of the coating. The instrument used is ZEISS SIGMA, Carl Zeiss Microscopy GmbH.

***Colorimetric evaluation*** – CIELAB coordinates were used to provide a solid color descriptor of the final coated product involving 3 parameters: "L" lightness ranging from 0 (black) to 100 (white), "a" redness-greenness of the color, positive values are red, negative values are green, "b" yellowness-blueness of the color, positive values are yellow, negative values are blue. ΔL, Δa, and Δb values provide a complete numerical descriptor of color differences between a sample and a reference (white paper). The higher the value, the greater the difference in that dimension. ΔE (total color difference) is calculated based on ΔL, Δa, and Δb and represents the distance between two points, the sample and the reference, in the CIELAB space, ΔE calculation is reported in Equation 8.[215]

$$\Delta E = \sqrt{(\Delta L)^2 + (\Delta a)^2 + (\Delta b)^2} \qquad \text{Equation 8}$$

***Antibacterial test in sol*** – The antibacterial activity of the suspensions was tested in compliance with EN 1040:2005 standardized method against *Escherichia coli* ATCC 10536 (Gram-negative) and *Staphylococcus aureus* ATCC 6538 (Gram-positive) at different concentrations (50, 10, 1, 0.5 and 0.05 $mg \cdot L^{-1}$), blank solutions (no AgNPs) were used as comparison to discriminate the activity of AgNPs and the synergistic effect combined with the capping agent.

***Antibacterial test on coated paper*** – The antibacterial activity was evaluated according to ASTM E 2149-01 "Standard test method for determining the antimicrobial activity of immobilized antimicrobial agents under dynamic contact conditions". The method is designed to evaluate the resistance of non-leaching antimicrobial treated specimens to the growth of microbes under dynamic contact conditions. *Escherichia coli* ATCC 11229 as Gram-negative and *Staphylococcus aureus* ATCC 6538 Gram-positive bacteria were studied. The antimicrobial activity was expressed in % reduction of the organisms after contact with the test specimen compared to the number of bacterial cells surviving after contact with the control.

***Antiviral test in sol*** – The antiviral activity was assessed in the Ag concentration range 18.75-300 $mg \cdot L^{-1}$ and then expressed as $IC_{50}$, the dose causing 50 % reduction of the virus replication with respect to the untreated control. SARS-CoV-2 and BK polyomavirus were studied representing respectively non-enveloped and enveloped viruses. The viral replication inhibition was studied with AgNPs pre-treated virus particles infecting target cells. The virus inhibition was assessed by RT-qPCR employing SARS-CoV-2 N1 gene RT-qPCR on RNA isolated from the supernatants of treated infected cells and by Plaque Reduction Assay, results are reported as replication inhibition percentage respect the starting untreated sample.[188]

***Antiviral test on coated paper*** – The antiviral results against SARS-CoV-2 of the nano-enabled products were assessed by applying the testing method ISO 18184:2019 "Determination of antiviral activity of textile products, which was properly adapted to paper substrates".

### 4.1.3. Antimicrobial polymeric films

***Introduction*** – Polymeric films are generally defined as thin continuous polymer-based materials with a thickness up to 200 μm. They can be manufactured from various resins to achieve the desired physical, optical, and functional properties. Usually they are prepared from thermoplastic resins following lot of different methods, such as extrusion, coextrusion, calendaring, skiving, casting, and coating.[216] Polymeric films find large use in lot of different applications, in membrane separation science they can be used as selective filtration barrier for liquid or gas by controlling the pore size, in the biomedical field they can be loaded with drugs and used for transdermal delivery and wound healing, and more in general polymeric films are widely applied in the packaging industry.[217,218]

Implementing antimicrobial and antioxidant properties in polymeric films may be particularly interesting and convenient in some applications like the already cited biomedical bandages or in the food packaging field, but in general reducing pathogens proliferation can be helpful in most of their applications. In this perspective, the synthesized AgNPs were implemented in polymeric films to exploit their antimicrobial properties.[219] The synthesis optimization is described in Chapter 3. Curcumin-capped AgNPs (AgCur) and two variants of quaternized hydroxyethyl cellulose-capped AgNPs (AgHEC_5.5_2.8 and AgHEC_6.4_1.4) were investigated as antimicrobial additives to polymeric films. A cellulose biopolymeric film was selected as substrate for the investigations, both water-based and solvent-based resins were loaded with AgNPs and applied as surface coating, also a water-based adhesive was tested to produce a double layer film (biopolymer-adhesive-biopolymer).

The antibacterial tests here reported were performed in collaboration with INRiM (National Metrology Institute of Italy, Torino).

***Results and discussion*** – A first screening of the AgNPs variants was performed at colloidal level to determine the most active compounds and the most suitable for the desired application. The selected variants underwent a compatibility study with the water- and solvent-based resins and the water-based adhesive, to determine the dispersibility of the particles in the working environment. After that, the most performing configuration was investigated, to determine if AgNPs antimicrobial activity can be better exploited if applied as direct coating or as internal adhesive in a double-layer set-up. Finally, the antibacterial activity of the best solutions in terms of AgNPs variant and film configuration was deeply studied. A scheme of the workflow is represented in Figure 101.

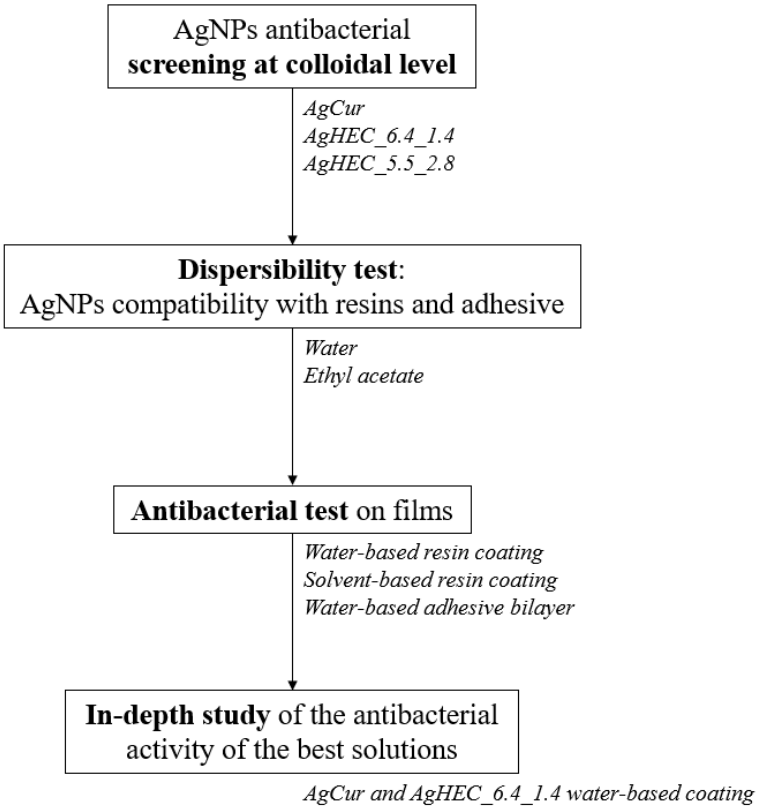


*Figure 101 – Schematic workflow of the production and characterization of antimicrobial polymeric films implementing AgNPs.*

***Antibacterial screening at colloidal level*** – Among several variants produced during the optimization of AgNPs syntheses, few promising compositions were selected, based on their antimicrobial activity, stability, and cytotoxicity. AgCur, AgHEC_6.4_1.4, and AgHEC_5.5_2.8 colloidal suspensions were tested against *Listeria innocua*, a Gram-positive bacterium. Results reported in Figure 102, Figure 103, and Figure 104 show a dose dependent behavior for the 3 AgNPs tested, increasing Ag concentration the antibacterial effect against *Listeria innocua* is

enhanced. In particular, it was identified 100 μg·mL$^{-1}$ as effective inhibitory concentration for all the AgNPs variants, corresponding to an exponential increase of the antibacterial activity. The 3 compositions demonstrated different activity at 100 μg·mL$^{-1}$, the most active is AgHEC_6.4_1.4 with a logarithmic bacterial reduction of 5.00, followed by AgCur with 3.04, and concluding with AgHEC_5.5_2.8 a reduction of 1.1 log. In this way an activity ranking was obtained, proposing AgHEC_6.4_1.4 as most active variant against *Listeria innocua*, also AgCur exhibited excellent antibacterial activity with a 99.9 % reduction, while AgHEC_5.5_2.8 demonstrated to be less active.

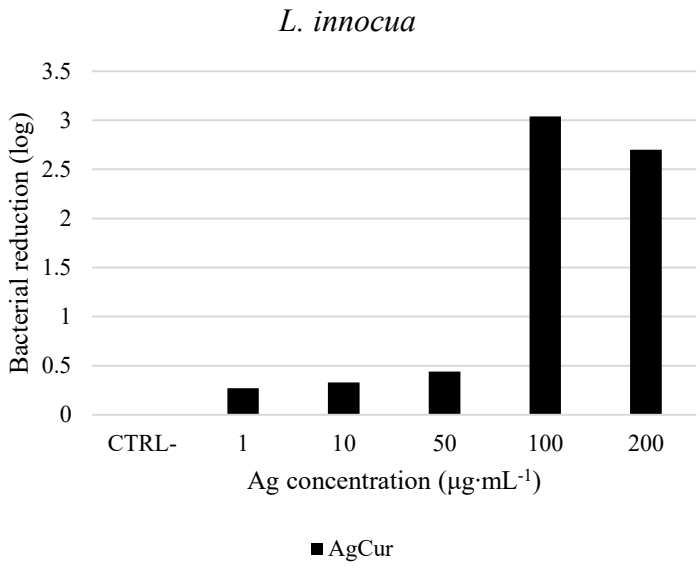


*Figure 102 – Antibacterial activity against L. innocua of AgCur nanoparticles. Results are expressed as logarithmic bacterial reduction induced by the selected silver concentrations.*

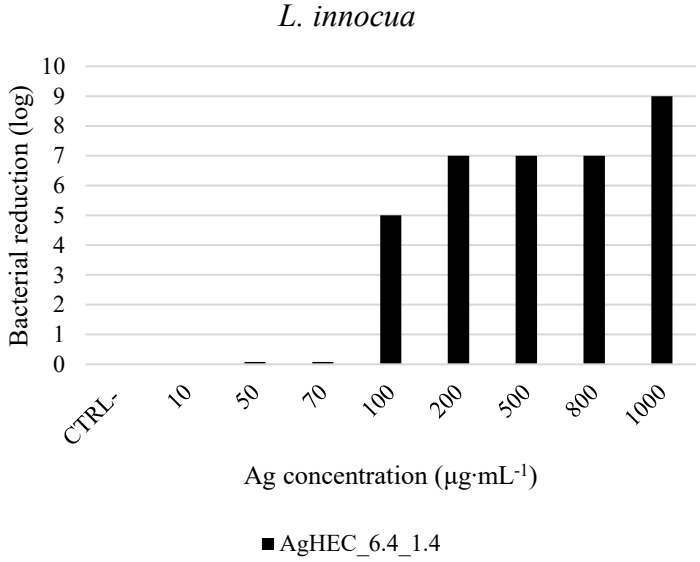


*Figure 103 – Antibacterial activity against L. innocua of AgHEC_6.4_1.4 nanoparticles. Results are expressed as logarithmic bacterial reduction induced by the selected silver concentrations.*

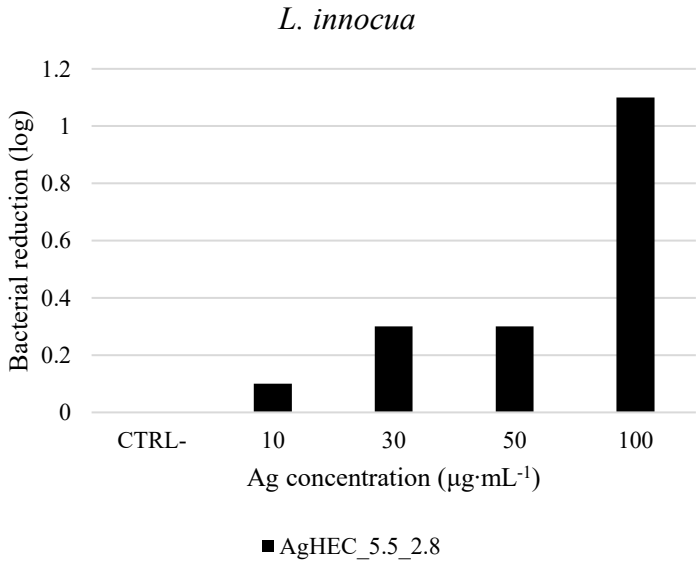


*Figure 104 – Antibacterial activity against L. innocua of AgHEC_5.5_2.8 nanoparticles. Results are expressed as logarithmic bacterial reduction induced by the selected silver concentrations.*

Since AgCur and AgHEC_6.4_1.4 demonstrated to be the most interesting solution, they were tested against *Escherichia coli* as Gram-negative reference bacterium. As previously observed in Chapter 3, AgNPs tends to be more active against Gram-negative bacteria, in fact against *Escherichia coli* both AgCur (Figure 105) and AgHEC_6.4_1.4 (Figure 106) demonstrated excellent bacterial reduction at low concentration, respectively 5.5 and 6.8 log. At high Ag concentrations (≥ 100 µg·mL$^{-1}$) there aren't appreciable differences between the two investigated

variants, but at low concentrations (≤ 50 μg·mL$^{-1}$) AgHEC_6.4_1.4 has slightly stronger antibacterial activity, confirming to be the most active variant against bacteria.

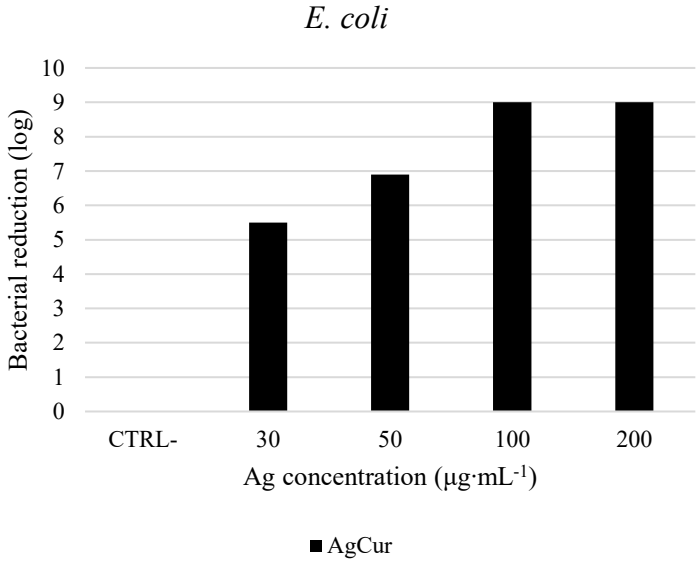


*Figure 105 – Antibacterial activity against E. coli of AgCur nanoparticles. Results are expressed as logarithmic bacterial reduction induced by the selected silver concentrations.*

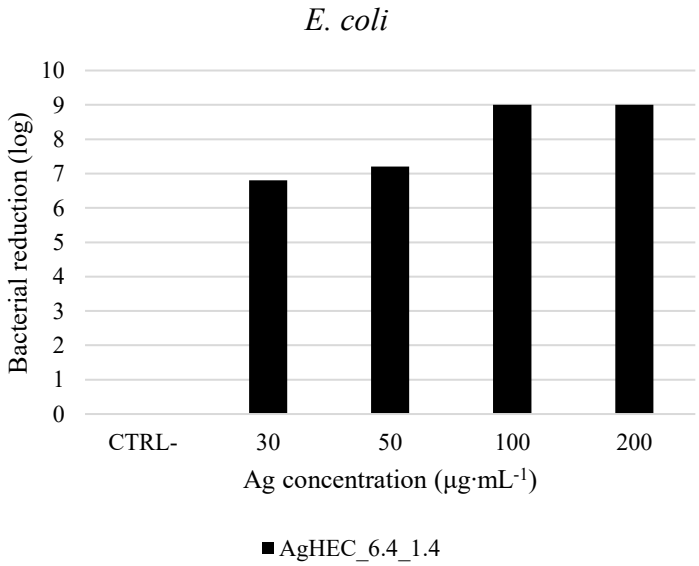


*Figure 106 – Antibacterial activity against E. coli of AgHEC_6.4_1.4 nanoparticles. Results are expressed as logarithmic bacterial reduction induced by the selected silver concentrations.*

AgCur and AgHEC_6.4_1.4 were selected as AgNPs variants to be implemented as coating for the polymeric film substrates.

***Antimicrobial polymeric films design*** – Cellulose biopolymeric films were used as substrate for the deposition of the antimicrobial layer. Two different configurations were tested, a scheme of the products is proposed in Figure 107:

- *Surface coating antimicrobial layer*: the surface coating was produced using either ACTEGA "FoodSafe GOLD" (FSG) or "232" water-based resins or a solvent-based resin. In this configuration, a direct contact between AgNPs and pathogens is promoted.
- *Internal adhesive antimicrobial layer*: the intermediate layer was produced using a water-based adhesive placed in between two cellulose layers to study the indirect contact mode.

The idea of implementing the antimicrobial AgNPs into an internal adhesive layer derives from the purpose to apply these materials in the food packaging field. To exploit the antimicrobial properties of AgNPs in this specific application requires to comply with the strict European Commission regulation regarding food contact materials.[220] The direct contact between food and AgNPs may favor the diffusion and migration of AgNPs or $Ag^+$ into foods.[221] To avoid this phenomenon it is necessary the nanoparticles confinement into a multilayer system. During the antibacterial tests an activity comparison will be assessed between the two configurations: direct contact and indirect contact.

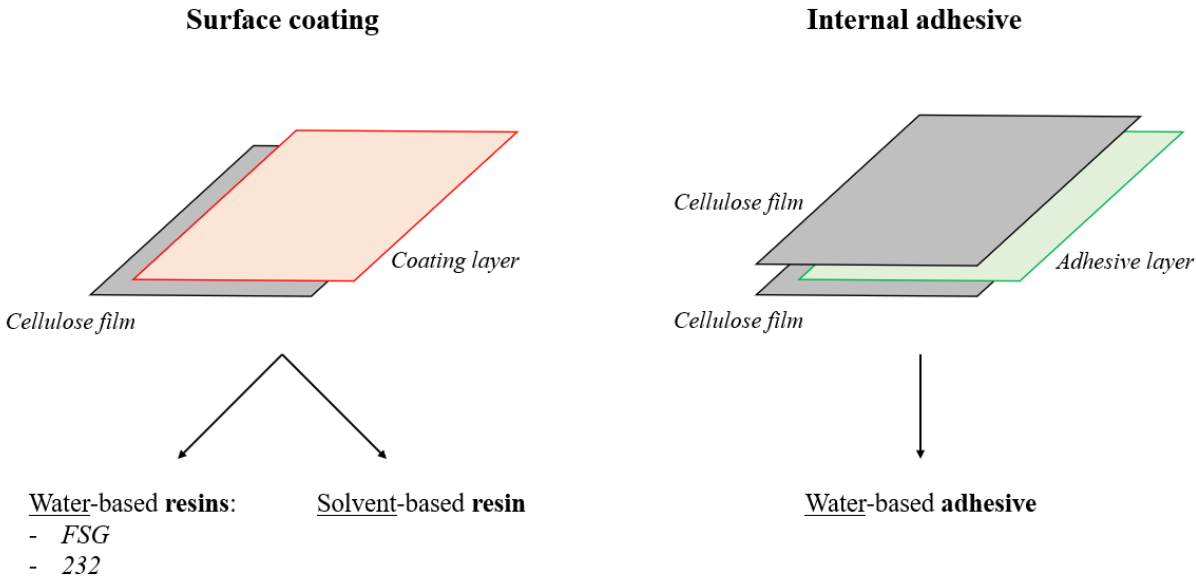


*Figure 107 – Schematic representation of the two antimicrobial film configurations tested: surface coating and internal adhesive. Water- and solvent-based resins were applied for the production of the surface coating layer, while the water-based adhesive was used as internal adhesive layer between two cellulose films.*

***AgNPs dispersibility test into varnishes*** – The compatibility test was performed to determine the dispersibility of AgNPs water-based colloidal suspension in the varnishes that will be used

to produce the antimicrobial polymeric films. Tests were divided depending on the polarity of the resin. AgNPs were dispersed into:

- *Water-based resin* (addressed to study the dispersibility into the water-based resin itself and water-based adhesive).
- *Solvent-based resin*.

AgHEC_5.5_2.8 and AgCur were used for this preliminary and qualitative work because they possess opposite zeta potential in water, positive for AgHEC_5.5_2.8 and negative for AgCur. In general, it was observed a good miscibility of the silver nanophases in both environments. In particular, perfect miscibility was obtained in water-based resin for AgHEC_5.5_2.8 and AgCur, Figure 108. The yellow coloration is due to the presence of AgNPs.

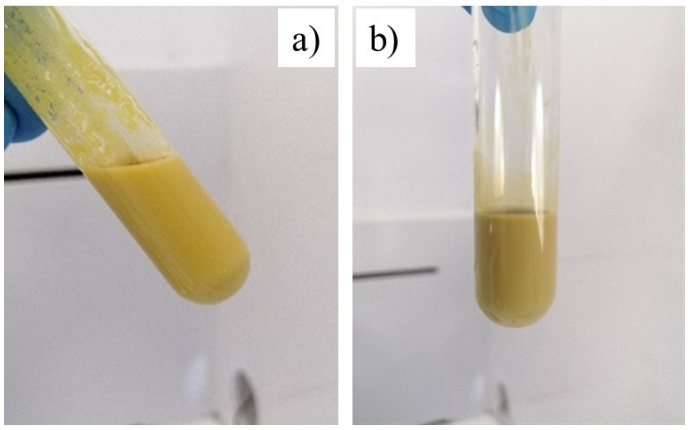


*Figure 108 – Dispersibility test in the water-based resin. a) AgHEC_5.5_2.8; b) AgCur.*

A good phase miscibility was obtained also for the solvent-based resin, Figure 109. AgHEC_5.5_2.8 visibly interacts with the resin exhibiting a color variation from the typical yellow-brown toward red.

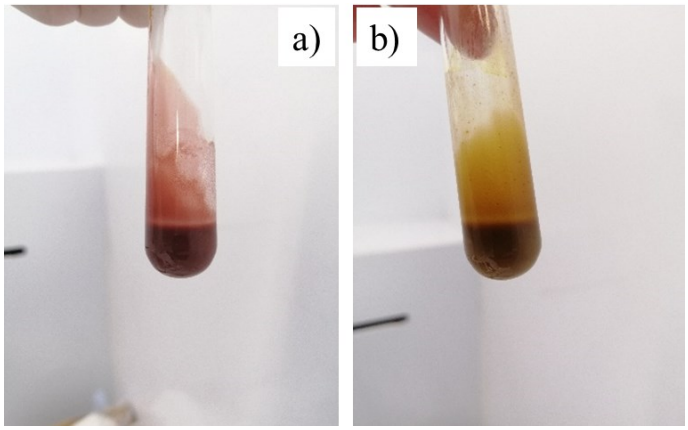


*Figure 109 – Dispersibility test in the solvent-based resin a) AgHEC_5.5_2.8; b) AgCur.*

To have a homogeneous AgNPs distribution in the final polymeric film, it is important to have a good dispersibility of the nanophase in the resin. This condition was fulfilled by both AgNPs in both resins. It is important to process the Ag-doped resins immediately after the dispersion to prevent any precipitation phenomena over time.

***Antibacterial tests on polymeric film*** – The antibacterial tests on the biopolymeric films were performed following the ISO 22196:2011 "Measurement of antibacterial activity on plastics and other non-porous surfaces" against *Escherichia coli*, *Staphylococcus aureus*, and *Listeria innocua*. The antibacterial activity against *L. innocua* was assessed together with the typical *E. coli* and *S. aureus* bacteria, representing respectively the Gram-negative and Gram-positive categories, because of *Listeria* spp. safety concerns related to potential contamination of food contact materials and packaging.[222,223,224,225]

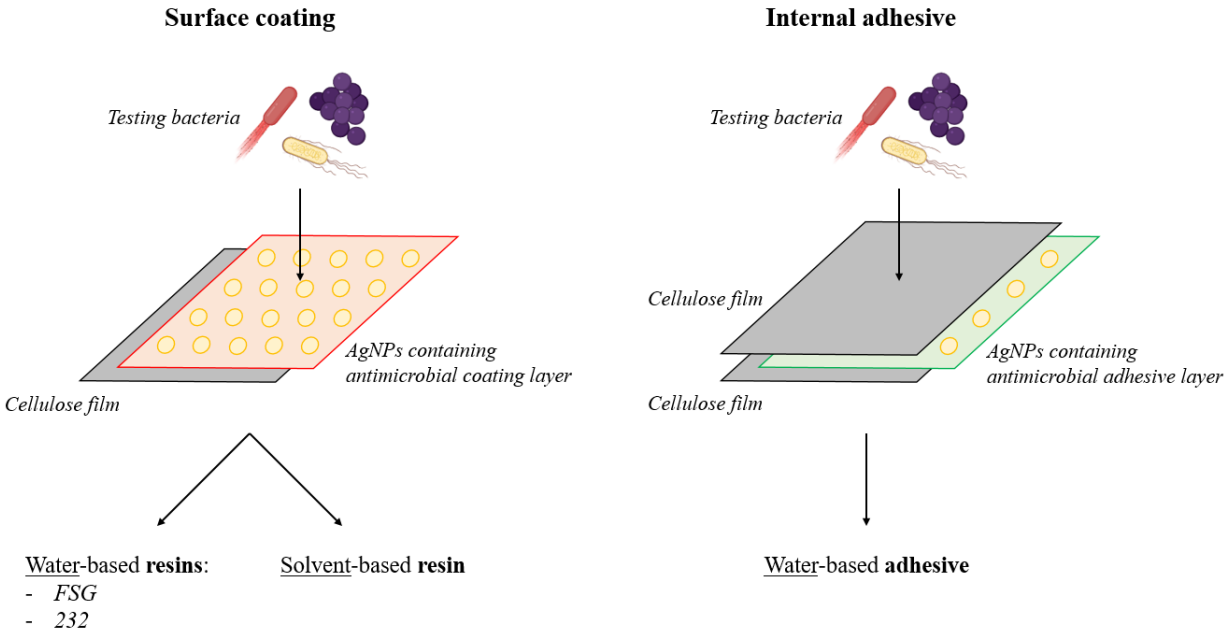


*Figure 110 – Schematic representation of the two antimicrobial film configurations tested: surface coating and internal adhesive. Water- and solvent-based resins were applied for the production of the surface coating layer in this configuration there is a direct contact between the silver containing layer and the bacteria. The water-based adhesive was used as internal adhesive layer between two cellulose films, in this case there is an indirect contact between the silver containing layer and the bacteria.*

AgNPs 0.5 %wt colloidal suspension was incorporated into the resin or adhesive at a concentration of 30 %wt, reaching a final Ag concentration in the tested layer of 0.15 %wt equivalent to 20 µg·cm$^2$. AgNPs dispersion was good and a homogenous product was obtained.

A scheme of the testing configurations is reported in Figure 110. In the case of surface coating a direct contact between bacteria and the AgNPs containing layer is achieved, while an indirect contact is tested in the internal adhesive layer configuration.

The first test was performed on AgHEC_6.4_1.4 dispersed in the solvent-based resin and in the water-based adhesive against *E. coli*. Results reported in Figure 111 are compared with the blank represented by the uncoated substrate. The two different configuration demonstrated very different results, in fact, the direct contact between the silver loaded layer and the bacterium it is necessary to exploit the antibacterial activity of AgNPs. The direct contact solvent-based coating exhibits excellent activity with a 5.3 log *E. coli* reduction respect to its blank. While there are no relevant differences between the activity of the water-based adhesive and its blank, in this case the silver layer is included between the two external cellulose films, impeding the direct contact with *E. coli*. From these results it is possible to assume that the direct contact between silver and the targeted pathogen is extremely important for the exploitation of the antibacterial activity. AgNPs recognized antibacterial mechanisms involves the nanoparticles adhesion and penetration of the cell wall inducing the cells lysis and death, the formation of reactive oxygen species (ROS), and the silver cations release which interfere with enzymes, proteins, and genetic material.[226,227] In the indirect contact configuration, it is possible that the confinement of the AgNPs within the two cellulose film suppresses the $Ag^+$ ions release and diffusion, and obstructs the nanoparticles contact with the bacteria, it could also reduce ROS production and favoring their quenching before the contact with bacteria, generally inhibiting the antibacterial activity.[221] Controlled permeability films could be an interesting solutions to avoid the direct contact with AgNPs, but this compromise could be not enough to match strict regulations such as in the food packaging field.

During the following steps, the adhesive indirect contact configuration was abandoned focusing only on the coating direct contact.

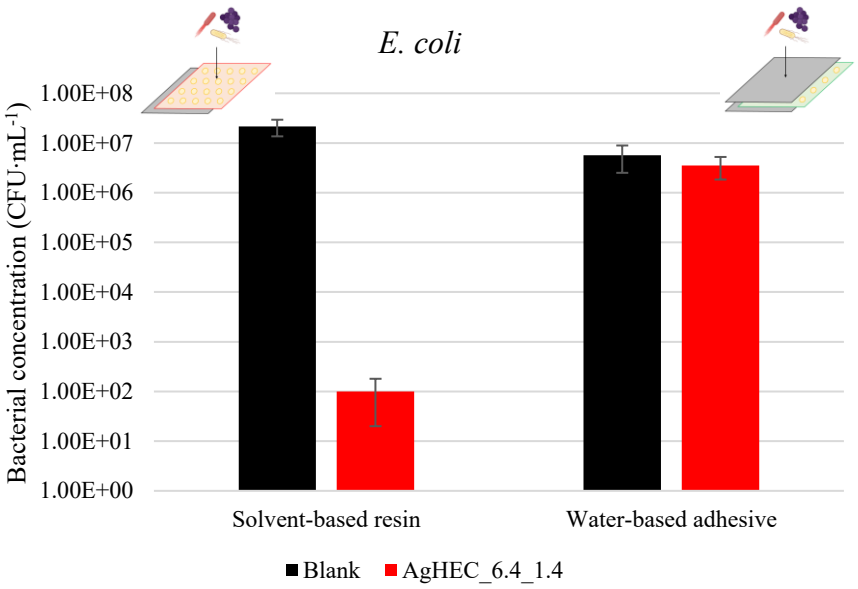


*Figure 111 – Antibacterial activity against E. coli of AgHEC_6.4_1.4 containing samples compared to the respective blanks prepared using the same varnishes without the AgNPs. The results are reported as bacterial concentration (CFU·mL$^{-1}$) after the contact with the samples prepared with solvent-based resin (direct contact) or water-based adhesive (indirect contact).*

A second test was carried out against *E. coli* using AgHEC_6.4_1.4 and AgCur dispersed in water-based resins 232 and FSG, Figure 112. Both AgNPs showed excellent antibacterial activity, which was even higher for AgHEC_6.4_1.4. Quantitative *E. coli* depletion was obtained by AgHEC_6.4_1.4 in both resins, while AgCur grants quantitative reduction dispersed in FSG and excellent reduction (4.3 log respect to the blank) in 232. It is interesting to compare the different activity of the blanks, in fact FSG demonstrated some kind of antibacterial activity itself, 1.3 log reduction respect to 232, indeed an antibacterial agent is present in FSG formulation. The synergistic activity between FSG resin and AgNPs push the AgCur sample *E. coli* reduction to completeness.

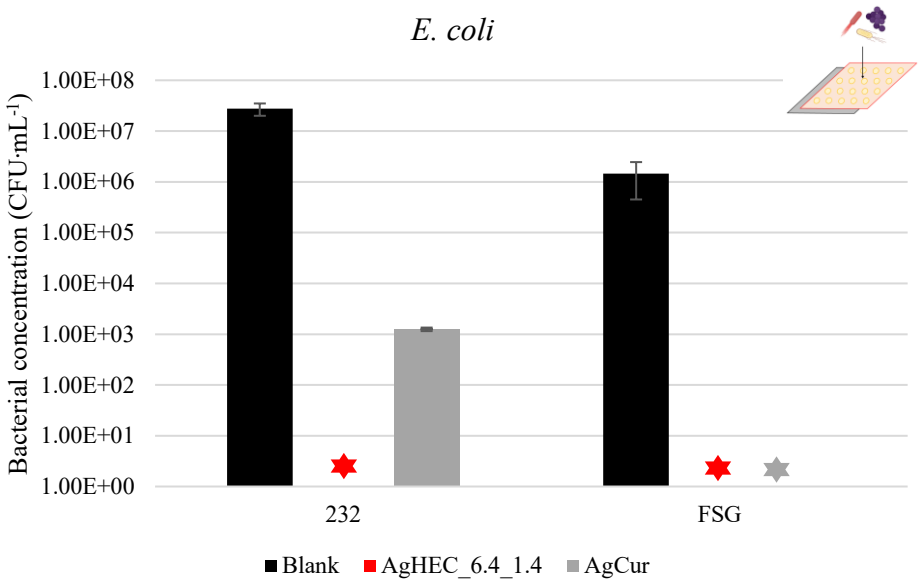


*Figure 112 – Antibacterial activity against E. coli of AgHEC_6.4_1.4 and AgCur containing samples compared to the respective blanks prepared using the same varnishes without the AgNPs. The results are reported as bacterial concentration (CFU·mL$^{-1}$) after the contact with the samples prepared with water-based resins 232 and FSG (direct contact). Asterisks represent values below the detection limit, approximated to 0.*

To test the activity of these materials against Gram-positive bacteria, *S. aureus* and *L. innocua* were selected. In Figure 113 is reported the activity of AgNPs water-based resin coatings against *S. aureus*. The behavior is similar to *E. coli*, AgHEC_6.4_1.4 confirms to be the most active AgNPs variant leading to a quantitative reduction of *S. aureus* in both 232 and FSG film. FSG demonstrates to have antibacterial activity itself also against Gram-positive bacteria, 2.9 log bacterial reduction respect to 232.

Once dispersed into the resins, AgCur highlights a reduced activity against S. aureus, showing 0.5 log reduction in 232 and 1.1 log reduction in FSG (compared to their respective blanks).

This is peculiar, since AgCur pristine colloidal suspension had showed excellent results against *S. aureus* reaching more than 4 log reduction (results reported in Chapter 3.2.4.). It is possible that the immobilization into the cellulose coating influenced the availability of the AgNPs and $Ag^+$ ions with more acute repercussions against Gram-positive bacteria.

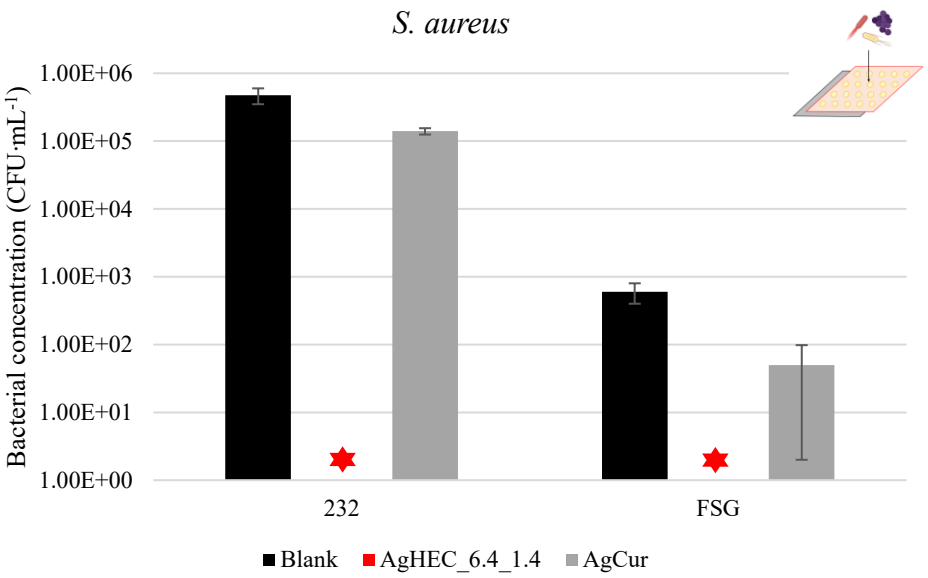


*Figure 113 – Antibacterial activity against S. aureus of AgHEC_6.4_1.4 and AgCur containing samples compared to the respective blanks prepared using the same varnishes without the AgNPs. The results are reported as bacterial concentration (CFU·mL$^{-1}$) after the contact with the samples prepared with water-based resins 232 and FSG (direct contact). Asterisks represent values below the detection limit, approximated to 0.*

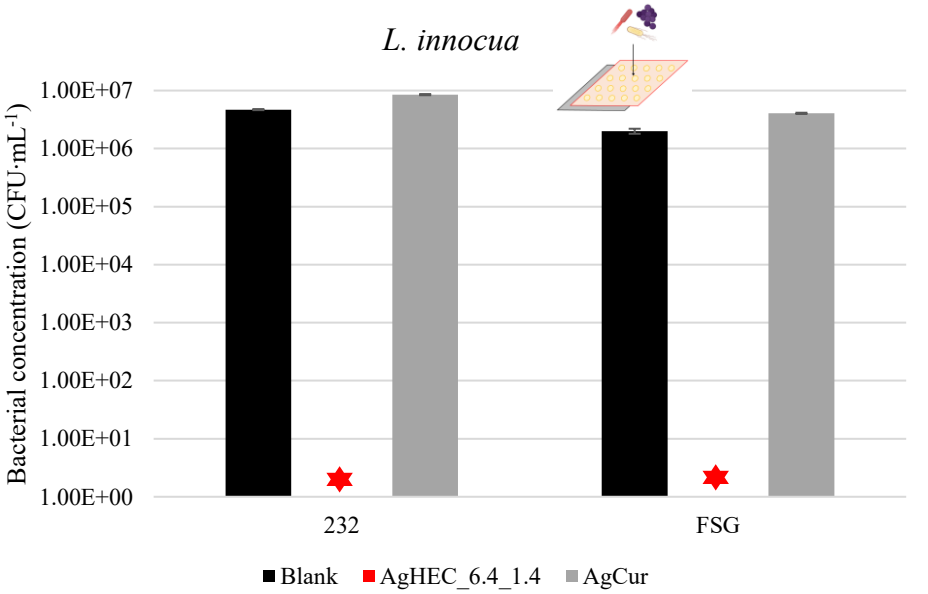


*Figure 114 – Antibacterial activity against L. innocua of AgHEC_6.4_1.4 and AgCur containing samples compared to the respective blanks prepared using the same varnishes without the AgNPs. The results are reported as bacterial concentration (CFU·mL$^{-1}$) after the contact with the samples prepared with water-based resins 232 and FSG (direct contact). Asterisks represent values below the detection limit, approximated to 0.*

*L. innocua* was tested as second Gram-positive bacterium, Figure 114, and also in this case AgHEC_6.4_1.4 demonstrated higher antibacterial activity in both varnishes. FSG demonstrated a certain degree of antibacterial activity, 0.4 log respect to 232. AgCur was non-active against *L. innocua*.

*E. coli*, Gram-negative, demonstrated to be more affected by the presence of AgNPs respect the two other Gram-positive bacteria, *S. aureus* and *L. innocua*. Since AgHEC_6.4_1.4 showed higher antibacterial efficacy against all the bacteria tested, it was selected to be tested in lower concentrations. The optimal configuration resulted to be a surface layer, so the coating with the resins was selected for the successive studies, in particular it was selected the water-based varnish 232, in order to avoid interferences generated by the intrinsic antimicrobial activity of FSG.

***In depth antibacterial study of the most effective configurations*** – From tests at 30 %wt load of 0.5%wt AgNPs suspension, AgHEC_6.4_1.4 resulted to be the most active variant tested. Furthermore, the direct contact activated mechanism required to exploit AgNPs antibacterial activity forced the selection of a surface varnish. In particular, water-based resin ACTEGA 232 (named 232) was selected to avoid the interferences from the antibacterial properties of ACTEGA FoodSafe GOLD (named FSG), and also to avoid the use of solvent for the solvent-based varnish.

Once the experimental configuration was arranged, 232 water-based resin was loaded with different concentration of AgHEC_6.4_1.4, ranging from 1 to 20 %wt, and then tested against *E. coli*, *S. aureus*, and *L. innocua* Figure 115, Figure 116, and Figure 117 respectively.

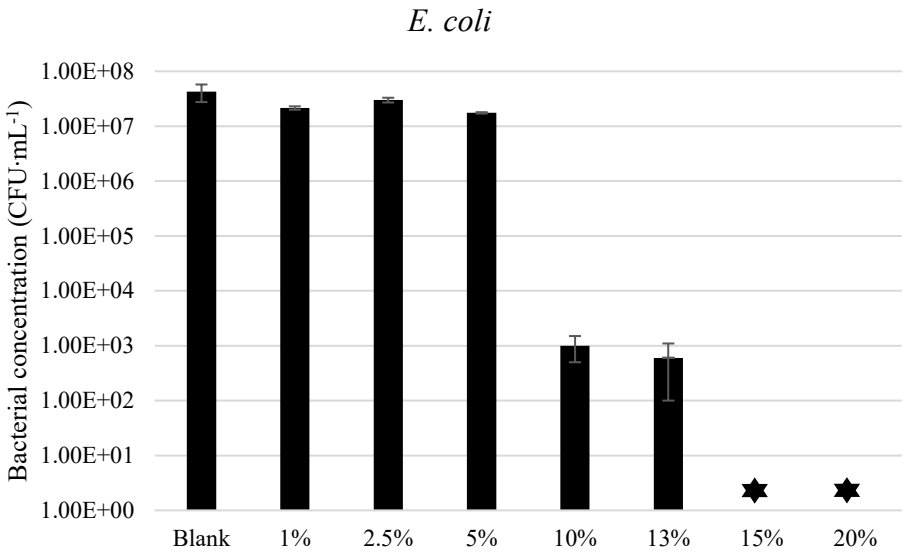


*Figure 115 – Antibacterial activity against E. coli of AgHEC_6.4_1.4 containing water-based resin 232 films (direct contact), compared to the blank prepared using the same varnish without the AgNPs. The results are reported as bacterial concentration (CFU·mL$^{-1}$) as function of the load of 5 g·L$^{-1}$ AgNPs suspension in the antimicrobial layer. Asterisks represent values below the detection limit, approximated to 0.*

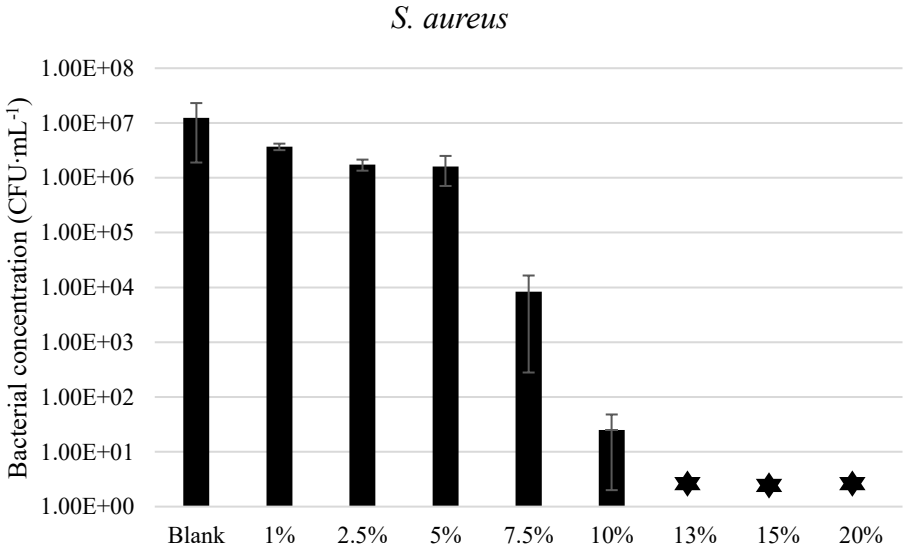


*Figure 116 – Antibacterial activity against S. aureus of AgHEC_6.4_1.4 containing water-based resin 232 films (direct contact), compared to the blank prepared using the same varnish without the AgNPs. The results are reported as bacterial concentration (CFU·mL$^{-1}$) as function of the load of 5 g·L$^{-1}$ AgNPs suspension in the antimicrobial layer. Asterisks represent values below the detection limit, approximated to 0.*

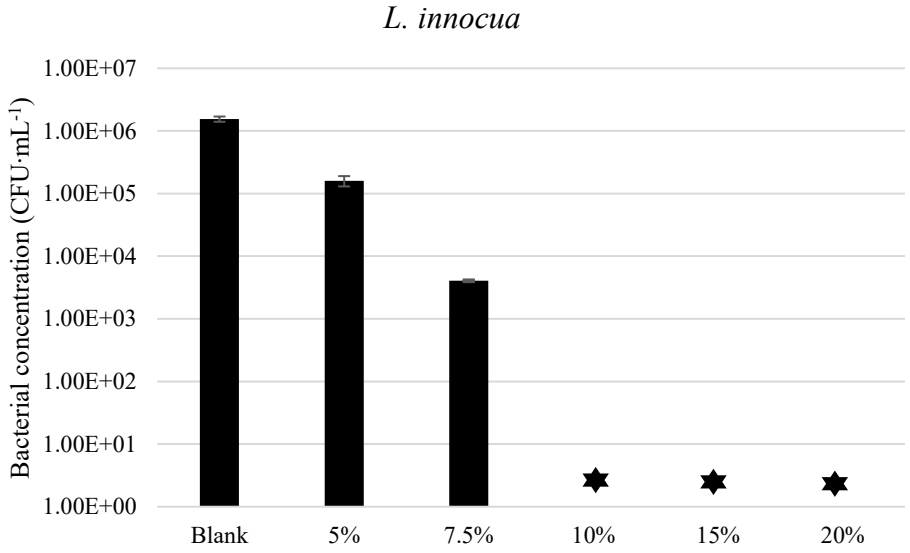


*Figure 117 – Antibacterial activity against L. innocua of AgHEC_6.4_1.4 containing water-based resin 232 films (direct contact), compared to the blank prepared using the same varnish without the AgNPs. The results are reported as bacterial concentration ($CFU \cdot mL^{-1}$) as function of the load of 5 $g \cdot L^{-1}$ AgNPs suspension in the antimicrobial layer. Asterisks represent values below the detection limit, approximated to 0.*

All the tests were conducted in triplicate for each bacterial strain. As expected, a concentration dependent behavior was identified. Increasing the silver load in the coating layer correspond to an increase in the antibacterial activity of the sample. A 10 %wt AgNPs suspension load, which corresponds to a 0.05%wt Ag concentration in the film and to a surface Ag concentration of 6.67 $\mu g \cdot cm^2$, was identified as the composition able to ensure at least 4 log bacterial reduction for each stain. In particular, 4.6 log reduction against *E. coli*, 5.7 log reduction against *S. aureus*, and 7.2 log reduction against *L. innocua*. AgHEC_6.4_1.4 incorporated into 232 water-based resin was more effective against Gram-positive bacteria.

Summarizing, direct contact coatings were identified as the best configuration for the production of these polymeric films, AgHEC_6.4_1.4 demonstrated to be the strongest antibacterial AgNPs variant, and finally a silver concentration of 0.05 %wt resulted enough to ensure at least 4 logarithmic bacterial growth reduction against each of the tested bacterial strains.

***Conclusions*** – The activities here described had as main goal the production of antimicrobial polymeric films. The antimicrobial coating containing AgNPs was deposited as a surface layer or as an intermediate layer acting as an adhesive between two neutral external films. Cellulose biopolymer was used as a substrate for these depositions and water- or solvent-based varnish and adhesive as a dispersive agent for the antibacterial silver nanoparticles.

A first screening of the antibacterial activity was carried out on the AgNPs suspension to identify the most active compositions, AgHEC_6.4_1.4 and AgCur were taken into consideration for the production of the film. Both of these particles demonstrated good dispersibility in the tested varnish and excellent antibacterial activity.

From the antibacterial characterization of the coated films, it was possible to understand the importance of the direct contact between the AgNPs loaded layer and the targeted pathogen, in fact only the surface coating resulted to be active, while the internal adhesive does not promote an antibacterial activity.

AgHEC_6.4_1.4 demonstrated the highest antibacterial activity against both Gram-negative and Gram-positive bacteria. The in-depth concentration-dependent study identified a superficial Ag concentration into the coating of 6.67 $\mu g \cdot cm^2$ enough to ensure a bacterial reduction of 4 logarithms. In particular, 4.6 log reduction against *E. coli*, 5.7 log reduction against *S. aureus*, and 7.2 log reduction against *L. innocua*. AgHEC_6.4_1.4 embedded into these nano-enabled products pointed out higher activity against Gram-positive bacteria.

Concluding, it was possible to develop biopolymeric films embedding AgNPs with relevant antimicrobial properties to a wide set of application fields such as packaging, food industry, and biomedical sector.

***Experimental section***

***Antibacterial test at colloidal level*** – The antibacterial screening at colloidal level was conducted against *Listeria innocua*. The activity was evaluated by monitoring the bacterial reduction by studying the optical density at 600 nm for 24 hours after the inoculum. The negative control was represented by the natural bacterial depletion. Dose dependent behavior was study in a silver concentration range of 1-1000 $\mu g \cdot mL^{-1}$. Sol antibacterial properties against *Escherichia coli* were evaluated in the silver concentration range 30-200 $\mu g \cdot mL^{-1}$.

***Dispersion protocol*** – Typically, 1 gram of matrix (either the water-based or solvent-based resin) was weighted into a glass test tube. Subsequently, about 0.2-0.3 g of 0.5 %wt AgNPs suspension were dispersed in the matrix. Eventually the product was then diluted 1:1 with Milli-Q water in the case of water-base resin or ethyl acetate in the case of solvent base resin. Finally, the dispersion protocol was ultimate by 10 minutes ultrasound treatment.

***Preparation of the coated antimicrobial polymeric films*** – Cellulose biopolymeric films were used as substrate for the deposition of the antimicrobial layer containing AgNPs. Two different configurations were implemented:

- Coating, where the AgNPs containing resin was deposited as surface coating on the cellulose film to have a direct contact with the pathogens. Solvent-based resin ADCOTE from Dow and water-based resins ACTEGA FoodSafe GOLD (named FSG) and ACTEGA 232 (named 232) from ACTEGA were used for the coating production.
- Adhesive, the adhesive loaded with AgNPs was added between two cellulose layers (cellulose-adhesiv-cellulose) to test the indirect contact with pathogens. SIMTACK water-based adhesive from IAB was used for this study.

AgNPs 0.5 %wt colloidal suspension was incorporated into the resin or adhesive at a concentration of 30 %wt, reaching a final Ag concentration in the tested layer of 0.15 %wt. AgNPs dispersion was good and a homogenous product was obtained. Subsequently, 4 g of product were deposited on a 300 $cm^2$ cellulose film, obtaining a silver surface concentration of 20 $\mu g \cdot cm^2$. Coated sheets were cut into 4 $cm^2$ pieces to be used for the antibacterial tests. Similar procedure with different AgNPs colloidal suspension load was used for the preparation of the samples for the concentration dependent study, in the rang 1-20 %wt.

***Antibacterial test on coated polymeric films*** – The antibacterial activity was evaluated against *Escherichia coli* (Gram-negative), *Staphylococcus aureus* (Gram-positive), and *Listeria innocua*

(Gram-positive). Tests were performed following the ISO 22196:2011 "Measurement of antibacterial activity on plastics and other non-porous surfaces", the cellulose films coated with the various matrixes without AgNPs were used as reference blank. The first general screening studying all the variables (AgHEC_6.4_1.4 and AgCur as AgNPs, as water-based resins FSG and 232, as well as solvent-based resin SIMTACK, and water-based-adhesive as dispersing matrix) was assessed preserving a constant Ag concentration 20 $\mu g \cdot cm^2$ (corresponding to a 30 %wt AgNPs suspension load). The in-depth study of the most promising configuration (AgHEC_6.4_1.4 dispersed in 232 water-based resin) was developed to find the optimal Ag concentration, the AgNPs loading range explored varied in between 1-20 %wt. Specifically, 1, 2.5, 5, 10, 13, 15, and 20% for *E. coli*, 1, 2.5, 5, 7.5, 10, 13, 15, and 20% for *S. aureus*, and 5, 7.5, 10, 15, and 20% for *L. innocua*.

### 4.1.4. Spray freeze-dried powder and embedding into biopolymers

AgNPs produced demonstrated good stability, in particular HEC capped AgNPs showed excellent stability for several months and up to two years shelf-life when stored at 4 °C in dark conditions. The stability and the preservation of the antimicrobial properties are key points, so preventing aggregation and sedimentation phenomena is a relevant topic for these materials. Furthermore, the optimized syntheses allow the production of AgNPs at a relatively high concentration, 0.5 %wt Ag, but still the large amount of water makes the transportation more difficult.

To overcome these issues, two solutions based on the low temperature water removal were proposed. The main target of this task it to enhance the stability, durability, and particularly the shelf-life of the produced nanomaterials. To reach the desired goal, the lyophilization technique was implemented for the low temperature water removal, in this way flocculation and aggregation phenomena should be limited or avoided, and the thermolabile organic shell surrounding AgNPs should be preserved.

Two solutions were proposed:

- Spray freeze drying of the colloidal suspension to obtain a micrometric lyophilized AgNPs powder.
- Embedding AgNPs into biopolymers to create solid 3-dimensional structures that will be subsequently lyophilized.

Both the solutions exploit lyophilization as final step to remove water, in this way no damages are inflicted to NPs structures, agglomeration and sedimentation phenomena are not possible and consequently the stability of the product should be extended minimizing his hindrance and weight.

***Spray freeze-dried powder***

The spray freeze drying technique is used for the conversion of liquid suspension, usually in aqueous environment, into solid powders. The process is constituted by two steps, a first one of granulation followed by a lyophilization stage. The granulation step is performed by the gas-assisted spray or atomization of the concentrated feeding suspension into a liquid nitrogen bath to instantaneously freeze the droplets. The frozen droplets are lyophilized and the solvent sublimation allows the formation of highly porous dried granules.

The spray freeze-drying process is commonly used for the encapsulation of active phases such are nanoparticles, drugs, or catalysts into a support matrix which could be either polymeric or ceramic. Nonetheless it could be used to extent the durability of products and nanomaterials. This process is suitable for nanometric and micrometric metals, ceramics, inorganic powders, and organic materials. In the nanotechnology field it is usually applied in the production of nanostructured micrometric granules, starting from a nanosuspension it is possible to obtain a micrometric powder which preserves the nanostructure and the activity typical of nanophases. This concept summarized as "from nano to micro" it is useful to improve the material handling and safety profile, because of all the complications involved in the nanophases processing and handling. The freeze-drying process must be concluded before the triple point of water is reached, otherwise, water fusion would lead to a liquid phase that could compromise desired the micro and nanostructure.[228]

Spray freeze drying technique was implemented in the AgNPs manufacturing to improve the durability, stability and in general the shelf-life of the AgNPs. Once they are lyophilized, aggregation phenomena and sedimentation are avoided, also the process working at low temperature does not damage both the nanoparticles and the organic coating.

***Powder production and characterization*** – AgHEC, AgCur, and AgSur underwent successfully to the spray freeze drying process leading to product with different characteristic. The biopolymer used as capping agent for AgHEC determines a brown sponge-like structure, with a network created by the macromolecule's entanglements. Differently, for AgCur and AgSur it was possible to obtain a powder-like darker material.

AgHEC in powder form was applied in the European Project ASINA Value chain 2 for the production of antimicrobial hand cream and antiaging skin care cream. As already mentioned in Chapter 4.1.1., ASINA Project (Anticipating Safety Issues at the Design Stage of NAno Product Development) aims to promote consistent, applicable and scientifically sound Safe-by-Design nano-practices, considering all nano-enabled products design dimensions: functionality,

production technologies, safety, environmental sustainability, cost effectiveness and regulatory requirements, in line with research responsible innovation policy.[48] The two project Value chains may be summarized as follow:

- Value chain 1 is focused on antimicrobial and depolluting coatings applied on two main case studies: photocatalytic filters and illumination systems based on titanium dioxide nanoparticles coating, and antimicrobial textiles based on silver nanoparticles coating.
- Value chain 2 studies nanostructured capsules delivering active phases in cosmetics, two products of interest were identified in antiaging skin care cream and antibacterial hand cream.

So, spray freeze-dried AgHEC was the focus of a deeper investigation respect AgCur and AgSur. AgHEC_5.5_2.8 was selected as variant object of study, characterizations were compared between the sol phase, named AgHECs, and the powder phase, named AgHECp.[22] The porous sponge-like structure obtained for AgHECp gives a limited specific surface area, it was determined by BET to be ≈ 2 $m^2 \cdot g^{-1}$. Typically, nanostructured materials reach value greater of 1 to 3 order of magnitude, probably the biopolymeric capping agent limits these parameters.

*Transmission electron microscopy* – Phase contrast TEM on the powder revealed spheroidal nanoparticles with size ranging from 5 to 50 nm and HRTEM images confirmed the presence of silver crystalline twinned domains, Figure 118. In general, the morphology and crystallinity are preserved if compared to the sol sample characterized in Chapter 3.2.1., but the HAADF-STEM images used for the statistical size analysis revealed a slight increase in the average size of these nanoparticles, Figure 119. The size of 168 NPs was measured in several images. The estimated average diameter is 18.9 nm with a standard deviation of 10.1 nm. Therefore, with a confidence interval of 99% the average diameter value is assumed 19 ± 2 nm. AgHECs measures for long and short axes were respectively 14.6 ± 0.7 nm and 12.4 ± 0.6 nm, the increase in the particle it is probably due to the spray freeze drying process, which avoid AgNPs fusion and recombination, but does not avoid completely aggregation phenomena. This trend was confirmed by the hydrodynamic DLS measurements.

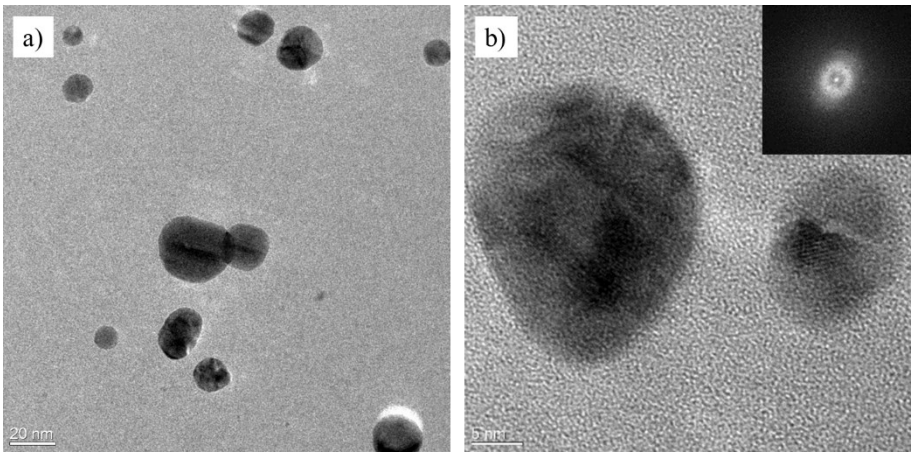


*Figure 118 – a) phase contrast TEM image of AgHECp showing particles size ranging from 5-50 nm; b) HRTEM image of AgHECp showing crystalline nanoparticles formed by twinned domains.*

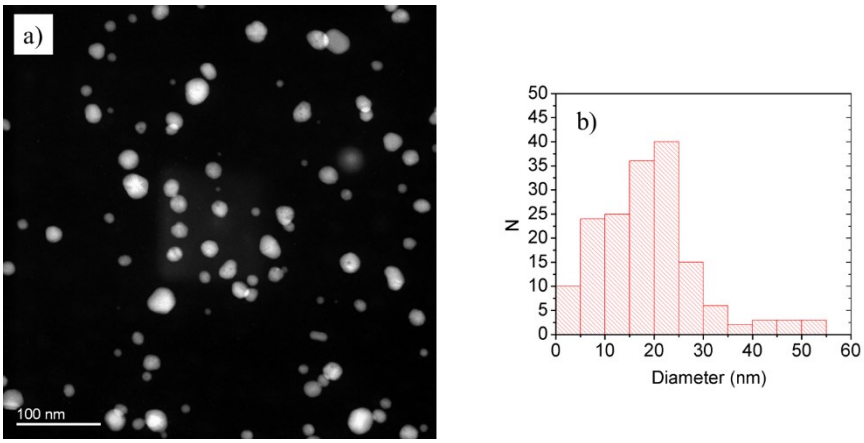


*Figure 119 – a) HAADF-STEM images of AgHECp used for the particle size statistical analysis; b) size distribution statistical analysis of the sample AgHECp, the estimated average diameter was 19 ± 2 nm with a confidence interval of 99%.*

*X-ray diffraction spectroscopy* – The results reported in Figure 120 for both AgHECs and AgHECp show a typical XRD pattern of AgNPs, the main peaks detected can be indexed as a face centered cubic (FCC) structure (JCPDS, file no. 4-0783). The patterns obtained show the presence of diffraction peaks at 38, 44, 64 and 77°, corresponding respectively to (111), (200), (220) and (311) Ag planes. The other peaks were identified as NaCl coproduct and AgCl byproduct, the broad band at about 20 ° is typical for amorphous compounds, in this case represented by the cellulose-based capping agent.

Crystallite size was determined using the Scherrer method on the main diffraction peak (111). AgHECs has a crystallite size of 8.8 nm, and AgHECp of 9.1 nm. The two samples show similar crystallite size, the powder has slightly larger domains, in agreement with TEM results.

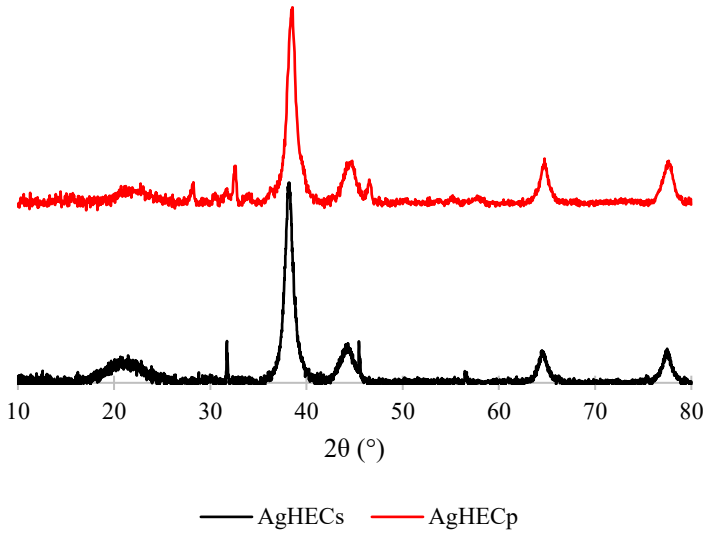


*Figure 120 – XRD spectra comparison of AgHECs and AgHECp presenting the typical face-centered cubic pattern of metallic silver and the diffraction band at 20 ° of the amorphous material represented by the biopolymer used as capping agent.*

*UV-Vis spectroscopy* – The powder was re-suspended in Milli-Q water and the colloidal characterization were repeated. UV-Vis absorption spectra reported in Figure 121 showed the typical surface plasmon resonance peak of AgNPs. The maximum absorption falls at 397 nm for AgHECp and at 410 nm for AgHECs, typical wavelengths of spheroidal AgNPs with size 10-20 nm. The spray freeze-drying process induces a blue shift and also gives a sharper absorption peak.[94,95,96,97,98]

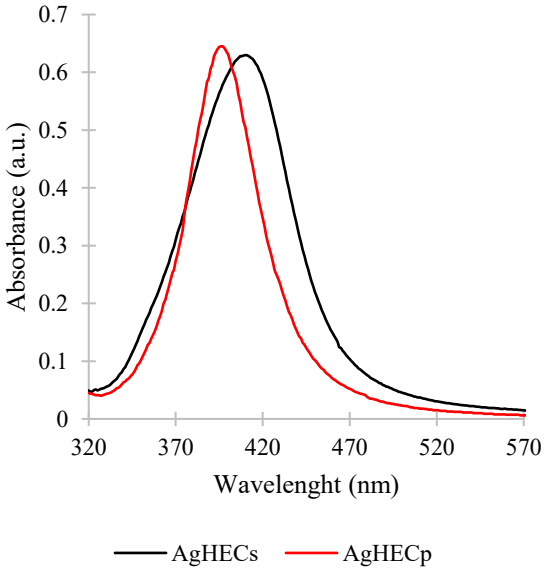


*Figure 121 – UV-Vis absorption spectra comparison between AgHECs and AgHECp presenting the typical SPR absorption peak of AgNPs with maximum absorption in the wavelength range of 397-410 nm.*

*Hydrodynamic diameter, polydispersity, and zeta potential* – As already shown by the TEM images, the spray freeze drying process induces a limited increase of the NPs dimensions. This trend is confirmed for the hydrodynamic diameter, AgHECp has a larger size (369 nm) than AgHECs (286 nm). The polydispersity is also increased, while the zeta potential is positive for both samples, ≈ 15 mV. The electrostatic repulsion, combined with the steric hindrance, contributes to the suspension stability. These results are summarized in Table 50.

*Table 50 – Colloidal characterization of the sol (AgHECs) and powder (AgHECp) samples: hydrodynamic diameter and polydispersity index assessed by DLS and zeta potential assessed by ELS.*

| Sample | Average hydrodynamic diameter (nm) | PDI | Zeta potential (mV) |
|---|---|---|---|
| AgHECs | 286 ± 5 | 0.323 ± 0.004 | 16.5 ± 0.3 |
| AgHECp | 369 ± 41 | 0.49 ± 0.06 | 14.0 ± 0.6 |

***Conclusion*** – The spray freeze drying technique was implemented to improve the handleability of the synthesize AgNPs and to extent their shelf-life. The physicochemical characterization of the powder AgHECp demonstrated lesser variation respect to the sol AgHECs. In particular, a limited increase in the particle size and subsequently in the crystallite size and hydrodynamic diameter was observed. This may be due to the solvent removal and a minimal coalescence of the particle during the spray or lyophilization processes. In general, the spray freeze drying may be a valid solution to facilitate the storage and the processing of these nanophases, the main disadvantage is related to the cost of the freeze-drying step, which is usually implemented for high added value products, like in the pharmaceutical or nutraceutical fields.

***Experimental part***

*Spray freeze drying* – The equipment used for the spray freeze drying process is the PowderPro lab-scale Granulator LS-2 coupled with the SRK Systemtechnik LYO GT2 freeze dryer. While the colloidal suspension batch is kept under magnetic stirring, a peristaltic pump makes flow the sample through a nozzle, fed together with a gas flow, typically nitrogen. The spray obtained by the nozzle is produced within a magnetically stirred liquid nitrogen bath at -196 °C. Droplet are instantly frozen and subsequently lyophilized, at the end of the process the water sublimation allows the production of a porous dry powder.

A typical spray freeze drying treatment of colloidal AgNPs suspension is performed under the following condition: the AgNPs suspension is properly diluted (typically 5- or 10-fold dilution for AgHEC because of its viscosity, while no dilution is required for AgCur and AgSur), the peristaltic pump is set at 20-40 rpm (slower liquid flow rate allows the production of finer spray and powder), the nitrogen pressure is 0.4 bar (higher gas pressure involves finer spray and powder), the nozzle size is 100 µm. The lyophilization process is performed at -1 °C and 1.5 mbar for 48 hours.

*Transmission electron microscopy* – AgHECp was dispersed in isopropyl alcohol and sonicated for 15 min. AgHECs is sonicated for 15 min. The obtained suspensions are deposited on a perforated carbon film supported by a gold grid. The preparation was then dried at 40 °C. TEM analyses were performed with a FEI TECNAI F20 microscope operating at 200 keV. The instrument is also equipped with a dispersion micro-analysis of energy (EDS) and the STEM accessory. The TEM image were taken in the phase contrast mode and selected area electron diffraction (SAED). STEM pictures were recorded using a High Angle Annular Dark Field (HAADF) detectors: in this imaging mode the intensity I is proportional to $Z^{1.7}t$, where Z is the mean atomic number and t is the thickness of the specimen.

*X-ray diffraction spectroscopy* – Few droplets of AgHECs 500 $mg \cdot L^{-1}$ suspension were deposited on glass substrate and dried at 80 °C, the procedure was repeated in order to obtain a homogenous layer. AgHECp was pressed into the sample holder. X-ray diffraction analyses were performed with Bruker D8 Advance (Cu Kα 1.5406 Å). Working conditions: 2θ interval 10-80°, step 0.04°, step time 0.5 s.

*UV-Vis spectroscopy* – AgHECs was diluted to 6 $mg \cdot L^{-1}$ with Milli-Q. AgHECp was dispersed in Milli-Q at the concentration of 6 $mg \cdot L^{-1}$. The instrument used is Perkin Elmer Lambda 750.

*Hydrodynamic diameter, polydispersity, and zeta potential measurements* – 50 $mg \cdot L^{-1}$ AgHECs suspension was prepared diluting the stock suspension in Milli-Q. AgHECp was dispersed in Milli-Q, 100 $mg \cdot L^{-1}$ suspension. Hydrodynamic Light Scattering (DLS) and Electrophoretic Light Scattering (ELS) measurement were performed with Zetasizer Nano ZSP, Malvern Instrument.

***Embedding into biopolymers*** – The purpose of this work is to make active nanophases more handleable designing a product that can immobilize them evenly within a macroscopic solid matrix. The study was focused on biocompatible, renewable and low environmental impact materials: chitosan and agarose are widely studied natural biopolymers. Agarose is obtained by the purification of agar, a gelatinous substance extracted from red algae, chitosan is a cationic polymer soluble at acidic pH obtained by deacetylation of chitin, derived from the exoskeleton of crustaceans.[229,230] Biopolymeric hydrogels are tridimensional structures constituted by entangled and crosslinked polymeric chains, they possess important features like biocompatibility, softness, and they can be easily shaped. The embedding of active nanophases into these structures during the hydrogel formation improve NPs biocompatibility, biodegradability, it is possible to better control the release of the active phase, making these materials very interesting for human safety and environmental remediation applications.[73]
Freeze drying offers the possibility of drying biopolymers, transforming them into porous, solid, light and stable matrices, able to accommodate nanophases inside them. The work has been focused in the production of a gelatinous matrix that allows the storage of the AgNPs for water treatment, products were subsequently freeze-dried to obtain a solid composite material. The prepared nano-enabled products were evaluated in terms of antibacterial activity.

***Results and discussion*** – The antibacterial tests were carried out by certified laboratories of CNR-STIIMA (Biella, Italy).
From the antibacterial results reported in Table 51 it is possible to see that the chitosan without AgNPs possesses a minimal antibacterial activity against *E. coli* (47.8% bacterial reduction), while no activity was observed for agarose (0.0 % bacterial reduction). Chitosan it is known as a natural antibacterial agent, thanks to its positive charge it can interact with the bacterial membrane modifying its permeability leading to lysis, or it can interact with the genetic material of the bacterium interfering with the protein synthesis.[231]
The antibacterial properties were enhanced by the crosslinking with glutaraldehyde, which is historically used as chemical disinfectant thanks to its wide-ranging mechanism of action against the bacterial cell wall, for this reason it is more effective against Gram-positive.[232] Crosslinked products reaches 84.6% and 99.5% *E. coli* reduction, respectively for chitosan and agarose. Since agarose itself didn't show any antibacterial activity, it is possible that unreacted glutaraldehyde has been partially released during the antibacterial test from the crosslinked product, determining that high *E. coli* reduction value. Even if chitosan possesses antibacterial activity the

enhancement is lower than agarose, this is probably due to a better interaction of aldehydic groups of glutaraldehyde with the ammine groups of chitosan, to form amide bridges.

Finally, AgNPs were embedded into biopolymeric scaffolds crosslinked with glutaraldehyde, AgCur and AgSur_04 variants were tested, scaffolds loaded with curcumin or sodium surfactin were considered as reference blanks. Excellent results were obtained against both *E. coli* and *S. aureus*, in fact, in this configuration all the combinations of biopolymeric scaffold and AgNPs granted 100% bacterial reduction. In this way it is difficult to discriminate the most effective solution, but in general it is possible to observe the excellent antibacterial activity of these nano-enabled products. The main consideration may be done regarding the scaffold stability, in this case agarose-based scaffold resulted to be more stable and resistant, they were found unaltered after the test (1 h and 190 rpm), while chitosan-based scaffolds were strongly damaged. For what concerns the blanks, if their activity against *E. coli* was compared with crosslinked agarose (99.5% reduction) and chitosan (84.6% reduction), it is possible to see how both curcumin and sodium surfactin determine a lesser depletion of the activity of the chitosan-based materials and leaves nearly unaltered the results of agarose-based samples. Furthermore, it was possible to confirm the higher susceptibility of Gram-positive bacteria in presence of glutaraldehyde.

*Table 51 – Antibacterial activity against E. coli and S. aureus of the biopolymeric scaffolds based on chitosan and agarose.*

| **Sample** | **Ag conc. (%wt)** | ***E. coli* reduction (%)** | ***S. aureus* reduction (%)** |
|---|---|---|---|
| Chitosan | 0 | 47.8 | / |
| Agarose | 0 | 0 | / |
| Chitosan-glutaraldehyde | 0 | 84.6 | / |
| Agarose-glutaraldehyde | 0 | 99.5 | / |
| Chitosan-glutaraldehyde-AgSur | 1.11 | 100 | 100 |
| Chitosan-glutaraldehyde-sodium surfactin | 0 | 68.3 | 99.5 |
| Agarose-glutaraldehyde-AgSur | 1.11 | 100 | 100 |
| Agarose-glutaraldehyde-sodium surfactin | 0 | 100 | 100 |
| Chitosan-glutaraldehyde-AgCur | 1.21 | 100 | 100 |
| Chitosan-glutaraldehyde-curcumin | 0 | 81.1 | 99 |
| Agarose-glutaraldehyde-AgCur | 1.21 | 100 | 100 |
| Agarose-glutaraldehyde-curcumin | 0 | 100 | 100 |

***Conclusions*** – AgNPs play an important role in the final antibacterial activity of these biopolymeric scaffolds, but a synergistic action between the biopolymer, the crosslinking agent and the active phase was observed, leading to a quantitative abatement of bacteria in the conditions tested. It was developed an antibacterial, stable, and resistant nano-enabled product, able to treat both Gram-negative and Gram-positive bacteria in aqueous environment.

***Experimental part***

*Biopolymeric scaffolds preparation* – The development of these materials involves the use of a biopolymeric matrix, a crosslinking agent to improve the mechanical properties and reduce the solubility of the product, and an active phase such as antimicrobial AgNPs. Chitosan and agarose were selected as embedding agents, glutaraldehyde as crosslinker, and AgCur and AgSur_04 as AgNPs variants to be tested. To discriminate the contribute of each phase, different products were prepared:

- Biopolymeric scaffolds, the typical procedure involves the dispersion of 1 g of biopolymer into 49 mL of Milli-Q water or a 2 %wt acetic acid solution in the case of chitosan, for a final biopolymer concentration of 2 %wt. The dispersion is performed under magnetic stirring at 80 °C for at least 20 minutes. Once the polymer is well-dispersed the suspension is casted into molds (Petri dish 3 cm diameter and 1 cm height) and cooled at room temperature. Samples were then frozen and lyophilized for 48 h obtaining the final product.
- Crosslinked biopolymeric scaffolds, 48.82 mL of Milli-Q water or 2 %wt acetic acid solution in the case of chitosan under magnetic stirring were used to disperse 1 g of biopolymer, with a final concentration of 2 %wt. The suspension is heated at 80 °C, 180 µL of glutaraldehyde 50 %wt are added under magnetic stirring and after for 20 minutes the suspension is cooled at room temperature. Samples were then frozen and lyophilized for 48 h obtaining the final crosslinked product.
- AgNPs embedded into crosslinked biopolymeric scaffolds, 46.32 mL of Milli-Q water or 2 %wt acetic acid solution in the case of chitosan under magnetic stirring were used to disperse 1 g of biopolymer, with a final concentration of 2 %wt. 2.5 mL of AgNPs 0.5 %wt Ag concentrated suspension are added, then the mixture is heated up to 80 °C, 180 µL of glutaraldehyde 50 %wt are added under magnetic stirring and after for 20 minutes the suspension is cooled at room temperature. Samples were then frozen and lyophilized for 48 h obtaining the final crosslinked product.

*Antibacterial test* – The biopolymeric scaffolds antimicrobial activity was evaluated according to ASTM E2149-01 "Standard test method for determining the antimicrobial activity of immobilized antimicrobial agents under dynamic contact conditions". The method is designed to evaluate the resistance of non-leaching antimicrobial treated specimens to the growth of microbes under dynamic contact conditions. The applied bacteria are *Escherichia coli* ATCC 11229 (Gram-negative) and *Staphylococcus aureus* ATCC 6538 (Gram-positive). The incubated test culture was diluted to give a concentration of $1.5–3.0\times10^5$ $CFU\cdot mL^{-1}$ (working dilution). Each sample (scaffolds about 0.5 g) was transferred to flask containing 25 mL of the working dilution. All flasks were shaken for 1 h at 190 rpm. After a series of dilutions, 1 mL of the solution was plated in nutrient agar. The inoculated plates were incubated at 37 °C for 24 h and surviving cells were counted. The antimicrobial activity was expressed as % reduction of the organisms after contact with the test specimen compared to the number of bacterial cells surviving after contact with the control. Each result is the average of three independent measurements.

## 4.3. Conclusions

Different case studies were used to explore antimicrobial silver nano-enabled products (NEPs). The silver nanoparticles synthesized following safe and sustainable principles and guidelines were implemented into a large variety of antimicrobial nano-enabled products: medical grade polyester fabrics, paper-based materials with high circulation rate, varnished cellulose biopolymeric films, biopolymeric scaffolds, and spray freeze-dried powder. The manufacturing step of AgNPs implementation into NEPs was performed thanks to different techniques, such as spray-coating, dip-coating, roll-to-roll printing, spray freeze drying, and hydrogel lyophilization. Different NEPs and different manufacturing techniques were exploited to have an overview of these AgNPs capabilities, and the products were evaluated in terms of antimicrobial efficacy and durability.

In the antimicrobial textiles case study, it was observed how the AgNPs variant has a strong influence on the washing fastness, in this particular case, the charge of the capping aged played a fundamental role. Positive AgCur nanoparticles displayed better washing fastness demonstrating a gradual silver release from the fabric. These products preserved excellent antimicrobial activity even after several washing or abrasion cycles. Effectiveness and durability combined makes AgCur coated textiles an interesting material for antimicrobial clothing. The comparison between spray-coating and dip-coating highlighted an easier industrial implementation for the spray technique, but the best results were obtained for a higher silver load inducted by the dipping. Spray-coating involves also a possible inhalation exposure route that must be considered, and safety containment measures must be implemented in the manufacturing plant, such as suction hoods.

The antimicrobial paper case study pointed out another important point, the aesthetical impact of the colored coating. For applications where the coloration is relevant, it must be considered the typical yellow coloration of AgNPs, in this case a compromise was reached between the antimicrobial and aesthetical properties of the NEP, selecting the minimal silver concentration able to grant the desired antimicrobial activity. AgHEC_6.4_1.4 was demonstrated to be the most active variant and it was selected for the scale-up to industrial roll-to-roll printing plant. Here a large-scale production with a lower Ag concentration was implemented. A homogenous coating was produced, and the Ag concentration-dependent antimicrobial activity was confirmed.

From the polymeric film case study emerged other important topics. First, the contact mode between AgNPs and pathogens, a direct contact is required to exploit the antimicrobial properties. Second, the dispersibility and the stability of the nanophase in the coating agent, in

this case solvent- and water-based resins were used, and AgNPs variants exhibited different affinity for the varnishes. AgHEC_6.4_1.4 confirmed to be the most active variant and a superficial Ag concentration in the coating of 6.67 $\mu g \cdot cm^2$ was enough to ensure at least 4 logarithms of bacterial reduction against *E. coli*, *S. aureus*, and *L. innocua*.

Embedding AgNPs into crosslinked biopolymers revealed synergistic effects among AgNPs, biopolymeric matrix, and the crosslinking agent. The spray freeze-drying process is confirmed to be an interesting technique to increase the handleability and stability of high added value active phases or products.

The case study importance lies in the possibility of studying various life cycle steps, starting from the synthesis of the nanomaterial, moving to the manufacturing where the workers' exposure may be considered, to the use phase where the performances, human exposure and environmental release are key points, and finally the end of life. Real implementation problems are taken into consideration, and project results can be easily exploited by industries and regulatory frameworks.

## 4.4. References

189. Vinod P. Raphael et al. In silico investigations on the repurposing of antivirals for Covid-19 and pharmacophore modelling. Current Chemistry Letters 13 (2024) 199–206.

190. Mohammed Salah et al. Insight into a new discovery of SARS-CoV-2 inhibitor activated through Chloroquine derivatives. Current Chemistry Letters 13 (2024) 49–60.

191. Dey R, Bishayi B. Microglial Inflammatory Responses to SARS-CoV-2 Infection: A Comprehensive Review. Cell Mol Neurobiol. 2023 Dec 15;44(1):2. doi: 10.1007/s10571-023-01444-3. PMID: 38099973.

192. Pasparakis G. Recent developments in the use of gold and silver nanoparticles in biomedicine. Wiley Interdiscip Rev Nanomed Nanobiotechnol. 2022 Sep;14(5):e1817. doi: 10.1002/wnan.1817. Epub 2022 Jul 1. PMID: 35775611; PMCID: PMC9539467.

193. Paesa M, Alejo T, Garcia-Alvarez F, Arruebo M, Mendoza G. New insights in osteoarthritis diagnosis and treatment: Nano-strategies for an improved disease management. Wiley Interdiscip Rev Nanomed Nanobiotechnol. 2023 Mar;15(2):e1844. doi: 10.1002/wnan.1844. Epub 2022 Aug 14. PMID: 35965293.

194. Hao P, Wang Y, Sun X, Wang J, Zhang LW. Derivation of the toxicological threshold of silicon element in the extractables and leachables from the pharmaceutical packaging and process components. Toxicol Ind Health. 2022 Dec;38(12):819-834. doi: 10.1177/07482337221123368. Epub 2022 Nov 11. PMID: 36368686.

195. Reinhilde Schoonjans, Jacqueline Castenmiller, Qasim Chaudhry, Francesco Cubadda, Takis Daskaleros, Roland Franz, David Gott, Jan Mast, Alicja Mortensen, Agnes G. Oomen, Hubert Rauscher, Stefan Weigel, Maria Chiara Astuto, Irene Cattaneo, Eric Barthelemy, Ana Rincon, José Tarazona, Regulatory safety assessment of nanoparticles for the food chain in Europe, Trends in Food Science & Technology, Volume 134, 2023, Pages 98-111, ISSN 0924-2244, https://doi.org/10.1016/j.tifs.2023.01.017.

196. Nanotechnology Clothing Global Market Report 2022, By Type, By Application, By End-User Sex. (2022). https://www.thebusinessresearchcompany.com/report/nanotechnology-clothing-global-market-report.

197. Ismar E, Kurşun Bahadir S, Kalaoglu F, Koncar V. Futuristic Clothes: Electronic Textiles and Wearable Technologies. Glob Chall. 2020 Mar 18;4(7):1900092. doi: 10.1002/gch2.201900092. PMID: 32642074; PMCID: PMC7330505.

198. The Global Textile and Clothing Industry, Technological Advances and Future Challenges, A volume in Woodhead Publishing Series in Textiles, Book 2012, R. Shishoo.

199. Attia, Nour Fathi and Mona Mousa. "Synthesis of smart coating for furniture textile and their flammability and hydrophobic properties." Progress in Organic Coatings 110 (2017): 204-209.

200. Dhanasekaran, R. et al. "Shape Memory Materials for Bio-medical and Aerospace Applications." Materials Today: Proceedings 5 (2018): 21427-21435.

201. Eyvaz, Murat et al. "Textile Materials in Liquid Filtration Practices: Current Status and Perspectives in Water and Wastewater Treatment." (2017).

202. Gibała A, Żeliszewska P, Gosiewski T, Krawczyk A, Duraczyńska D, Szaleniec J, Szaleniec M, Oćwieja M. Antibacterial and Antifungal Properties of Silver Nanoparticles-Effect of a Surface-Stabilizing Agent. Biomolecules. 2021 Oct 7;11(10):1481. doi: 10.3390/biom11101481. PMID: 34680114; PMCID: PMC8533414.

203. Abu-Qdais, H.A., Abu-Dalo, M.A., & Hajeer, Y.Y. (2021). Impacts of Nanosilver-Based Textile Products Using a Life Cycle Assessment. Sustainability.

204. McGillicuddy E, Murray I, Kavanagh S, Morrison L, Fogarty A, Cormican M, Dockery P, Prendergast M, Rowan N, Morris D. Silver nanoparticles in the environment: Sources, detection and ecotoxicology. Sci Total Environ. 2017 Jan 1;575:231-246. doi: 10.1016/j.scitotenv.2016.10.041. Epub 2016 Oct 12. PMID: 27744152.

205. Aguda ON, Lateef A. Recent advances in functionalization of nanotextiles: A strategy to combat harmful microorganisms and emerging pathogens in the 21st century. Heliyon. 2022 Jun 22;8(6):e09761. doi: 10.1016/j.heliyon.2022.e09761. PMID: 35789866; PMCID: PMC9249839.

206. Wei L, Lu J, Xu H, Patel A, Chen ZS, Chen G. Silver nanoparticles: synthesis, properties, and therapeutic applications. Drug Discov Today. 2015 May;20(5):595-601. doi: 10.1016/j.drudis.2014.11.014. Epub 2014 Dec 24. PMID: 25543008; PMCID: PMC4433816.

207. Liao C, Li Y, Tjong SC. Bactericidal and Cytotoxic Properties of Silver Nanoparticles. Int J Mol Sci. 2019 Jan 21;20(2):449. doi: 10.3390/ijms20020449. PMID: 30669621; PMCID: PMC6359645.

208. Yin IX, Zhang J, Zhao IS, Mei ML, Li Q, Chu CH. The Antibacterial Mechanism of Silver Nanoparticles and Its Application in Dentistry. Int J Nanomedicine. 2020 Apr 17;15:2555-2562. doi: 10.2147/IJN.S246764. PMID: 32368040; PMCID: PMC7174845.

209. Deshmukh SP, Patil SM, Mullani SB, Delekar SD. Silver nanoparticles as an effective disinfectant: A review. Mater Sci Eng C Mater Biol Appl. 2019 Apr;97:954-965. doi: 10.1016/j.msec.2018.12.102. Epub 2018 Dec 28. PMID: 30678983; PMCID: PMC7127744.

210. Marija Gorjanc et al, Multifunctional Textiles – Modification by Plasma, Dyeing and Nanoparticles, DOI: 10.5772/53376.

211. Jing Zhou et al, Excellent binding effect of l-methionine for immobilizing silver nanoparticles onto cotton fabrics to improve the antibacterial durability against washing, RSC Adv., 2018,8, 24458-24463, https://doi.org/10.1039/C8RA04401E.

212. Noor N, Mutalik S, Younas MW, Chan CY, Thakur S, Wang F, Yao MZ, Mou Q, Leung PH. Durable Antimicrobial Behaviour from Silver-Graphene Coated Medical Textile Composites. Polymers (Basel). 2019 Dec 3;11(12):2000. doi: 10.3390/polym11122000. PMID: 31816952; PMCID: PMC6961056.

213. Fernandes, M.; Padrão, J.; Ribeiro, A.I.; Fernandes, R.D.V.; Melro, L.; Nicolau, T.; Mehravani, B.; Alves, C.; Rodrigues, R.; Zille, A. Polysaccharides and Metal Nanoparticles for Functional Textiles: A Review. Nanomaterials 2022, 12, 1006. https://doi.org/10.3390/nano12061006.

214. Luceri, A., Perero, S., Cochis, A. et al. Washing resistant antibacterial composite coatings on cotton textiles. Cellulose 30, 9877–9897 (2023). https://doi.org/10.1007/s10570-023-05471-7.

215. Buckley, R.R., Giorgianni, E.J. (2016). CIELAB for Color Image Encoding (CIELAB, 8-Bit; Domain and Range, Uses). In: Luo, M.R. (eds) Encyclopedia of Color Science and Technology. Springer, New York, NY. https://doi.org/10.1007/978-1-4419-8071-7_14.

216. Uzair Khaleeq uz Zaman, Mickael Rivette, Ali Siadat, Seyed Meysam Mousavi, Integrated product-process design: Material and manufacturing process selection for additive manufacturing using multi-criteria decision making, Robotics and Computer-Integrated Manufacturing, Volume 51, 2018, Pages 169-180, ISSN 0736-5845, https://doi.org/10.1016/j.rcim.2017.12.005.

217. H. Strathmann, Membrane separation processes, Journal of Membrane Science, Volume 9, Issues 1–2,1981, Pages 121-189, ISSN 0376-7388, https://doi.org/10.1016/S0376-7388(00)85121-2.

218. 6 - Drug delivery systems, Editor(s): Marcos Luciano Bruschi, Strategies to Modify the Drug Release from Pharmaceutical Systems, Woodhead Publishing, 2015, Pages 87-194, ISBN 9780081000922, https://doi.org/10.1016/B978-0-08-100092-2.00006-0.

219. Giulia Barzan, Luca Rocchetti, Chiara Portesi, Francesco Pellegrino, Angelo Taglietti, Andrea Mario Rossi, Andrea Mario Giovannozzi, Surface Minimal Bactericidal Concentration: A comparative study of active glasses functionalized with different-sized silver nanoparticles, Colloids and Surfaces B: Biointerfaces, Volume 204, 2021, 111800, ISSN 0927-7765, https://doi.org/10.1016/j.colsurfb.2021.111800.

220. https://food.ec.europa.eu/safety/chemical-safety/food-contact-materials/legislation_en#active-intelligent

221. Syed Sayeed Ahmad, Silver nanoparticles as an active packaging ingredient and its toxicity, July 2021Packaging Technology and Science 34(1). DOI: 10.1002/pts.2603.

222. Yage Shi et al. Pasteurizing Cold Smoked Salmon (Oncorhynchus nerka): Thermal Inactivation Kinetics of Listeria monocytogenes and Listeria innocua. Journal of Aquatic Food Product Technology, Volume 24, 2015 - Issue 7. https://doi.org/10.1080/10498850.2013.808303

223. McMeekin TA, Baranyi J, Bowman J, Dalgaard P, Kirk M, Ross T, Schmid S, Zwietering MH. Information systems in food safety management. Int J Food Microbiol. 2006 Dec 1;112(3):181-94. doi: 10.1016/j.ijfoodmicro.2006.04.048. Epub 2006 Aug 28. PMID: 16934895.

224. Karli A, Sensoy G, Unal N, Yanik K, Cigdem H, Belet N, Sofuoglu A. Ventriculoperitoneal shunt infection with Listeria innocua. Pediatr Int. 2014 Aug;56(4):621-3. doi: 10.1111/ped.12302. PMID: 25252053.

225. R. Y. Murphy et al. D and z Values of Salmonella, Listeria innocua, and Listeria monocytogenes in Fully Cooked Poultry Products. May 2003Journal of Food Science 68(4):1443 – 1447. DOI: 10.1111/j.1365-2621.2003.tb09664.x.

226. Yin IX, Zhang J, Zhao IS, Mei ML, Li Q, Chu CH. The Antibacterial Mechanism of Silver Nanoparticles and Its Application in Dentistry. Int J Nanomedicine. 2020;15:2555-2562. https://doi.org/10.2147/IJN.S246764.

227. You C, Han C, Wang X, Zheng Y, Li Q, Hu X, Sun H. The progress of silver nanoparticles in the antibacterial mechanism, clinical application and cytotoxicity. Mol Biol Rep. 2012 Sep;39(9):9193-201. doi: 10.1007/s11033-012-1792-8. Epub 2012 Jun 22. PMID: 22722996; PMCID: PMC7089021.

228. Lolli, A., Blosi, M., Ortelli, S., Costa, A.L., Zanoni, I., Bonincontro, D., Carella, F., & Albonetti, S. (2019). Innovative synthesis of nanostructured composite materials by a spray-freeze drying process: Efficient catalysts and photocatalysts preparation. Catalysis Today.

229. de Souza Neves Ellendersen, L., Milinsk, M.C., Feroldi, M., Volkweis Zadinelo, I., Dena dos Santos, L., Bolzon de Muniz, G.I., Gasparrini, L.J., & Alves, H.J. (2018). Biopolymer foam for remediation of aquatic environments contaminated with particulates and heavy metals. Journal of Environmental Chemical Engineering.

230. Halanur M. Manohara et al. Progress in marine derived renewable functional materials and biochar for sustainable water purification. DOI: 10.1039/D1GC03054J (Critical Review) Green Chem., 2021, 23, 8305-8331.

231. Hosseinnejad M, Jafari SM. Evaluation of different factors affecting antimicrobial properties of chitosan. Int J Biol Macromol. 2016 Apr;85:467-75. doi: 10.1016/j.ijbiomac.2016.01.022. Epub 2016 Jan 11. PMID: 26780706.

232. Gorman SP, Scott EM, Russell AD. Antimicrobial activity, uses and mechanism of action of glutaraldehyde. J Appl Bacteriol. 1980 Apr;48(2):161-90. doi: 10.1111/j.1365-2672.1980.tb01217.x. PMID: 6780502.

# Chapter 5

## *Green synthesis of noble metals-based nanoparticles for catalytic applications*

Part of the content of this chapter has been published as Master's Thesis of I. Bonvicini "Sintesi assistita al microonde di nanoparticelle Au/Pt per applicazioni catalitiche" 2022.

## 5.1. Introduction

One of the main targets in the industrial chemical field is to substitute oil-based processes with new routes employing biomass-derived renewable feedstock to produce desired chemical building block molecules. An example may be 5-hydroxymethyl furfural (HMF), an abundant biomass-derived molecule that could be conveniently converted in 2,5-furandicarboxylic acid (FDCA), via catalytic oxidation route. Then FDCA can be polymerized into polyethylene furan dicarboxylate (PEF), the resulting polymer has similar properties as polyethylene terephthalate (PET) commonly used for plastics production such as water bottles. FDCA as well as other biomass-derived platform molecule could be an extremely important advancement in the progressive substitution of fossil fuels.[233,234] The first step of conversion of HMF into FDCA still requires further optimization to be industrially competitive. This reaction can be carried out by expensive noble metal catalysts, promising results were achieved in the last years, but still further improvements are required.

In catalysis, the development of new, more efficient, and selective catalysts is becoming increasingly important aiming at the reduction of the environmental impact of various productive processes. In this scenario, nanostructured materials plays a fundamental role due to the high surface/volume aspect ratio that makes them particularly reactive and suitable to be applied in catalysis.[234] The study of the size, electronic structure, and surface properties of nanoparticles is fundamental for the determination of catalytic activity and selectivity.[235] The preparation method implemented, the reagents used, the presence of stabilizers, as well as other parameters, influence the physicochemical properties of the product and therefore also the catalytic properties.[236] Furthermore, to promote new sustainable processes, it is necessary to favor nanomaterials synthetic processes involving a limited impact on human and environmental health.

***Nanoparticles in catalysis*** – Nanoparticles play a very important role in today's chemistry, and in particular in catalysis.[237] In fact, the peculiar physicochemical properties of these materials made them a fundamental subject of study and research in the scientific community. Nanoparticles and nanomaterials in general, have a much larger surface/volume ratio than their common bulk form, creating more active sites and more accessible.[234] Furthermore, the nanometric structure provides the material with peculiar electronic properties different from the classical massive form. Fundamental aspects of the study of nanoparticles are: the method of preparation, the dimensions, and eventually the support used in heterogeneous catalysis. The method of preparation can affect the chemical and physical structure of nanoparticles, whether

or not it encourages the formation of different species that can generate substantial changes to catalytical behavior. In heterogenous catalysis, the use of a support is essential, not only to facilitate the catalyst separation process from the reaction mixture, but also because the support itself can selectively provide particular physicochemical properties. However, the size and the surface/volume aspect ratio are the most important properties for catalysts. Many properties depend on the surface such as solubility, reactivity, melting point, electronic structure, and stability.[238] The atoms on the surface of the catalysts are the ones active during catalytic reactions. Due to less coordination and more free bonds on the surface, the outermost atoms act as active sites for reactions. For this purpose, research for the synthesis of metallic nanoparticles is based on the attempt to develop different methodologies for the formation of small nanoparticles.

***Sustainable methods for catalyst preparation*** – In the early 1990s, interest in the environment and the sustainability of processes led to the enunciation of the twelve principles of Green Chemistry by Paul Anastas and John Warner.[239] The principles for sustainable chemistry have several purposes: to safeguard the environment by paying special attention to raw materials used in processes, respond in an alternative way to energy demand and safeguard the health of works by using non-hazardous substances or at least reduce their use. In agreement with R. A. Sheldon, principles of sustainable chemistry aim at a more functional use of resources to avoid excessive formation of waste, reduce the energetic impact of processes and increase production from renewable substances by breaking away from dependence on oil. Catalysis has also begun to play a key role in this. Thanks to reactions using catalysts, the use of reagents is reduced, selectivity toward desired products is increased and waste and reaction by-products are reduced. Today, green or low environmental impact chemical processes are still difficult to apply on an industrial level, both because of the cost associated with the new instrumentation required for such processes, and because most of the green reagents are still very expensive. Sustainable processes are those in which the principles of Green Chemistry are followed in all levels of production, and every single step is programmed based on them. For this purpose, catalysis is essential, but also catalyst synthesis plays an important role. The synthesis of metal nanoparticles catalysts is usually carried out into organic solvents, which have a higher cost of disposal and a stronger impact on environmental pollution, to solve this problem, new synthetic routes have been developed using water as a solvent. For the synthesis of metallic nanoparticles in an aqueous environment it is necessary to consider the non-chelating nature of the solvent. This nature prevents the solvent from being able to act, even in a small part, as steric stabilizer of

nanoparticles and for this reason it is necessary to use of protective capping agent. Even for the choice of the reducing agent it is necessary to apply the principles of sustainable chemistry and for this reason many syntheses use glucose as a reducing agent, during the reduction of the metal precursor, glucose is partially oxidized forming gluconate, which is able to coordinate the metal and to act as a stabilizer of the freshly synthesized nanoparticles.

***Aim of the work*** – The safe and sustainable approach described in previous chapters for the synthesis of silver nanoparticles exploited into nano-enabled products for antimicrobial purposes, may be extended to a large variety of nanomaterials, composite materials, and advanced materials. For example, the need to safeguard the environment has led to an important development of catalytic processes, aimed at maximizing the efficiency of the reactions involved, with particular attention to the aspects of sustainability and environmental impact. Metal nanoparticles, known for their excellent catalytic properties, play a key role in the field of heterogeneous catalysis.[234] The preparation of metallic nanoparticles, to be used as catalysts, should focus on innovative methods with low environmental impact. In order to trigger synergistic effects and achieve better performing catalysts, research has increasingly focused on the study of bimetallic or multicomponent nanoparticles. In this contest, the production of bi-metallic alternatives to expensive platinum-based catalyst may help in the development of industrially affordable technologies for the biomass valorization exploiting synergistic effects of gold-platinum alloy and core-shell structures.

The purpose of this work is to develop gold-platinum bi-metallic nanoparticles applicable as catalysts, through a microwave-assisted synthesis with reduced environmental impact, able to promote the formation of nanophases in aqueous solvent, and exploiting glucose as reducing agent. The use of microwave as heating system has been selected because it ensures a uniform heating, without important temperature gradients. Aiming to provide bi-metallic nanoparticles in suspension maximizing reaction yield and understanding how process parameter influence the reduction reaction, and the nucleation and growth phenomena, the main synthesis variables were extensively explored. After a precise physicochemical characterization of the materials, optimal synthesis conditions were identified. In order to promote the formation of gold-platinum bi-metallic structures, the miscibility range of the two elements was investigated, moreover two different procedures were optimized aiming to obtain an alloy or a core-shell nanostructure where the core is constituted by gold and the external shell by platinum. The purpose of preparing bi-metallic catalysts lies in the possibility of obtaining positive synergistic effects, in terms of catalytic activity, with respect to the individual components. These synergistic effects should be

promoted by the precise combination of the two elements in the same nanostructure. The samples prepared according to the optimized processes were tested in the model hydrogenation reaction of reduction of 4-nitrophenol to 4-aminophenol. This model reaction was used to evaluate and compare the catalytic activity of different samples, correlating performances to composition and synthetic procedure. In this way it was possible to identify positive or negative synergistic effects triggered by the interactions of gold and platinum nanophases.

## 5.2. Results and discussion

In this chapter are reported the results regarding the green synthesis of noble metals mono- and bi-metallic nanoparticles based on gold and platinum. The main purpose of this work is to develop the synthesis of noble metals nanoparticles with relevant catalytic activity, via sustainable chemistry routes. In particular, avoiding the use of toxic reagents, and harmful organic solvents, optimizing highly selective syntheses, minimizing the wastes, and using efficient energy sources such as microwave heating.

A wide-ranging physicochemical characterization of the products was carried out to optimize the synthesis conditions and develop the most active composition for these materials. The catalytic activity was studied in the model reaction of reduction of 4-nitrophenol to 4-aminophenol.

The design of the materials started from the synthesis of gold nanoparticles (AuNPs) and platinum nanoparticles (PtNPs), then it moved towards gold-platinum nanoparticles (AuPtNPs) as alloy (AuPtNPs-a) or core-shell (AuPtNPs-cs) structures.

A schematic workflow of the catalyst optimization process is represented in Figure 122.

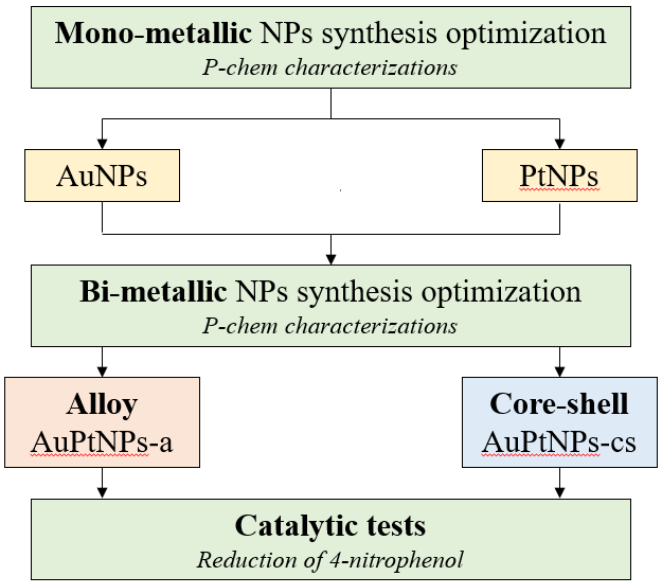


*Figure 122 – Schematic workflow of the preparation and characterization of mono- and bi-metallic nanoparticles based on Au an Pt with applications in catalysis.*

### 5.2.1. Synthesis of gold nanoparticles

***Synthesis*** – The microwave assisted synthesis of gold nanoparticles was performed using glucose as a reducing agent and polyvinylpyrrolidone (PVP) as capping agent. Both reagents are well known in literature for their application in the synthesis of metal and metal-oxide nanoparticles, they were selected because of their safety profile, in fact bot glucose and PVP are approved for food applications, the first one is common sugar while PVP can be used as food additive labeled as E1201.[240,241] The synthesis starts from $HAuCl_4$ as a precursor, and the gold reduction is activated in a basic environment thanks to NaOH. The reaction is conducted at 90 °C for 10 minutes exploiting fast and homogeneous microwave heating. The final theoretical concentration of gold is 1000 $mg \cdot L^{-1}$. The selected molar ratios are: glucose/Au 2, NaOH/Au 8, and PVP/Au 2.75 (PVP molar ratio is calculated based on the monomer).

***Colloidal physicochemical characterization*** – Following this standardized procedure for the synthesis of AuNPs it was possible to obtain reproducible results. The colloidal parameters of the typical synthesis of AuNPs are reported in Table 52.

*Table 52 – Summary of the colloidal physicochemical properties of AuNPs.*

| Sample | Hydrodynamic diameter (nm) | PDI | Zeta potential (mV) | pH | Au conversion (%) | Au concentration ($mg \cdot L^{-1}$) |
|---|---|---|---|---|---|---|
| AuNPs | 24 ± 1 | 0.22 ± 0.01 | -14 ± 1 | 7 | 100 | 1000 |

As shown in Table 52, the synthesis process provides AuNPs with a controlled size, small hydrodynamic diameter 24 nm, and a good monodispersed population (PDI 0.22). The particles are negatively charged at the natural pH of 7, the zeta potential is -14 mV which is not a very high absolute value for the electrostatic stabilization of the colloid, but the PVP helps with the steric stabilization, in fact the particles stored at 4 °C in dark conditions does not show any precipitate even after week. The reaction is quantitative, no $Au^+$ cations were detected in the filtered samples.

***UV-Vis spectroscopy*** – The samples produced had the typical red coloration of small-sized AuNPs and the related surface plasmon resonance absorption band was detected via UV-Vis spectroscopy. The spectrum, reported in Figure 123, shows the maximum absorption peak at 529

nm, another absorption band in the UV region is observed, this is due to the organic material surrounding the NPs.

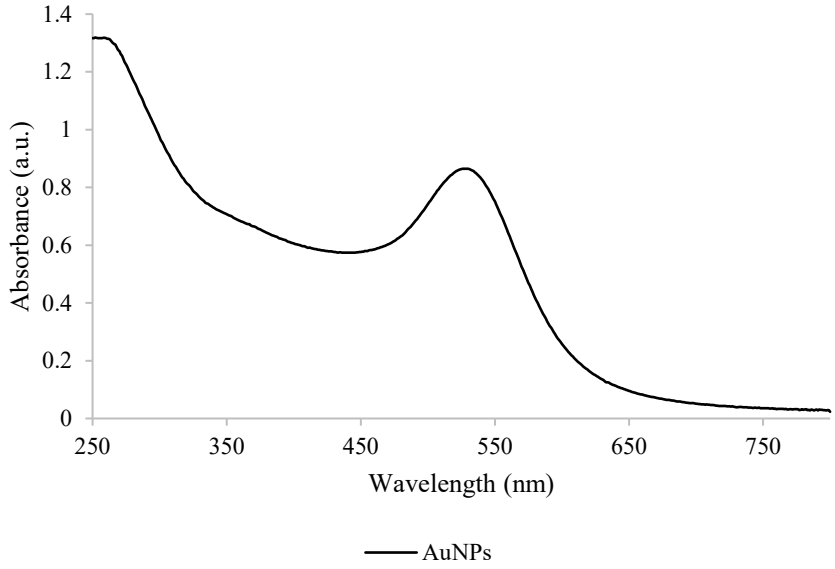


*Figure 123 – UV-Vis spectroscopy of AuNPs presenting SPR maximum absorption at 529 nm.*

***X-ray diffraction spectroscopy*** – The XRD pattern of AuNPs is reported in Figure 124, the formation of metallic Au is confirmed by the presence of the peak at 38.2 °, representative of the main reflection (111) of the face-centered cubic crystalline structure, it also possible to appreciate the peak of the face (200) at 44.4 °. The broad shape of these peaks is due to the short-range order available in nanometric structures. The sharp peak at 31.7 ° most likely represents the main NaCl refraction, the face (200) due to the formation of NaCl as reaction co-product, from the counterions of $HAuCl_4$ and NaOH used during the synthesis, also the small peak at 45.5 ° can be attributed to NaCl face (220).

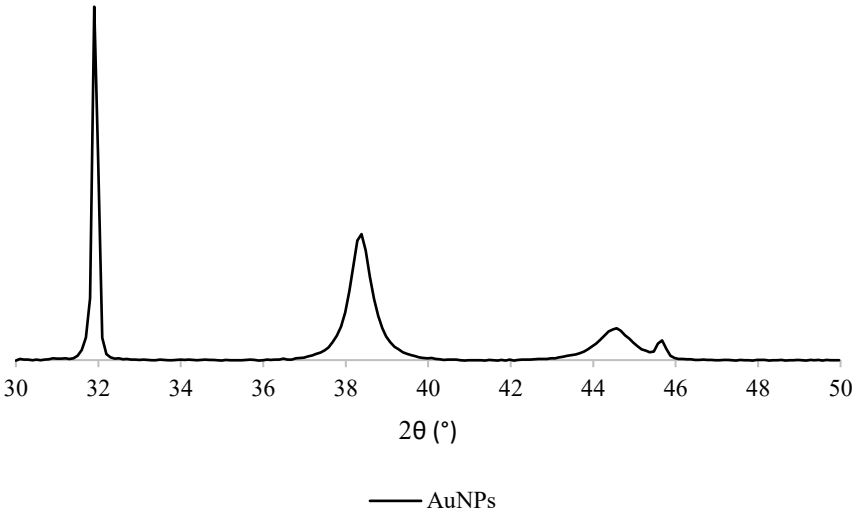


*Figure 124 – XRD spectrum of AuNPs presenting the characteristic peaks of Au face-centered cubic crystalline structure and the diffraction peaks of sodium chloride obtained as reaction co-product.*

Applying the Scherrer's equation to the (111) reflection of AuNPs it was possible to estimate the crystallite size of the nanoparticles of about 4 nm.

### 5.2.2. Synthesis of platinum nanoparticles

The synthesis of PtNPs starting from $H_2PtCl_6$ followed the same principles and methodologies as AuNPs, but Pt was found more difficult to be reduced. In fact, if we consider the standard electrode potential, reported in the following Equation 9 for Au and in Equation 10 and Equation 11 for Pt, it is possible to understand that the chloroplatinic acid ($Pt^{4+}$) requires a 2-step reduction process to reach the metallic state that pass through a stable intermediate state ($Pt^{2+}$), with a higher total standard electrode potential respect to the reduction of chloroauric acid.[242]

$$Au: \quad [AuCl_4]^- + 3e^- \leftrightarrow Au_{(s)} + 4Cl^- \quad 0.93\,V \qquad \text{Equation 9}$$

$$Pt: \quad [PtCl_6]^{2-} + 2e^- \leftrightarrow [PtCl_4]^{2-} + 2Cl^- \quad 0.726\,V \qquad \text{Equation 10}$$

$$[PtCl_4]^{2-} + 2e^- \leftrightarrow Pt_{(s)} + 4Cl^- \quad 0.758\,V \qquad \text{Equation 11}$$

Replicating the same conditions as for the synthesis of AuNPs, no or few metallic Pt was obtained, the reaction solution remained transparent. To overcome this issue, longer reaction time (30 minutes) and higher temperature (95 °C) were implemented, in this way the result was a dark grey/brown stable suspension of PtNPs.

***Design of experiment*** – To optimize the process, several syntheses were prepared varying the key reagent molar ratios. The content of PVP, used as capping agent, was preserved in a molar ratio PVP/Pt of 2.75, while the reducing sugar (glucose) molar ratio was explored in a range Glugose/Pt between 2-5, and the second parameter modified was the molar ratio NaOH/Pt studied in the interval 16-40. The composition explored are reported in the graph in Figure 125.

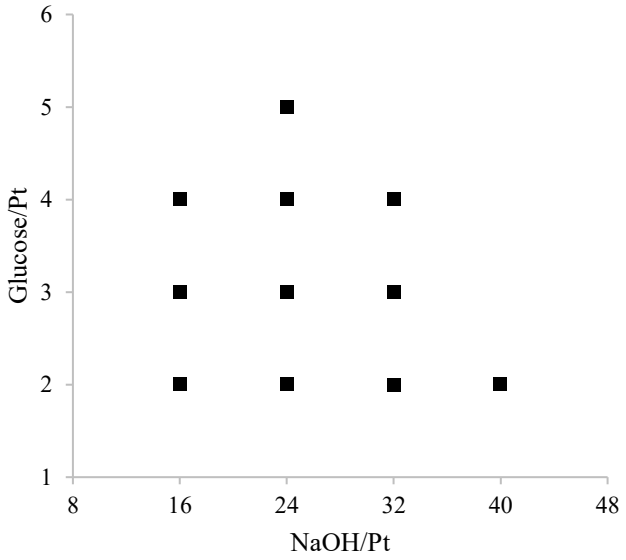


*Figure 125 – Design of experiment assessed to optimize the reagent molar ratios (glucose/Pt and NaOH/Pt) of the PtNPs synthesis performed using PVP as capping agent.*

***Colloidal physicochemical characterization*** – After an in-depth physicochemical characterization of the colloidal properties of all the syntheses prepared, the most promising composition was identified. It was found no correlation between the hydrodynamic diameter and the glucose/Pt molar ratio, in fact both monomodal and bimodal distributions were observed for each molar ratio tested from 2 to 5. The hydrodynamic diameter seems to be more influenced by the NaOH/Pt ratio, since the basic condition induced by NaOH activate the reduction reaction and have a relevant role in the nucleation rate of NPs. The smallest hydrodynamic diameters were observed for the intermediate NaOH/Pt ratios, like 24 and 32, in a range of 20-80 nm. The zeta potential is negative, due to the presence of gluconate, from glucose oxidation, that can be adsorbed on the NPs surface. Most of the synthesis showed zeta potential included in the range between -25 and -30 mV, an absolute value high enough to grant a good level of electrostatic repulsion, that combined to the steric hindrance from the PVP generate a stable colloidal suspension. The main limiting factor was the conversion of the platinum salt to metallic platinum. Even the strongest conditions applied led to a maximum of 74 % of conversion. Willing to choose the most promising solution, two constrains were set: maximize the conversion of chloroplatinic acid to increase the efficiency and sustainability of the process and minimize the hydrodynamic diameter to select smaller nanoparticles which are also likely to be more active in catalysis. Two syntheses respected these requirements, the last decision was based on the diameter population distribution, one was monomodal and the other bimodal. The monomodal distributed sample was selected to have a more homogeneous population of PtNPs, the

composition is represented by the following molar ratios: glucose/Pt 3, NaOH/Pt 24, and PVP/Pt 2.75. The main properties of this sample are reported in Table 53.

*Table 53 – Summary of the colloidal physicochemical properties of PtNPs.*

| Sample | Hydrodynamic diameter (nm) | Zeta potential (mV) | pH | Pt conversion (%) | Pt concentration ($mg \cdot L^{-1}$) |
|---|---|---|---|---|---|
| PtNPs | 72 ± 35 | -27 ± 1 | 10.2 | 61 | 100 |

The syntheses were performed at a total Pt concentration of 100 $mg \cdot L^{-1}$, since the conversion is not quantitative this must be considered in the post-washing dilution. In general, the hydrodynamic diameters registered for PtNPs were larger than AuNPs, and the zeta potential more negative.

***X-ray diffraction spectroscopy*** – The selected composition was analyzed by XRD to verify the formation of the metallic platinum phase. The spectrum is reported in Figure 126, where it is possible to observe the presence of metallic Pt with the main peak at 39.8 ° related to the face (111) of the face-centered cubic crystallin structure, and the face (200) at 46.2 °. These broad peaks are typical of nanophases, due to the short-range order impose by the size of the nanoparticles. On the other hand, sharper peaks are observed at 31.7 and 45.5 ° representing respectively face (200) and (220) of NaCl formed as reaction co-product.

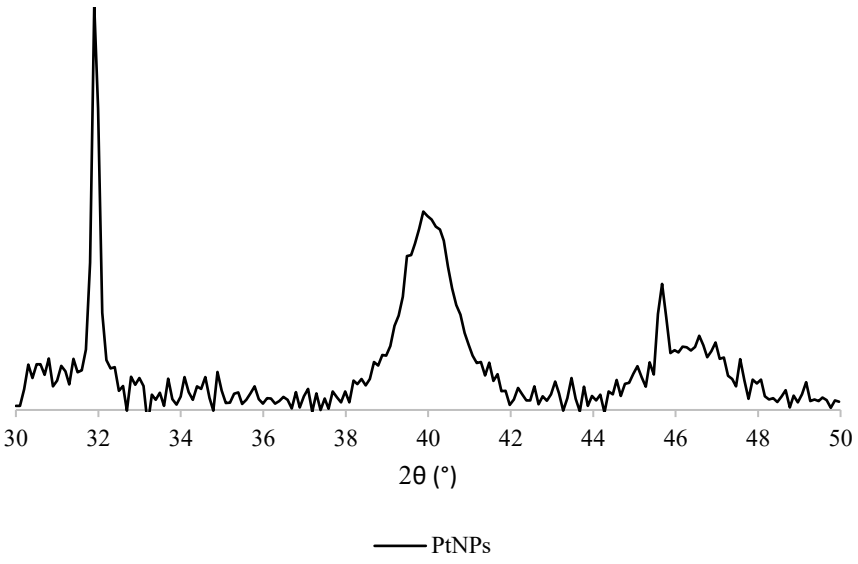


*Figure 126 – XRD spectrum of PtNPs presenting the characteristic peaks of Pt face-centered cubic crystalline structure and the diffraction peaks of sodium chloride obtained as reaction co-product.*

The crystallite size of these PtNPs was estimated applying Scherrer's equation to the main peak (111), and the resulting size is about 9 nm. Both the hydrodynamic diameter and the crystallite size of PtNPs are more than double the ones of AuNPs. This may be due to the stronger conditions required for the synthesis, and in particular the longer reaction time, that favor also the growth of the nanoparticles.

***Synthesis optimization*** – The synthesis was repeated at a higher concentration, 250 $mg \cdot L^{-1}$ in Pt. Increasing the concentration a reduction of the colloidal stability was observed, due to an increase in the attractive forces of Van del Waals within the system, consistently with the DLVO theory.[175] At this concentration, longer reaction times were taken into consideration to push the Pt conversion toward completeness. At 90 minutes no improvement in the Pt conversion was observed. After 420 minutes at 95 °C, a relevant enhancement was reached with a platinum conversion of 83 %. With the time it is also observed an increase in terms of hydrodynamic diameter, but no variation of crystallite size. This may be due to the fact that aggregation phenomena are favored respect to the growth of the crystal seeds. In the following Table 54 are resumed the information collected during these tests at higher platinum concentration (250 $mg \cdot L^{-1}$) and longer reaction time (30, 90, and 420 minutes).

*Table 54 – Summary of the physicochemical properties of AuNPs, study of the influence of the reaction time.*

| Sample | Reaction time (min) | $\varphi_{hydro}$ 1 (nm) | $\varphi_{hydro}$ 2 (nm) | Zeta potential (mV) | pH | Pt conv. (%) | Crystallite size (nm) |
|---|---|---|---|---|---|---|---|
| PtNPs | 30 | 31 ± 8 | 101 ± 10 | -19 ± 1 | 10.9 | 62 | 7 |
| PtNPs | 90 | 24 ± 6 | 114 ± 24 | -20 ± 1 | 10.7 | 60 | 5 |
| PtNPs | 420 | 59 ± 8 | 124 ± 12 | -22 ± 2 | 10.1 | 83 | 6 |

### 5.2.3. Synthesis of gold-platinum nanoparticles: alloy and core-shell structures

***Bi-metallic synthesis optimization*** – To synthesize bi-metallic AuPtNPs the idea was to implement the same experimental conditions as for PtNPs since platinum is the hardest to convert. So, the first step of optimization of the parameters started working at 95 °C for 30 minutes, the molar ratio between the two metals Pt/Au was 1, and PVP/metals 2.75, while NaOH/metals and glucose/metals were the variables to study. In this first screening a 50:50 composition Pt:Au was selected to study the phenomenon involved in the synthesis of bi-metallic nanoparticles, the selected procedure was the one to synthesize the alloy structure (AuPtNPs-a). The total metal concentration selected is 500 $mg \cdot L^{-1}$, which represents 250 $mg \cdot L^{-1}$ Au and 250 $mg \cdot L^{-1}$ Pt.

***Design of experiment*** – The compositions explored at this optimization stage are summarized in the graph in Figure 127. These points were selected based on the mono-metallic nanoparticles results, focusing on the most promising molar ratios.

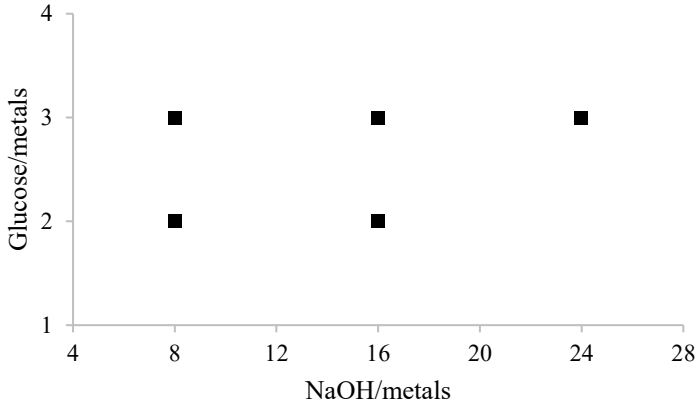


*Figure 127 – Design of experiment assessed to optimize the reagent molar ratios (glucose/metals and NaOH/metals) of the bi-metallic AuPtNPs synthesis performed using PVP as capping agent.*

Different molar ratios tested showed little influence on both hydrodynamic diameter ranging from 39 to 56 nm, and zeta potential included in between -13 and -18 mV. The same for the crystallite size (4-5 nm), and the gold conversion is always quantitative (100 %). The major influences were observed on the pH ranging from 4.0 to 11.2, and platinum conversion from 11 to 98 %. As expected, the lowest content of NaOH represented by the molar ratio NaOH/metals 2 leads to more acidic pH (4.0-6.5) compared to the highest NaOH/metals amount of 3 where the pH is basic (10.1-11.2). The most important information gathered by this set of samples is

the one related to the Pt conversion, which ranges from 11 to 57 % in NaOH/metals ratios 16 and 24, while once this ratio is lowered to 8 it is possible to reach nearly quantitative platinum conversion (96 and 98 %). The co-presence of gold helps the reduction of platinum especially with a lower amount of NaOH. At this high platinum concertation (Pt/Au molar ratio 1) it is likely to create segregated phases, and gold may act as heterogenous seed for the nucleation of metallic platinum in different conditions compared to the optimize PtNPs synthesis.

***Colloidal physicochemical characterization*** – The most promising composition was identified in the one with the highest conversion of platinum (98 %), represented by the molar ratios NaOH/metals 8 and glucose/metals 2. The main properties of the material are reported in Table 55.

*Table 55 - Summary of the colloidal physicochemical properties of AuPtNPs.*

| Sample | $\varphi_{hydro}$ (nm) | Zeta potential (mV) | pH | Au conv. (%) | Pt conv. (%) | Crystallite size (nm) |
|---|---|---|---|---|---|---|
| AuPtNPs | 45 ± 5 | -13 ± 1 | 6.5 | 100 | 98 | 4 |

***X-ray diffraction spectroscopy*** – From the XRD spectrum reported in Figure 128, it is not possible to observe well distinguished characteristic peaks of both face-centered cubic structures of Au (38.2 and 44.4 °) and Pt (39.8 and 46.2 °). Instead it is possible to observe two broad bands between 37 and 42 ° for (111) face and between 43 and 47 ° for (200) face. Since Au and Pt cell parameters are similar, it may be due to the superimposition of the respective peaks of Au and Pt or to the formation of the alloy mixed phase, combined with the typical broadening of the nanophases. Also, are present the characteristic sharp peaks of NaCl at 31.7 °C (200) and 45.5 ° (220).

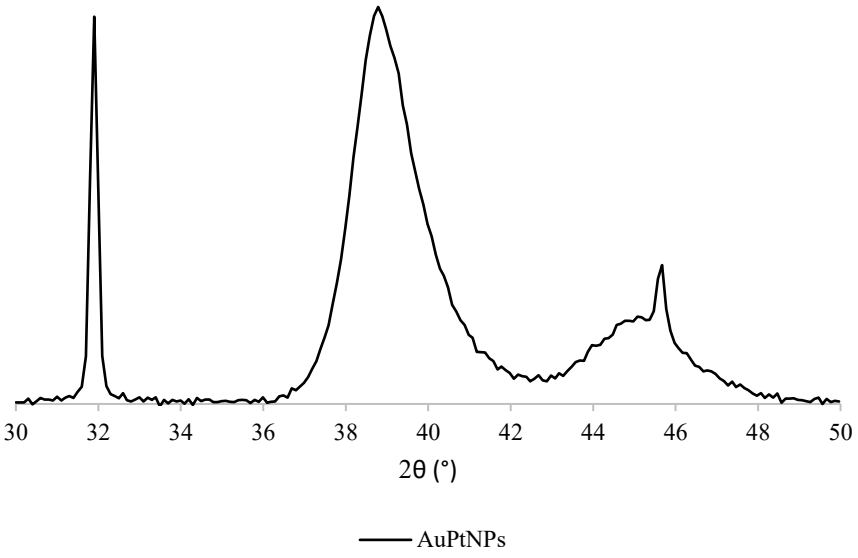


*Figure 128 – XRD spectrum of AuPtNPs presenting a broader band in correspondence of the characteristic peaks of Au and Pt face-centered cubic crystalline structures, coupled with the diffraction peaks of sodium chloride obtained as reaction co-product.*

***UV-Vis spectroscopy*** – It was not possible to identify the characteristic surface plasmon resonance absorption peak of AuNPs. This is probably justified by the presence of PtNPs that cause a background absorption on all the visible range due to the dark grey/brown coloration.[243] In the spectrum reported in Figure 129, a little change of slope in the curve may be observed about 525 nm where the gold absorption should occur.

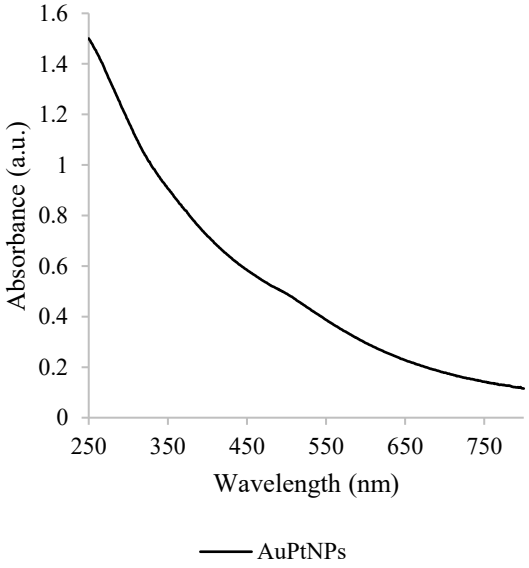


*Figure 129 – UV-Vis spectroscopy of AuPtNPs presenting a background absorption in the visible range probably due to the presence of platinum masking the SPR absorption of AuNPs.*

***Synthesis optimization*** – Once glucose/metals and NaOH/metals molar ratios were optimized, Pt/Au ratio was studied. First, the starting ratio of 1 was moved toward an excess of platinum (Pt/Au 2) or gold (Pt/Au 0.5), results are summarized in Table 56. No relevant variations of physicochemical properties are observed, what is highlighted by these results is the fact that operating in an excess of gold (Pt/Au 0.5) leads to a reduction in the platinum conversion (85 % respect to the previously registered 98 % for Pt/Au 1). Even if gold has been demonstrated to favor the conversion of platinum acting as seed for nucleation, a large excess in the composition results as a detrimental factor.

*Table 56 - Summary of the colloidal physicochemical properties of AuPtNPs, study of the influence of the metals' molar ratio.*

| Sample | Pt/Au molar ratio | $\varphi_{hydro}$ (nm) | Zeta potential (mV) | pH | Au conv. (%) | Pt conv. (%) | Crystallite size (nm) |
|---|---|---|---|---|---|---|---|
| AuPtNPs | 1 | 45 ± 5 | -13 ± 1 | 6.5 | 100 | 98 | 4 |
| AuPtNPs | 0.5 | 51 ± 11 | -11 ± 1 | 7,0 | 100 | 85 | 5 |
| AuPtNPs | 2 | 45 ± 8 | -12 ± 1 | 5,9 | 100 | 99 | 4 |

Even if gold and platinum have the same face centered cubic crystalline structure and similar lattice parameters and atomic radius, they do not show perfect miscibility in metallic form at low temperature. The miscibility diagram is reported in Figure 130.[244] Since the goal is to produce both an alloy and a core-shell structure, to avoid the formation of undesired segregated phases during the synthesis procedure at 95 °C, it has been decided to work with a platinum content included in 2.5-10 %wt range. In this way, it should be possible to obtain a homogenously distributed bi-metallic phase following the alloy synthesis procedure, and a thin layer of platinum covering the gold core following the core-shell method.

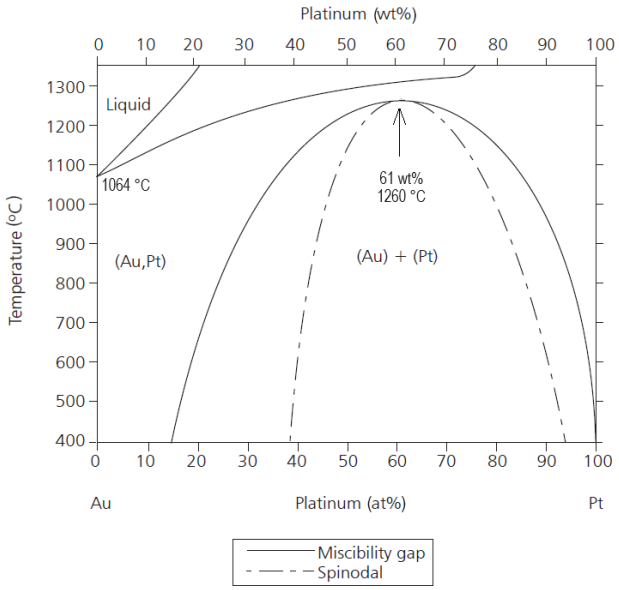


*Figure 130 – Gold-platinum miscibility phase diagram.*

***Gold platinum alloy nanoparticles (AuPtNPs-a)*** – The synthesis of the AuPt alloy followed the previously optimized procedure, the selected Pt contents are 10, 7.5, 5, and 2.5 %wt and they were respectively labeled as: $Au_{90}Pt_{10}$-a (90 %wt of Au and 10 %wt of Pt), $Au_{92.5}Pt_{7.5}$-a (92.5 %wt of Au and 7.5 %wt of Pt), $Au_{95}Pt_{5}$-a (95 %wt of Au and 5 %wt of Pt), and $Au_{97.5}Pt_{2.5}$-a (97.5 %wt of Au and 2.5%wt of Pt). The resulting information related to this set of samples are gathered together with the AuNPs results in Table 57.

***Colloidal physicochemical characterization*** – In the compositional range 90-100 % of gold, it is observed an increase in the hydrodynamic diameter moving from 90 to 100 %, finding a maximum value at 95 %, to drop to the value of AuNPs. On the other side, no relevant trends were observed for the zeta potential, pH, and crystallite size. In general, samples prepared in the miscibility range present a more negative zeta potential, representative of a better colloidal stability. Gold conversion is always 100 %, while the platinum conversion moves between 46 and 60 %. As demonstrated by the first compositional test, moving the molar ratio in favor of gold helps in the formation of the alloy but at the same time reduces the conversion of platinum.

*Table 57 - Summary of the physicochemical properties of alloy structures of AuPtNPs with different platinum content, compared to the pristine PtNPs and AuNPs.*

| Sample | $\varphi_{hydro}$ (nm) | Zeta potential (mV) | pH | Au conv. (%) | Pt conv. (%) | Crystallite size (nm) |
|---|---|---|---|---|---|---|
| PtNPs | 72 ± 35 | -27 ± 1 | 10.2 | n.d. | 61 | 9 |
| $Au_{90}Pt_{10}$-a | 34 ± 13 | -23 ± 7 | 7.5 | 100 | 54 | 5 |
| $Au_{92.5}Pt_{7.5}$-a | 45 ± 15 | -27 ± 4 | 7.2 | 100 | 57 | 5 |
| $Au_{95}Pt_{5}$-a | 51 ± 16 | -19 ± 4 | 7.4 | 100 | 60 | 6 |
| $Au_{97.5}Pt_{2.5}$-a | 30 ± 10 | -34 ± 5 | 7.4 | 100 | 46 | 5 |
| AuNPs | 28 ± 2 | -10 ± 1 | 7 | 100 | n.d. | 5 |

***X-ray diffraction spectroscopy*** – As previously reported is not possible to distinguish the diffraction peaks of Au and Pt in these bi-metallic samples, due to similar lattice, close maximum and the alloy formation. Furthermore, the reduced platinum content respect to gold can't be appreciated. In fact, spectra represented in Figure 131 show broad peaks corresponding to Au planes (111) at 38.2 ° and (200) at 44.4 °, covering also the same faces of Pt (111) at 39.8 ° and (200) 46.2 °. NaCl sharp peaks are always well recognizable in these samples at 31.7 °C (200) and 45.5 ° (220).

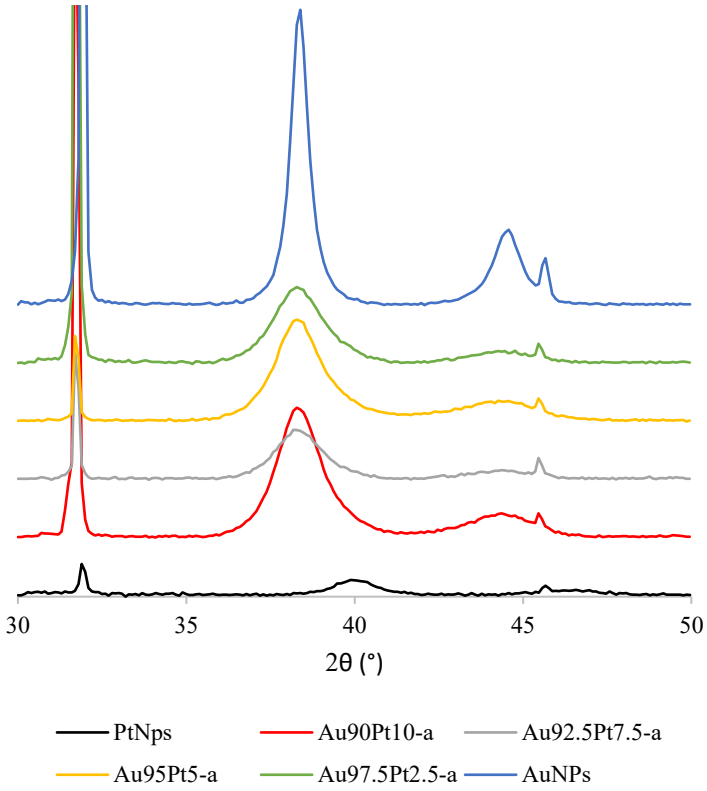


*Figure 131 – XRD spectra of AuPtNPs-a samples. In the graph are compared: PtNPs, Au90Pt10-a, Au92.5Pt7.5-a, Au95Pt5-a, Au97.5Pt2.5-a, and AuNPs.*

***UV-Vis spectroscopy*** – Since the main component is Au, it is possible to observe the surface plasmon resonance absorption peak in every one of these samples. An important background from Pt is registered, also it was possible to observe the shift of the maximum absorption toward Au reducing the content of platinum in the alloy. Recorded spectra are reported in Figure 132 and maximum absorption are summarized in Table 58.

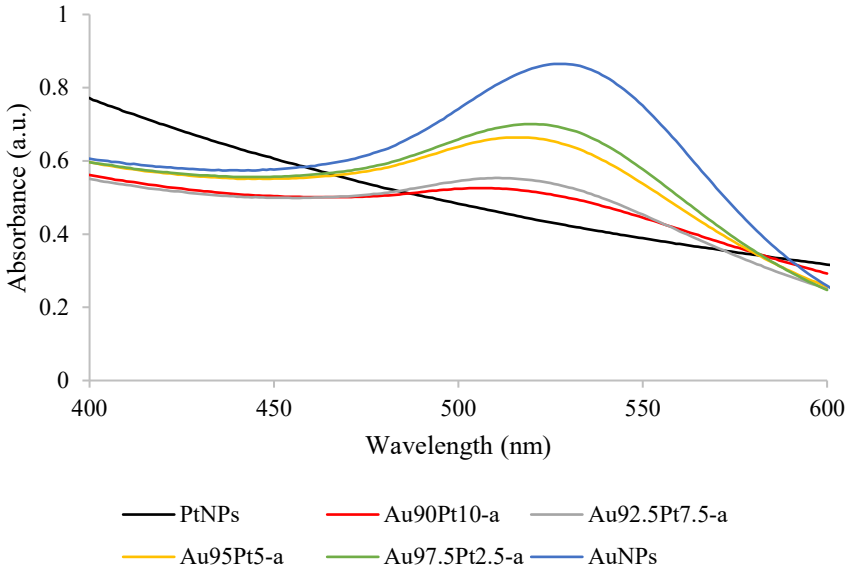


*Figure 132 – UV-Vis absorption spectra of AuPtNPs-a samples. In the graph are compared: PtNPs, Au90Pt10-a, Au92.5Pt7.5-a, Au95Pt5-a, Au97.5Pt2.5-a, and AuNPs. The increasing platinum content reduce the intensity of the SPR AuNPs peak.*

*Table 58 – UV-Vis maximum absorption peaks of the alloy structures of AuPtNPs with different platinum content, compared to the pristine PtNPs and AuNPs.*

| Sample | $\lambda_{max}$ (nm) |
|---|---|
| PtNPs | n.d. |
| $Au_{90}Pt_{10}$-a | 510 |
| $Au_{92.5}Pt_{7.5}$-a | 508 |
| $Au_{95}Pt_{5}$-a | 513 |
| $Au_{97.5}Pt_{2.5}$-a | 517 |
| AuNPs | 529 |

***Synthesis optimization*** – Since the long reaction time, 30 minutes, may lean toward undesired growth of the nanoparticles and aggregation phenomenon, the reaction time was reduced to 10 minutes as for the synthesis of pure AuNPs. By the comparison of the two set of samples, $Au_{90}Pt_{10}$-a, $Au_{92.5}Pt_{7.5}$-a, $Au_{95}Pt_{5}$-a, and $Au_{97.5}Pt_{2.5}$-a, synthesized either in 30 or 10 minutes, there were no particular differences in the size of the respective samples, both in terms of hydrodynamic diameter and crystallite size. 10 minutes synthesis showed lower platinum conversion, on average about 10 % conversion points less respect to 30 minutes synthesis, furthermore the zeta potential was less negative, on average about 10 mV difference was detected. So, the reaction time was not a key variable in the range 10 to 30 minutes for the

synthesis of these bi-metallic alloy, but working at 30 minutes allowed to reach higher platinum conversions and have more stable colloids, without excessive growth or aggregation processes.

***Transmission electron microscopy*** – $Au_{97.5}Pt_{2.5}$-a was selected for TEM analysis.

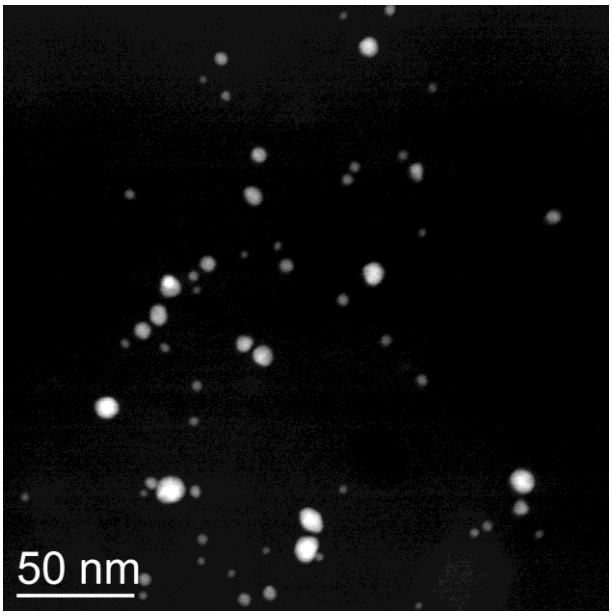


*Figure 133 – HAADF-STEM image of $Au_{97.5}Pt_{2.5}$-a used for the particle size statistical analysis. The nanoparticles size ranges from 2.5-22 nm.*

HAADF-STEM images of $Au_{97.5}Pt_{2.5}$-a are reported in Figure 133. The nanoparticles are crystalline and the size ranges from 2.5 to 22 nm. They are well dispersed on the support carbon film. These images were used for statistical size analysis measuring the major and minor axis of each particle. The size of 316 NPs in different images were measured, long axis estimated mean value is 6.0 nm with a standard deviation of 3.1 nm. Therefore, with a confidence interval of 99 % the average value is 6.0 ± 0.5 nm. The short axis estimated mean value is 5.2 nm with a standard deviation of 2.5 nm. Therefore, with a confidence interval of 99 % the average value is 5.2 ± 0.4 nm.

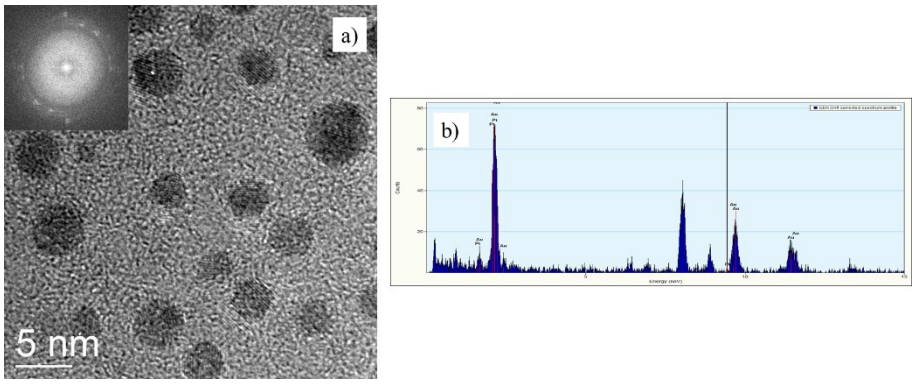


*Figure 134 – a) HRTEM image of $Au_{97.5}Pt_{2.5}$-a showing crystallin nanoparticles and don't display a core-shell aspect; b) EDX spectrum of $Au_{97.5}Pt_{2.5}$-a confirming the presence of platinum in the NPs.*

The high-resolution transmission (HRTEM) images of $Au_{97.5}Pt_{2.5}$-a represented in Figure 134 show crystalline nanoparticles and don't display a core-shell aspect. The presence of platinum is confirmed by EDS analysis reported in Figure 134.

***Gold platinum core-shell nanoparticles (AuPtNPs-cs)*** – A two-step experimental procedure was adopted for the synthesis of the core-shell structure. The alloy was obtained by working with a mixture of gold and platinum precursors, while the core-shell needs first to synthesize AuNPs by the optimized method, then the product washed by reaction co- and by-products is used as seed for the synthesis of Pt, following its own 30 minutes optimized procedure, that will grow as a shell surrounding the AuNPs. To have a direct comparison between alloy and core-shell structures, the same weight content of the two metals were used: $Au_{90}Pt_{10}$-cs, $Au_{92.5}Pt_{7.5}$-cs, $Au_{95}Pt_{5}$-cs, and $Au_{97.5}Pt_{2.5}$-cs.

***Colloidal physicochemical characterization*** – The physicochemical properties of the core-shell samples are reported in Table 59.

*Table 59 – Summary of the physicochemical properties of the core-shell structures of AuPtNPs with different platinum content, compared to the pristine PtNPs and AuNPs. Synthesis duration 30 minutes.*

| Sample | $\varphi_{hydro}$ (nm) | Zeta potential (mV) | pH | Au conv. (%) | Pt conv. (%) | Crystallite size (nm) |
|---|---|---|---|---|---|---|
| PtNPs | 72 ± 35 | -27 ± 1 | 10.2 | n.d. | 61 | 9 |
| $Au_{90}Pt_{10}$-cs | 41 ± 14 | -24 ± 3 | 6.4 | 100 | 100 | 6 |
| $Au_{92.5}Pt_{7.5}$-cs | 65 ± 2 | -24 ± 1 | 7.2 | 100 | 100 | 6 |
| $Au_{95}Pt_{5}$-cs | 62 ± 1 | -29 ± 10 | 7.8 | 100 | 100 | 6 |
| $Au_{97.5}Pt_{2.5}$-cs | 43 ± 3 | -26 ± 3 | 7.1 | 100 | 100 | 6 |
| AuNPs | 28 ± 2 | -10 ± 1 | 7 | 100 | n.d. | 5 |

The most important information in Table 59 is for sure the platinum conversion that is quantitative for all the core-shell syntheses. To use already synthesized AuNPs as nucleation seed for the platinum shell is very effective and allows to obtain a 100 % conversion of Pt. Another interesting trend is the one observed in the hydrodynamic diameter, the highest value corresponds to PtNPs and the lowest one to AuNPs. Reducing the platinum content, the hydrodynamic diameter of AuPtNPs-cs decreases, supporting the trend towards smaller AuNPs size and also representing a smaller thickness of the external platinum shell. An outlier value is reported for the highest amount of platinum $Au_{90}Pt_{10}$-cs, where some segregated platinum phase may be formed. The zeta potential of the core-shell samples corresponds to the one of PtNPs, confirming a similar surface chemistry and so the desired formation of the platinum shell. The

same assumption may be formulated looking at the crystallite size, where all the core-shell structures demonstrated a growth to 6 nm respect the starting 5 nm if AuNPs.

***X-ray diffraction spectroscopy*** – From XRD spectra recorded in Figure 135 it is not possible to observe the clear presence of the platinum in the core-shell samples. The only observation is regarding the broadening of the Au peaks. This may be due to the little amount of platinum or to the formation of an alloy in the external shell, surrounding the Au core.

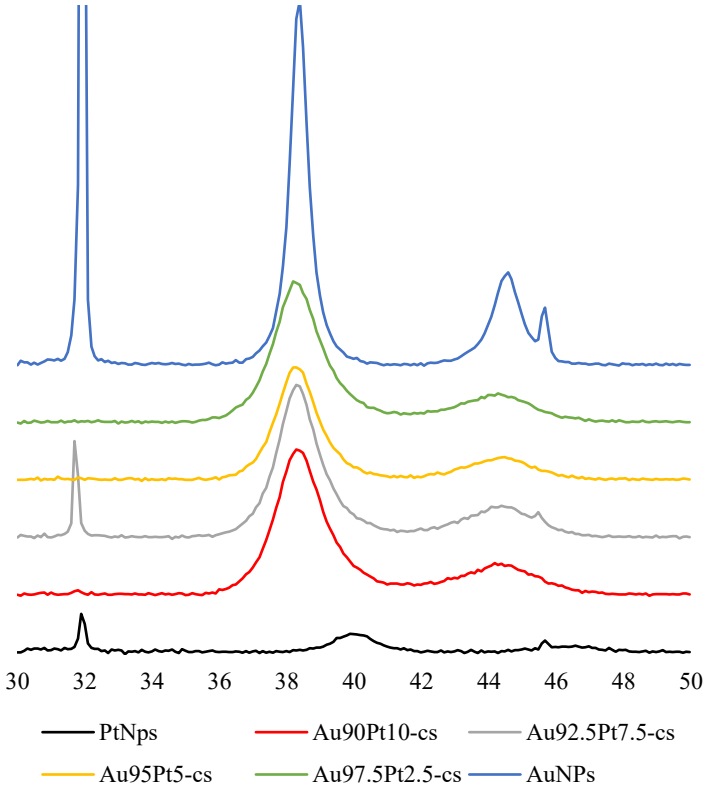


*Figure 135 – XRD spectra of AuPtNPs-cs samples. In the graph are compared: PtNPs, Au90Pt10-cs, Au92.5Pt7.5-cs, Au95Pt5-cs, Au97.5Pt2.5-cs, and AuNPs.*

***UV-Vis spectroscopy*** – From the spectra represented in Figure 136 it is possible to recognize AuNPs typical absorption peak. Also, an increasing blue-shift with the platinum content was observed, maximum absorption wavelengths are reported in Table 60.

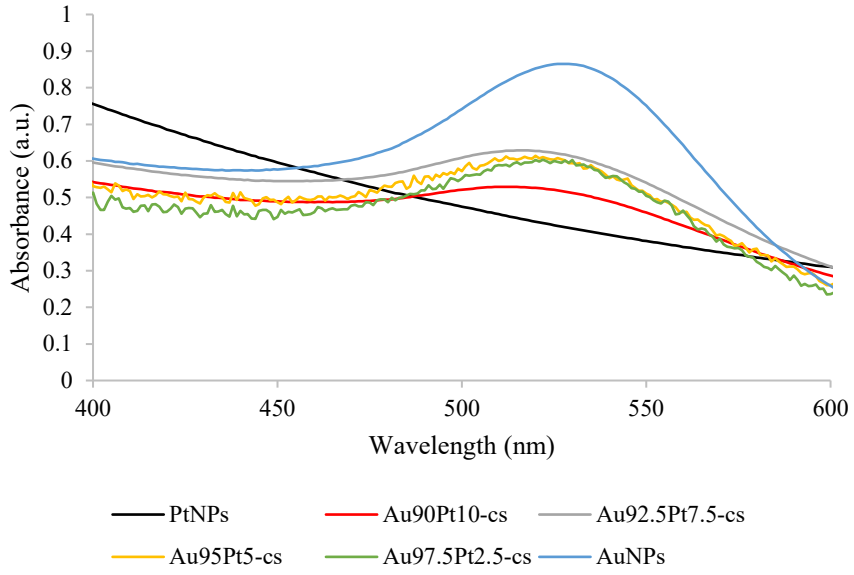


*Figure 136 – UV-Vis absorption spectra of AuPtNPs-cs samples. In the graph are compared: PtNPs, Au90Pt10-cs, Au92.5Pt7.5-cs, Au95Pt5-cs, Au97.5Pt2.5-cs, and AuNPs. The increasing platinum content reduce the intensity of the SPR AuNPs peak.*

*Table 60 – UV-Vis maximum absorption peaks of the core-shell structures of AuPtNPs with different platinum content, compared to the pristine PtNPs and AuNPs.*

| Sample | $\lambda_{max}$ (nm) |
|---|---|
| PtNPs | n.d. |
| $Au_{90}Pt_{10}$-a | 512 |
| $Au_{92.5}Pt_{7.5}$-a | 517 |
| $Au_{95}Pt_{5}$-a | 520 |
| $Au_{97.5}Pt_{2.5}$-a | 522 |
| AuNPs | 529 |

***Synthesis optimization*** – Differently from what observed for alloys, the core-shell structures benefit from the reduction of the reaction time for the synthesis of the external platinum shell. Alloys required a total reaction time of 30 minutes, the core-shell synthesis is split into two consecutive reactions, the first one for the Au core optimized on 10 minutes, and the second one for the platinum shell where the Pt optimized synthesis suggested 30 minutes. The synthesis time for the Pt shell was reduced to 10 minutes, the physicochemical properties of these samples are reported in Table 61. Platinum conversion was preserved quantitatively, only the highest amount of Pt (10 %wt) stopped close to quantitative conversion (98 %). The crystallite size is similar or slightly smaller to the corresponding 30 minutes samples, and the zeta potential is nearly unchanged confirming once again the formation of the platinum shell. The main improvement is

related to the hydrodynamic diameter, which is smaller stopping the synthesis after 10 minutes. As shown in the graph in Figure 137, the size of the colloidal kinetic unit is always smaller in the case of 10 minutes synthesis for all the compositional range explored.

*Table 61 – Summary of the physicochemical properties of the core-shell structures of AuPtNPs with different platinum content, compared to the pristine PtNPs and AuNPs. Optimization of the synthesis duration: 10 minutes.*

| Sample | $\varphi_{hydro}$ (nm) | Zeta potential (mV) | pH | Au conv. (%) | Pt conv. (%) | Crystallite size (nm) |
|---|---|---|---|---|---|---|
| PtNPs | 72 ± 35 | -27 ± 1 | 10.2 | n.d. | 61 | 9 |
| $Au_{90}Pt_{10}$-cs | 33 ± 1 | -24 ± 5 | 6.7 | 100 | 98 | 5 |
| $Au_{92.5}Pt_{7.5}$-cs | 43 ± 1 | -21 ± 4 | 6.4 | 100 | 100 | 6 |
| $Au_{95}Pt_{5}$-cs | 40 ± 1 | -24 ± 3 | 6.4 | 100 | 100 | 6 |
| $Au_{97.5}Pt_{2.5}$-cs | 35 ± 2 | -21 ± 1 | 6.3 | 100 | 100 | 5 |
| AuNPs | 28 ± 2 | -10 ± 1 | 7 | 100 | n.d. | 5 |

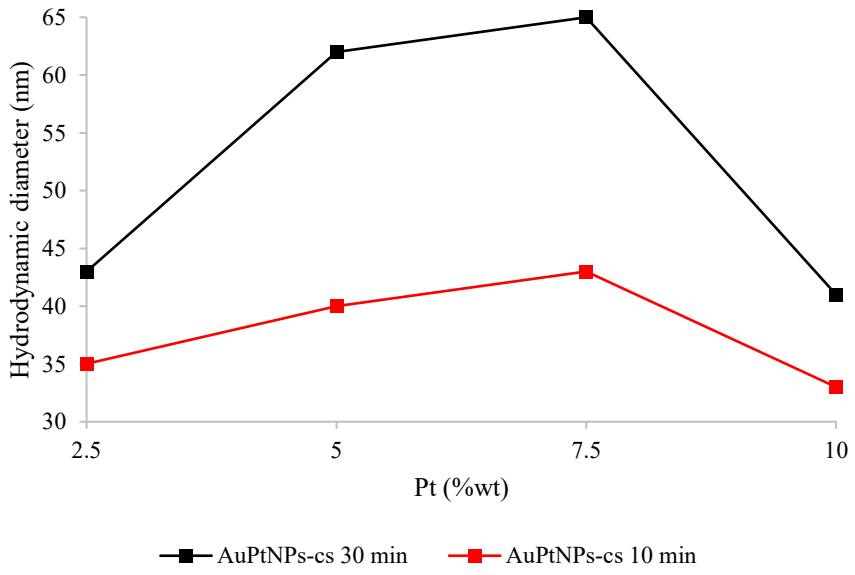


*Figure 137 – AuPtNPs-cs synthesis optimization: assessment of the influence of the platinum content in the core-shell structures on the hydrodynamic diameter. The analyses were performed on samples produced by 30 and 10 minutes reaction time.*

No relevant changes were detected in the XRD and UV-Vis spectra.

In conclusion, it is possible to reduce the reaction time for the platinum shell, minimizing energy and time consumption, preserving the Pt conversion, and obtaining also smaller hydrodynamic diameter.

***Transmission electron microscopy*** – $Au_{92.5}Pt_{7.5}$-cs was selected for TEM analysis.

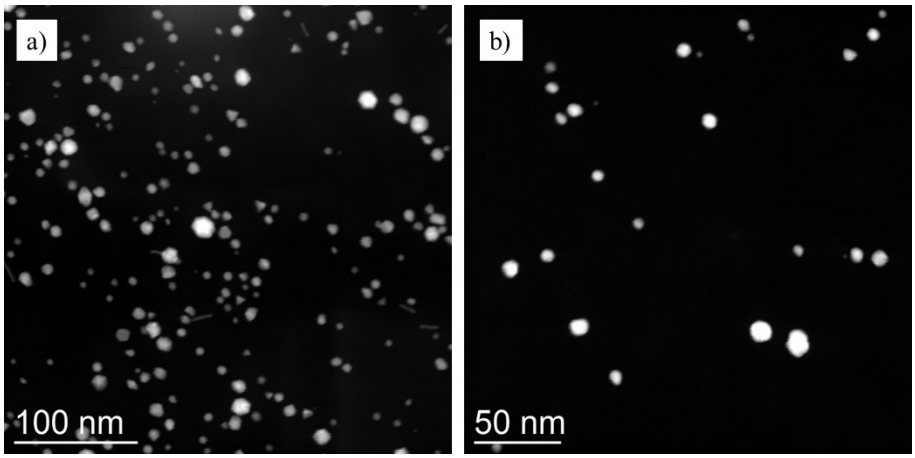


*Figure 138 – HAADF-STEM image of $Au_{92.5}Pt_{7.5}$-cs used for the particle size statistical analysis. The nanoparticles size ranges from 2-22 nm.*

HAADF-STEM images of $Au_{92.5}Pt_{7.5}$-cs are represented in Figure 138. The nanoparticles are crystalline and the size ranges from 2 to 22 nm. They are well dispersed on the support carbon film. These images were used for statistical size analysis measuring the major and minor axis of each particle.The size of 360 NPs in different images were measured and the long axis estimated mean value is 7.2 nm with a standard deviation of 2.8 nm. Therefore, with a confidence interval of 99 % the average value is 7.2 ± 0.4 nm. The short axis estimated mean value is 6.1 nm with a standard deviation of 2.3 nm. Therefore, with a confidence interval of 99 % the value is 6.1 ± 0.4 nm.

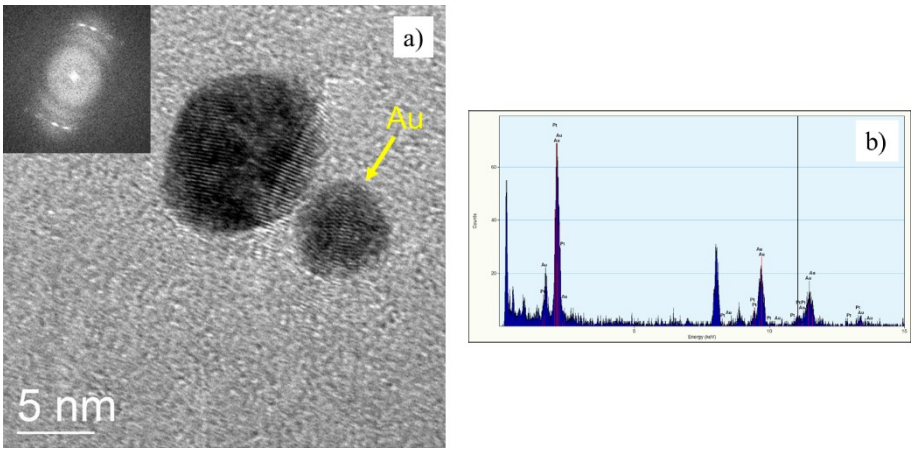


*Figure 139 – a) HRTEM image of $Au_{92.5}Pt_{7.5}$-cs showing crystallin nanoparticles displaying a core-shell aspect; b) EDX spectrum of $Au_{92.5}Pt_{7.5}$-cs confirming the presence of platinum in the NPs.*

$Au_{92.5}Pt_{7.5}$-cs high-resolution transmission (HRTEM) images reported in Figure 139 exhibit crystalline nanoparticles and display a core-shell aspect. The smallest particle probably has a gold core. This statement is based on interplanar spacing measurements. The presence of platinum is also confirmed by EDS analysis, as shown in Figure 139.

### 5.2.4. Catalytic activity in the reduction of 4-nitrophenol

The model reaction of reduction of 4-nitrophenol to 4-aminophenol was selected to study the catalytic activity of the synthesized mono- and bi-metallic nanoparticles. The scheme of the reaction is represented in Figure 140, where it is possible to see how the nitrophenolate ion is the active species that interact with the catalyst and the hydrogenation to amino phenolate ion is carried out thanks to the hydrogen released by the borohydride.

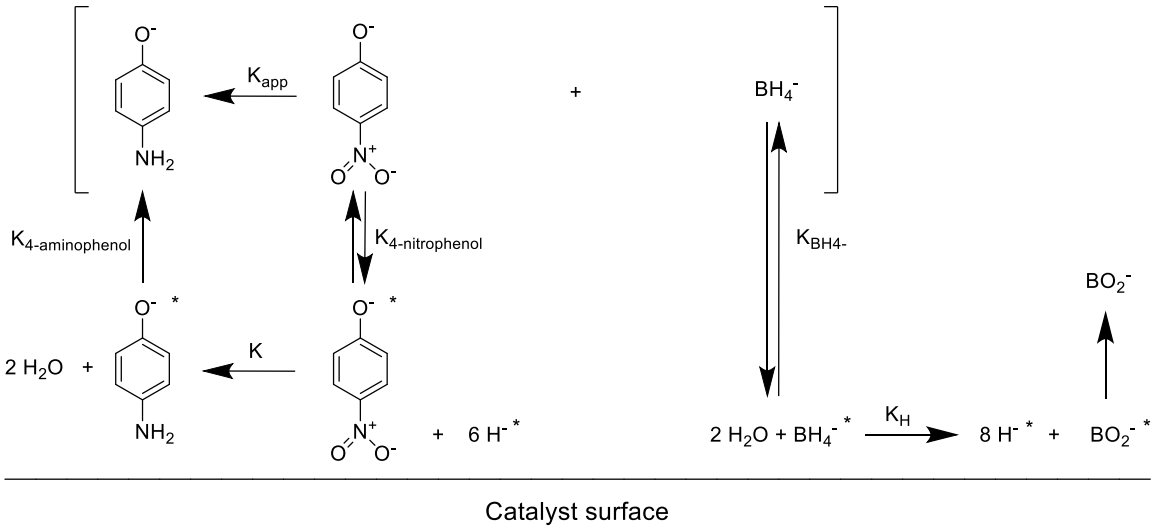


*Figure 140 – Reaction mechanism of the catalytic activated reduction of nitrophenol to aminophenol assisted by sodium borohydride.*

The tests were carried out at room temperature and pressure, in a water environment, and with an excess of sodium borohydride, allowing the approximation to a pseudo-first-order reaction respect to 4-nitrophenol. 4-nitrophenol absorbs at 317 nm, but in presence of $NaBH_4$ forms the nitrophenolate ion and undergoes a red-shift to 400 nm, associated to a yellow coloration. The advancement of the reaction has been monitored by spectrophotometry, analyzing the depletion of the reagent, since the reaction product is colorless. Creating a graph of $\ln(A_t \cdot A_0^{-1})$ as a function of time, where $A_t$ is the absorbance at time t and $A_0$ the initial absorbance. This is a linearized graph and the slope of the curve corresponds to the kinetic constant k of the reaction, the higher the constant the more efficient is the catalyst. Some samples showed an induction time, in literature it has been explained that it may be caused by: dissolved oxygen, diffusion/adsorption of the reagent to the catalyst surface, surface oxidation of the catalyst, phenolate ion formation, or steric hindrance of the catalytic sites due to the capping agent.[245]

***Catalytic test on mono-metallic AuNPs and PtNPs suspensions*** – First tests were carried out on AuNPs and PtNPs to discriminate whether the mono-metallic nanoparticles were more or less active in the catalysis of the model reaction. It is worth to mention that the reaction does not occur without the catalyst.

As an example, is reported in Figure 141 the graph of the UV-Vis spectra registered for the reaction carried out with PtNPs. The 4-nitrophenol (4-NP) peak at 400 nm is decreasing overtime representing the advancement of the reaction.

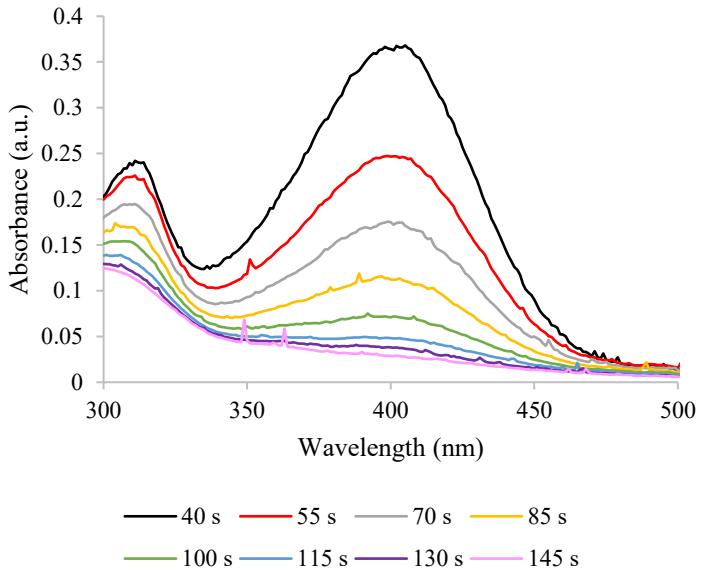


*Figure 141 – UV-Vis spectroscopy applied for the monitoring of the 4-nitrophenol conversion during the reaction carried out with PtNPs as catalyst.*

As it is possible to see by both conversion and kinetic graph reported in Figure 142, platinum is more efficient than gold in the catalysis of the studied reaction. This is due to the fact that Pt does not present any induction time, the reaction starts immediately, while for gold about 294 seconds estimated induction time is observed. Pt has also a better kinetic constant respect to Au, even considering only the post-induction time for gold. The kinetic constant calculated as slope of the $\ln(A_t \cdot A_0^{-1})$ as function of time graph is $1.2 \cdot 10^{-2}$ $s^{-1}$ for AuNPs and double for PtNPs $2.5 \cdot 10^{-2}$ $s^{-1}$. Platinum has overall better performances than gold in this model reaction, this behavior could be expected because platinum is largely applied in the catalysis of hydrogen involving reactions, due to the affinity of Pt for hydrogen species, in this case produced by $NaBH_4$.

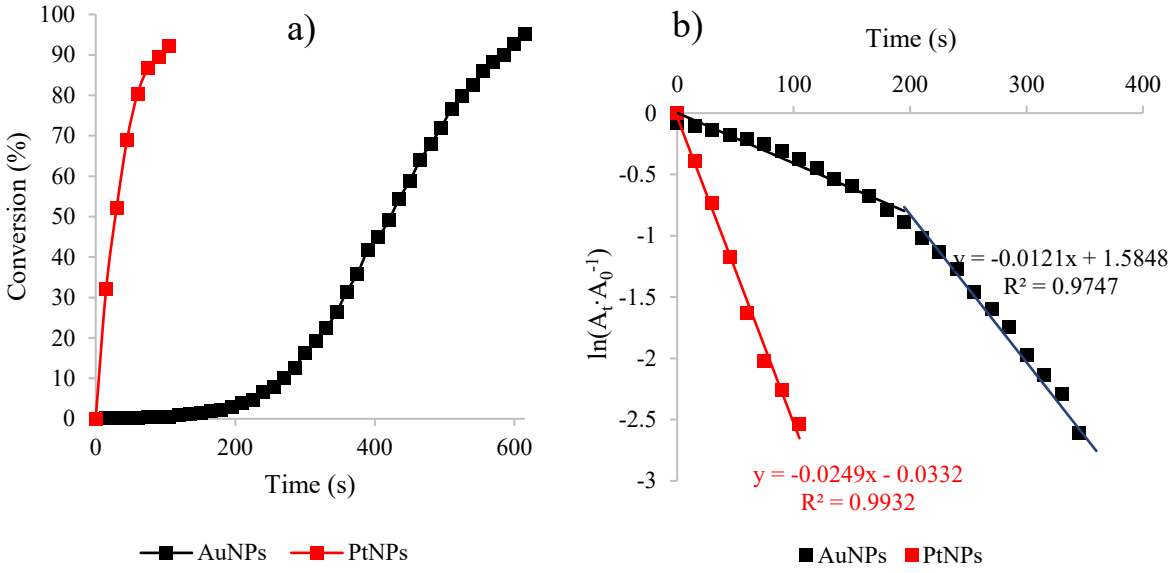


*Figure 142 – 4-nitrophenol reduction reaction catalyzed by AuNPs or PtNPs. a) conversion graph as function of time; b) pseudo-first-order kinetic linearized graph.*

***Catalytic test on AuPtNPs-a*** – Alloy bi-metallic nanoparticles have been tested to identify composition-dependent trends. In Figure 143 are reported the temporal evolution of the conversion and the kinetics of the alloy samples compared with the mono-metallic nanoparticles. Alloys show a trending behavior as function of the platinum content, the higher is the amount of platinum the shorter is the induction time, with the only exception of $Ag_{95}Pt_5$-a that is nearly superimposed to AuNPs. It is possible that some oxide generated on the surface of $Ag_{95}Pt_5$-a suppressed its performance.

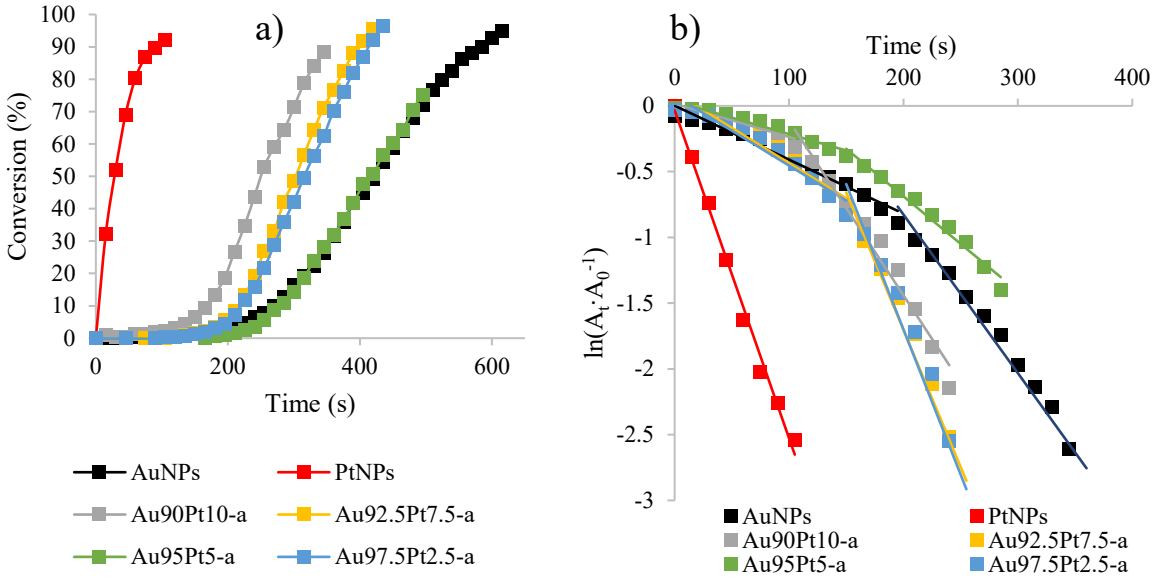


*Figure 143 – 4-nitrophenol reduction reaction, AuPt alloy catalysts activity comparison: AuNPs, PtNPs, $Au_{90}Pt_{10}$-a, $Au_{92.5}Pt_{7.5}$-a, $Au_{95}Pt_5$-a, and $Au_{97.5}Pt_{2.5}$-a. a) conversion graph as function of time; b) pseudo-first-order kinetic linearized graph.*

From the $\ln(A_t \cdot A_0^{-1})$ as function of time graph reported in Figure 143, it is clear that all of the alloy phases are subjected at an induction time as it is for AuNPs. Kinetic constants and induction times are summarized in Table 62. If the induction time trend respects what it could be expected by the compositions, it is not the same for the kinetic constant where the opposite trend is observed, the lowest amount of platinum in $Ag_{97.5}Pt_{2.5}$-a determines the highest kinetic constant $2.2 \cdot 10^{-2}$ $s^{-1}$ close to PtNPs $2.5 \cdot 10^{-2}$ $s^{-1}$, $Ag_{95}Pt_5$-a confirms to be out of trend both in terms of induction time and kinetic constant $0.7 \cdot 10^{-2}$ $s^{-1}$, slower than AuNPs $1.2 \cdot 10^{-2}$ $s^{-1}$.

*Table 62 – Catalytic performance of the alloy structures of AuPtNPs with different platinum content, compared to the pristine PtNPs and AuNPs. Induction time and kinetic constant comparisons.*

| Sample | Induction time (s) | Kinetic constant ($s^{-1}$) |
|---|---|---|
| PtNPs | 0 | $2.5 \cdot 10^{-2}$ |
| $Au_{90}Pt_{10}$-a | 155 | $1.3 \cdot 10^{-2}$ |
| $Au_{92.5}Pt_{7.5}$-a | 205 | $2.1 \cdot 10^{-2}$ |
| $Au_{95}Pt_5$-a | 253 | $0.7 \cdot 10^{-2}$ |
| $Au_{97.5}Pt_{2.5}$-a | 215 | $2.2 \cdot 10^{-2}$ |
| AuNPs | 294 | $1.2 \cdot 10^{-2}$ |

Summarizing, it is not possible to avoid the alloys induction time, but synergistic effects enhance the activity of samples with a low platinum content, highlighting outstanding performances of the composition with the lowest amount of platinum, $Ag_{97.5}Pt_{2.5}$-a.

***Catalytic test on AuPtNPs-cs*** – Subsequently, the optimized core-shell structures were tested in the same model reaction. For the induction time of this set of samples, it is not possible to identify a composition dependent trend. In fact, there are two groups, one with a behavior similar to PtNPs and one to AuNPs, but this grouping is not related to the platinum content. As it possible to observe in Figure 144, $Au_{92.5}Pt_{7.5}$-cs and $Au_{97.5}Pt_{2.5}$-cs have short induction time and a faster kinetic, like the platinum alone, while $Au_{90}Pt_{10}$-cs and $Au_{95}Pt_{5}$-cs have even longer induction time respect to gold alone, and a similar slope.

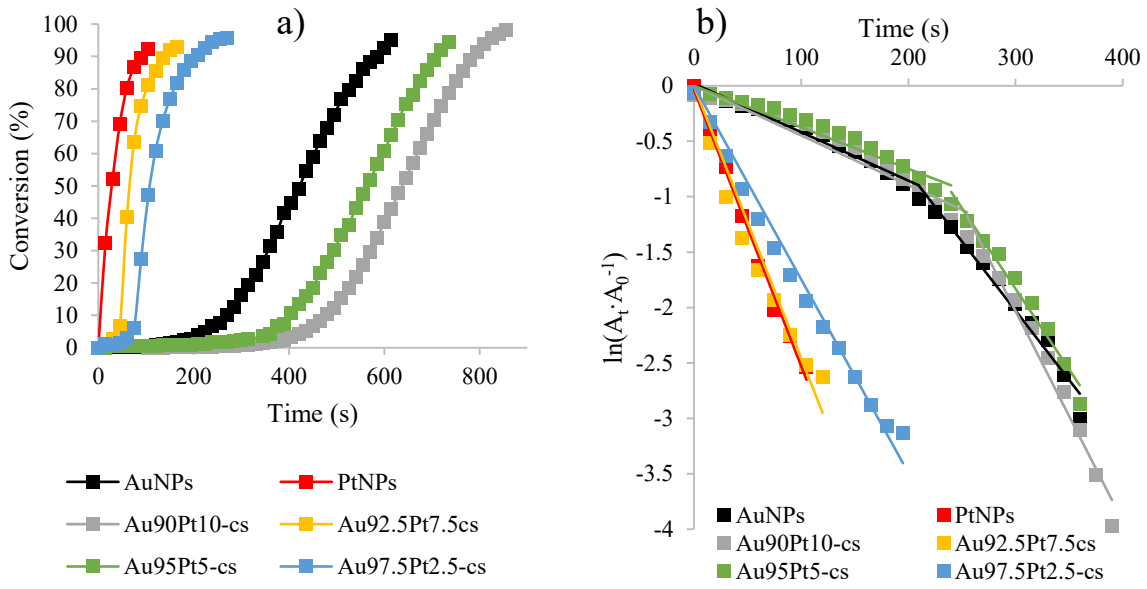


*Figure 144 – 4-nitrophenol reduction reaction, AuPt core-shell catalysts activity comparison: AuNPs, PtNPs, $Au_{90}Pt_{10}$-cs, $Au_{92.5}Pt_{7.5}$-cs, $Au_{95}Pt_{5}$-cs, and $Au_{97.5}Pt_{2.5}$-cs. a) conversion graph as function of time; b) pseudo-first-order kinetic linearized graph.*

Focusing on the kinetic constant, the external platinum shell in this structure tends to level the composition related differences. For the alloys, higher differences in kinetic constant and more marked trend were observed. In this case the best performing sample is $Au_{92.5}Pt_{7.5}$-cs with a kinetic constant of $2.5 \cdot 10^{-2}$ $s^{-1}$, equal to PtNPs, Table 63. It is interesting to notice that the composition with a platinum content of 5 %wt is the worst in terms of catalytic activity in both structures, alloy and core-shell. It is possible that this weight ratio in the synthesis adopted favors the formation of undesired segregated phases, or a passivating oxide surface layer.

*Table 63 – Catalytic performance of the core-shell structures of AuPtNPs with different platinum content, compared to the pristine PtNPs and AuNPs. Induction time and kinetic constant comparisons.*

| Sample | Induction time (s) | Kinetic constant ($s^{-1}$) |
|---|---|---|
| PtNPs | 0 | $2.5 \cdot 10^{-2}$ |
| $Au_{90}Pt_{10}$-cs | 423 | $1.9 \cdot 10^{-2}$ |
| $Au_{92.5}Pt_{7.5}$-cs | 85 | $2.5 \cdot 10^{-2}$ |
| $Au_{95}Pt_{5}$-cs | 411 | $1.4 \cdot 10^{-2}$ |
| $Au_{97.5}Pt_{2.5}$-cs | 115 | $1.8 \cdot 10^{-2}$ |
| AuNPs | 294 | $1.2 \cdot 10^{-2}$ |

To have a final confirmation of the structures obtained and how they influence the activity of these catalyst, physical blends of AuNPs and PtNPs in the same weight ratio of the samples were tested in the model reaction. The physical blends are labeled as $Au_xPt_x$-b, where x is the element weight percentage, the kinetic constants are compared in the graph in Figure 145.

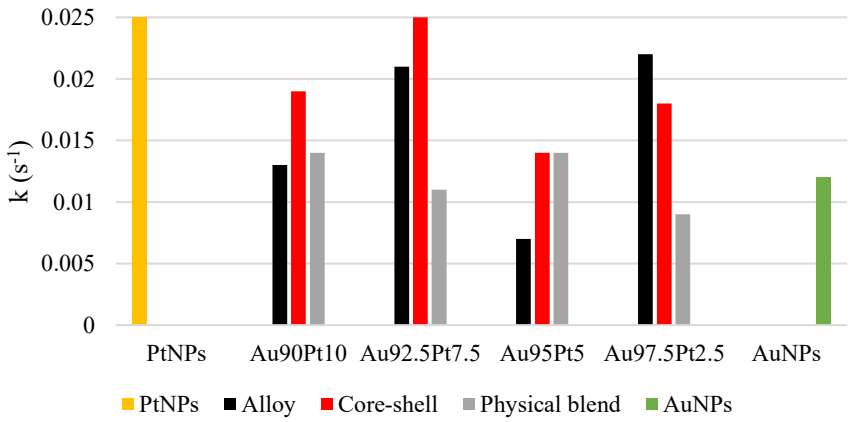


*Figure 145 – Kinetic constant comparison of the tested compositions ($Au_{90}Pt_{10}$, $Au_{92.5}Pt_{7.5}$, $Au_{95}Pt_5$, and $Au_{97.5}Pt_{2.5}$) in form of alloy, core-shell and physical blend, compared to the pristine mono-metallic PtNPs and AuNPs.*

***Catalytic tests conclusions*** – In general, it is possible to say that core-shell structures work better than alloys, as highlighted by comparing the kinetic constants and taking into consideration that the induction time is always present in the alloy configuration. Furthermore, the composition containing 5 %wt of platinum confirms to be the worst both for core-shells and alloys, in this case the physical blend activity is comparable with the core-shell and even better than the alloy. The highest platinum content 10 %wt, demonstrated to be probably in excess with respect to the solubility limit for the alloy formation, probably generating segregated phases with an activity comparable with the physical blend. On the other side, the lowest amount of Pt 2.5 %wt gave

rise to the most active alloy phase, as if the platinum acted as doping agent for gold, enhancing the activity reaching better kinetic constant than the same core-shell composition. Also, the 2.5 %wt content may be not enough to grant an active platinum shell.

The physical blend showed similar induction time to the alloy phase for all the samples, except for $Au_{95}Pt_5$, where the physical blend induction time was shorter than bot alloy and core-shell, confirming once again the problem of this composition.

In general, $Au_{92.5}Pt_{7.5}$ and $Au_{97.5}Pt_{2.5}$ demonstrated to be the most interesting composition, due to problems registered $Au_{95}Pt_5$ and the excess of platinum in $Au_{90}Pt_{10}$. $Au_{92.5}Pt_{7.5}$-cs showed the same catalytic activity as PtNPs, and $Au_{97.5}Pt_{2.5}$-a is the best alloy composition.

## 5.3. Conclusions

The work described led to the optimization of eco-friendly synthetic processes of noble metal nanoparticles for catalytic application. Microwave-assisted water-based synthesis was adopted for all the sample produced, avoiding the use of harmful reagents or organic solvents.

First, mono-metallic AuNPs and PtNPs synthesis were optimized implementing different parameters and precautions, since platinum synthesis requirements were stricter. A wide-ranging physicochemical characterization supported this optimization process leading to the best compromise between the energy and time-consuming parameters, and the desired properties of the product. Subsequently, the alloy and core-shell bi-metallic structures were produced developing ad hoc synthetic processes, one-pot synthesis in the case of alloy and two-step synthesis for core-shell. It was observed how the presence of gold helped in the reduction process of the platinum precursor, otherwise more temperature and time demanding. The achievement of the two desired structures, alloy and core-shell, was confirmed by the surface chemistry of the samples analyzed by zeta potential measurement, and by the lattice distances monitored by transmission electron microscopy. The size of the bi-metallic nanoparticles produced is suitable for catalytic applications, in fact, TEM statistical measurements revealed small diameter for both structures, in particular in the range 5-6 nm for alloy and 5-7 nm for core-shell.

The samples demonstrated interesting catalytic activity in the model reaction of reduction of 4-nitrophenol. Different behaviors and synergistic effects were observed for the bi-metallic materials. Bi-metallic product had faster kinetic respect to the physical blend of AuNPs and PtNPs in the same proportion, proof that the intimal interanion in a bi-metallic structure enhance the catalytic activity of these noble metal nanoparticles. Furthermore, synergistic effects were recorded, enhancing the performance of the material way higher respect to the simple weighted average based on the composition. Platinum is very active in these hydrogenation reactions, and it was possible to reach comparable results with both core-shell and alloy structures, considering a maximum amount of platinum of 10 %wt. Outstanding results were obtained by the core-shell sample $Au_{92.5}Pt_{7.5}$-cs that grants the same kinetic constant of PtNPs. In general, core-shell structures works better since they have platinum exposed on the surface of the NPs, but still, excellent activity was reached by specific alloy structures were platinum acts as doping agent in the gold lattice.

Usually, these materials are supported on an inorganic substrate, such as by impregnation of titanium dioxide powder, to be tested in real application model reaction. An example in the biomass valorization field is the multi-step reaction of oxidation of 5-hydroxymethyl furfural

(HMF) to 2,5-furan dicarboxylic acid (FDCA). FDCA is a biomass-derived monomer that can be polymerized to obtain polyethylene furan dicarboxylate (PEF), which is a product with similar properties as polyethylene terephthalate (PET) commonly used for plastics production.[246,247]
In this case, the production of bi-metallic alternatives to expensive platinum-based catalyst may help in the development of industrially affordable technologies for the biomass valorization exploiting synergistic effects of gold-platinum alloy and core-shell structures.

## 5.4. Experimental section

In this section synthesis procedures of mono- and bi-metallic nanoparticles will be described together with the physicochemical characterization techniques adopted during the study, and the catalytic test implemented to evaluate the activity of the products.

### 5.4.1. Synthesis of noble metals nanoparticles

All the noble metals nanoparticles were obtained thanks to a microwave assisted synthesis, using the microwave for synthesis Microsynth Plus (Milestone) with reflux.[181]

***Gold nanoparticles (AuNPs)*** – The synthesis of AuNPs exploit uniform and homogeneous microwave heating to reach the desired temperature of 90 °C for the reduction reaction of the gold precursor to metallic nanoparticles.

From the typical synthesis of AuNPs adopted, 100 mL of 1000 $mg \cdot L^{-1}$ Au are obtained. The procedure involves the dissolution of 0.1815 g of glucose (CAS Number 50-99-7) from Sigma-Aldrich (Product Number G7021, purity ≥ 99.5 %) as reducing agent, and 0.1534 g of polyvinylpyrrolidone (PVP) average $M_w \approx 29000$ (CAS Number 9003-39-8) from Sigma-Aldrich (Product Number 234257) as capping agent, in 80 mL of Milli-Q water. 10 mL of 0.4 M NaOH (CAS Number 1310-73-2) from Sigma-Aldrich (Product Number S5881, purity ≥ 98 %) are added to the reaction suspension to create a basic environment, then the batch is placed in the microwave oven. The sample is kept under magnetic stirring for the whole synthesis time, a heating ramp is set to reach 90 °C in 3 minutes with a maximum power provided by the instrument of 350 W. When the temperature reaches 80 °C, 10 mL of 0.05 M $HAuCl_4$ (CAS Number 16903-35-8) from Sigma-Aldrich (Product Number 484385, 99.99 % trace metals basis, 30 %wt in dilute HCl) are added. Then, the temperature is maintained at 90 °C for 10 minutes with a maximum power of 200 W. Finally, the reaction is quenched in an ice-bath and the product was stored at 4 °C in dark conditions. The selected molar ratios are: glucose/Au 2, NaOH Au 8, and PVP/Au 2.75.

***Platinum nanoparticles (PtNPs)*** – As for AuNPs, the synthesis of PtNPs required microwave heating, but the platinum is more difficult to be reduced so a higher temperature and a longer duration of the synthesis were selected, 95 °C for 30 minutes.

The synthesis of PtNPs required an optimization of the molar ratios of the reagents, here are reported the molar ratio of glucose and sodium hydroxide respect to platinum tested. NaOH/Pt: 16, 24, 32, and 40. Glucose/Pt: 2, 3, 4, and 5. The optimal molar ratios were identified as NaOH/Pt 24 and glucose/Pt 3.

The optimized synthesis produces 100 mL of 100 $mg \cdot L^{-1}$ Pt. 27.7 mg of glucose (CAS Number 50-99-7) from Sigma-Aldrich (Product Number G7021, purity ≥ 99.5 %) as reducing agent, and 15.3 mg of polyvinylpyrrolidone (PVP) average $M_w \approx 29000$ (CAS Number 9003-39-8) from Sigma-Aldrich (Product Number 234257) as capping agent, were dissolved in 87 mL of Milli-Q

water. 3 mL of 0.4 M NaOH were added to the reaction mixture, then the batch was placed in the microwave oven under magnetic stirring. A heating ramp from room temperature to 95 °C in 3 minutes was set with a maximum power of 350 W, then the temperature was kept constant at 95 °C for 30 minutes with a maximum power of 200 W. The platinum precursor was added when the reaction mixture reached 85 °C, 10 mL of 5.1 mM $H_2PtCl_6$ (CAS Number 16941-12-1) from Sigma-Aldrich (Product Number 262587, 8 %wt in water). The reaction was quenched with an ice-bath, the product was stored at 4 °C in dark conditions.

***Gold-platinum alloy nanoparticles (AuPtNPs-a)*** – To prepare the gold-platinum alloy phase it was necessary to take into consideration the miscibility diagram of the two metals reported in Figure 146.[244]

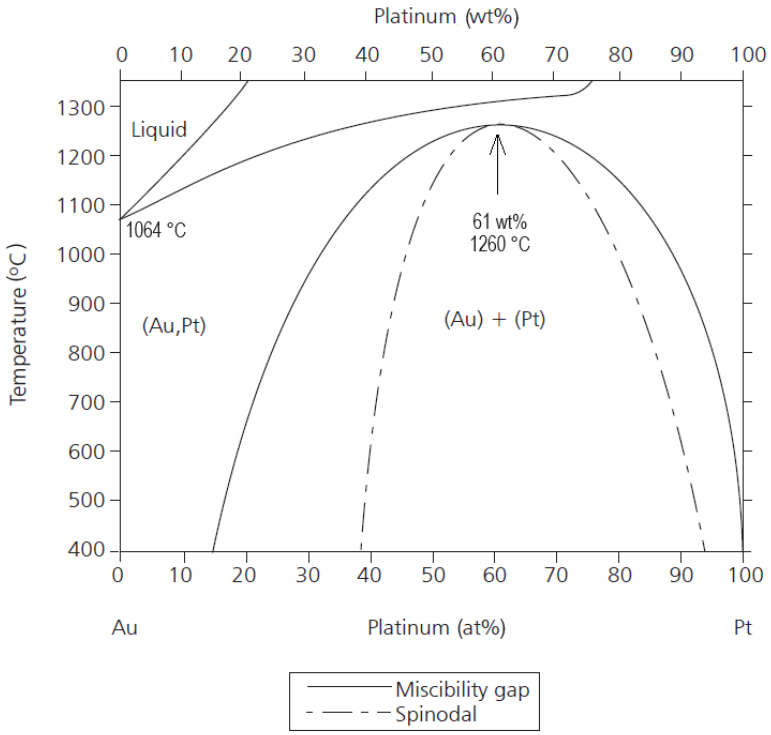


*Figure 146 – Gold-platinum miscibility phase diagram.*

Since the synthesis is performed at about 100 °C, it is possible to assume from the slope of the curve in the graph in Figure 146 that the miscibility gap is close to the 10 %wt of Pt load. Knowing that, 4 composition with a decreasing content of Pt from 10 to 2.5 %wt were proposed: $Au_{90}Pt_{10}$ (90 %wt of Au and 10 %wt of Pt), $Au_{92.5}Pt_{7.5}$ (92.5 %wt of Au and 7.5 %wt of Pt), $Au_{95}Pt_5$ (95 %wt of Au and 5 %wt of Pt), and $Au_{97.5}Pt_{2.5}$ (97.5 %wt of Au and 2.5%wt of Pt). The total metals concentration (Au+Pt) was fixed at 500 $mg \cdot L^{-1}$, the PVP/metals molar ratio is

2.75 as for the mono-metallic synthesis, while for NaOH/metals were explored the molar ratios 8, 16, and 24, and for glucose/metals 2 and 3. The optimized composition involves the following molar ratios: NaOH/metals 8, glucose/metals 2, and PVP/metals 2.75. Since the platinum is more difficult to be reduced, the higher temperature (95 °C) was selected for the microwave heating, and bot 30 minutes reaction times, later reduced to 10 minutes to avoid the undesired growth of the particles size. The procedure adopted is the same as for the mono-metallic suspension, with the hereabove mentioned compositions, and using as metals precursor a solution containing both Au and Pt precursors in the proper ratio.

***Gold-platinum core-shell nanoparticles (AuPtNPs-cs)*** – The core-shell structure was built by a gold core and a platinum shell. The synthesis of the core was performed following wat cited in "Gold nanoparticles (AuNPs)" paragraph, working with the optimized composition and a final gold concentration of 500 $mg \cdot L^{-1}$. The reaction product was washed by centrifugation at 20 °C and 1500 rpm for 20 minutes using a Centrisart G-16C (Sartorius) centrifuge mounting an Amicon Ultra-15 centrifugal filter (Millipore) with a filtering membrane of regenerated cellulose and a 30 kDa molecular weight cut-off (MWCO) also labeled as nominal molecular weight limit (NMWL). The washed AuNPs were properly diluted and then used as reaction environment for the synthesis of PtNPs in order to act seed for the nucleation of the metallic platinum phase. In this way a surrounding shell of Pt was generated around the Au core, and the bi-metallic core-shell nanoparticles were obtained. The composition selected were the same as for the alloys: $Au_{90}Pt_{10}$ (90 %wt of Au and 10 %wt of Pt), $Au_{92.5}Pt_{7.5}$ (92.5 %wt of Au and 7.5 %wt of Pt), $Au_{95}Pt_{5}$ (95 %wt of Au and 5 %wt of Pt), and $Au_{97.5}Pt_{2.5}$ (97.5 %wt of Au and 2.5%wt of Pt). The synthesis of the Pt outer layer adopted the same parameters as the alloys AuPtNPs-a.

### 5.4.2. Physicochemical characterization of noble metals nanoparticles

Mono- and bi-metallic colloidal suspensions were characterized in terms of hydrodynamic diameter (DLS), zeta potential (ELS), surface plasmon resonance absorption (UV-Vis), nanoparticle and ionic fraction concentrations (ICP-OES), crystalline phase (XRD), and size and morphology (TEM) of nanoparticles. The instruments settings and the principle of the techniques are described in the chapter "3.4.4. Physicochemical characterization of silver nanoparticles".

***Hydrodynamic diameter*** – The instrument used for the study of the hydrodynamic diameter and the polydispersity index is the Zetasizer Nano ZSP (Malvern Panalytical) equipped with MPT-2 multipurpose titrator and vacuum degasser accessories. The analyses were performed on about 1 mL of 500 $mg \cdot L^{-1}$ concentrated suspensions for all the samples.

***Zeta potential*** – The instrument used for the study of the zeta potential is the Zetasizer Nano ZSP (Malvern Panalytical) equipped with MPT-2 multipurpose titrator and vacuum degasser accessories. The analyses were performed on about 1 mL of 500 $mg \cdot L^{-1}$ concentrated suspensions for all the samples.

***UV-Vis spectroscopy*** – The study of the surface plasmon resonance absorption peaks of gold and platinum nanophases was performed thank to a Lambda 750 spectrophotometer (PerkinElmer). Position and shape of the SPR peak depend on the size, morphology, and composition of the nanoparticles. Typically, AuNPs exhibit an absorption peak about 520 nm, while PtNPs UV-Vis absorption spectrum is characterized by a broad band with maximum absorption in the far UV region.[248,249]

***Nanoparticle and ionic silver fractions quantification by ICP-OES*** – The instrument, Agilent 5100 ICP-OES with mounted the autosampler Agilent SPS 3 (Agilent Technologies) allowed the quantification of Au and Pt, both in metallic nanoparticle and ionic form. The selected emission lines of Au are: 191.896, 197.742, 208.207, and 267.594 nm. The selected emission lines of Pt are: 203.646, 214.424, 217.468, and 265.945 nm. The calibration curve was prepared analyzing standards at the following concentrations: 100, 10, 1, 0.1 and 0 $mg \cdot L^{-1}$. The standard solutions are Au 1000 $mg \cdot L^{-1}$ in a matrix of 2 %wt HCl (CPAchem) and Pt $mg \cdot L^{-1}$ 1000 in a matrix of 10 %wt HCl (CPAchem). The internal calibration verification was assessed analyzing a solution of Au or Pt prepared from the standards in a concentration included within the calibration curve.

The quantification of total Au and Pt were assessed on samples diluted to a theoretical concentration of 70 $mg \cdot L^{-1}$. The analysis of the ionic fraction was performed on filtered suspensions, by Amicon Ultra-15 centrifugal filter (Millipore) with a filtering membrane of regenerated cellulose and a 30 kDa molecular weight cut-off (MWCO) also labeled as nominal molecular weight limit (NMWL). The filtration is performed via centrifugation 4500 rpm, 45 minutes, and 20 °C using a Centrisart G-16C (Sartorius). Mono- and bi-metallic nanoparticles are retained by the filtering membrane, while the aqueous media and dissolved silver ions pass through. All the samples and the standards were acidic digested before being analyzed, thanks to a 10 %v/v of ≥ 65 %wt $HNO_3$ (Sigma-Aldrich) and a 10 %v/v of 30 %wt $H_2O_2$ (Sigma-Aldrich).

***Crystalline structure and size by XRD spectroscopy*** - The instrument used for the determination of the x-ray diffraction (XRD) pattern of the nanoparticles synthesized is the D8 ADVANCE (Bruker) operating in 2θ mode and using a copper target (Cu Kα, λ = 0.15406 nm). The selected working conditions are 10-80 ° 2θ range, acquiring the signal every 0.02 ° 2θ step, and acquisition time of 0.5 seconds. To focus on the main diffraction peak of Au and Pt, some spectra were acquired scanning 30-50 ° 2θ range, taking points every 0.1 ° 2θ step, and acquisition time of 10 s. Crystallite size was estimated using the Scherrer's equation.
Samples were prepared by drop-casting the colloidal suspensions on a glass substrate and then dried in an oven at 70 °C.

***Particle size by TEM*** - Morphological evaluation and particle size determination were assessed by transmission electron microscopy (TEM) using a Tecnai F20 (FEI) microscope operating at 200 keV. The instrument is equipped with an energy dispersive x-ray spectroscopy (EDX) micro-analysis and the scanning transmission electron microscopy (STEM) accessories. The TEM images were taken in phase contrast mode, high-resolution transmission electron microscopy (HRTEM), and selected area electron diffraction (SAED). STEM pictures were recorded using a high angle annular dark field (HAADF) detector.
The sample preparation involves a solution dilution 1:100 in volume in Milli-Q water and sonication for 10 minutes, then the sample is deposited on a holey carbon film supported copper grid. The preparation was then dried at 80 °C.

### 5.4.3. Catalytic test: model reaction of reduction of 4-nitrophenol

The evaluation of the catalytic activity of the synthesized mono- and bi-metallic nanoparticles was assessed thanks to the model reaction of reduction of 4-nitrophenol (4-NP) to 4-aminophenol (4-AP). The reaction scheme is reported in Figure 147, and it requires two reagents: 4-nitrophenol (CAS Number 100-02-7) from Sigma-Aldrich (Product Number 241326, purity ≥ 99 %) as main reagent, sodium borohydride (CAS Number 16940-66-2) from Sigma-Aldrich (Product Number 213462, purity 99 %) as hydrogen source for the reduction, and the catalyst which is constituted by the synthesized AuNPs, PtNPs, AuPtNPs-a, or AuPtNPs-cs.

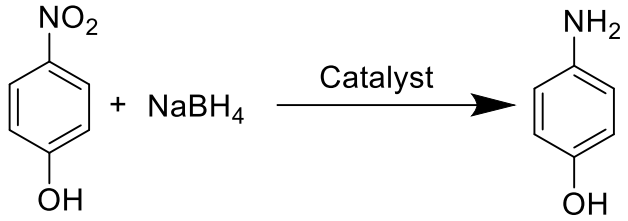


*Figure 147 – Catalytic model reaction of reduction of 4-nitrophenol to 4-aminophenol assisted by sodium borohydride.*

Same conditions were adopted for all the samples to compare properly the results. The reaction was carried out using 5 mL of a $9 \cdot 10^{-5}$ M weekly prepared solution of 4-NP, 1 mL of a 0.742 M freshly prepared solution of $NaBH_4$, and 10 mL of the catalyst colloidal suspension with a total metals concentration of $1.1 \cdot 10^{-5}$ M. Mono- and bi-metallic samples were washed from unreacted reagents and reaction by-products and co-products, thanks to a filtration by centrifugation at 20 °C and 1500 rpm for 20 minutes using a Centrisart G-16C (Sartorius) centrifuge mounting an Amicon Ultra-15 centrifugal filter (Millipore) with a filtering membrane of regenerated cellulose and a 30 kDa molecular weight cut-off (MWCO). The NPs retained on the membrane of the filter were suspended in Milli-Q water and diluted to the desired concentration for the catalytic test.

The reaction was performed at room temperature and pressure, under magnetic stirring. 4-NP and $NaBH_4$ were mixed under stirring for 10 minutes to favor the formation of the phenolate ion which is the reactive species, the reduction reaction doesn't occur without a catalyst. Subsequently, the catalyst is added and immediately after that, the aliquot for UV-Vis monitoring of the reaction evolution is taken. If the catalyst tends to form a non-active oxide surface layer, the reaction order can be modified adding first the catalyst and the $NaBH_4$ under stirring for 10 minutes, once the catalyst is activated the 4-NP can be added. Since this is not the case for these water suspensions AuPtNPs, the standard method was adopted.

Since the concentration of $NaBH_4$ is exceeding the stoichiometry, the reaction can be approximated to a pseudo-first-order respect to the concentration of 4-NP. In this case the reaction rate (v) only depends on the molar concentration of 4-NP ([4-NP]) and the kinetic constant (k), the relation is reported in the Equation 12.

$$v = k \cdot [4\text{-NP}] \qquad \text{Equation 12}$$

The reaction advancement is monitored by UV-Vis spectrophotometry, 4-NP has the maximum absorption at 317 nm, that after the formation of the phenolate ion due to the addition of $NaBH_4$ undergoes a red-shift toward 400 nm. So, the nitrophenolate ion ha a yellow coloration, and its consumption to form the amine is monitored by the decreasing of the intensity of the absorption in the visible region. The tests were conducted with a spectrophotometer Cary 3500 UV-Vis (Agilent Technologies) acquiring spectra in the wavelength range 300-500 nm. The instrument mounts a stirring system for the cuvettes allowing to perform the whole test with the same aliquot. Stirring speed was set to 600 rpm to grant a homogeneous reaction environment and to favor the removal of the gas bubbles formed. Spectra were registered every 15 seconds to study the advancement of the reaction until its completeness.

## 5.5. References


233. Sayan Kar et al. Catalytic Furfural/5-Hydroxymethyl Furfural Oxidation to Furoic Acid/Furan-2,5-dicarboxylic Acid with H2 Production Using Alkaline Water as the Formal Oxidant. J. Am. Chem. Soc. 2022, 144, 3, 1288–1295. https://doi.org/10.1021/jacs.1c10908.

234. Zelin Li, Lei Zhao, Bolong Li, Shuchang Bian, Jianhua Wang, Hailan Zhang, Chen Zhao, Base metal catalyzed oxidation of 5-hydroxy-methyl-furfural to 2,5-furan-dicarboxylic acid: A review, Catalysis Today, Volume 408, 2023, Pages 64-72, ISSN 0920-5861, https://doi.org/10.1016/j.cattod.2022.09.002.

235. Jan-Dierk Grunwaldt, Christoph Kiener, Clemens Wögerbauer, Alfons Baiker, Preparation of Supported Gold Catalysts for Low-Temperature CO Oxidation via "Size-Controlled" Gold Colloids, Journal of Catalysis, Volume 181, Issue 2, 1999, Pages 223-232, ISSN 0021-9517, https://doi.org/10.1006/jcat.1998.2298.

236. Musselwhite, N., Somorjai, G.A. Investigations of Structure Sensitivity in Heterogeneous Catalysis: From Single Crystals to Monodisperse Nanoparticles. Top Catal 56, 1277–1283 (2013). https://doi.org/10.1007/s11244-013-0150-y

237. Rao, C.N., & Cheetham, A.K. (2001). Science and technology of nanomaterials: current status and future prospects. Journal of Materials Chemistry, 11, 2887-2894.

238. Hutchings GJ, Kiely CJ. Strategies for the synthesis of supported gold palladium nanoparticles with controlled morphology and composition. Acc Chem Res. 2013 Aug 20;46(8):1759-72. doi: 10.1021/ar300356m. Epub 2013 Apr 15. PMID: 23586905.

239. Sheldon, R.A. (2000). Atom utilisation, E factors and the catalytic solution. Comptes Rendus De L Academie Des Sciences Serie Ii Fascicule C-chimie, 3, 541-551.

240. Andi Alijagic, Francesco Barbero, Daniela Gaglio, Elisabetta Napodano, Oldřich Benada, Olga Kofroňová, Victor F. Puntes, Neus G. Bastús, Annalisa Pinsino, Gold nanoparticles coated with polyvinylpyrrolidone and sea urchin extracellular molecules induce transient immune activation, Journal of Hazardous Materials, Volume 402, 2021, 123793, ISSN 0304-3894, https://doi.org/10.1016/j.jhazmat.2020.123793.

241. Pauzi, N., Mohamad, S., Ghazali, S. et al. Evaluation of Glucose Reduction for Silver Nanoparticles Synthesis with Nanocrystalline Cellulose Matrix. BioNanoSci. 13, 1695–1702 (2023). https://doi.org/10.1007/s12668-023-01167-1.

242. Allen J. Bard and Larry R. Faulkner, Electrochemical Methods: Fundamentals and Applications, New York: Wiley, 2001, 2nd ed.. Russian Journal of Electrochemistry 38, 1364–1365 (2002). https://doi.org/10.1023/A:1021637209564.

243. Watanabe A, Kajita M, Kim J, Kanayama A, Takahashi K, Mashino T, Miyamoto Y. In vitro free radical scavenging activity of platinum nanoparticles. Nanotechnology. 2009 Nov 11;20(45):455105. doi: 10.1088/0957-4484/20/45/455105. Epub 2009 Oct 16. PMID: 19834242.

244. Okamoto, H., Massalski, T.B. The Au−Pd (Gold-Palladium) system. Bulletin of Alloy Phase Diagrams 6, 229–235 (1985). https://doi.org/10.1007/BF02880404.

245. Neal, R.D., Hughes, R.A., Sapkota, P., Ptasińska, S., & Neretina, S.S. (2020). Effect of Nanoparticle Ligands on 4-Nitrophenol Reduction: Reaction Rate, Induction Time, and Ligand Desorption. ACS Catalysis, 10, 10040-10050.

246. Muhammad Sajid et al. Production of 2,5-furandicarboxylic acid (FDCA) from 5-hydroxymethylfurfural (HMF): recent progress focusing on the chemical-catalytic routes. Green Chem., 2018,20, 5427-5453. https://doi.org/10.1039/C8GC02680G.

247. Chunlin Chen, Lingchen Wang, Bin Zhu, Zhenqiang Zhou, Soliman I. El-Hout, Jie Yang, Jian Zhang, 2,5-Furandicarboxylic acid production via catalytic oxidation of 5-hydroxymethylfurfural: Catalysts, processes and reaction mechanism, Journal of Energy Chemistry, Volume 54, 2021, Pages 528-554, ISSN 2095-4956, https://doi.org/10.1016/j.jechem.2020.05.068.

248. Haiss W, Thanh NT, Aveyard J, Fernig DG. Determination of size and concentration of gold nanoparticles from UV-vis spectra. Anal Chem. 2007 Jun 1;79(11):4215-21. doi: 10.1021/ac0702084. Epub 2007 Apr 26. PMID: 17458937.

249. Watanabe A, Kajita M, Kim J, Kanayama A, Takahashi K, Mashino T, Miyamoto Y. In vitro free radical scavenging activity of platinum nanoparticles. Nanotechnology. 2009 Nov 11;20(45):455105. doi: 10.1088/0957-4484/20/45/455105. Epub 2009 Oct 16. PMID: 19834242.

# Chapter 6

## *Functional materials for wastewater remediation*

Part of the content of this chapter has been published as M. Blosi et. al. “Chlorella vulgaris meets $TiO_2$ NPs: Effective sorbent/photocatalytic hybrid materials for water treatment application” Journal of Environmental Management 304 (2022) 114187, and as Master’s Thesis of S. Amadori “Sviluppo ed ingegnerizzazione di materiali compositi multifunzionali applicabili nell’abbattimento di microrganismi patogeni e nel trattamento acque” 2023.

## 6.1. Introduction

The environmental problem related to the increasing pollution of hydric resources, caused by both industrial and urban human activities, has highlighted the need to develop new technologies and devices for water purification. Although, the composition of wastewaters varies depending on the industrial or urban sector involved, the most common and impactful pollutants are usually heavy metals and organic pollutants.[250] To remediate these types of effluents, it is necessary to devise a product that is capable of reducing the content of heavy metals and at the same time of organic compounds. Therefore, the goal is to study and develop a low environmental impact multifunctional device optimizing adsorbing functionalities targeting the desired pollutants.

The adsorption of organic and inorganic pollutants by biopolymers is a fundamental aspect in the field of water bioremediation because of the high degree of sustainability, circularity, and biodegradability of biomass-derived materials.[229] This work aimed at increasing active phases' handleability thanks to the immobilization into a biopolymer matrix that can facilitate their exploitation. The study focused on biocompatible, renewable and environmentally friendly materials using biopolymers derived from biomass such as chitosan, agarose, and k-carrageenan and adsorbent materials of natural origin, like clays and hydrotalcites. The active phases were first immobilized into biopolymeric hydrogels, then the composite materials were freeze-dried, creating porous adsorbent structures, characterized by improved material handleability and stability during use, storage, and transportation.

### 6.1.1. Natural inorganic adsorbent materials

The increasing industrialization and growth rate of human population are endangering the environment. Wastewaters are harmed by the presence of pollutants of extremely varied nature, both organic and inorganic: heavy metals, colorants, pesticides, oils, microplastics, and many other categories. Among various water treatment technologies, adsorption is considered one of the most effective, thanks to its convenience, universal availability, and ease of use.[251]

The use of natural clays-like materials is widely exploited in water purification treatments, because of the low cost, high natural abundance, and the various helpful physicochemical properties like the large specific surface area, the excellent ion exchange capability, and the tendency to absorb water within their layered structures.[252]

***Hydrotalcites*** – Layered double hydroxides (LDH), also known as hydrotalcite-like compounds, are anionic clays that have attracted considerable attention in recent years due to the presence of large interstitial spaces between their positively charged layers capable of hosting a significant number of exchangeable anions. LDH general structure is reported in Equation 13, where $M^{2+}$ and $M^{3+}$ are respectively bivalent (like $Mg^{2+}$, $Co^{2+}$, $Ni^{2+}$, and $Cu^{2+}$) and trivalent (like $Al^{3+}$, $Fe^{3+}$, and $Ga^{3+}$) cations, x value is included in between 0.20 and 0.33 and it represents the molar fraction of $M^{3+}$, and finally An- represents the interlayer anion (like $CO_3^{2-}$, $Cl^-$, $NO_3^-$, and $SO_4^{2-}$). The structural positive charges are counterbalanced by the interlayer anions. The charge density of the hydroxide layers is determined by the molar ratio $M^{2+}/M^{3+}$, for synthetic hydrotalcites this value can be modulated. The structure of these materials is based on the typical hydroxides octahedral unit, by heating to about 450-500 °C the LDH can be converted into mixed metal oxides (MMO). An important property of MMO is the so-called "memory effect", calcined anionic clays can restore their original layered structure after adsorption of anions. The high anionic exchange capacity and large surface area of the LDH, their flexible interlayer region accessible to various ionic and non-ionic compounds are promising features for the development of performant contaminants adsorbent devices to treat aqueous system.[253]

$$\left[M_{1-x}{}^{2+}M_x{}^{3+}(OH)_2(A^{n-})_{x/n}\right]^{x+} \cdot mH_2O \qquad \text{Equation 13}$$

***Bentonite*** – Bentonite is a natural clay, its structure is a phyllosilicate hydrate ($Al_2O_3$-$SiO_2$-$4H_2O$). It can be found as clays smectite sediments containing a variety of swelling silicate and others phases like illite, kaolinite, quartz cristobalite, dolomite, calcite, plagioclase. In bentonite

structure, the isomorphic substitution of $Si^{4+}$ in the tetrahedral site with trivalent ions, and $Al^{3+}$ in the octahedral site with bivalent ions determines the negative charge of the structural layers. To remove water pollutants, it is possible to exploit the electrostatic attraction and the formation of surface complexes. For these reasons, bentonite is widely used in environmental protection, for the detoxification of drinking water and the treatment of wastewater. Recently, a variety of procedures have been proposed for the modification of natural clays and clay minerals, including physical, chemical, and thermal treatments, in order to improve their adsorption capacity of specific harmful classes of pollutants.[254,255]

### 6.1.2. Biopolymeric scaffolds

During the last decades, marine-derived biomacromolecules, such as alginates, chitin, agar, carrageenan, and other bioderived molecules like cellulose and collagen, have been exploited as highly low environmental impact efficient functional materials for water purification treatments.[230] The variety of natural and modified molecular structures allows different interaction and adsorption selectivity toward general or specific classes of compounds, furthermore the gelling properties of these biopolymers may be exploited for the production of hydrogel to embed active phases.[256] Hydrogels are tridimensional networks constituted by polymeric chains entangled and crosslinked with a high degree of biocompatibility and malleability. Working with these materials it is possible to produce bio-composites dispersing active phases in the hydrogel structure, like adsorbing clays, to exploit synergistic effects of the functionalized scaffold in the wastewater treatment.[73]

***Chitosan*** – Chitosan is a biopolymer obtained by the deacetylation of chitin extracted by crustacean shells, usually considered as a waste. Chitosan is a natural derived cationic polysaccharide soluble in water constituted by β-(1,4)-linked D-glucosamine (deacetylated unit) and N-acetyl-D-glucosamine (acetylated unit). Hydroxyl and amine functionalities allow its dispersion in acidic solutions, and also the interaction with organic and inorganic species via electrostatic interaction, coordination, or hydrogen bonds. Chitosan can be considered an ecological complexing agent due to its renewability, low cost, non-toxicity, hydrophilicity, and biodegradability, furthermore, it possesses antibacterial properties.[257]

***Agarose*** – Agarose is a linear natural biopolymer extracted by the cell wall or red algae. It is a polysaccharide and together with agaropectin is one of the main constituents of agar. Agarose is biodegradable, biocompatible, and hydrophilic, in water it forms stable and reversible gel structures. It is constituted by D-galactose and 3,6-anhydrous-L-galactose, bound alternating α-(1,3) and β-(1,4) glycoside bonds. Hydroxyl groups may be exploited for the pollutants adsorption.[258]

***Carrageenan*** – Carrageenan is a linear polysaccharide extracted by red algae, it is enriched with sulphate functionalities and it may form polyanions structures. It is constituted by alternating 3-linked β-D-galactopyranose (G-units) and 4-linked α-D-galactopyranose (D-units) or 4-linked 3,6-anhydro-a-D-galactopyranose (DA-units), this is the base disaccharide repeating unit.

Carrageenan is divided in three main products iota, kappa, and lambda, kappa is the most interesting compound since it presents the most pronounced gelling properties.[259]

## 6.2. Results and discussion

Hydrotalcites and bentonite were used as active adsorbing phases for the functionalization of biopolymeric hydrogels. Each material underwent physicochemical characterization and its absorption properties were studied.

Two commercial hydrotalcite-like compounds were selected with different $M^{2+}/M^{3+}$ molar ratio, Pural standard magnesium-aluminum hydrotalcite with molar ratio 1.4 (LDH1.4) or 2 (LDH2). Bentonite commercial sample was grinded and sifted 80 µm, to obtain a fine and homogenous white powder. In this way it was possible to better disperse bentonite in the hydrogels. Both bentonite and hydrotalcites were characterized by XRD, BET, ELS, and in the absorption of metal cations and organic colorants.

The biopolymers tested in the hydrogel formation were chitosan, agarose, and k-carrageenan from Sigma-Aldrich. The first is a positively charge compound, the other bring negative charges on their chain. Biopolymers white powders were dispersed in water and characterized by ELS, after the hydrogel formation their swelling and dissolution were assessed and then they were tested in the absorption of metal cations and organic colorants. The hydrogels were crosslinked with glutaraldehyde to improve their mechanical properties, and these tests were repeated.

Finally, the active phases (bentonite and hydrotalcites) were embedded into biopolymers for the production of adsorbent scaffolds for water remediation. A general concept map of the process is schematized in Figure 148.

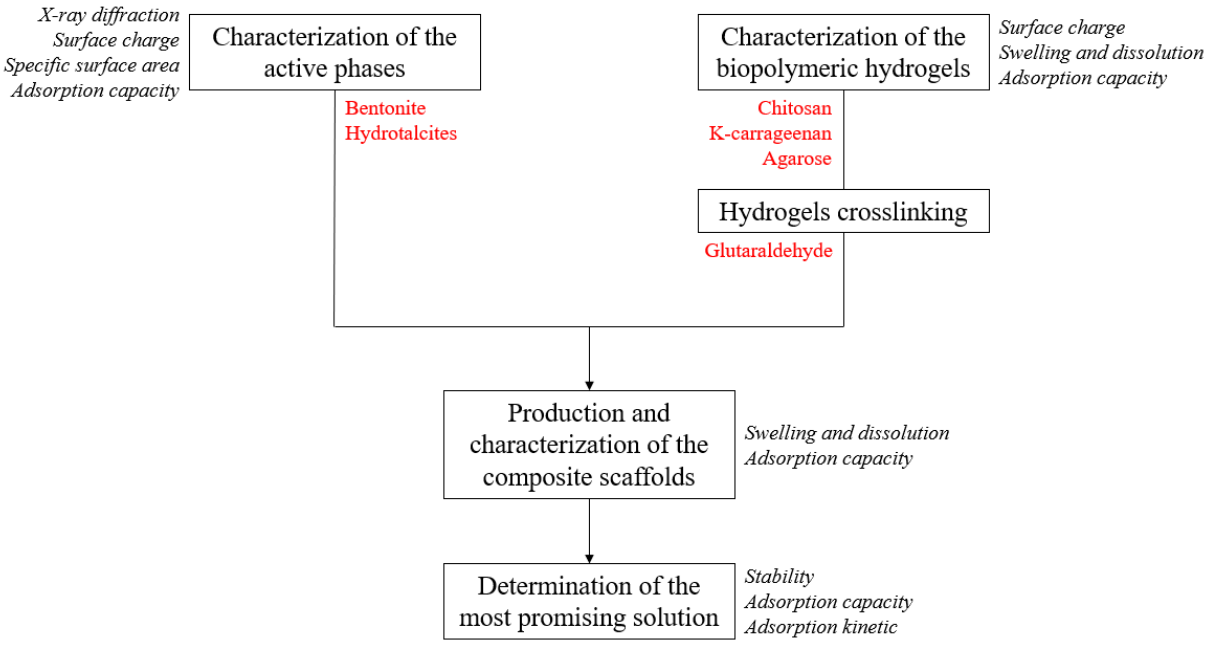


*Figure 148 – Scheme of the concept map for the preparation of biopolymeric scaffolds embedding active phases for the wastewater remediation.*

### 6.2.1. Hydrotalcite-like materials and natural clays

Hydrotalcites and bentonite powders were characterized by XRD and BET, then they were dispersed in water and the zeta potential was studied to understand the interaction with charged species, like metal cations or organic polar and ionic colorants. Finally, their adsorption capacity and the kinetic of the adsorption process were studied.

***X-ray diffraction spectroscopy*** – Bentonite XRD spectrum reported in Figure 149 reveals how the clay is constituted by different mineral phases, mainly montmorillonite and quartz.

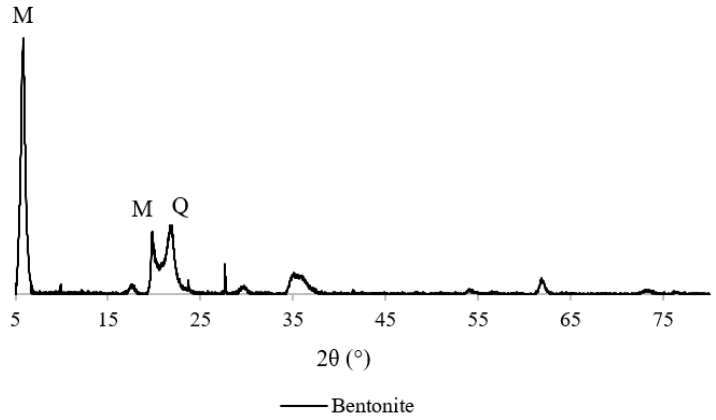


*Figure 149 – XRD spectrum of bentonite powder showing the presence of two main phases: montmorillonite (M) and quartz (Q).*

Hydrotalcites LDH1.4 and LDH2 XRD spectra reported in Figure 150 demonstrate that the $M^{2+}/M^{3+}$ molar ratio differences do not affect the crystalline structure. The main diffraction peaks a clearly observable for both samples, LDH2 sharper peaks correspond to more extended crystalline domains.

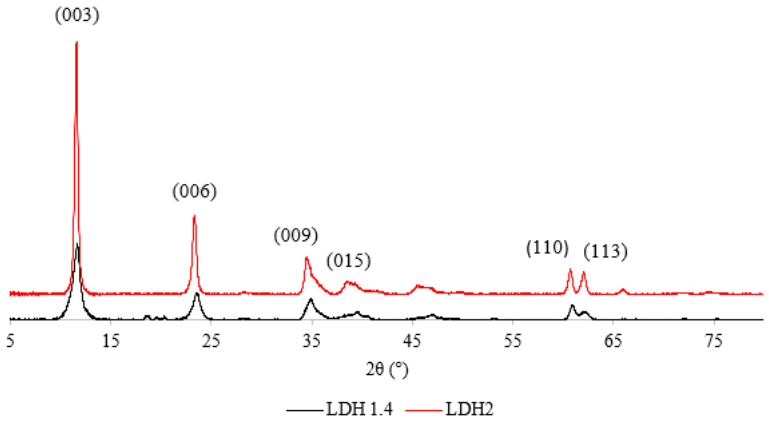


*Figure 150 – XRD spectra of the studied hydrotalcites (LDH1.4 and LDH2) showing the typical layered double hydroxide diffraction pattern.*

***Specific surface area*** – From BET analysis it was possible to observe significative differences among the samples. Bentonite has a specific surface area one order of magnitude greater compared to the hydrotalcites, reaching more than 100 $m^2 \cdot g^{-1}$, as it is possible to see in Table 64. The higher surface area value is promising for the adsorption application, higher surface means a greater number of active sites for the adsorption in the interlayer of clays and hydrotalcites. This parameter influences also the swelling behavior of the material once dispersed in water. The water adsorption and consequent swelling strongly affect the mechanical properties of the material and the filtering properties. From these results bentonite should be more effective in the wastewater remediation adsorption treatments. LDHs are usually applied after a thermal treatment, to convert the hydroxide structure into an oxide, removing the interlayer counterions. These samples after mechanical grinding usually presents high surface area values.

*Table 64 – Specific surface area of bentonite and hydrotalcites LDH2 and LDH1.4, assessed by BET analysis.*

| Sample | Specific surface area ($m^2 \cdot g^{-1}$) |
|---|---|
| Bentonite | 118 |
| Hydrotalcite LDH2 | 54 |
| Hydrotalcite LDH1.4 | 16 |

***Isoelectric point*** – The desired application is the adsorption of water pollutants, so it is important to study the behavior of these material once dispersed in water. In particular, the surface charge of these compounds could play an important role in the adsorption properties. Together with Van del Waals interaction, polar interaction and the ion exchange give fundamental contributes to the adsorption mechanisms. For these reasons the zeta potential of the samples was studied as

function of pH, to determine the isoelectric point (IEP), which is the pH that corresponds to neutral zeta potential.

The samples dispersed in water have a starting pH of about 8-9, from the titration reported in Figure 151 it is noticeable how the behavior of the two LDHs is nearly superimposable with an IEP of 5.5 unit of pH. It was not possible to observe the IEP of bentonite (B), which is likely to be at pH lower than 1, region acidic enough to favor also clays dissolution phenomena.

The pH it is an important parameter in the adsorption process, it influences the surface charge of adsorbent materials and its functional groups ionization degree, as well as the solubility and the ionic form of the targeted pollutants. Surface charge results positive at pH lower than the IEP and vice versa. The most favorable conditions are represented by opposite charged adsorbent and pollutant, maximizing these materials interaction thanks to electrostatic interaction and ion exchange.

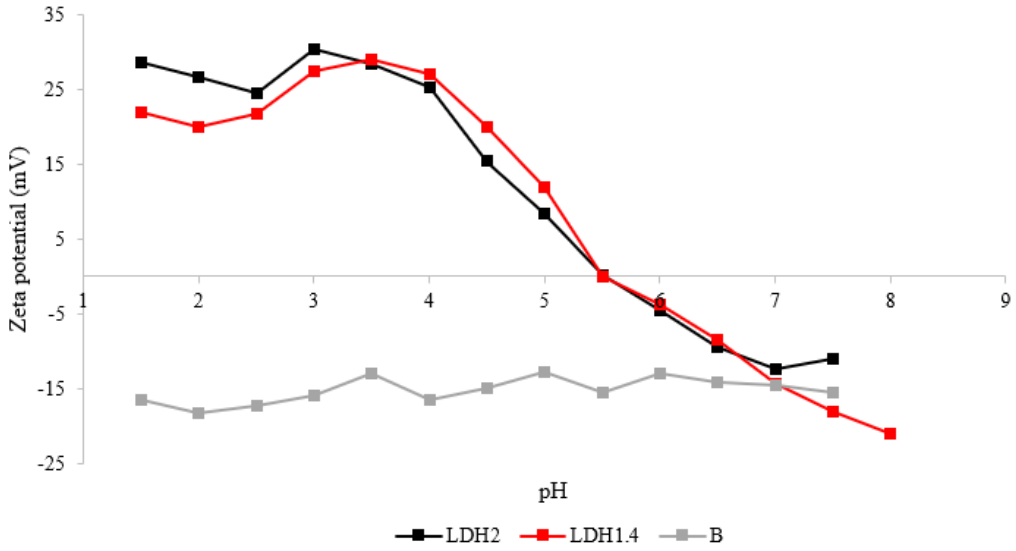


*Figure 151 – Zeta potential titration as function of the pH of the active phases hydrotalcites (LDH2 and LDH1.4) and bentonite (B).*

***Adsorption tests*** – Wastewaters contaminated by colorant, pesticides, or antibiotics are usually treated by conventional methods like membrane filtration, osmosis, oxidation, coagulation, ozonation, ion exchange, or adsorption. Adsorption is appealing because of the easy large-scale application, as well as for the general-purpose application.

In this study the cationic colorant rhodamine B (RhB), the anionic colorant methyl orange (MO), and the cupric cation ($Cu^{2+}$) are used as simulated model pollutants to study the adsorption capacity of clays and hydrotalcites, combined with a kinetic study of the process.

*Rhodamine B* – Starting from the adsorption of rhodamine B, in Figure 152 it is possible to see the adsorption capacity of the samples expressed as milligram of rhodamine B adsorbed per gram of sample as function of time. Bentonite has a slightly better adsorption capacity respect to LDHs, ≈ 7 $mg \cdot g^{-1}$, this is probably due to the higher surface area. Moreover, bentonite structure is characterized by negatively charged layers with positive counterions like $Na^{+}$ or $Ca^{2+}$ in the interlayer. This opens the possibility to cation exchange, favoring the absorption of the positively charged RhB molecule. The 5.59 pH of the suspension higher than the bentonite IEP (< 1) generate a diffused negative charge on the clay structure, favoring the interactions with RhB. For all the samples a stable equilibrium is reached within the first 5 minutes. Typically, the contact time it is an important parameter regulating the adsorption processes. The adsorption increases during time until the equilibrium is reached between the adsorption sites and the adsorbate gradient of concentration. Bentonite reaches a nearly quantitative RhB removal ≈ 99%, while LDHs close to 88%, starting from a 7 $mg \cdot L^{-1}$ RhB solution.

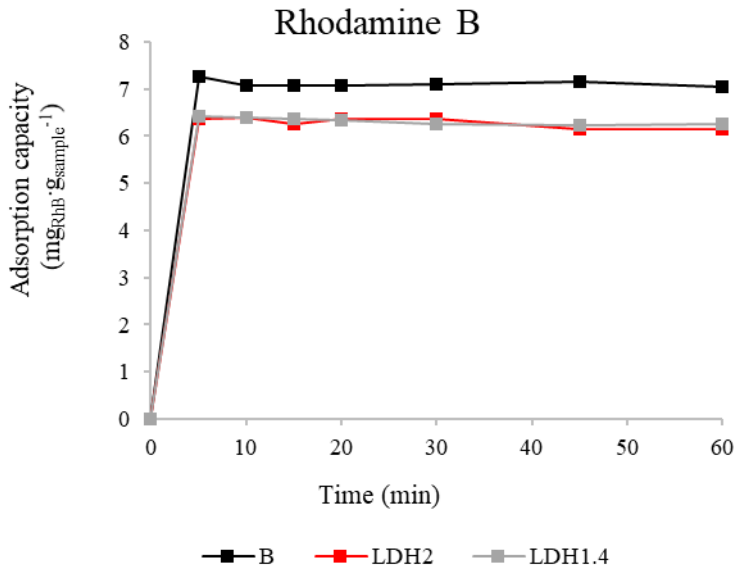


*Figure 152 – Rhodamine b adsorption test. Adsorption capacity of bentonite (B) and hydrotalcites (LDH2 and LDH1.4) as function of the adsorption time.*

*Methyl orange* – The opposite conditions occur in the adsorption of methyl orange, this is a negatively charged molecule which better interact with positively charged surfaces. As it is possible to see from the graph in Figure 153, hydrotalcites works better than bentonite, this is due to the positively charged LDHs layer generated by the substitution of $M^{2+}$ with $M^{3+}$ cations in the lattice. Anion exchange helps the adsorption of methyl orange on LDHs, in particular LDH2 reaches important adsorption capacity values, ≈ 40 $mg \cdot g^{-1}$. Characterization demonstrated

a similar behavior for LDH2 and LDC1.4, the main difference lays in the surface area, LDH2 (54 $m^2 \cdot g^{-1}$) has higher surface area respect LDH1.4 (16 $m^2 \cdot g^{-1}$), this strongly improve the methyl orange adsorption. Even if bentonite has greater surface area (118 $m^2 \cdot g^{-1}$), the electrostatic repulsions between the negative adsorbent and the negative adsorbate impede the process, resulting with a negligible adsorption of methyl orange on bentonite. LDHs reach a stable equilibrium within the first 5 minutes, while no activity was observed for bentonite with a ≈ 2% removal after 60 minutes. Tests started with a methyl orange concentration of 20 $mg \cdot L^{-1}$, LDH2 granted a ≈ 90 % removal, while only ≈ 13% for LDH1.4.

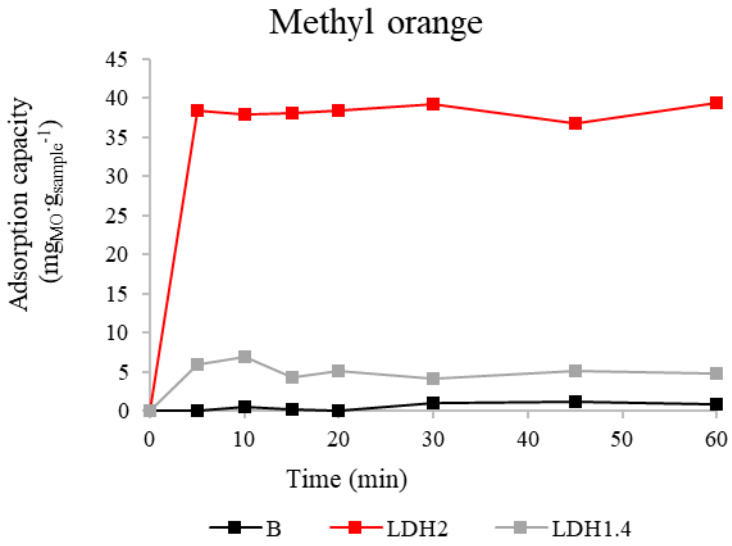


*Figure 153 – Methyl orange adsorption test. Adsorption capacity of bentonite (B) and hydrotalcites (LDH2 and LDH1.4) as function of the adsorption time.*

*$Cu^{2+}$* – The copper removal from a 10 $mg \cdot L^{-1}$ $Cu^{2+}$ solution is reported in Figure 154. Since the pH of the samples is higher than IEP, the negative charge on the adsorbent surface should favor the copper cation removal. In fact, all the samples showed good activity, in particular bentonite and LDH1.4 were the best performing samples reaching removal values respectively of 77% and 89% after 30 minutes. Bentonite is favored in the copper adsorption by the cation exchange capabilities, it is surprising that LDH1.4 worked better than LDH2 even if it has a lower specific surface area. Copper adsorption is slower respect to the colorants, the removal grew slowly with time.

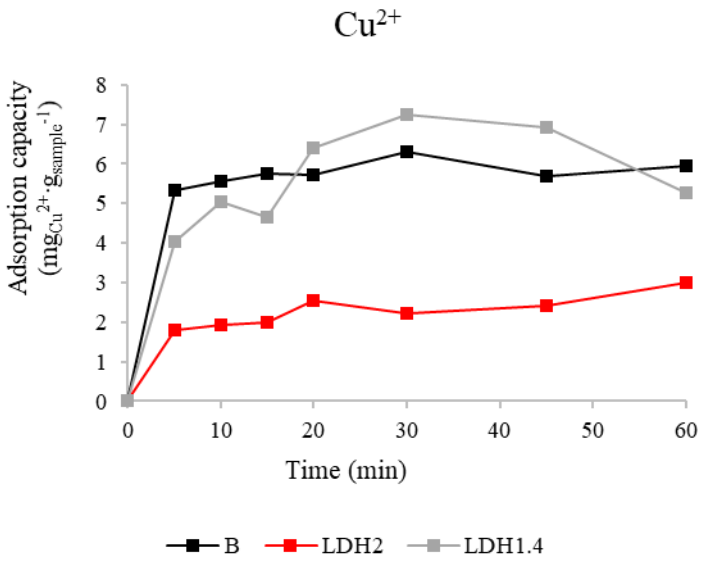


*Figure 154 – $Cu^{2+}$ adsorption test. Adsorption capacity of bentonite (B) and hydrotalcites (LDH2 and LDH1.4) as function of the adsorption time.*

*Kinetics* – The experiential data collected were fitted into a pseudo-second-order (PSO) kinetic model. As representative result, it is reported in Figure 155 the linearized graph of the pseudo-second-order model applied to rhodamine B adsorption. The theoretical model demonstrated high compatibility with the experimental results, recording $R^2$ values close to 1. The linearized form developed by Ho and McKay in 1999 was used, it is reported in Equation 14 where t is the time, $q_t$ is the adsorption capacity at time t, $q_e$ is the adsorption capacity at the equilibrium, and k is the kinetic constant.[260,261]

$$\frac{t}{q_t} = \frac{1}{q_e} \cdot t + \frac{1}{k q_e^{\,2}} \qquad \text{Equation 14}$$

From the kinetic results bentonite emerges as a faster absorbent of rhodamine B, this information combined with the previous data regarding the adsorption capacity confirm the theoretical prevision regarding the major affinity of bentonite for positively charged molecules.

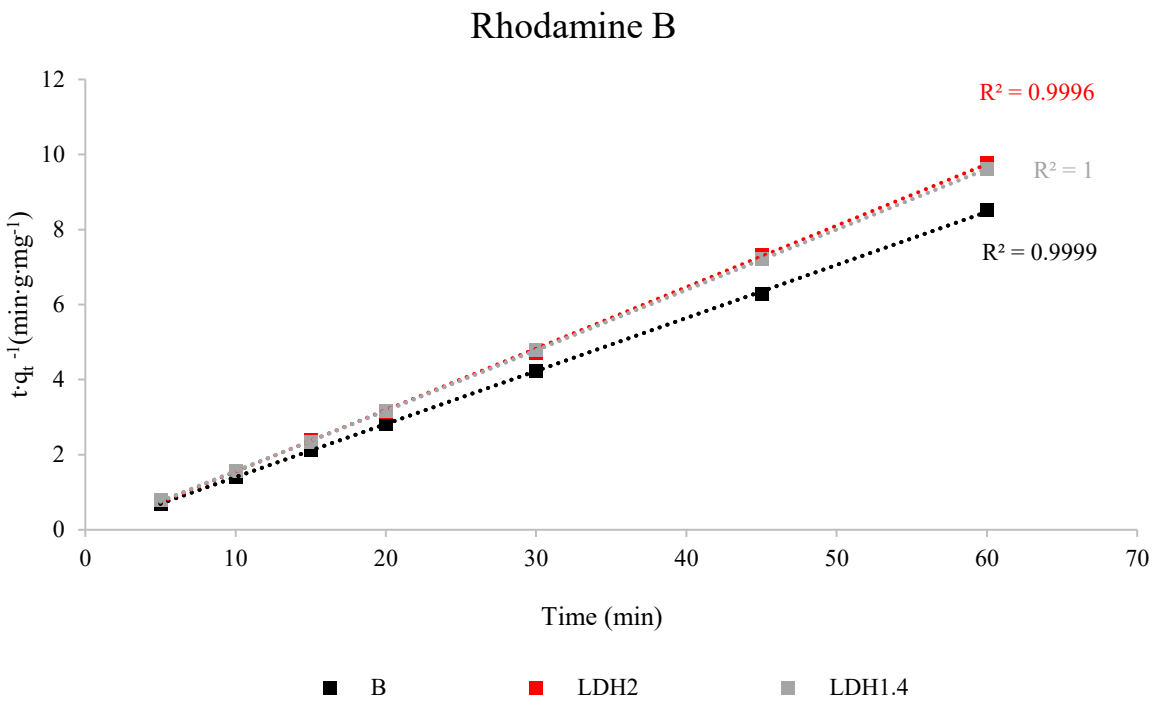


*Figure 155 – Rhodamine b adsorption test. Linearized pseudo-second-order adsorption graph of bentonite (B) and hydrotalcites (LDH2 and LDH1.4).*

### 6.2.2. Biopolymers

The stability in water of the synthesized biopolymeric hydrogels was assessed evaluating the swelling behavior and the dissolution in water. The samples constituted by chitosan, agarose, or k-carrageenan were also tested in the adsorption of the model pollutants to determine if it is possible to exploit biopolymers functional groups (hydroxyl and amine in chitosan, hydroxyl in agarose, hydroxyl and sulfate in k-carrageenan) to develop synergistic effect with the active phases that will be implemented in the scaffolds.

***Isoelectric point*** – The determination of the isoelectric point (IEP), and the zeta potential trend during a pH titration was performed by electrophoretic light scattering. The titration curves reported in the graph in Figure 156 reveal a positive charge for chitosan characterized by the presence of amine groups, a more neutral behavior for agarose which has only hydroxyl groups, and negative zeta potential for k-carrageenan which possesses sulfate groups. The isoelectric point of these materials was determined to be 5.82 for chitosan, and < 1 for k-carrageenan and < 2 for agarose. From this information, it is possible to assume that chitosan and k-carrageenan will have opposite affinities for anions (higher for chitosan) and cations (higher for k-carrageenan). Furthermore, chitosan is poorly soluble in water, it can be better dispersed in diluted acetic acid solutions, working in acidic conditions its positive charge will be accentuated ($pK_a$=6.3).

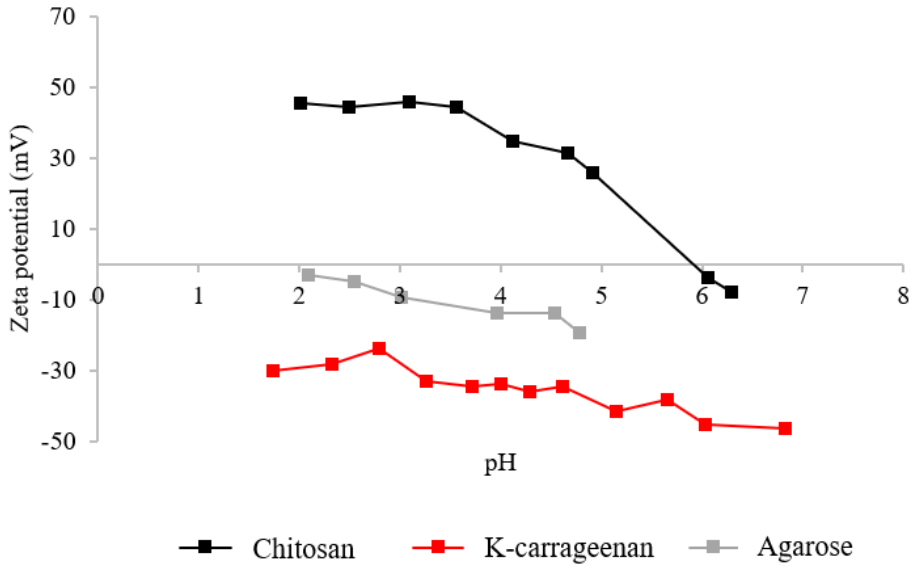


*Figure 156 – Zeta potential titration as function of the pH of the biopolymers used as embedding matrices: chitosan, k-carrageenan, and agarose.*

***Swelling and dissolution tests*** – Biopolymeric hydrogels water resistance and durability were tested assessing the swelling behavior and the dissolution in aqueous environment. These tests were used to study the mechanical resistance of the hydrogel structure in a simulated working environment. Higher swelling degrees represent an intimate contact between water and hydrogel structure, favoring the interaction between the biopolymer functional groups and the pollutants to be removed. The swelling was estimated as water absorbing capacity, grams of water absorbed per gram of gel, while the dissolution was calculated on the dry mass loss during the test. Results in Table 65 point out the sample with the higher absorbing capacity (77.5 $g \cdot g^{-1}$) and dissolution (35.1%), representing the most promising adsorbent but also the structure that requires more mechanical improvements, which will be provided by a crosslinking agent. On the opposite k-carrageenan is the most stable sample with a 5.7% dissolution, but the less water-absorbing material 20.3 $g \cdot g^{-1}$. The crosslinking action improves the stability of hydrogels reducing the dissolution of chitosan (8.1%) and agarose (10.1%). The paid price for chitosan is the reduction of water permeability, determining reduction in the water adsorption. The opposite action is obtained for k-carrageenan, probably the sulfate groups and glutaraldehyde are not compatible, reducing the stability of the hydrogel, leading to a higher dissolution (18.0%).
Based on these results the most promising composition are chitosan crosslinked with glutaraldehyde, agarose crosslinked with glutaraldehyde, and k-carrageenan not crosslinked.

*Table 65 – Swelling and dissolution test in water of the biopolymeric hydrogels pristine and crosslinked with glutaraldehyde.*

| Sample | Water absorption ($g_{H2O} \cdot g_{gel}^{-1}$) | Dissolution (%) |
|---|---|---|
| Chitosan | 77.5 | 35.1 |
| K-carrageenan | 20.3 | 5.7 |
| Agarose | 26.2 | 20.5 |
| Chitosan + glutaraldehyde | 26.4 | 8.1 |
| K-carrageenan + glutaraldehyde | 12.8 | 18.0 |
| Agarose + glutaraldehyde | 28.0 | 10.1 |

***Adsorption tests*** – Biopolymeric hydrogels that will be used as a matrix for the scaffolds containing the active phases, were tested in the adsorption of rhodamine B (RhB), methyl orange (MO), and $Cu^{2+}$ replicating the condition used for bentonite and LDHs. Both the natural and crosslinked hydrogels were tested. Here are reported the results of the most interesting composition selected on the base of the swelling and dissolution tests, which are: chitosan

crosslinked with glutaraldehyde (CG), agarose crosslinked with glutaraldehyde (AG), and k-carrageenan not crosslinked (KG).

*Rhodamine B* – The selected hydrogels demonstrated to be nearly inert to rhodamine B representing the negatively charged colorant class. As it is possible to see in the graph in Figure 157 the adsorption capacity is negligible. After 60 minutes adsorption the calculated rhodamine B removal is about 1-3%.

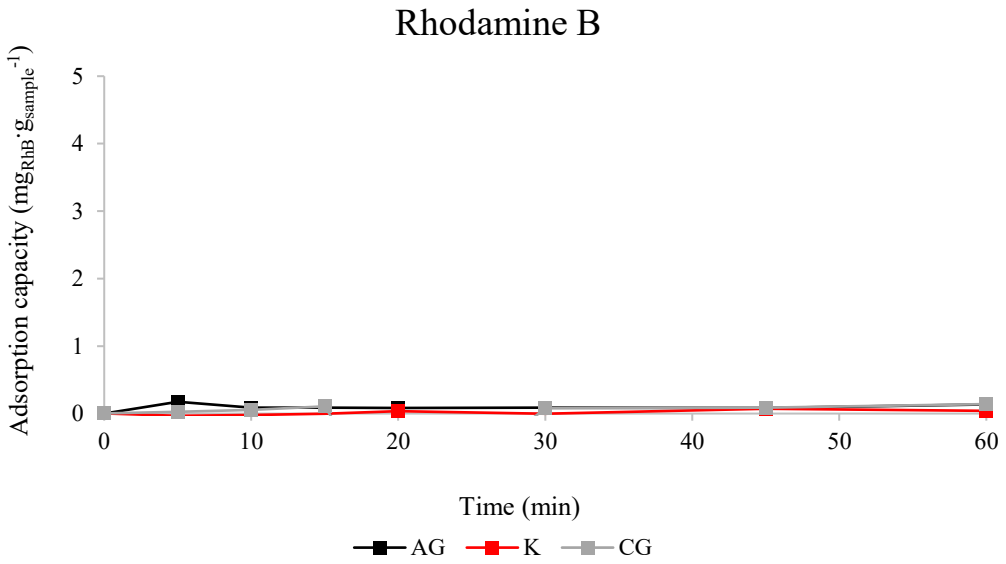


*Figure 157 – Rhodamine b adsorption test. Adsorption capacity of agarose crosslinked with glutaraldehyde (AG), k-carrageenan (K), and chitosan crosslinked with glutaraldehyde (CG) as function of the adsorption time.*

*Methyl orange* – The adsorption of anionic colorants is represented by methyl orange, in this case different efficacies are displayed by the tested samples, Figure 158. Glutaraldehyde crosslinked chitosan (CG) was demonstrated to be the most active composition with an absorption capacity of about 8 $mg \cdot g^{-1}$, slowly reaching the adsorption equilibrium approximately after 1 hour. The other two hydrogels, k-carrageenan (K) and glutaraldehyde crosslinked agarose (AG), resulted completely saturated after 5 minutes, with a lower adsorption capacity of ≈ 1 $mg \cdot g^{-1}$. Crosslinked chitosan removed ≈ 95% of methyl orange, this is due to the favorable interaction between the positively amine group at working pH and the anionic nature of methyl orange. The other two samples gave significantly lower removal, crosslinked agarose ≈ 12% and k-carrageenan ≈ 9%, demonstration less affinity for these class of pollutants.

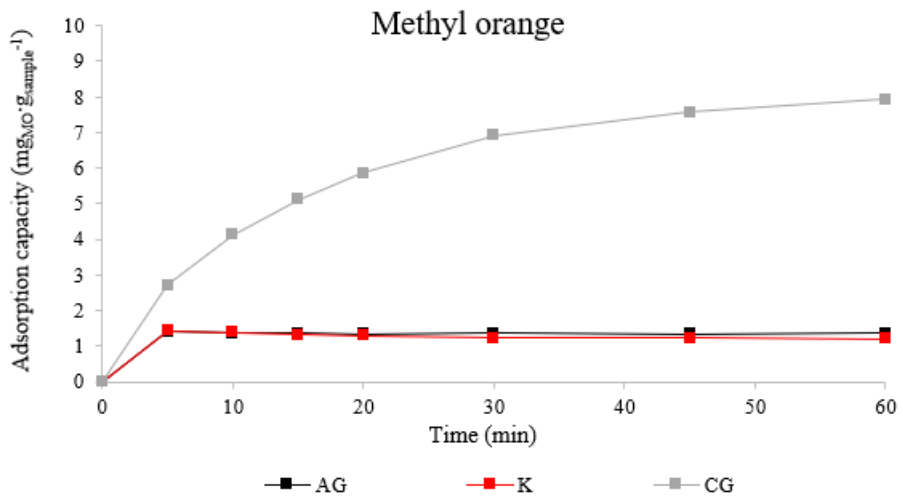


*Figure 158 – Methyl orange adsorption test. Adsorption capacity of agarose crosslinked with glutaraldehyde (AG), k-carrageenan (K), and chitosan crosslinked with glutaraldehyde (CG) as function of the adsorption time.*

*$Cu^{2+}$* – For what concerns the copper cation, representing the class of heavy metals, there are no relevant differences in the behavior of the three hydrogels, Figure 159. The equilibrium was quickly reached within 5 minutes, smaller improvements were registered during the whole duration of the tests. The recorded adsorption is not either particularly good or bad, probably it is determined by weak electrostatic interaction, reaching after 60 minutes a $Cu^{2+}$ removal of 51-52%.

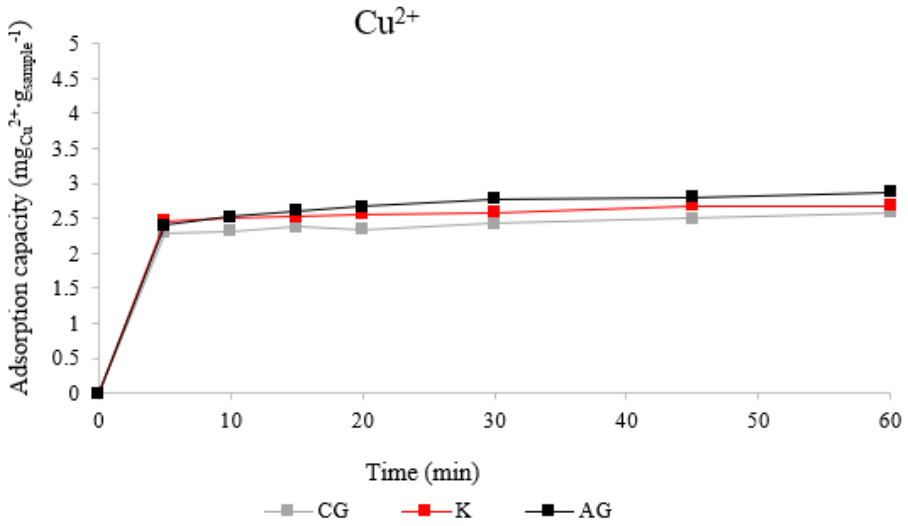


*Figure 159 – $Cu^{2+}$ adsorption test. Adsorption capacity of agarose crosslinked with glutaraldehyde (AG), k-carrageenan (K), and chitosan crosslinked with glutaraldehyde (CG) as function of the adsorption time.*

*Kinetics* – In this case, it was not possible to do any modelling with the rhodamine B data, because of the inactivity of the samples against this pollutant. On the other hand, both methyl

orange and $Cu^{2+}$ adsorption process well fitted the pseudo-second-order kinetic model. In Figure 160 is reported as example the graph of $Cu^{2+}$, $R^2$ values confirms a good interpolation of the linearized form equation. Slope and intercept were used for the kinetic constant calculations, the kinetic constant is reported together with the equilibrium adsorption capacity and $R^2$ values in Table 66, as previously mentioned analyzing the adsorption graph the three samples give similar results. With k-carrageenan, the non-crosslinked structure, showing a slightly faster kinetic, and crosslinked agarose a little better adoptions capacity, but these are lesser speculations.

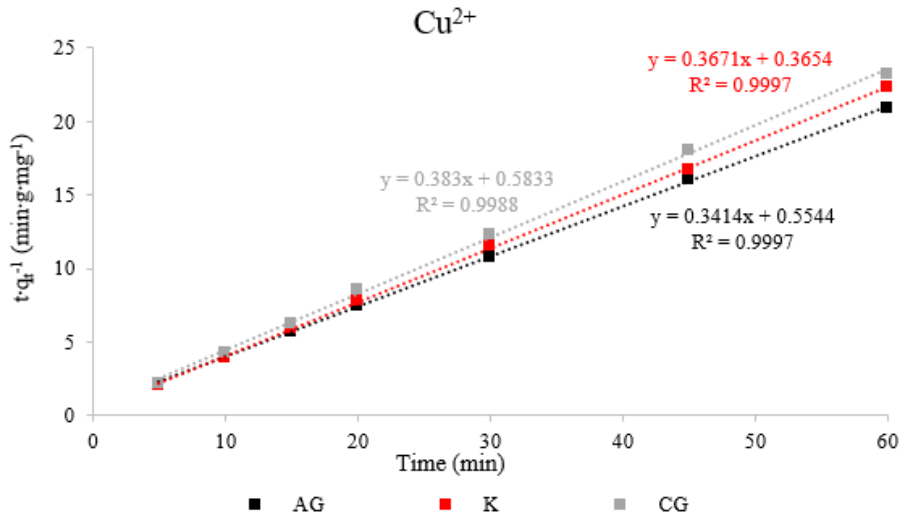


*Figure 160 – $Cu^{2+}$ adsorption test. Linearized pseudo-second-order adsorption graph of agarose crosslinked with glutaraldehyde (AG), k-carrageenan (K), and chitosan crosslinked with glutaraldehyde (CG).*

*Table 66 – Adsorption parameters of $Cu^{2+}$ on the selected biopolymer, extrapolated by the linearized pseudo-second-order graph: coefficient of correlation ($R^2$), equilibrium adsorption capacity ($q_e$), and kinetic constant (k).*

| Sample | $R^2$ | $q_e$ (mg·g$^{-1}$) | k (min·g·mg$^{-1}$) |
|---|---|---|---|
| Agarose + glutaraldehyde | 0.9997 | 2.9 | $2.1 \cdot 10^{-1}$ |
| K-carrageenan | 0.9997 | 2.7 | $3.7 \cdot 10^{-1}$ |
| Chitosan + glutaraldehyde | 0.9988 | 2.6 | $2.5 \cdot 10^{-1}$ |

### 6.2.3. Embedding active phases into biopolymeric scaffolds

In literature biopolymers are implemented for the production of composites with natural clays for the exploitation of their adsorbing properties.[262] With the purpose of studying possible synergistic effects enhancing the adsorption capabilities, the tested active phases were embedded into biopolymeric hydrogels. These composite structures were freeze-dried to improve their handleability, obtaining solid tridimensional light products.

The activities of this phase were focused on the three selected matrixes chitosan and agarose crosslinked with glutaraldehyde and k-carrageenan. They were used to contain bentonite and hydrotalcites (LDH1.4 and LDH2) as adsorbent. A representative image of the full set of samples produced is reported in Figure 161, where it is possible to see the typical adsorbent loaded hydrogel casted into petri dish. As well as for the previous steps, swelling and dissolution tests were used to estimate the stability of the materials, subsequently they were tested in simulated pollutants removal (rhodamine B, methyl orange, and $Cu^{2+}$).

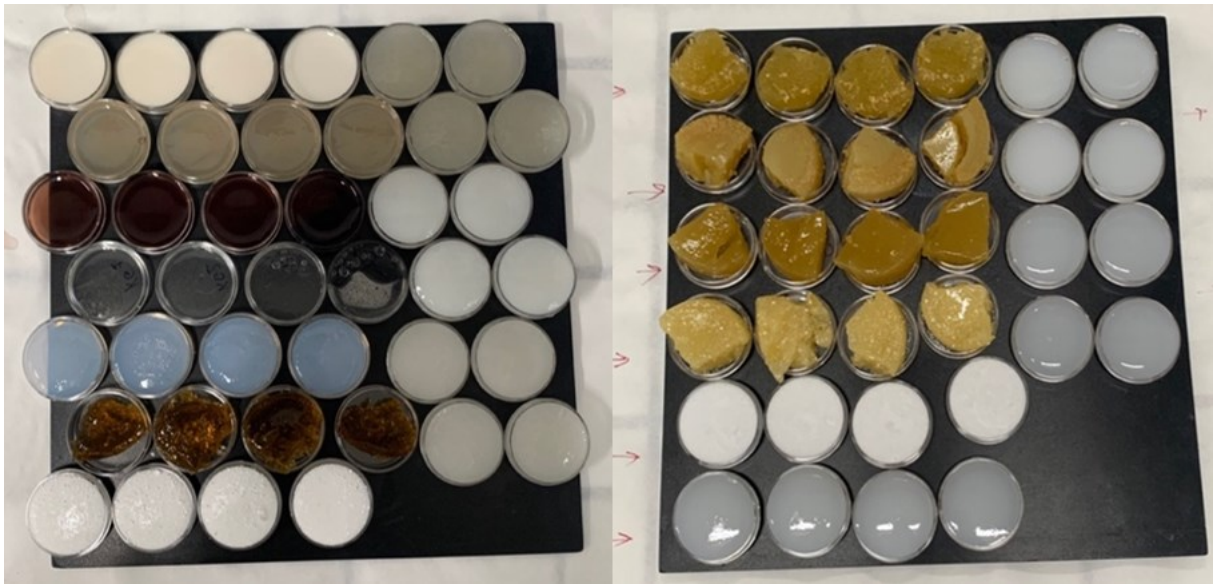

*Figure 161 – Biopolymeric scaffolds made of agarose crosslinked with glutaraldehyde, k-carrageenan, and chitosan crosslinked with glutaraldehyde embedding the selected active phases bentonite and hydrotalcites (LDH2 and LDH1.4).*

***Swelling and dissolution tests*** – As it is possible to see from the data in Table 67, the introduction of inorganic material into the hydrogels structure involves modifications of the swelling behavior. The presence of the inorganic powder dispersed in the biopolymeric network determines a strengthening of the mechanical properties of the material, leading to a lesser deformable lattice, and so implying a lesser water absorption. This reinforcement has consequences also on the stability, where it is possible to observe a reduction of the dissolution.

The only exception is represented by chitosan loaded with hydrotalcites, in this case it was possible to observe macroscopic fragmentation of the gel.

*Table 67 – Swelling and dissolution behavior in water. Comparison of the results of the three selected biopolymeric matrices (agarose crosslinked with glutaraldehyde, k-carrageenan, and chitosan crosslinked with glutaraldehyde) embedding the active adsorbent phases (bentonite and hydrotalcites).*

| Sample | Water absorption ($g_{H2O} \cdot g_{gel}^{-1}$) | Dissolution (%) |
|---|---|---|
| Agarose + glutaraldehyde | 28.0 | 10.1 |
| Agarose + glutaraldehyde + bentonite | 12.76 | 10.97 |
| Agarose + glutaraldehyde + LDH2 | 7.78 | 6.81 |
| Agarose + glutaraldehyde + LDH1.4 | 14.96 | 6.95 |
| K-carrageenan | 18.1 | 15.4 |
| K-carrageenan + bentonite | 20.77 | 13.58 |
| K-carrageenan + LDH2 | 13.48 | 9.34 |
| K-carrageenan + LDH1.4 | 16.64 | 11.45 |
| Chitosan + glutaraldehyde | 26.4 | 8.1 |
| Chitosan + glutaraldehyde + bentonite | 17.82 | 8.19 |
| Chitosan + glutaraldehyde + LDH2 | 15.80 | 29.12 |
| Chitosan + glutaraldehyde + LDH1.4 | 14.40 | 27.71 |

***Adsorption tests*** – The composite materials were tested in the absorption of methyl orange, rhodamine B, and copper cations to evaluate the affinity for positively and negatively charged organic molecules and heavy metal ions, both relevant species studied in the water remediation field.

*Methyl orange* – Based on single components methyl orange removal, it is possible to predict the activity of the composites.

Chitosan was the most active biopolymer with an adsorption capacity of ≈ 8 $mg \cdot g^{-1}$ while the other hydrogels reached values close to 1 $mg \cdot g^{-1}$. Bentonite resulted to be inert, excellent adsorption was registered for LDH1.4 ≈ 40 $mg \cdot g^{-1}$ and only ≈ 5 $mg \cdot g^{-1}$ for LDH2. From these data, the most promising solution should be crosslinked chitosan containing LDH1.4, but from dissolution data, chitosan and hydrotalcites demonstrated to not be well compatible, in fact as it is possible to see from results in Figure 162 chitosan alone displays the best adsorption capacity

with a ≈ 95% methyl orang removal. LDHs loaded chitosan fast reaches saturation at ≈ 3 $mg \cdot g^{-1}$ (82-86% dye removal), while the bentonite (B) composite has a slower process reaching the similar removal, close to ≈ 4 $mg \cdot g^{-1}$ (76% dye removal).

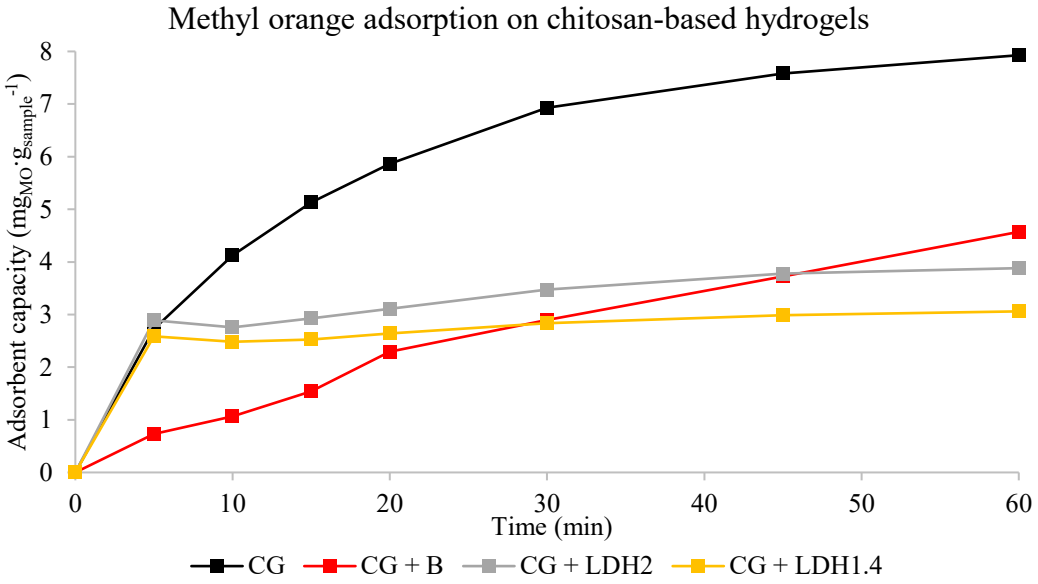


*Figure 162 – Methyl orange adsorption test. Adsorption capacity as function of the adsorption time: chitosan-based hydrogels crosslinked with glutaraldehyde (CG) embedding bentonite (B) or hydrotalcites (LDH2 or LDH1.4).*

For the other two hydrogels, similar behavior is observed, both k-carrageenan (Figure 163) and crosslinked agarose (Figure 164), quickly reached the saturation equilibrium at ≈ 1.5 $mg \cdot g^{-1}$. The addition of the inorganic phases is slow down the process limiting also the adsorbent capacity at values ≤ 1 $mg \cdot g^{-1}$, with the only exception of agarose coupled with LDH1.4 where the process is slower but after 1-hour test demonstrated greater removal respect agarose alone.

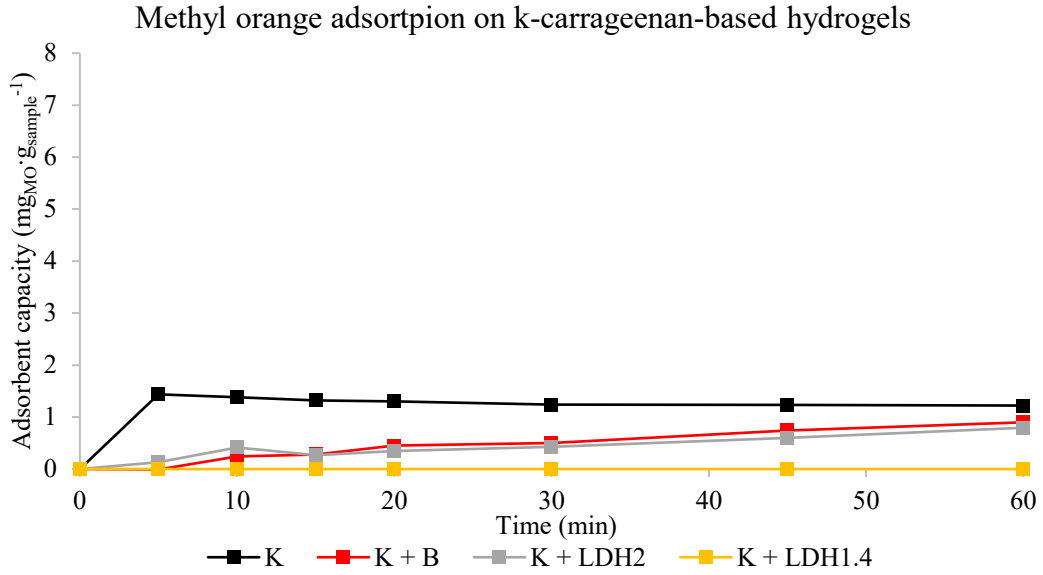


*Figure 163 – Methyl orange adsorption test. Adsorption capacity as function of the adsorption time: k-carrageenan-based hydrogels (K) embedding bentonite (B) or hydrotalcites (LDH2 or LDH1.4).*

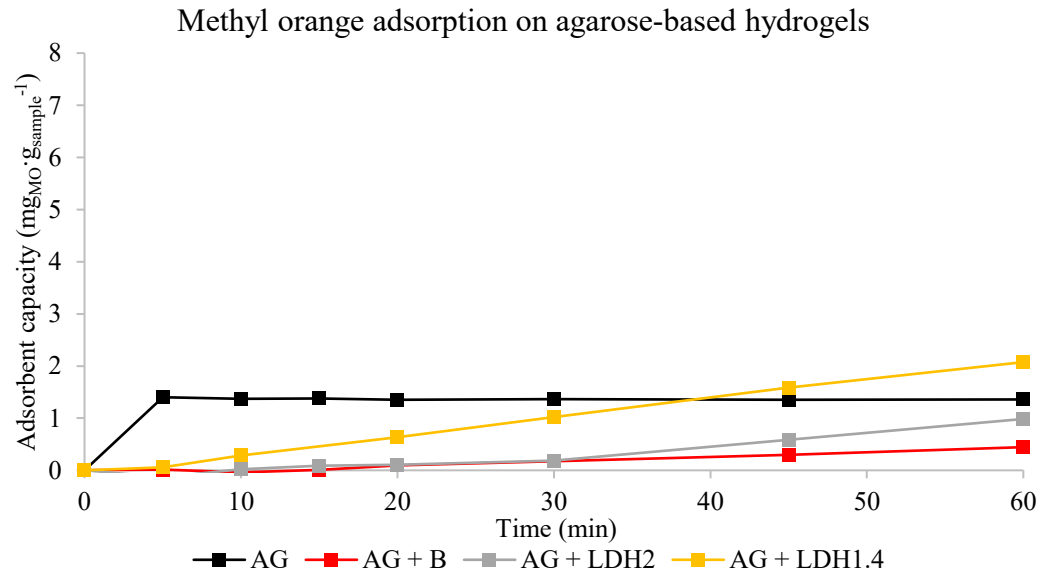


*Figure 164 – Methyl orange adsorption test. Adsorption capacity as function of the adsorption time: agarose-based hydrogels crosslinked with glutaraldehyde (AG) embedding bentonite (B) or hydrotalcites (LDH2 or LDH1.4).*

*Rhodamine B* – Regarding the adsorption of the cationic colorant rhodamine B, it was more difficult to develop composite material with a good efficiency. This is mainly because the biopolymeric matrices do not adsorb rhodamine at all. Even if the active phases had a good adsorption capacity ≈ 6-7 $mg \cdot g^{-1}$, the encapsulation within the hydrogel limit the contact with the pollutant and the available active sites. This determines a negligible activity of the hydrotalcite-loaded scaffolds, with a 0.05 $mg \cdot g^{-1}$ adsorption capacity in the best-case scenario.

Better properties were recorded for the bentonite (B) containing samples, Figure 165, in particular embedded in crosslinked agarose (AG+B) reaching ≈ 2.5 mg·g$^{-1}$, in this case there was a relevant effect of the active phase doping reaching ≈ 56% of dye removal. Lower values were recorded for k-carrageenan (K+B) ≈ 12% and crosslinked chitosan (CG+B) ≈ 6%.

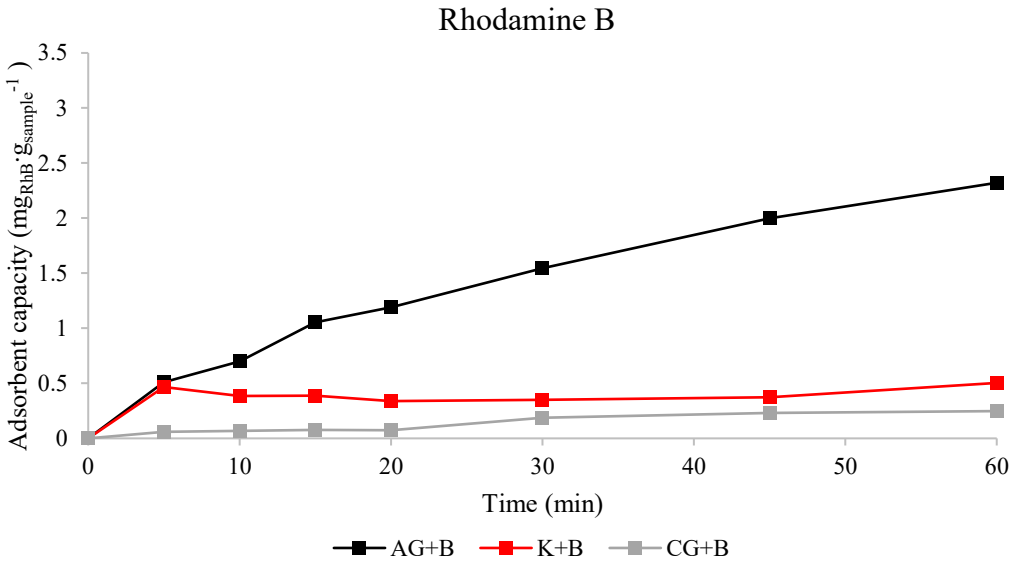


*Figure 165 – Rhodamine b adsorption test. Adsorption capacity as function of the adsorption time: bentonite (B) containing samples embedded into agarose crosslinked with glutaraldehyde (AG), k-carrageenan (K), or chitosan crosslinked with glutaraldehyde (CG).*

*Cu*$^{2+}$ – A minimal detrimental effect was observed in the absorption of the cupric cation determined by the implementation of clays into the hydrogels. The three biopolymers had similar activity ≈ 2.5 mg·g$^{-1}$, while the active phases had the following adsorption capacity at 60 minutes: bentonite 6 mg·g$^{-1}$, LDH1.4 5 mg·g$^{-1}$, and LDH2 3 mg·g$^{-1}$. The composite scaffold activity ranged between 0.7-1.5 mg·g$^{-1}$ in the case of agarose with the best results for the bentonite composite, 0.3-1.2 mg·g$^{-1}$ for chitosan where the LDH2 composite is the most performing, and finally the best scaffold resulted to be the one based on k-carrageenan, with adsorption capacity ranging between 1.8-2.3 mg·g$^{-1}$. K-carrageenan composites results are reported in Figure 166 and reveal a gradual increase of the adsorption capacity until the instauration of the equilibrium only after 60 minutes, with a dye removal comprised between 54-62%.

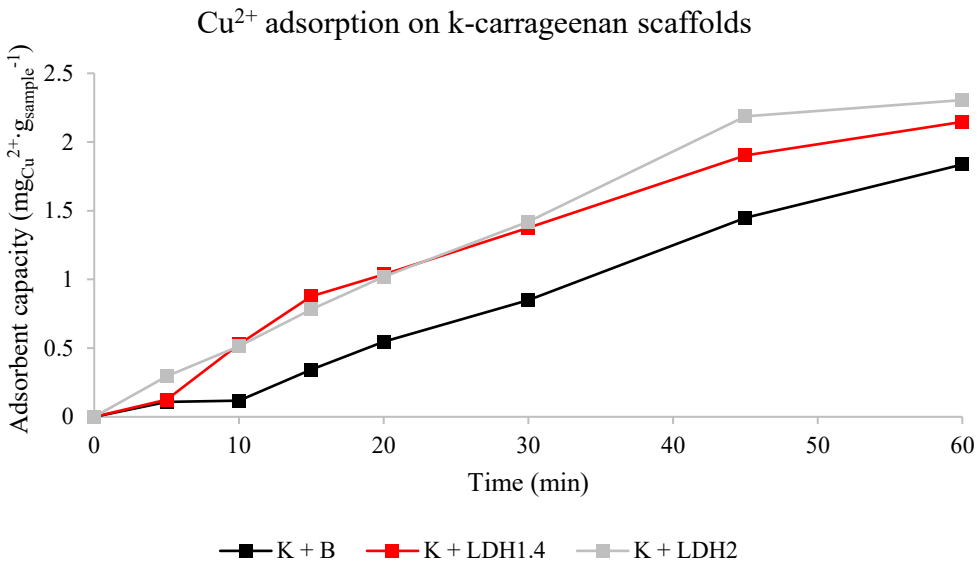


*Figure 166 – $Cu^{2+}$ adsorption test. Adsorption capacity as function of the adsorption time: k-carrageenan-based scaffolds (K) embedding bentonite (B) or hydrotalcites (LDH1.4 or LDH2).*

*Kinetics* – The kinetic modeling of the composite materials resulted in being more difficult with respect the various phases analyzed individually. This is probably due to the structural interferences generated by the presence of an inorganic phase in the hydrogel network, together with the combination of the action of the biopolymer and the active phase. As well as for the previous kinetic studies, the pseudo-first-order model was not reliable and the pseudo-second-order was used. For the abovementioned reasons the scaffolds coefficients of correlation result to be lower respect to the previously reported data of clays and biopolymers. Nevertheless, the process can be properly modeled as a pseudo-second-order kinetic. In Figure 167 it is reported as an example the graph of crosslinked chitosan samples loaded with bentonite (CG+B), LDH2 (CG+LDH2), and LDH1.4 (LDH1.4) applied for the adsorption of methyl orange. Hydrotalcites composites better fitted the linearized plot, while a lower correlation was found for bentonite adsorption.

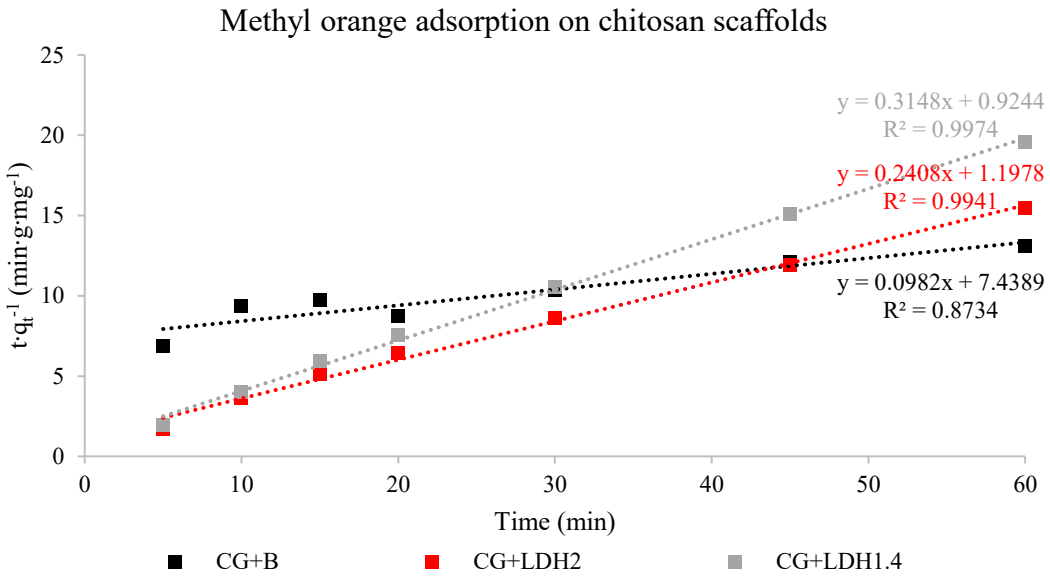


*Figure 167 – Methyl orange adsorption test. Linearized pseudo-second-order adsorption graph of chitosan crosslinked with glutaraldehyde (CG) embedding bentonite (B) or hydrotalcites (LDH2 or LDH1.4).*

The calculated kinetic constant and the equilibrium adsorption capacity are reported in Table 68. The kinetic constant values reflect what it was observed in the adsorption capacity graph in Figure 167. The hydrotalcites doping of the crosslinked chitosan hydrogel led to a faster adsorption kinetic, reaching the equilibrium in the first 5 minutes of the test, while for bentonite it reaches adsorption value close to the equilibrium after 60 minutes. Bentonite composite had the slowest kinetic but the highest adsorption capacity, so for a fast methyl orange removal it is better to apply hydrotalcites composites, while for large quantities removal the bentonite composite is more promising.

*Table 68 – Adsorption parameters of the methyl orange adsorption on chitosan-based scaffolds, extrapolated by the linearized pseudo-second-order graph: coefficient of correlation ($R^2$), equilibrium adsorption capacity ($q_e$), and kinetic constant (k).*

| Sample | $R^2$ | $q_e$ (mg·g$^{-1}$) | k (min·g·mg$^{-1}$) |
|---|---|---|---|
| Chitosan + glutaraldehyde + bentonite | 0.8734 | 10.2 | $1.3 \cdot 10^{-3}$ |
| Chitosan + glutaraldehyde + LDH2 | 0.9941 | 4.2 | $4.8 \cdot 10^{-2}$ |
| Chitosan + glutaraldehyde + LDH1.4 | 0.9974 | 3.2 | $1.1 \cdot 10^{-1}$ |

***Conclusions*** – The performances of the scaffolds tested in the adsorption of methyl orange (MO), rhodamine B (RhB), and $Cu^{2+}$ are graphically summarized in the Table 69. The samples are classified based on the adsorption capacity, labelling excellent performances for an adsorption ≥ 4.5 mg·g$^{-1}$, good 4.4-2-5 mg·g$^{-1}$, limited 2.4-0.5 mg·g$^{-1}$, and bad < 0.5 mg·g$^{-1}$. The

implementation of the inorganic phase into biopolymers network not always improve the product adsorption capacity. The general trend for the adsorption of methyl orange and copper can be described as a loss of performance due to the introduction of clays and hydrotalcites. This could be due to the stiffening of the lattice, limiting the swelling properties and the internal contact with water and pollutants. Different behavior was registered for bentonite loaded scaffolds for the adsorption of rhodamine B, in this case the ion exchange effect brought by the inorganic phase helps the adsorption of the cationic colorant, which is otherwise negligible for the pure biopolymers. Further optimization is required for these composite materials to pave the road of a real-world application for the wastewater remediation.

*Table 69 – Summary of the performance of the selected scaffold in the adsorption of methyl orange, rhodamine b, and $Cu^{2+}$.*

| Sample | Methyl orange | Rhodamine B | $Cu^{2+}$ |
|---|---|---|---|
| Agarose + Glutaraldehyde | ↑ | X | ↑↑ |
| Agarose + Glutaraldehyde + Bentonite | X | ↑ | ↑ |
| Agarose + Glutaraldehyde + LDH1.4 | ↑ | X | ↑ |
| Agarose + Glutaraldehyde + LDH2 | ↑ | X | ↑ |
| Chitosan + Glutaraldehyde | ↑↑↑ | X | ↑↑ |
| Chitosan + Glutaraldehyde + Bentonite | ↑↑ | ↑ | X |
| Chitosan + Glutaraldehyde + LDH1.4 | ↑↑ | X | ↑ |
| Chitosan + Glutaraldehyde + LDH2 | ↑↑ | X | ↑ |
| K-carrageenan + Glutaraldehyde | ↑ | X | ↑↑ |
| K-carrageenan + Glutaraldehyde + Bentonite | ↑ | X | ↑ |
| K-carrageenan + Glutaraldehyde + LDH1.4 | X | X | ↑ |
| K-carrageenan + Glutaraldehyde + LDH2 | ↑ | X | ↑ |

*Labelling: excellent performances for an adsorption ≥ 4.5 $mg \cdot g^{-1}$ (↑↑↑), good 4.4-2-5 $mg \cdot g^{-1}$ (↑↑), limited 2.4-0.5 $mg \cdot g^{-1}$ (↑), and bad < 0.5 $mg \cdot g^{-1}$ (X).*

### 6.2.4. Semi-mobile prototype system for water treatment

Within SOS ACQUA project, funded by the Italian Ministry of Defence, the adsorbent materials previously studied were tested into a semi-mobile prototype system for water treatment. the purpose of the project is to develop a portable device that allows the removal and degradation of water pollutant and meanwhile the production of hydrogen from water splitting. In this work the focus is on the filtering unit, studied to remove heavy metals and organic pollutants.

The population involved in natural disasters, wars, or simply living in remote regions may suffer the lack of drinking water, the implementation of efficient multifunctional filtering units into exploitable devices may bring an important improvement of the quality of life in these extreme conditions. The use of semi-mobile systems may be the perfect solution to gran logistic sustainability, furthermore, the exploitation of efficient natural adsorbent material in the filtering unit increases environmental and economical sustainability of the product.

Here are reported the results of the test in a continuous flow prototype, the filtering unit allows the water recirculation until the desired pollutant removal is obtained, an image of the prototype is reported in Figure 168. A peristaltic pump allows the flow of the polluted water through the filtering unit, entering from the bottom and percolating once filtered, then the outcoming flow is leaded by gravity force and can be either recollected or recirculated into the device.

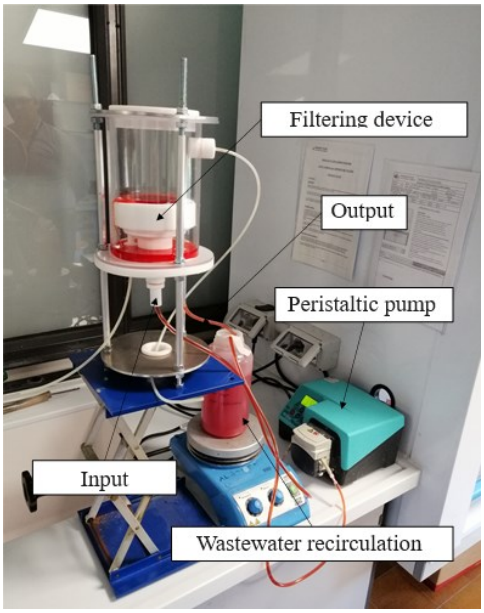


*Figure 168 – Prototype of a semi-mobile continuous flow water-filtering system.*

The filtering unit is composed of the adsorbent materials previously studied. The adsorbents micrometric powder obtained by spray freeze drying or simple granulation processes was confined into filtering capsules using biodegradable and thermally sealable cellulose or a PET

80 mesh net. This solution was used to produce the filtering unit for the desire water treatment device and then tested in the continuous flow apparatus.

***Results and discussion*** – A first screening of the adsorption capacity of $Cu^{2+}$ and $Fe^{3+}$ from a simulated polluted water in batch conditions was assessed. Several samples were tested, mostly clays (montmorillonite, bentonite, kaolin, and several feldspars), hydrotalcites, activated carbon, and microalgae (*Chlorella vulgaris*). The most promising adsorbents for this application were selected: montmorillonite, bentonite, and *C. vulgaris*, these materials displayed a good affinity for both $M^{2+}$ and $M^{3+}$ metal cations.

The first test on the continuous flow apparatus was performed locating in the filtering unit two filters constituted by a PET 80 mesh net, one filled with 10 g of bentonite granules and the other with 10 g of montmorillonite granules. Granules were obtained by producing, crushing, and then sifting (30 mesh) a tablet from the clays powder. 1 L of simulated wastewater ($Cu^{2+}$ 10 $mg \cdot L^{-1}$, $Fe^{3+}$ 10 $mg \cdot L^{-1}$, and methyl orange 50 $mg \cdot L^{-1}$) under 600 rpm magnetic stirring was treated, pumping speed 55 rpm that correspond to ≈ 50 $mL \cdot min^{-1}$. Periodic aliquots were withdrawn and methyl orange content was analyzed by UV-Vis, while metal cations concentration was assessed by ICP-OES.

Heavy metals removal is reported in Figure 169, the adsorption is fast, after 30 minutes 70% of the copper and 100% of the iron are removed. After 2 hours the concentration of both metals is negligible. Similar results to free powder in batch tests are obtained with the major difference of the time required for the quantitative abatement of the pollutants content, in that case these values were obtained in few minutes. The change in the configuration and the form of the adsorbent impact the kinetic of the process. Granules have a reduced surface area available respect to the powder. To test the saturation of the adsorbents, after 180 minutes pollutants were refilled, $Cu^{2+}$ 3 $mg \cdot L^{-1}$, $Fe^{3+}$ 10 $mg \cdot L^{-1}$, and methyl orange 50 $mg \cdot L^{-1}$. As it is possible to see in the graph in Figure 169 adsorbent filters were not saturated yet and similar 60 minutes removal were obtained. In Figure 170 is reported the adsorption capacity calculated as total heavy metal adsorbed or specific for iron and copper. The cumulated adsorbent capacity of montmorillonite and bentonite against copper and iron results to be 1.9 $mg \cdot L^{-1}$ after the first test and 3.1 $mg \cdot L^{-1}$ after the pollutants refill.

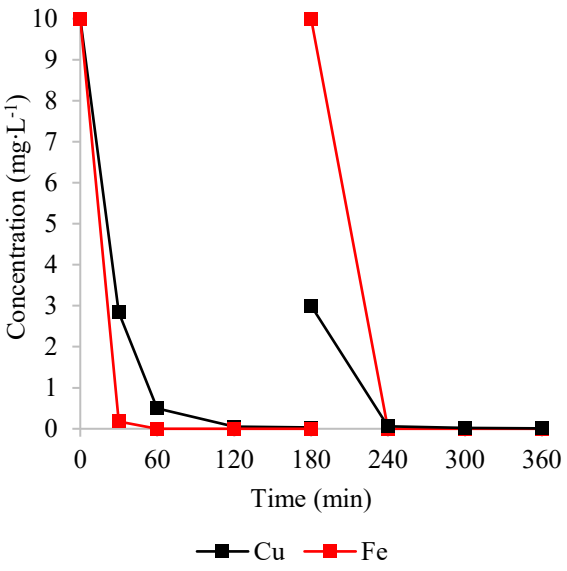


*Figure 169 – Heavy metals adsorption test. Copper and iron residual concentration during the adsorption test in the continuous flow filtering system with recirculation of the filtered water. After 180 minutes the copper and iron were reintegrated in the wastewater flow.*

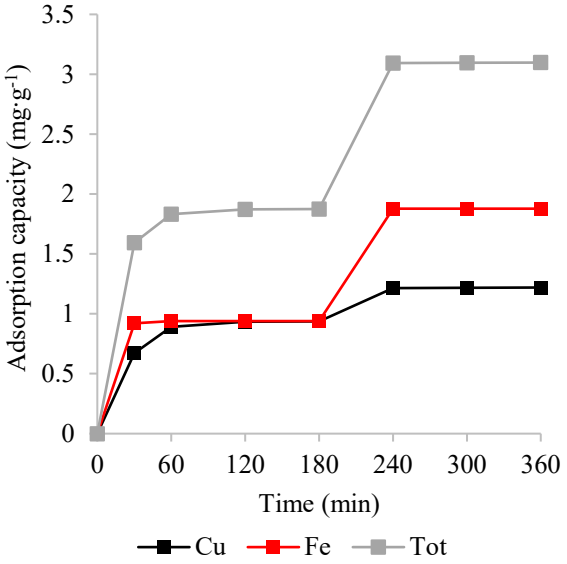


*Figure 170 – Heavy metals adsorption test. Adsorption capacity of copper, iron, and total metals during the adsorption test in the continuous flow filtering system with recirculation of the filtered water. After 180 minutes the copper and iron were reintegrated in the wastewater flow.*

Similar considerations may be proposed for the removal of the anionic dye methyl orange (MO), Figure 171. The instauration of the equilibrium at ≈ 93% dye removal is slower respect using free powders as adsorbing agents, ≈ 2 hours are required. Even the colorant was refilled after 180 minutes, in this case the second phase was significantly slower, indicating a situation closer

to the saturation respect the starting point, after additional 3 hours treatment the dye removal reaches 81%. The slower kinetic requires longer exposure time to reach the new equilibrium.

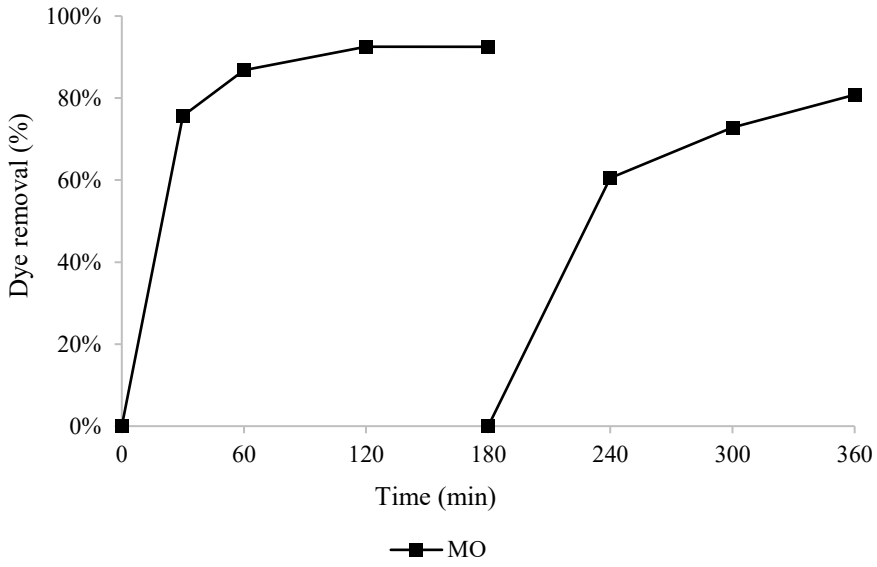


*Figure 171 – Methyl orange adsorption test. Dye removal during the adsorption test in the continuous flow filtering system with recirculation of the filtered water. After 180 minutes the methyl orange was reintegrated in the wastewater flow.*

A new configuration was tested, of bentonite and hydrotalcite Pural MG70 in a weight ratio 70:30 were dried at 70 °C for 1 hour, then converted into a pellet using a 30 $kg \cdot cm^{-2}$ linear press. The capsules were grinded and the 400-500 μm was isolated. Subsequently, 10 g granules were inserted in 2 cellulose-based capsules, 5 g each, Figure 172.

*Figure 172 – Cellulose-based capsule containing bentonite-hydrotalcite Pural MG70 (weight ratio 70:30) grinded pellets.*

These capsules were used as filtering unit in the continuous flow testing system. To evaluate the reusability of the product and to separate the different pollutants adsorption, five different cycles of the duration of 300 minutes each on the same capsules were tested:

1. 500 mL of 50 $mg \cdot L^{-1}$ methyl orange.
2. 500 mL of 50 $mg \cdot L^{-1}$ $Cu^{2+}$ and 50 $mg \cdot L^{-1}$ $Fe^{3+}$.
3. 500 mL of 50 $mg \cdot L^{-1}$ methyl orange.
4. 500 mL of 50 $mg \cdot L^{-1}$ $Cu^{2+}$ and 50 $mg \cdot L^{-1}$ $Fe^{3+}$.
5. 500 mL dichlorodiphenyldichloroethylene (DDE) 1.051 $mg \cdot L^{-1}$.

Between on cycle and the following one, the capsule was rinsed with water and dried at 70 °C. The other experimental conditions were preserved.

The collected results revealed that the first cycle involves the adsorption of 90% of the methyl orange, aligned with previous data. During the second cycle 100% iron and 86% copper removal were registered. The third cycle once again against methyl orange demonstrate even a higher activity removing 98% of the dye. The fourth cycle shows a limited copper removal 64% and 100% for iron. Trivalent cations are adsorbed in a stronger way respect to bivalent cations due to the higher charge density and consequent stronger electrostatic interactions and favorable ion exchange. Finally, the fifth cycle is against DDE, the filtering unit resulted efficient even against this pollutant representing the pesticides family, with a 90% removal. The sample tested revealed excellent adsorption capacity and reusability potential. In fact, during all the cycles, the equilibrium was established after ≈ 60 minutes, with only a loss in the copper adsorption during the repeated cycles, preserving the activity against the other pollutants.

After every adsorption cycle and its correlated rinsing and drying process, the capsules weight was monitored to evaluate the sample loss due to eventual dissolution of the granules, images of post treatment capsules are reported in Figure 173. The most important weight loss was registered during the first cycle, where an average 14% loss occurred mostly due to the fine powder remaining after the sifting, the successive cycles involved an average 6% weight loss each. This imply a good stability of the material and a good confinement of the granules within the cellulose films, but improvements could be made in this direction by using granulating agents like polyethylene glycol (PEG).

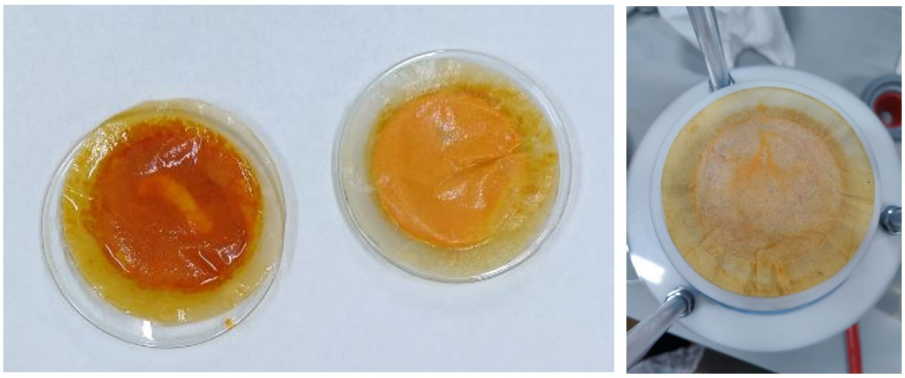

*Figure 173 – Filtering cellulose-based capsules containing the adsorbent phase made of bentonite-hydrotalcites pellets after the adsorption of methyl orange. Wet and dried capsules.*

In general, the capsules developed resulted in a promising solution for the implementation of natural adsorbent phases for the adsorption of wastewater pollutants. Further improvements are due for the development of a semi-mobile prototype which will implement also antimicrobial and hydrogen production features.

Hydrotalcites embedded into biopolymers were tested in the adsorption of methyl orange and rhodamine B in the continuous flow plant. The results reported in Figure 174 confirmed a higher affinity of these materials for the anionic dye methyl orange compared to the cationic counterpart represented by rhodamine B. The overall process is slower than the same materials in a powder form, this is due to the different interactions and diffusion processes required by an embedded material. The adsorption equilibrium was reached after ≈ 8 hours, and the equilibrium adsorption capacity of these scaffolds resulted to be ≈ 15 $mg \cdot g^{-1}$ against methyl orange and ≈ 2 $mg \cdot g^{-1}$ against rhodamine B.

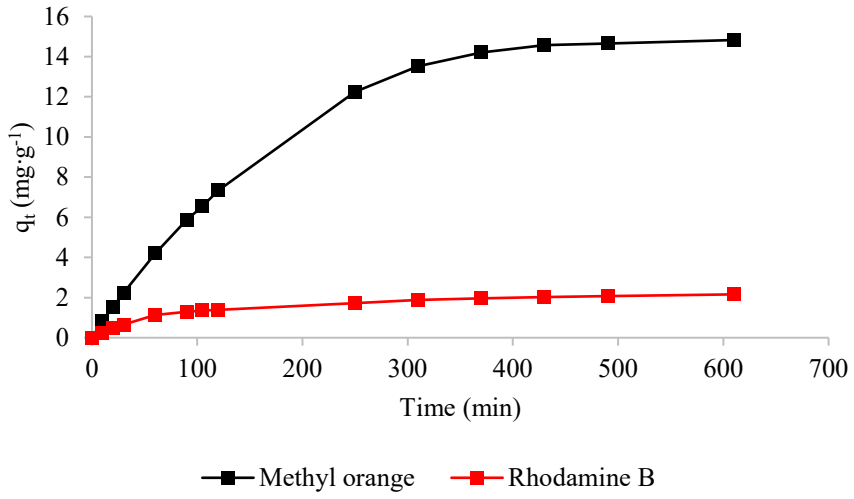


*Figure 174 – Methyl orange and rhodamine b adsorption on hydrotalcites embedded into biopolymers. Adsorption capacity as function of the adsorption time.*

The kinetic modeling fitted relatively well the pseudo-second-order equation, Figure 175.

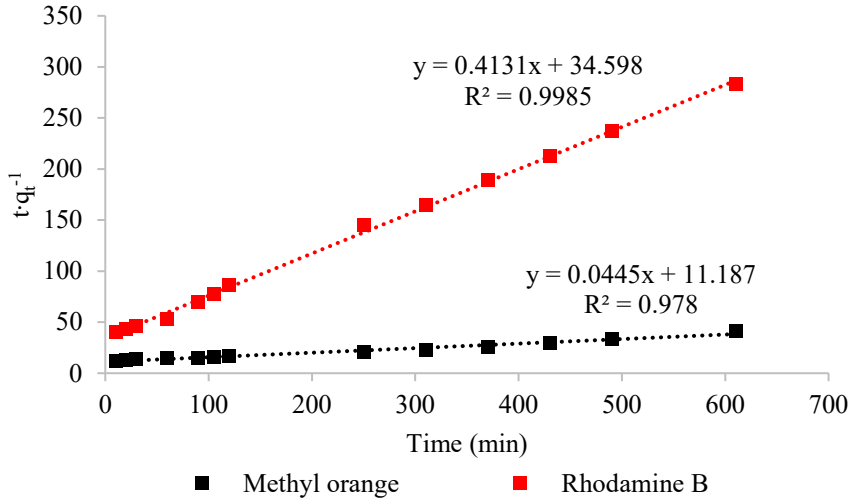


*Figure 175 – Methyl orange and rhodamine b adsorption on hydrotalcites embedded into biopolymers. Linearized pseudo-second-order adsorption graph.*

It was possible to successfully implement the studied adsorbent phases into exploitable product for the production of a filtering device for the treatment of wastewater. The prototype demonstrated good adsorption capability against both heavy metals and organic pollutants. It was possible to modulate the active phase depending on the target pollutant and different embedding solution were proposed for the device development.

The major improvements required regard the stability of the samples, and the time efficiency of the filtration. This topic must me better studied before a possible scale-up of the treatment devices.

### 6.2.5. Microalgae coupled with photocatalytic nanomaterials

In high anthropogenic pressured region heavy metals are one of the most relevant pollutants, due to their persistency they can be bioaccumulated passing through the food chain from the environment to microorganisms and organisms till the human accumulation.[263] Clean water is one the goals set by the United Nations in 2015.[264] The presence of persistent heavy metals in water resources is an obstacle to this goal. In the recent years, bioremediation demonstrated to be a valid alternative for the tertiary industrial wastewater treatment plants.[250] The implementation of algae and microalgae in this field represents a huge opportunity, because of the strong affinity for metals algae can be efficiently exploited for the heavy metal biosorption. Furthermore, abundance, availability, cost-effectiveness, and functional properties of these compounds make them a promising solution to be applied in the wastewater remediation.[265]

*Chlorella vulgaris* microalgae represent one interesting candidate for this role, in fact several studies demonstrated it heavy metals biosorption capability, exploiting the functional groups constituting the external layer of the cell wall.[266,267,268]

On the other side, titanium dioxide is one of the most known photocatalytic materials, it the last decades it has been widely studied, and its photoactivity has been enhanced to increase the organic pollutants photodegradation efficiency. One of the proposed solutions involves the production of a nanostructured composite based on silicon dioxide and titanium dioxide, obtaining a boost of the photocatalytic activity of the raw material.[228,268,269,270]

The successful coupling the inorganic photocatalytic phase with the bio-sorbent algal biomass would lead to the production of a multifunctional hybrid material for wastewater treatment, able to abate both organic pollutant and heavy metals content. In this work the spray freeze drying technique was implemented for the production of hybrid nanostructured material constituted by an inorganic matrix of silicon dioxide-titanium dioxide composite material functionalized with *C. vulgaris* biomass. The obtained products were tested in the adsorption of $Cu^{2+}$ and the photodegradation of rhodamine B.[268]

***Results and discussion*** – First, bi-component samples were studied, *C. vulgaris* was used as doping agent for $TiO_2$. A wide range of *C. vulgaris* concentration was tested, from 0.01 to 9 %wt. These materials were characterized, from both physicochemical and functional perspective, then best performing compositions were selected for the production of the tri-component materials, using as inorganic matrix a $TiO_2$-$SiO_2$ composite in a weight ratio 1:3. Here is reported the study of the 0.06 %wt load of *C. vulgaris*, resulted to be the most promising

material developed: TC-0.06 (titanium dioxide-*C. vulgaris*) and TSC-0.06 (titanium dioxide-silicon dioxide-*C. vulgaris*).

***Colloidal hetero-coagulation*** – Zeta potential titration as function of the pH were used to determine the electric charge surrounding the algae cells and the inorganic phase nanoparticles. In this way it was possible to predict if the hetero-coagulation of the two suspended phases is possible. The results reported in Figure 176 revealed a negative charge in the whole range of pH explored for *C. vulgaris* biomass, with an isoelectric point at ≈ 1.4 unit of pH. The negative zeta potential, close to -30 mV at pH 7 is due to the negatively charged functional groups on the cell wall of the algae, they are also responsible for the adsorption of heavy metal cations. An opposite behavior is registered for the titanium dioxide nanoparticles, the inorganic phase is positively charged at acidic pH, with an isoelectric point at ≈ 6.5. The opposite surface charge of the two phases helps in the hetero-coagulation of the product. The hybrid sample TC-0.06 titration curve is also reported, even if the biomass load is only 0.06 %wt it is possible to observe how impactful it is to the zeta potential of the hybrid material. The trend is nearly superimposable to the one of *C. vulgaris*, with an isoelectric point at 1.8 unit of pH.

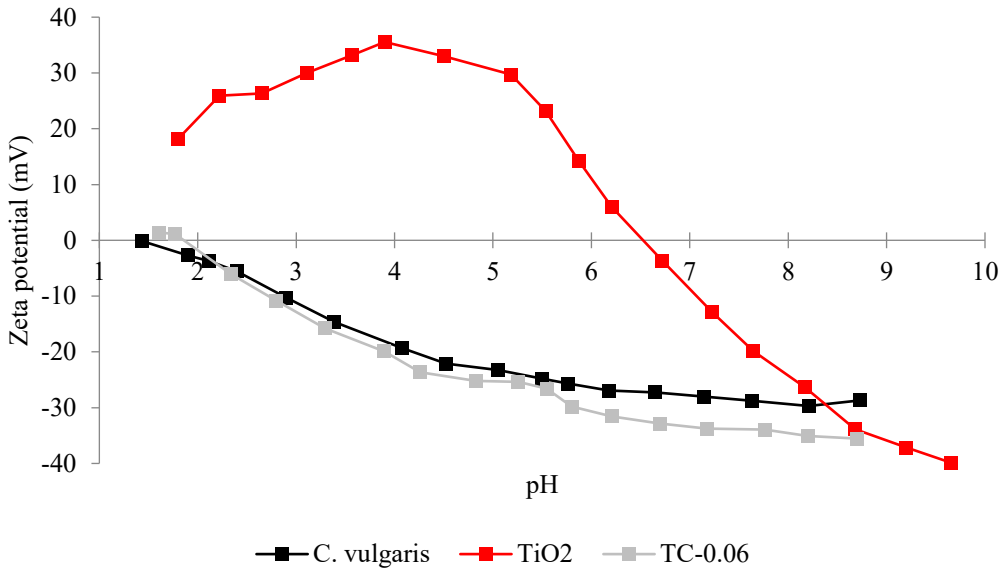


*Figure 176 – Zeta potential titration as function of the pH of Chlorella vulgaris microalgae, titanium dioxide suspension, and the hybrid sample TC-0.06.*

***Physicochemical characterization*** – The commercial $TiO_2$ nanopowder used had a specific surface area of 46 $m^2 \cdot g^{-1}$. BET analysis was repeated on the spray freeze-dried granulated powders, obtaining the following results: $TiO_2$-SFD 63 $m^2 \cdot g^{-1}$, $SiO_2$-SFD 203 $m^2 \cdot g^{-1}$, $TiO_2$-$SiO_2$-

SFD 223 $m^2 \cdot g^{-1}$ (Table 70). Specific surface area is an extremely important parameter in photodegradation processes, in fact, higher surface determines a higher photocatalytic activity exposing a larger quantity of active sites for the production of reactive oxygen species (ROS). The granulation and in particular the composite with silicon dioxide enormously increment the specific surface area of titanium dioxide. Introducing micrometric sized unicellular biomass may hinder part of the nanostructure reducing the available active sites for the photocatalysis. *C. vulgaris* microalgae had an average diameter of 3.8 ± 0.1 µm measured by optical microscopy, but its minimal content in the hybrid material only marginally affected the BET results: TC-0.06 39 $m^2 \cdot g^{-1}$ and TSC-0.06 169 $m^2 \cdot g^{-1}$ (Table 70). From the FESEM images reported in Figure 177 it is possible to see *C. vulgaris* cells embedded into the inorganic nanostructured matrix. Granules obtained by spray freeze drying granulation are characterized by micrometric size in the range 1-100 µm, with the most populated fraction at 20-30 µm, and a nanostructured skeleton. The production of the composite material with silicon dioxide or the hybrid material with C. vulgaris had a lesser influence on the band gap value of titanium dioxide, Table 70. In fact, for $TiO_2$ 3.17 eV band gap value was registered while for the other sample a minimal increase was registered, maximum till 3.21 eV. This confirming that eventual variation of the photocatalytic activity, positive for silicon dioxide and negative for *C. vulgaris*, are not related to this parameter. But are more likely to be determined by the different surface available for the ROS production.

*Table 70 – Specific surface area and band gap of the tested samples. Comparison between the pristine inorganic phases and the hybrid materials containing the C. vulgaris microalgae.*

| Sample | Components | Specific surface area ($m^2 \cdot g^{-1}$) | Band gap (eV) |
|---|---|---|---|
| $TiO_2$ | $TiO_2$ | 46 | 3.17 |
| $TiO_2$-SFD | $TiO_2$ | 63 | / |
| $SiO_2$-SFD | $SiO_2$ | 203 | / |
| $TiO_2$- $SiO_2$-SFD | $TiO_2$-$SiO_2$ | 223 | 3.19 |
| TC-0.06 | $TiO_2$-*C. vulgaris* | 39 | 3.21 |
| TSC-0.06 | $TiO_2$- $SiO_2$-*C. vulgaris* | 169 | 3.21 |

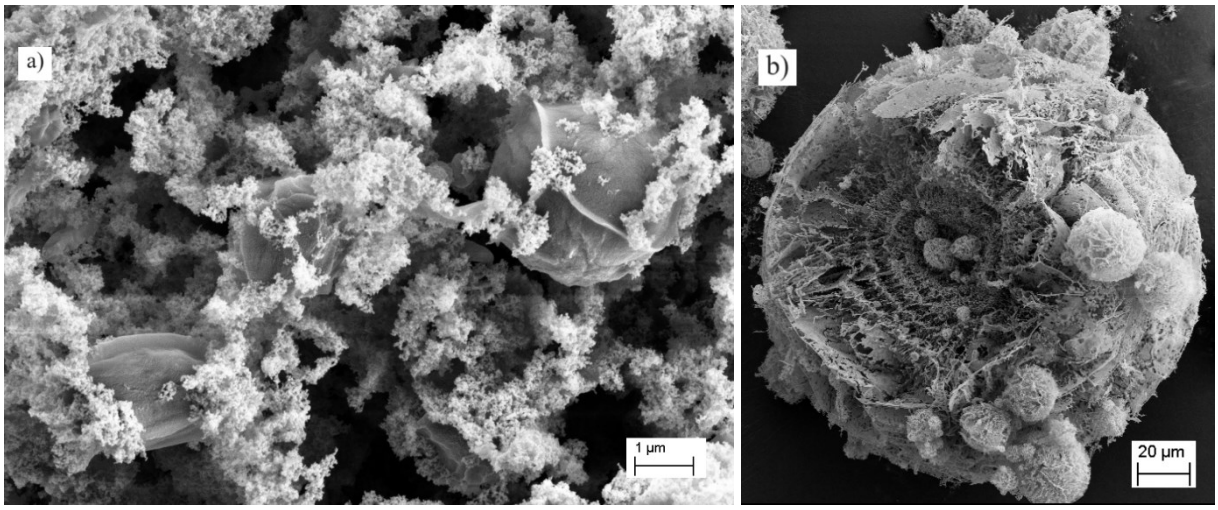


*Figure 177 – FESEM images of a) TC-0.06 (titanium dioxide and C. vulgaris) and b) STC-0.06 (titanium dioxide, silicon dioxide, and C. vulgaris) samples.*

***Adsorption tests*** – The samples were tested in the adsorption of $Cu^{2+}$ from a 10 $mg \cdot L^{-1}$ $CuCl_2$ solution, results are summarized in Table 71. Raw materials adsorption capacity was first assessed, from the results it was possible to determine that only *C. vulgaris* showed excellent $Cu^{2+}$ adsorption capacity 103 $mg \cdot g^{-1}$, while the inorganic phases had negligible activity, $TiO_2$ 0.33 $mg \cdot g^{-1}$ and $SiO_2$ 0.32 $mg \cdot g^{-1}$. The dispersion of the biomass on the inorganic structure obtained in samples TC-0.06 and TSC-0.06 led to an important improvement of the adsorption capacity even with a minimal load of algae (0.06 %wt). TC-0.06 reached a $Cu^{2+}$ adsorption of 3.00 $mg \cdot g^{-1}$ and TSC-0.06 2.86 $mg \cdot g^{-1}$. The importance of this result is even more clear if the adsorption values of the composite materials are compared with the theoretical adsorption calculated based the weighted average of the adsorption of the constituting elements. TC-0.06 should be 0.39 $mg \cdot g^{-1}$ and TSC-0.06 0.38 $mg \cdot g^{-1}$, there is an improvement of one order of magnitude determined by synergistic effects of dispersion *C. vulgaris* cells on the inorganic matrix. Excluding the matrix contribute, the algae specific adsorption of composite materials is estimated to be 4460 $mg \cdot g^{-1}$ for TC-0.06 and 4050 $mg \cdot g^{-1}$ for TSC-0.06, confirming the one order of magnitude improvement respect to the simple suspension of algae cells 103 $mg \cdot g^{-1}$. Cells dispersion on the inorganic substrate may play a crucial role in this synergy, exposing a larger cell surface to the external environment it is possible to better exploit all the adsorbent functionalities of the algae.

*Table 71 – Adsorption capacity of the pristine raw materials compared to the hybrid products. the results are expressed as experimental adsorption capacity of the sample, theoretical adsorption capacity calculated on the basis of the sample composition, and the calculated C. vulgaris specific contribution in the adsorption within the hybrid material.*

| Sample | Components | Adsorption capacity ($mg \cdot g^{-1}$) | Theoretical adsorption capacity ($mg \cdot g^{-1}$) | *C. vulgaris* adsorption capacity ($mg \cdot g^{-1}$) |
|---|---|---|---|---|
| *C. vulgaris* | *C. vulgaris* | 103 | / | / |
| $TiO_2$ | $TiO_2$ | 0.33 | / | / |
| $SiO_2$ | $SiO_2$ | 0.32 | / | / |
| TC-0.06 | $TiO_2$-*C. vulgaris* | 3.00 | 0.39 | 4460 |
| TSC-0.06 | $TiO_2$- $SiO_2$-*C. vulgaris* | 2.86 | 0.38 | 4050 |

***Photocatalytic tests*** – Samples were tested in the photodegradation of rhodamine B (RhB), an organic dye used as probe molecule. The kinetic of the process can be modeled as a pseudo-first-order reaction. The photocatalytic activity comparison was performed on the base of kinetic constant and conversion of the degradation process, monitored via UV-Vis spectroscopy analyzing the maximum absorption of RhB at 554 nm, results are reported in Table 72. $TiO_2$ P25 is a well-known photocatalyst, and the kinetic constant of its granulated powder was calculated to be $8.70 \cdot 10^{-2}$ $min^{-1}$, granting a 99% degradation during the 60 minutes test. As expected the silicon dioxide-titanium dioxide composite enhanced the photocatalytic activity of the material with a kinetic constant of $9.45 \cdot 10^{-2}$ $min^{-1}$ and a quantitative conversion (100%) at 60 minutes. As suspected, the introduction of algae cells on the photocatalyst surface is an obstacle for the light irradiation and the production of reactive oxygen species, slowing down the photodegradation process in the case of TC-0.06 with a kinetic constant of $2.44 \cdot 10^{-2}$ $min^{-1}$ and a 60 minutes conversion of 92%. It is different the case for the tri-component material TSC-0.06 where the boost granted by the composite inorganic matrix is enough to preserve an excellent photocatalytic activity, kinetic constant $10.62 \cdot 10^{-2}$ $min^{-1}$ and a 100% 60 minutes conversion.

*Table 72 – Photocatalytic performance of the samples expressed as kinetic constant of the process and the rhodamine b degradation after 60 minutes of irradiation.*

| Sample | Components | $k \cdot 10^{-2}$ ($min^{-1}$) | Conversion at 60 min (%) |
|---|---|---|---|
| $TiO_2$ | $TiO_2$ | 8.70 | 99 |
| $TiO_2$-$SiO_2$ | $TiO_2$-$SiO_2$ | 9.45 | 100 |
| TC-0.06 | $TiO_2$-*C. vulgaris* | 2.44 | 92 |
| TSC-0.06 | $TiO_2$- $SiO_2$-*C. vulgaris* | 10.62 | 100 |

***Conclusions*** – During this work it was possible to produce a novel hybrid material based on an inorganic composite matrix of titanium dioxide and silicon dioxide mixed with *Chlorella vulgaris* microalgae. The photocatalytic activity of the inorganic matrix was exploited for the photodegradation of organic pollutants, while the algal biomass was used for the biosorption of heavy metals. The materials were prepared via colloidal hetero-coagulation process exploiting opposite charged surfaces for the auto-assembly of the hybrid phase. Subsequently, a granulated powder was obtained by means of spray freeze drying process. The best performing sample TSC-0.06 demonstrated excellent photocatalytic activity, better than $TiO_2$ P25, and at the same time a reliable adsorption capacity. The synergistic effect of dispersion of *C. vulgaris* on the inorganic surface allowed the preservation of the photocatalytic activity, enhancing the specific algae biosorption capacity of one order of magnitude. The possibility to exploit algal biomass and the synergistic coupling of two wastewater remediation functionalities make this material an interesting sustainable solution to be implemented in water treatment devices and plants.

## 6.3. Conclusions

The increasing need of drinking water and the expansion of rural and industrial human activities make it vital to improve the available wastewater treatments. The exploitation of natural and renewable resources like biopolymers, clays, and microalgae it is one of the ways proposed to reach these targets.

The study here reported aimed the development of material and devices exploitable in the water remediation field. The production of stable, durable, and handleable composite materials was studied in order to fight the water pollution related to heavy metals and organic pollutants.

Three gelling biopolymers were selected for the production of the scaffolds with different functional groups available, namely chitosan (-OH, $-NH_2$), agarose (-OH), and k-carrageenan ($-SO_3^-$). These hydrogels were loaded with bentonite, a phyllosilicate with exchangeable cations in the interlayer, or magnesium-aluminum hydrotalcites, in molar ratio $M^{2+}/M^{3+}$ 1.4 and 2, anion exchange materials. Raw material and the final composite scaffolds were tested in the adsorption of simulated pollutant: $Cu^{2+}$ representing heavy metals, and rhodamine B and methyl orange representing respectively positively and negatively charged organic pollutants. Bentonite and hydrotalcites ion exchange properties were exploited together with the electrostatic interaction generated by biopolymers functional groups for the pollutant's removal. The experimental data demonstrated that the introduction of an inorganic phase in the hydrogel increased the mechanical stability reducing the water dissolution of the biopolymer, at the expenses of a reduction in the adsorbent capacity. A more rigid structure resulted less permeable to water limiting the adsorption activity.

Bentonite demonstrate a higher affinity for rhodamine B thanks to the cations exchange, hydrotalcites for methyl orange due to the anion exchange. The most promising hydrogel composition were selected based on their stability, which were chitosan crosslinked with glutaraldehyde, k-carrageenan, and agarose crosslinked with glutaraldehyde. These biopolymers were used as matrixes for the production of the scaffolds implementing the active phases. Tests revealed how the improved handleability of the scaffolds pays the price in a limited adsorption activity of the active phases, which are confined in the biopolymer networks. Finally, the adsorption kinetics were successfully fitted into pseudo-second-order model.

Granulated adsorbent materials were successfully implemented as filtering unit into a semi-mobile water treatment prototype. The results pointed out a good efficacy and reusability of these products, resulting to be a promising solution in the wastewater remediation field.

Furthermore, *Chlorella vulgaris* microalgae was coupled with titanium dioxide-silicon dioxide inorganic matrix to exploit synergist effects generated by the dispersion of the algae cells on the inorganic matrix. In this way it was possible to enhance the heavy metals biosorption ability of *C. vulgaris* preserving an excellent photocatalytic activity of the inorganic matrix in the degradation of organic pollutants.[268]

The different class of composite materials tested represent an interesting solution for the water remediation treatments, but the technology must be improved to enhance the stability of the composites and preserve the adsorption activity of the embedded phases, possibly establishing synergistic effects in the scaffolds.

## 6.4. Experimental part

***Production of the biopolymeric scaffolds*** – Chitosan, agarose and k-carrageenan from Sigma-Aldrich were used for the production of the scaffolds. Biopolymers' raw material are three white powders. The product development is based on three steps, each of which is represented by a product: hydrogels, crosslinked hydrogels, biopolymeric scaffolds embedding the active phases. The experimental procedure for their production is:

- Hydrogel. A typical biopolymeric hydrogel is prepared by dispersing 1 g of the biopolymer into 49 g of Milli-Q water (chitosan must be dispersed in 2 %wt acetic acid) by magnetic stirring obtaining a concentration of 2 %wt, the product is heated up to 80 °C, this temperature is maintained for 20 minutes. Then the product is cast into the desired molds, usually petri dish (3 cm diameter and 1 cm height), cooled at room temperature observing an increment of viscosity. Subsequently, the product is frozen and finally lyophilized for at least 48 hours.
- Crosslinked hydrogel. Crosslinked products are obtained following a similar procedure as hydrogels. Typically, 1 g of biopolymer is dispersed into 48.82 g of Milli-Q water (chitosan must be dispersed in 2 %wt acetic acid) by magnetic stirring obtaining a concentration of 2 %wt, the product is heated up to 80 °C, 180 µL of 50%wt glutaraldehyde solution are added as crosslinker, the temperature is maintained for 20 minutes. Then the product is casted into the desired molds, usually petri dish (3 cm diameter and 1 cm height), cooled at room temperature observing an increment of viscosity. Subsequently, the product is frozen and finally lyophilized for at least 48 hours.
- Biopolymeric scaffolds embedding the active phases. A typical scaffold is produced by dispersing 1 g of biopolymer into 48.32 g of Milli-Q water (chitosan must be dispersed in 2 %wt acetic acid) by magnetic stirring obtaining a concentration of 2 %wt. 0.5 g of adsorbent active phase (either bentonite or hydrotalcites) are added to the suspension. The product is heated up to 80 °C, when the crosslinking is required 180 µL of 50%wt glutaraldehyde solution are added, the temperature is maintained for 20 minutes. Then the product is casted into the desired molds, usually petri dish (3 cm diameter and 1 cm height), cooled at room temperature observing an increment of viscosity. Subsequently, the product is frozen and finally lyophilized for at least 48 hours.

***Production of the microalgae-titanium dioxide composite*** – For this study titanium dioxide nanopowder (Aeroxide®P25, Evonik) and silica nanosol (Ludox HS-40, Grace Davison) were

used for the production of the inorganic porous matrix. *Chlorella vulgaris* microalgae (Micoperi Blue Growth, Italy) was used as 0.18 $g \cdot L^{-1}$, directly frozen once extracted from the bioreactor.

- *Colloidal hetero-coagulation* – The typical colloidal hetero-coagulation process involves the dripping of the inorganic suspension into the algae suspension. Typical parameters are: total volume 100 mL and solid concentration 3 %wt. The algae weight fraction respect to the inorganic phase explored ranged from 0.01 to 9 %wt, the best compromise was found at 0.06 %wt. The inorganic phase was constituted by $TiO_2$ or $TiO_2$-$SiO_2$ in weight ratio 1:3. $TiO_2$-$SiO_2$ was prepared by previously treating $SiO_2$ with a cation exchange resin (Dowex 50 WX8 20–50, LennTech) to adjust the pH from 9.7 to 4, then the oxides mix was treated by ball-milling for 24 hours. Finally, the suspension containing both microalgae and the inorganic phase was gently mixed for 24 hours, then granulated by spray freeze drying.
- *Spray freeze drying* – Highly porous micrometric granulated powders were produced starting from nanosols by spray freeze drying using a lab-scale apparatus (Labscale Granulator LS-2, Powder Pro). The suspension was atomized through a 100 μm nozzle and nebulized into a stirred liquid nitrogen, the suspension flow is regulated by a peristaltic pump, and the spray is assisted by nitrogen gas at 0.4 bar. Droplets are instantly frozen and then freeze-dried thanks to LYO GT 2, SRK System Technik lyophilized working at 0.15 mbar and a -1 ◦C for 48 h.

***Materials characterization*** – Here are reported the physicochemical characterization procedures of the raw materials and products.

*X-ray diffraction spectroscopy* – Bentonite and hydrotalcites powders x-ray diffraction spectra were collected with a Bruker D8 Advance (Cu Kα 1.5406 Å). Working conditions: 2θ interval 5-80°, step 0.04°, step time 0.5 s.

*Specific surface area* – The specific surface area was determined via nitrogen physisorption using single point BET analysis method. For clays and hydrotalcites the instrument used is the Thermo Scientific Surfer and o eliminated possible humidity residual, samples were thermally pretreated at 100 °C for 2 hours in vacuum. In the case of the photocatalytic titanium dioxide composites with *C. vulgaris* Sorpty 1750 CE instruments apparatus was used, pretreating samples at 120 °C in vacuum for 2 hours.

*Zeta potential titration* – The determination of the isoelectric point (IEP), the pH value that correspond to 0 mV zeta potential, was assessed by electrophoretic light scattering analysis thanks to the Zetasizer Nano ZSP (Malvern Panalytical) equipped with MPT-2 multipurpose titrator and vacuum degasser accessories. The instrument operates with an incident laser characterized by a wavelength of 633 nm and it detects the back-scattered radiation at a working angle of 173 °, in this way multiple scattering problems are avoided or limited. Analyses were conducted at 25 °C, in aqueous media. Thanks to the automatic titrator it was possible to perform zeta potential titration as pH function, to identify the isoelectric point (IEP) and the zeta potential behavior. Titration required about 10 mL of sample and were performed using 0.1 M and 0.01 M HCl for acidic titrations or 0.1 M and 0.01 M NaOH for basic titrations. Microalgae composites were diluted at 0.1–0.5 $g \cdot L^{-1}$. The pH was constantly monitored with the instrument's pH-meter MV 114-SC SEN 0106.

*Scanning electron microscopy* – The morphological analysis of powders was assessed thanks to Field Emission Scanning Electron Microscope, FESEM Carl Zeiss Sigma NTS.

*Optical microscopy* – Microalgae suspension was observed thanks to 3D digital optical microscope (Hirox RH-2000) equipped with a high intensity LED lamp (5700K) and a magnification range of 35–5000x. Particle mean diameter was calculated as average of at least 100 particles.

*Band-gap* – The band gap energy was derived from Tauc plot derived from reflectance spectra collected in the 250–800 nm range by PerkinElmer Lambda 750 spectrophotometer. $BaSO_4$ was used as blank.

***Functional tests*** – The efficacy of the materials was tested in the adsorption of simulated water pollutants. $Cu^{2+}$ represents the class of heavy metals, while methyl orange and rhodamine B colorants represent respectively negative and positive charged organic pollutants. The stability and durability of the samples was tested simulating a real-application scenario in the wastewater remediation field, the tests performed allowed the study of the swelling behavior and the dissolution resistance.

*Hydrogel swelling and dissolution tests* – The swelling, or the volume gain of a solid due to the absorption of a liquid, was evaluated by simple Milli-Q water immersion of the freeze-dried

hydrogel. Higher swelling degree is an indirect information of a higher affinity for water, a largely swelling sample is also likely to have better adsorption capacity due to a better interaction of the targeted pollutants with the biopolymeric chains. The swelling behavior was estimated by water adsorption. The sample is weighted before and after the immersion Milli-Q water for 1 hour. The water absorption is calculated by the equation reported in Equation 15.

$$\text{Water absorption capacity} = \frac{m_{wet} - m_{initial}}{m_{initial}} \qquad \text{Equation 15}$$

The sample is frozen and then freeze-dried for at least 48 hours. Subsequently the final residual mass is weighted and the dissolution degree is calculated as reported in Equation 16.

$$\text{Dissolution (\%)} = \frac{m_{initial} - m_{final}}{m_{initial}} \cdot 100 \qquad \text{Equation 16}$$

*Hydrogel adsorption tests* – The selected simulated pollutants for the adsorption tests are $Cu^{2+}$ as representative of the heavy metals, and methyl orang and rhodamine B colorants representing organic pollutants.

- $Cu^{2+}$ adsorption. The test is performed at 25 °C. 200 mL of 10 mg·L$^{-1}$ $Cu^{2+}$ solution, prepared from $CuCl_2$ salt from Sigma-Aldrich (99% purity), under magnetic stirring (400 rpm powders and 150 rpm hydrogel), are treated with the sample. 3 mL aliquots are taken after 5, 10,15, 20, 30, 45, and 60 minutes. The copper quantification is performed by ICP-OES (Agilent Technologies 5100 ICP-OES mounting an Agilent Tecnologies SPS 3 autosampler). The calibration curve is prepared from Cu ICP standard 1000 10 mg·L$^{-1}$, and it is constituted by the following points: 10, 1, 0.1, and 0.05 10 mg·L$^{-1}$. Both the samples and the calibration curve are acidic digested before the analysis with a 10 %v/v of 65 %wt $HNO_3$ and 30%wt $H_2O_2$. Samples were analyzed in triplicates and the selected copper emission lines are: 213.598, 223.009, 224.700, 324.754, and 327.395 nm.
- Rhodamine B. The test is performed at 25 °C. 170 mL of 7 mg·L$^{-1}$ rhodamine B solution, prepared from rhodamine B powder from Sigma-Aldrich (95% purity), under magnetic stirring (400 rpm powders and 150 rpm hydrogel), are treated with the sample. 3 mL aliquots are taken after 5, 10,15, 20, 30, 45, and 60 minutes. Rhodamine B quantification is performed by UV-Vis absorption spectroscopy analyzing the maximum absorption peak at 554 nm using a Perkin Elmer Lambda 750 spectrophotometer.

- Methyl orange. The test is performed at 25 °C. 100 mL of 20 mg·L$^{-1}$ methyl orange solution, prepared from methyl orange powder from Sigma-Aldrich (88% purity), under magnetic stirring (400 rpm powders and 150 rpm hydrogel), are treated with the sample. 3 mL aliquots are taken after 5, 10,15, 20, 30, 45, and 60 minutes. Methyl orange quantification is performed by UV-Vis absorption spectroscopy analyzing the maximum absorption peak at 464 nm using a Perkin Elmer Lambda 750 spectrophotometer.

The calculation of the concentration of the colorants was performed applying the Lambert-Beer law reported in Equation 17 were A is the absorption, ε the molar absorption coefficient (mol$^{-1}$·L·cm$^{-1}$), b is the length of the optical path (cm), and C the analyte concentration (mol·L$^{-1}$).

$$A = \varepsilon bC \qquad \text{Equation 17}$$

The kinetic of the studied adsorption processes can be modeled as pseudo-second-order. The equation implemented is reported in Equation 18, where t is the time (min), $q_t$ is the absorption capacity (mg·g) at time t, qe is the adsorption capacity at the equilibrium (mg·g), and k is the kinetic constant of the process (min·g·mg$^{-1}$).

$$\frac{t}{q_t} = \frac{1}{q_e} \cdot t + \frac{1}{k \cdot {q_e}^2} \qquad \text{Equation 18}$$

Equation 18 can be converted in a linearized graph plotting $t \cdot q_t^{-1}$ as function of t, the best fit line parameters slope (m) and intercept (b) can be used to calculate the kinetic constant of the process k as $m^2 \cdot b^{-1}$ and the equilibrium adsorption capacity $q_e$ as $m^{-1}$.[261]

*Microalgae biosorption test* – $Cu^{2+}$ adsorption capacity test was performed using 2.5 g·L$^{-1}$ adsorbent to treat 10 mg·L$^{-1}$ solution of $CuCl_2$. The tests were performed under magnetic stirring at 25 °C for 30 minutes working at pH 4.5. $Cu^{2+}$ concentration was assessed by ICP-OES, analyzing the non-adsorbed $Cu^{2+}$ separated by filtration with ultracentrifugation at 4500 rpm for 40 minutes with centrifugal filter units (Polyether sulfone, Amicon filter 10 KDa). The calculation of the theoretical adsorption of the hybrid material was performed as weighted average of the single constituting elements as reported in Equation 19. The calculation of the specific adsorption capacity of the microalgae in the hybrid materials was calculated subtracting the weighted contributes of the inorganic matrix using the invers formula of Equation 19.

$$\text{Theoretical adsorption} = \left(\text{TiO}_2\ \text{adsorption} \cdot \frac{\text{TiO}_2\ \%\text{wt}}{100}\right) + \left(C.vulgaris\ \text{adsorption} \cdot \frac{C.vulgaris\ \%\text{wt}}{100}\right) + \left(\text{SiO}_2\ \text{adsorption} \cdot \frac{\text{SiO}_2\ \%\text{wt}}{100}\right) \qquad \text{Equation 19}$$

*Photocatalytic test* –Rhodamine B (RhB) photocatalytic degradation tests were conducted at room temperature, using 20 mg of photocatalyst to treat 200 mL of a 7 $mg \cdot L^{-1}$ RhB aqueous solution. To establish the absorption/desorption equilibrium of RhB on the catalyst surface, the sample was kept in the dark conditions for 30 minutes, it was verified to have a negligible effect on the overall photocatalytic reaction. The suspension was magnetic stirred and UV irradiated 350 nm 50 $W \cdot m^{-2}$ (Osram ULTRA-Vitalux lamp 300 W). RhB photolytic phenomena were not registered without the catalyst. The photodegradation reaction progress was monitored at 5, 10, 15, 20, 30, 40, 50, and 60 minutes analyzing by UV-Vis spectroscopy (HachLange, DR 3900) at 554 nm, 3 mL 0.22 µm filtered aliquots, using distilled water as blank. The process could be approximated to a pseudo-first-order reaction, Equation 20, where t is the time, $C_0$ is the initial concentration, C is the concentration at time t, and k the kinetic constant.

$$\ln\frac{C_0}{C} = k \cdot t \qquad \text{Equation 20}$$

According to the Lambert-Beer law, Equation 17, the concentration could be calculated by the absorbance. The kinetic constant was determined as slope of the plot $\ln(C_0 \cdot C\text{-}1)$ versus time. The conversion was calculated after 60 minutes using Equation 21, where $A_0$ is the initial absorbance and $A_t$ is the absorbance at time t.

$$\text{Conversion}\ (\%) = \frac{A_0 - A_t}{A_0} \cdot 100 \qquad \text{Equation 21}$$

## 6.5. References


250. Fazal, T., Mushtaq, A., Rehman, F., Khan, A.U., Khan, A.U., Rashid, N., Farooq, W., Rehman, M.S., Rehman, M.S., Rehman, M.A., & Xu, J. (2018). Bioremediation of textile wastewater and successive biodiesel production using microalgae. Renewable & Sustainable Energy Reviews, 82, 3107-3126.

251. S. Qiu, Q. Li, X. Li, J. Ma, L. Wu, X. Xie, L. Wu, S. Askari, N. Dewangan, J. Ashok, X. Gao, S. Kawi, Biomass-Derived Carbon Materials for the Adsorption of Organic Pollutants. Adv. Sustainable Syst. 2024, 2300340. https://doi.org/10.1002/adsu.202300340

252. Darder, M., Colilla, A.M., & Ruiz-Hitzky, E. (2003). Biopolymer−Clay Nanocomposites Based on Chitosan Intercalated in Montmorillonite. Chemistry of Materials, 15, 3774-3780.

253. Zhongzhu Yang et al. Utilization of LDH-based materials as potential adsorbents and photocatalysts for the decontamination of dyes wastewater: a review. RSC Adv., 2016,6, 79415-79436. DOI https://doi.org/10.1039/C6RA12727D.

254. Shattar SFA, Foo KY. Sodium salt-assisted low temperature activation of bentonite for the adsorptive removal of methylene blue. Sci Rep. 2022 Feb 15;12(1):2534. doi: 10.1038/s41598-022-06254-z. PMID: 35169180; PMCID: PMC8847366.

255. Manel Bergaoui, Asma Nakhli, Jason Yi Juang Yeo, Felycia Edi Soetaredjo, Suryadi Ismadji, Jaka Sunarso, Mohamed Khalfaoui, Novel insights on the adsorption ability of bentonite and its chitosan composite: Deep understanding of antibiotics removal as hazardous agents, Journal of Molecular Liquids, Volume 387, 2023, 122550, ISSN 0167-7322, https://doi.org/10.1016/j.molliq.2023.122550.

256. Esmaeil Sheibani, Asieh Hosseini, Ali Sobhani Nasab, Kourosh Adib, Mohammad Reza Ganjali, Seied Mahdi Pourmortazavi, Farhad Ahmadi, Elnaz Marzi Khosrowshahi, Somayeh Mirsadeghi, Mehdi Rahimi-Nasrabadi & Hermann Ehrlich (2023) Application of polysaccharide biopolymers as natural adsorbent in sample preparation, Critical Reviews in Food Science and Nutrition, 63:16, 2626-2653, DOI: 10.1080/10408398.2021.1978385.

257. Farouq, R., & Yousef, N.S. Equilibrium and Kinetics Studies of adsorption of Copper ( II ) Ions on Natural Biosorbent.

258. Guastaferro, M.; Baldino, L.; Cardea, S.; Reverchon, E. Different Drying Techniques Can Affect the Adsorption Properties of Agarose-Based Gels for Crystal Violet Removal. Appl. Sci. 2023, 13, 463. https://doi.org/10.3390/app13010463.

259. Gholam Reza Mahdavinia, Fatemeh Bazmizeynabad & Behnam Seyyedi (2015) kappa-Carrageenan beads as new adsorbent to remove crystal violet dye from water: adsorption kinetics and isotherm, Desalination and Water Treatment, 53:9, 2529-2539, DOI: 10.1080/19443994.2013.870741.

260. Y.S Ho, G McKay, Pseudo-second order model for sorption processes, Process Biochemistry, Volume 34, Issue 5, 1999, Pages 451-465, ISSN 1359-5113, https://doi.org/10.1016/S0032-9592(98)00112-5.

261. Emmanuel D. Revellame, Dhan Lord Fortela, Wayne Sharp, Rafael Hernandez, Mark E. Zappi, Adsorption kinetic modeling using pseudo-first order and pseudo-second order rate laws: A review, Cleaner Engineering and Technology, Volume 1, 2020, 100032, ISSN 2666-7908, https://doi.org/10.1016/j.clet.2020.100032.

262. Luo, J., Han, G., Xie, M. et al. Quaternized chitosan/montmorillonite nanocomposite resin and its adsorption behavior. Iran Polym J 24, 531–539 (2015). https://doi.org/10.1007/s13726-015-0343-2.

263. Kumar, K., Dahms, H., Dahms, H., Won, E., Lee, J., & Shin, K. (2015). Microalgae - A promising tool for heavy metal remediation. Ecotoxicology and environmental safety, 113, 329-52.

264. United Nations A/RES/70/1, 2015. Transforming Our World: the 2030 Agenda for Sustainable Development, Governing through Goals: Sustainable Development Goals as Governance Innovation.

265. He J, Chen JP. A comprehensive review on biosorption of heavy metals by algal biomass: materials, performances, chemistry, and modeling simulation tools. Bioresour Technol. 2014 May;160:67-78. doi: 10.1016/j.biortech.2014.01.068. Epub 2014 Feb 4. PMID: 24630371.

266. Almomani, F., & Örmeci, B. (2016). Performance Of Chlorella Vulgaris, Neochloris Oleoabundans, and mixed indigenous microalgae for treatment of primary effluent, secondary effluent and centrate. Ecological Engineering, 95, 280-289.

267. Volesky B. Biosorption and me. Water Res. 2007 Oct;41(18):4017-29. doi: 10.1016/j.watres.2007.05.062. Epub 2007 Jun 23. PMID: 17632204.

268. M. Blosi, A. Brigliadori, I. Zanoni, S. Ortelli, S. Albonetti, A.L. Costa, Chlorella vulgaris meets TiO2 NPs: Effective sorbent/photocatalytic hybrid materials for water treatment

application, Journal of Environmental Management, Volume 304, 2022, 114187, ISSN 0301-4797, https://doi.org/10.1016/j.jenvman.2021.114187.

269. Baldisserri, C., Ortelli, S., Blosi, M., & Costa, A.L. (2018). Pilot- plant study for the photocatalytic/electrochemical degradation of Rhodamine B. Journal of environmental chemical engineering, 6, 1794-1804.

270. Ortelli, S., Blosi, M., Albonetti, S., Vaccari, A., Dondi, M., & Costa, A.L. (2014). TiO2 based nano-photocatalysis immobilized on cellulose substrates. Journal of Photochemistry and Photobiology A-chemistry, 276, 58-64.

# Chapter 7

*Final conclusions*

## 7.1. Final conclusions

In response to the European Green Deal action, the work here presented paves the way for the implementation of the eco-design approach to develop new advanced materials applicable in the field of clean technology for the protection of human health and the environment.

Three classes of advanced materials for different purposes have been successfully developed:

- Ag-based NPs with improved antimicrobial activity were explored for different applications through their incorporation into a set of nano-enabled products (NEPs).
- Noble metal nano-catalysts for the biomass valorization.
- Composite materials for wastewater remediation coupling photocatalytic and adsorption functionalities through inorganic nanophases embedded into natural-based biomasses.

***Ag-based antimicrobial NPs***

The principal results deal with the development of effective antimicrobial AgNPs through different eco-friendly methods. Several design options were explored to achieve the expected properties in the final NEPs. Water-based and low-temperature syntheses were developed implementing natural- or bio-derived capping agents. Three capping agents were selected to produce AgNPs and the Design of Experiment approach was implemented to select the optimal synthesis conditions and cope with the expected key performance indicators (KPIs). The workflow was advanced in agreement with the Safe and Sustainable by Design (SSbD) perspective addressing relevant physicochemical and functional characterizations to different life-cycle stages.

- *Quaternized hydroxyethyl cellulose-capped AgNPs*. From this synthesis, performed exploiting a natural-derived biopolymer as capping agent, it was obtained the most active variant AgHEC_6.4_1.4, able to fight effectively against Gram-negative and Gram-positive bacteria as well as enveloped viruses.
- *Curcumin-capped AgNPs*. Thanks to its intrinsic biocompatibility and antioxidant properties, curcumin exploited as a capping agent delivers low *in-vitro* cytotoxicity for this class of AgNPs. The selectivity against SARS-CoV-2, calculated as the ratio between the cytotoxic concentration and the viral inhibition concentration resulted to be excellent and improved also if compared with other commercial products.
- *Sodium surfactin-capped AgNPs*. Sodium surfactin is a biomolecule obtained from bacterial metabolism. Its application in the synthesis of AgNPs delivers a product with outstanding antimicrobial activity, coupled with a high *in-vitro* cytotoxicity. This is

probably due to the surfactant lysis of the external cell wall, but the high antimicrobial activity could be explored for applications within the safe concentration window.

Thanks to the antiviral studies against SARS-CoV-2 and BK polyomavirus an antiviral mechanism hypothesis was proposed. AgNPs antiviral mechanism involves the interaction of nanoparticles with the viral envelope inhibiting the attachment to cell's receptors. In fact, AgNPs exhibited excellent activity against SARS-CoV-2, which is an enveloped virus, but no activity was observed against BK polyomavirus, a non-enveloped virus. Furthermore, the antiviral action is effective when the virus is incubated with AgNPs before the inoculum into the target cells, inhibiting the virus from the attachment to cells receptor.

AgNPs were applied for the preparation of several NEPs, used as case studies such as antimicrobial textiles, paper, and biopolymeric films and scaffolds. Different results were observed depending on the capping agent allowing to define a structure-activity correlation and provide some guidelines for the material designers. For instance, curcumin-capped AgNPs coated textiles exhibited the best washing fastness and abrasion resistance in terms of silver release, while the best antimicrobial properties were obtained with the quaternized hydroxyethyl cellulose-capped AgNPs.

***AuPt-based NPs for catalysis***

Green chemistry principles, aligned with the SSbD approach, were applied to prepare AuPtNPs for catalytic applications. These catalysts find a strong application potential in the biomass valorization field, where the target is the production of chemical building blocks starting from biomass wastes. The results highlighted for gold-platinum core-shell and alloy structures a synergistic effect between the two noble metals improving the catalytic activity if compared with pure gold and platinum isolated nanoparticles. The improvement gained in the catalytic efficiency combined with the green approach of the synthesis pave the way for promising future improvements in the circular economy route of biomass waste valorization into higher added-value products.

***Naturally-derived inorganic/biomass composite materials for wastewater remediation***

Finally, naturally-derived materials and nanophases such as clays, hydrotalcites, and biopolymer were applied for the production of scaffolds to be applied in the wastewater remediation field. Clays and hydrotalcites layered structures and ion exchange capabilities were exploited for the adsorption of heavy metals and organic pollutants. Subsequently, to improve their handleability they were successfully embedded into biopolymeric renewable matrixes extracted from algae

such as k-carrageenan, chitosan, and agarose. These materials were freeze-dried into a solid scaffold and tested in the adsorption of simulated pollutants. The designed products effectively removed the tested pollutants following a pseudo-second-order kinetics and demonstrating tunable properties depending on the active phase and the embedding agents.

***Final remarks***

In conclusion, it was possible to apply different design strategies of a set of advanced materials in alignment with the overall eco-design principles and consistent with the SSbD approach. The exploitation of natural and bio-derived raw materials coupled with the no energy-intensive processes, water-based environment, and the use of non-hazardous reagents allowed the production of a variety of advanced materials and nano-enabled products with different fields of application, ranging from antimicrobial products, catalysis, and wastewater remediation. For each topic studied, it was possible to distill a set of guidelines. These guidelines assist in the sustainable design or eco-design of novel advanced materials and nano-enabled products. They aim to maximize or improve the risk/benefit profile with respect to the impact on humans and the environment.